DESIGN OPTIMIZATION OF PERMANENT MAGNET ACTUATORS

by

G. P. WIDDOWSON

An investigation conducted in the Department of Electronic and Electrical Engineering of the University of Sheffield under the supervision of Professor D. Howe, BTech., MEng., PhD., and Dr. T. S. Birch, BEng., PhD.

A thesis submitted for the degree of PhD., in the Department of Electronic and Electrical Engineering, University of Sheffield.

August 1992.

SUMMARY

This study describes the design optimization of permanent actuators, of both rotary and linear topologies. Parameter scanning, constrained single and multi-criterion optimization techniques are developed, with due emphasis on the efficient determination of optimal designs.

The modelling of devices by non-linear lumped reluctance networks is considered, with particular regard to the level of discretization required to produce accurate global quantities. The accuracy of the lumped reluctance technique is assessed by comparison with non-linear finite element analysis. Alternative methods of force/torque calculation are investigated, e.g. Lorentz equation, Virtual Work, and Maxwell Stress Integration techniques, in order to determine an appropriate technique for incorporation in a non-linear iterative optimization strategy.

The application of constrained optimization in a design environment is demonstrated by design studies and experimental validation on selected prototype devices of both topologies.

ACKNOWLEDGEMENTS

The author would like to express his thanks to his tutors Professor D. Howe and Dr. T. S. Birch for their guidance, encouragement and support throughout this thesis. He would also like to acknowledge the members of the Machines & Drives group, Sheffield University for their invaluable discussions and humour. Thanks is expressed to Rolfe Industries for their technical assistance throughout this thesis.

Special gratitude is expressed toward the S.E.R.C. for the award of a research studentship.

Finally, great thanks is expressed to Ellen for her patience.

CONTENTS

CHAPTER 1

INTRODUCTION

1.1 Review of Permanent Magnet Actuator Technology

Limited motion permanent magnet actuators are being increasingly applied in motion control systems[1.1], the range of applications embracing disc drive voice-coil motors[1.2], studio tracking actuators[1.3], artificial heart actuators[1.4] and raster scanning actuators[1.5], for example. Such electromagnetic devices have certain advantages over alternative pneumatic and hydraulic technologies, such as transportability, reduced running costs, greater reliability and better controllability[1.6], but are being considered principally for low power applications. Hydraulic and pneumatic actuators are effectively limited in power capability only by the maximum seal pressures and the mechanical strengths of the materials from which they are manufactured, and will remain the preferred format for high power applications[1.6]. In addition, pneumatic systems require air conditioning filters and a mechanism for the separation of oil and water and can suffer from large friction/stiction forces while hydraulic devices require oil processing facilities etc. and both of these technologies require compressors, storage facilities and extensive pipework which can substantially increase the overall cost of a system. However, the increasing actuation power levels attainable from polarized electromagnetic actuators based on rare-earth permanent magnets and incorporating improved soft magnetic materials, is helping electromagnetic devices to displace fluid based actuators in many applications.

In addition, alternative actuator technologies are emerging based on piezoelectric and magnetostrictive materials and electro-rheological fluids. For example, a piezo-electric 'travelling wave' motor is being developed by Daimler-Benz AG[1.7] for automatic

window winding for which it is suitable because of its thin, flat shape. A 'stationary wave' 'piezoelectric Micropush motor' is also under development[1.8], which has the advantage of ease of construction and high efficiency but it has the limitation of being undirectional. Piezoelectric actuators have been reported as having 5-10 times the energy/weight ratio compared with electromagnetic devices, and are capable of developing high torques at low speeds. One of the principal advantages of piezoelectric actuators is that they have no power loss in steady state operation. The main disadvantage is that a 20-50 kHz power supply is required to activate the 'stack' of piezoelectric material. In addition, because of their capacitive nature the voltage requirements are typically 500-1000 volts and only relatively small displacements are possible, which limits their application. Magnetostrictive actuators, using rare-earth materials such as terbium, are the magnet equivalent to piezoelectric devices and are a type of micro-actuator being employed as accurate sensors with displacement levels of 50-100μm and an accuracy of 0.1μm[1.9]. However, the manufacture of the magnetostrictive device remains extremely demanding and expensive. Furthermore, a large magnetic field is required to actuate the devices. Electro-rheological devices are being exploited for latching/clutch applications[1.10] for which permanent magnet devices compete such as bistable actuators[1.11]. The device uses an electrostatically controlled change in the viscosity of the rheological fluid to produce the large forces. High force, fast response Helenoid actuators, in which a solenoid is coiled like a spring, and the current carrying winding is wound along the root of one helix and then reversed so that current passes through the conductors in opposite directions in adjacent threads, and the magnetic flux is therefore additive across the working faces to produce a large specific force, have been cited for numerous applications, such as variable valve timing, for which alternative electromagnetic topologies cannot meet the specifications. However, these have been subjected to very little design optimization and testing[1.12]. Other actuation technologies include electro-chemical and thermal devices, which although still in the development stage are envisaged as being suitable for specific applications[1.13]. Fig(1.1) illustrates some of the actuator technologies described above.

With the emergence of high energy-product rare-earth based sintered and polymer-bonded permanent magnets, such as neodymium iron boron(NdFeB) and both 1:5 and 2:17 samarium cobalt ($SmCo_5$,Sm_2Co_{17}), the power levels at which permanent magnet excited actuators are being implemented continues to expand[1.14]. However, they are also required to meet more demanding specifications, and in many circumstances they cannot match the pneumatic or hydraulic actuators on the basis of power-to-weight or power-to-volume considerations alone. It is therefore essential that electromagnetic topologies offer other performance advantages such as increased reliability, better controllability and/or technological superiority, for example.

The use of direct drive, limited motion linear actuators has been most evident in applications for which a cheaper rotary motor in conjunction with a gearbox would previously have been used, such as in missile guidance systems in aerospace applications[1.15]. They have appeared due to their reduced component count, and their increased acceleration rate, which the geared systems cannot meet. The space previously reserved for the gearbox can also usually be utilised, effectively increasing the volume available for the active part of the actuator.

Alternative topologies of permanent magnet actuator can be categorized according to whether they are moving-coil, moving-iron, or moving-magnet, and whether the motion is linear or rotary. In the case of moving-iron and moving-magnet topologies, they can be further sub-divided into constant or variable airgap devices. However, within each of these groups there exists a large variety of geometries and design variants. For example, a linear voice-coil actuator may employ a shorted turn secondary in order to improve dynamic performance, which in turn alters the design procedure[1.16].

With the advances in Computer Aided Design and Analysis facilities over the last twenty years or so, sophisticated packages have been developed to ensure that prototype devices are manufactured only when their design has been predicted to meet the specification with reasonable confidence. These include 3-dimensional finite element analysis packages and actuation system simulation procedures. However, both these techniques

depend to a greater or lesser degree on the experience of the design engineer to identify the 'design space of interest' before detailed analysis is undertaken. In addition, almost all design facilities rely on repeated design/analysis based upon heuristic methods. One technique for reducing the 'design space' is by the implementation of expert system shells which in theory guide the user towards a feasible 'region of interest'[1.17]. However, optimal designs can also be obtained by the use of constrained optimization procedures, in which only the constraints on the design variables are declared and the parameters requiring optimization specified in order to minimize a performance related objective function.

The first publications concerning the application of constrained optimization methods to electrical machines were applied to high-power three-phase induction motors[1.18-1.22] where the objective was to maximize the efficiency in order to minimize running costs. However, due to the lack of computational power available to the design engineers they failed to displace design synthesis techniques, which usually involved graphical optimization processes, based upon either algebraic, lumped parameter or discrete finite element/finite difference field analysis. Further, a significant advantage of such traditional optimization methodologies is that they allow comparisons between alternative designs to be made by experienced engineers and not determined solely by a specified constraint in a computer program. In other words they permitted a form of sensitivity analysis. Another disadvantage with the constrained optimization methods which were evolving was that, in general, the most powerful procedures, i.e. those which required the fewest number of objective function evaluations - such as conjugate gradient and variable metric techniques, were the least reliable since they often located a local minimum instead of the global minimum.

More recently however, with the availability of enhanced computational power, there has been a resurgence of interest in the subject of constrained optimization and its application to various classes of electrical design problems, ranging from the minimization of magnet volume in synchronous machines[1.23], maximization of force

in variable airgap linear force motors[1.24], to the design of minimum volume high power transformers[1.25].

In the field of semiconductor device design, 'Simulated Annealing' algorithms have been used extensively to solve problems which were previously thought to be intractable due to their excessive computation requirements[1.26]. A Simulated Annealing algorithm was implmented in this research and is coupled to a direct optimization procedure in an attempt to reduce computation time.

The use of multi-criterion optimization techniques enables a number of objective functions to be investigated simultaneously, thus allowing the sensitivity of a design to be examined. The majority of previous research on the application of multi-criterion optimization to engineering problems has simply treated all but one of the objective functions as flexible inequality constraints[1.27], and altered the value of these constraints to test the sensitivity of the optimum design. The use of scalar weighting values has been used with limited success, due to the combinatorial increase in the number of optimization solutions required with the addition of extra objective functions to the problem[1.28]. Equation fitting methods have also been investigated so that compromise optimized designs can be obtained for a number of objective functions. However, Oszycka[1.29] found that the results varied greatly depending upon the order of the exponential fit to the objective functions, and recommended that a range of solutions be obtained with the final choice being made by the user.

If optimization procedures are to be used frequently for the design of electromagnetic devices, it is essential that accurate methods of determining global performance quantities of all the devices are available. However, as tighter tolerances are placed on both the accuracy of the field solution and the convergence of the optimization procedure, the computational effort increases significantly. Therefore, it becomes necessary to trade-off the reliability and accuracy of solutions with the time a user is prepared to wait before obtaining an acceptable design.

An important reason for the increased use of permanent magnets in limited motion actuators is the possible reduction in size and weight which can result. A common figure of merit for permanent magnets is the maximum energy-product, and fig(1.2) shows how this has increased rapidly over the last century due to the successive discoveries of the magnetic steel alloys, ceramic ferrites, and, most recently, the rare-earth alloy families of permanent magnets. Although the rare-earth alloy materials are much superior to the ferrite and Alnico types, their widespread application has been hindered to a large degree by their relatively high cost. Despite the fact that the price of certain raw materials is steadily reducing[1.30] as can be seen in table(1.1), the processing costs remain significant. The samarium cobalt and Alnicos are likely to remain expensive due to the high cost of cobalt, which has been designated a strategic material. Nd, and Fe on the other hand are relatively inexpensive. However, as is shown in table(1.2) the cost of NdFeB magnets remains high due to the processing cost[1.30]. This may reduce in the future, as the market matures, as is projected in fig(1.3), and as new processing techniques are developed, e.g. HDDR (Hydrogenation Disproportionation Desorption and Recombination), mechanical alloying, etc. Nevertheless, at present, unless there is a need for miniaturization, high efficiency, or fast dynamic response, ferrites are invariably selected. However, rare-earth magnet actuators are making an impact in specific applications, such as voice-coil motors for computer disc-drives for which fig(1.4) shows their influence on the sales of NdFeB as well as a forecast into the next century. It will be noted however, that in terms of the total sales value, permanent magnet generators/motors account for a larger proportion than voice-coil motors[1.30].

Raw Material	1984 Cost ($/kg)	1985 Cost ($/kg)	1989 Cost ($/kg)
Sm	132	165	143
Nd	77-88	77-88	60-66
Pr	77-88	77-88	NA
Co	24-27	24-27	33-35
Fe	0.44-1.10	0.44-1.10	0.44-1.10
Fe_2O_3	0.33-0.66	0.33-0.66	0.33-0.66
Sm_2O_3	55	66	176
Nd_2O_3	9	9	20
Pr_2O_3	38	38	38
FeB	NA	NA	5.50

Table 1.1 Magnet raw material prices [1.30]. NA indicates not available.

Material	Energy Product (kJ/m^3)	Magnet Cost ($/kg)	Raw Material Cost($/kg)	Estimated Raw Materials Cost as % of Selling Price	Cost /unit kJ/m^3 ($/$kJ/m^3$)
Ferrite					
Ceramic 8	15.6	3.3	0.81	24.6	0.095
Super 8	13.6	4.4	0.81	18.5	0.147
Cast ALNICO	23.3	40.7	9.0	22.0	0.792
Sintered SmCo	85.6	385.0	134.6	35.0	2.030
NdFeB					
Bonded	38.9	165.0	58.3	35.0	1.928
Sintered	136.2	209.0	52.5	25.0	0.696

Table 1.2 Average global producer's prices, cost per kJ/m^3, and raw material cost as a percentage of selling price. (Assumes the simplest shapes in mass production [1.30].)

Since, in principle, the minimum volume of magnet required for a device is inversely proportional to its maximum energy-product, the miniaturization of permanent magnet excited devices has continued with the emergence of rare-earth materials. An estimate of the highest theoretical maximum energy-product can be obtained by considering Permendur(50% Co). This has a saturation magnetization of approximately 2.4 T, which is the highest value at room temperature of any known material and gives an estimated maximum possible energy-product of 1146 kJ/m^3. However, this is never likely to be obtained because of the need for additional non-magnetic elements to cause the material

to develop coercivity. A realistic value for the maximum achievable energy-product at room temperature is 520 kJ/m^3[1.31], which can be compared with the current maximum of ~356kJ/m^3 obtained for the best grade of NdFeB[1.32].

It will be shown in chapter 6 that for both NdFeB and SmCo, the energy product increases approximately linearly as the operating temperature is reduced to approximately 77K at which point a spin reorientation occurs to degrade the performance[1.33]. However, the maximum energy product of praseodymium iron boron magnets continues to increase down to 4.2K, at which point it exhibits a remanence of 1.45T and a maximum energy product in excess of 400 kJ/m^3.

One of the major markets for NdFeB magnets is likely to be the aerospace industry where a high power/weight ratio is essential. However, its adoption has been hindered by two fundamental problems, viz:

1) Corrosion, which causes a degradation and loss of performance. However, various protective coatings can be applied to the surface of the magnet, such as ion vapour deposited aluminium, electroplated nickel and resins[1.30]. Maximum corrosion protection has been achieved by the combination of an epoxy resin coating applied over either the aluminium or nickel coating[1.30]. Alloying modifications through the addition of vanadium and molybdenum to NdFeB are also being investigated in order to make the material inherently more corrosive resistant[1.30].

2) The maximum operating temperature is limited to ~150^oC, because of the high temperature coefficients of both remanence and coercivity. Hence, SmCo magnets are preferred for high power, high ambient temperature applications. Nevertheless, special grades of NdFeB with higher operating temperatures are being developed by incorporating small amounts of cobalt to increase the Curie temperature and by the addition of elements such as aluminium, dysprosium, gallium and terbium to increase the intrinsic coercivity. The effect has been to increase the maximum operating

temperature to ~ $200^{o}C$ albeit at extra cost, a reduction in energy-product, and with the use of strategic elements[1.30].

1.2 Characteristics of Permanent and Soft Magnetic Materials

The characteristics of permanent magnet and soft magnetic materials are presented in appendix A.

1.3 Scope of Research

Chapter 2 discusses the use of lumped parameter network and discrete finite element techniques to establish the field distribution in permanent magnet excited devices, accounting for the effects of saturation and leakage flux. The level of discretization required for both these techniques is considered in relation to a limited motion voice-coil actuator. The incorporation of these field solution methods into design optimization procedures is also introduced. The limitations of the lumped parameter method in terms of accuracy of the field solution is discussed, together with the limitations of the finite element method in constrained optimization problems, in terms of computation time. Alternative numerical methods of calculating force are discussed and applied, the results being compared with measurements on a prototype device.

Chapter 3 assesses the use of constrained single-criterion optimization methodologies. It describes a number of techniques which have been implemented in order that an optimum actuator design can be identified in the minimum possible computation time, whilst at the same time being reliable and robust. The incorporation and minimization of multi-variable objective functions is described, including the constrained minimization of the copper loss of a voice-coil actuator, as well as methods of dealing

with constraints and bounds on the variables. Techniques based upon non-linear simplex minimization[1.34] and variable rotation[1.35] are presented, as well as a novel combination of a direct search method to a Simulated Annealing algorithm in order to reduce the computation requirement.

Chapter 4 uses the procedures established in Chapter 3 to solve representative multi-criterion optimization problems. The various techniques are compared to determine their effectiveness.

Chapters 5 and 6 describe the application of the optimization techniques to two topologies of actuator, a linear voice-coil actuator to be operated at liquid helium temperature for a telescope application and a toroidally wound moving-magnet rotary actuator. Comparisons of the constrained optimization methods are presented and also compared with a very simple parameter scanning approach. In addition, the accuracy of the lumped reluctance method for both devices is considered.

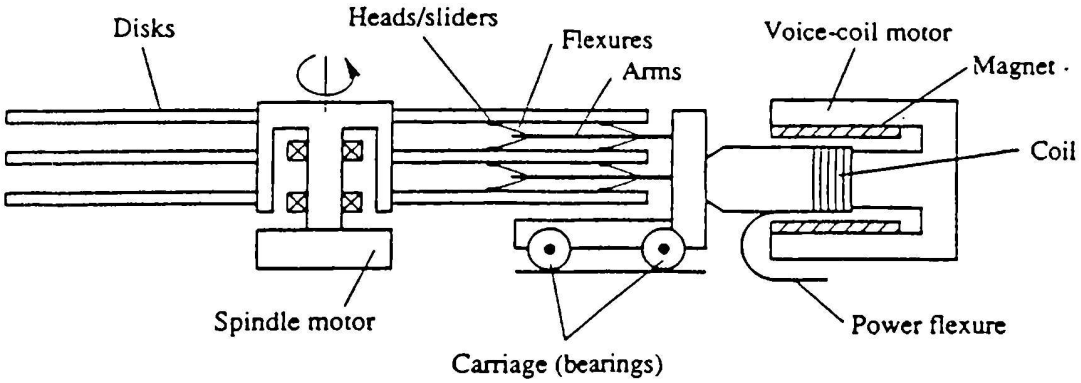

Fig 1.1.a Schematic cross-section view of a disc-drive mechanism with voice-coil actuator.

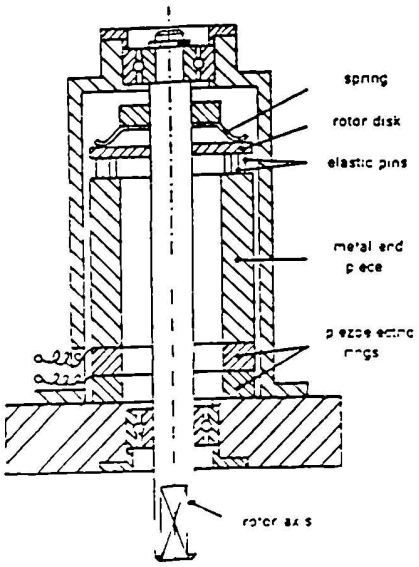

Fig 1.1.b Cross-section view of Philips micro-push motor[1.8].

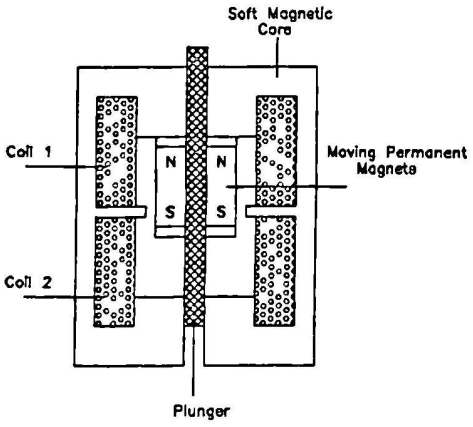

Fig 1.1.c Schematic cross-section through a bistable permanent magnet actuator.

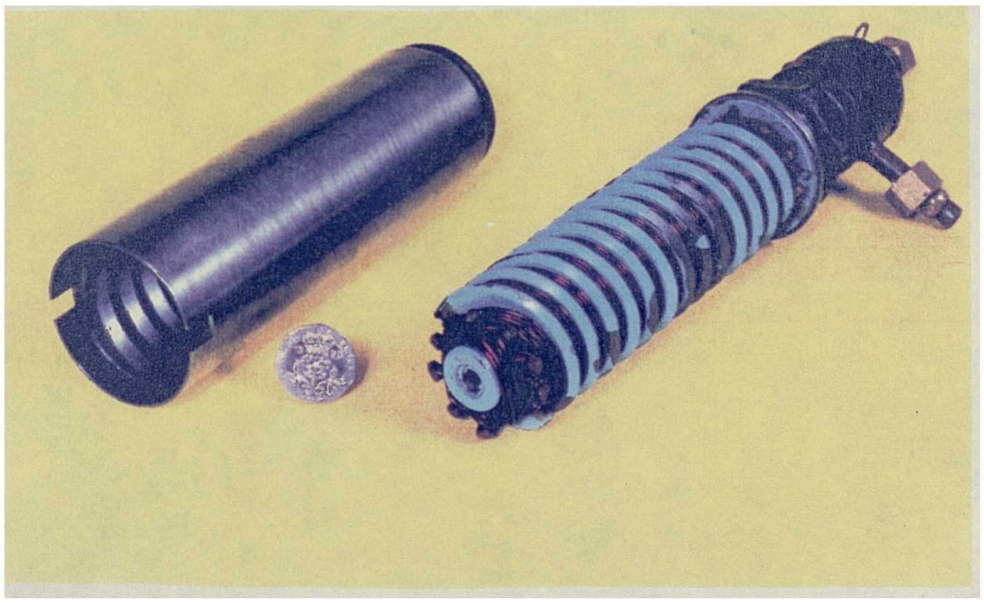

Fig 1.1.d Helenoid Actuator.

Fig 1.1 Alternative actuator technologies.

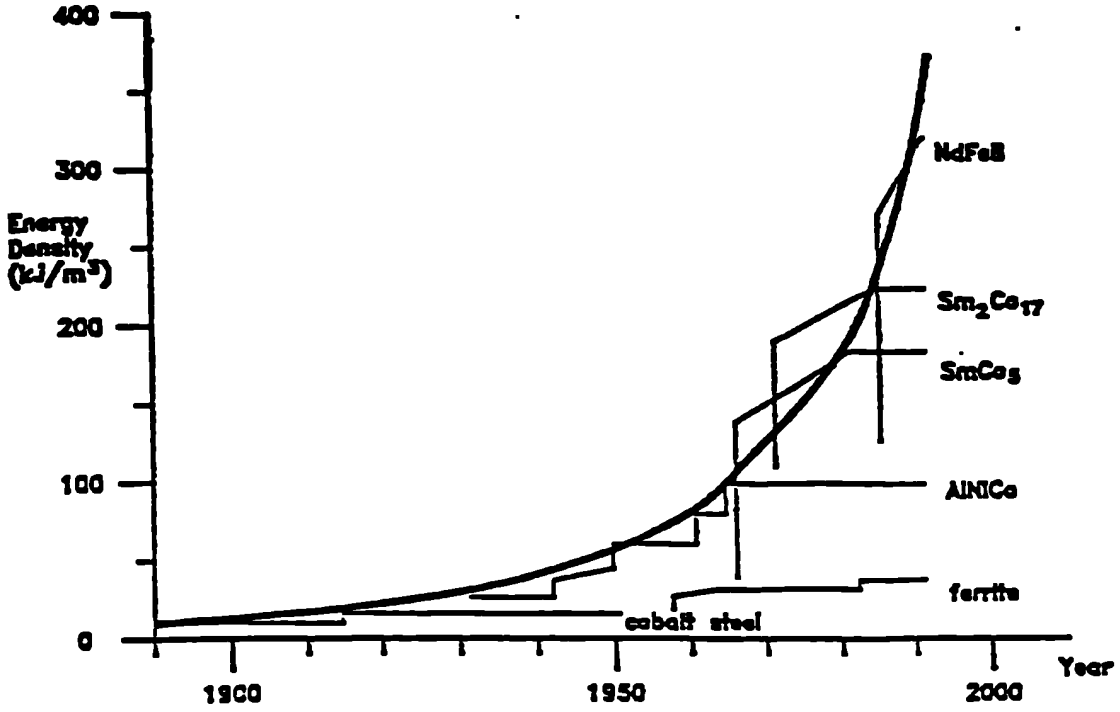

Fig 1.2 Increase in the maximum energy-product during the last century.

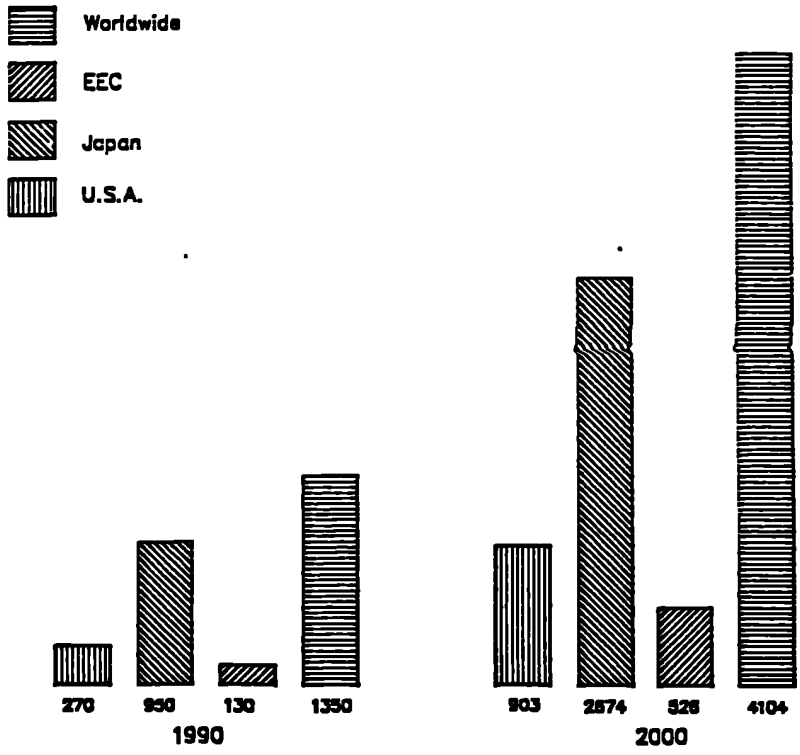

Fig 1.3 Actual and projected sales of permanent magnets(in tonnes), in 1990 and 2000[1.30].

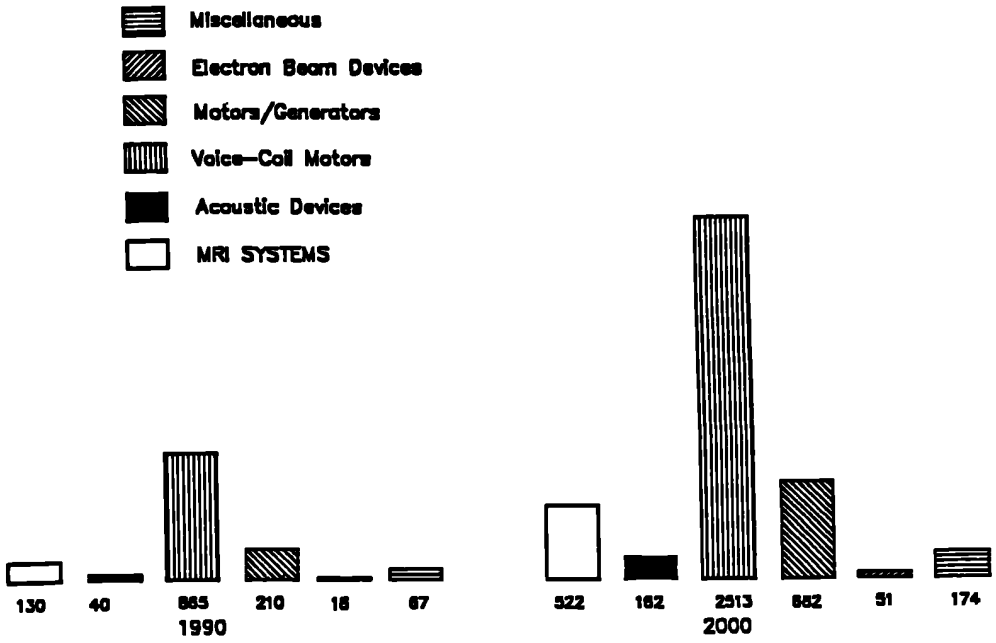

Fig 1.4 Actual and projected sales of permanent magnets(in tonnes) by application, in 1990 and 2000[1.30].

CHAPTER 2

ELECTROMAGNETIC MODELLING TECHNIQUES

2.1 Introduction

In the design of permanent magnet actuators, the static electromagnetic field distribution must be calculated with sufficient accuracy that the global quantities by which most devices are compared, such as force, torque, inductance and coil flux linkages, can be reliably estimated. For certain applications it may be sufficiently accurate to assume linear magnetic material characteristics and that the flux is totally contained within the magnetic circuit, such that flux fringing and leakage can be disregarded. Under these conditions, simple algebraic equations may be utilised to compute the field distribution. However, in general this approach is not sufficiently accurate, especially if an optimum design is required, since the optimization of most objective functions requires maximum utilisation of the soft magnetic material and consequently operation in the non-linear region of its initial magnetization characteristic.

Whilst the finite element numerical method can be successfully employed in determining the global parameters of a single design[2.1], their computational requirements often make them inappropriate for incorporation in a repetitive optimization procedure[2.2]. An alternative approach is to employ a much less computationally demanding lumped reluctance model during the main optimization routine and then switch to a more refined finite element model in the vicinity of a local optimum. This chapter describes the development of suitable lumped parameter models for a linear voice-coil actuator and discusses the sensitivity of the results to the number of lumped reluctances used in the network. Two alternative techniques for determining the effective areas and lengths of

the lumped reluctance elements are presented and their effects upon the results established. The lumped parameter solutions are compared with experimental and finite element results, and in addition, methods of electromagnetic force calculation, using the rate of change of stored energy with displacement[2.3] and the Lorentz equation are also compared, to establish if either has a significant advantage in terms of accuracy and computational effort.

2.2 First Order Linear Lumped Circuit Analysis

In its simplest form the lumped parameter technique uses linear algebraic expressions to establish the governing equations for the electromagnetic design. For example, in the circuit of fig(2.1), assuming the soft iron magnetic material is infinitely permeable and there is no leakage or fringing flux, then the magnet will be operating at a single working point (B_m, H_m) and the following expressions can be derived.

i) Assuming flux continuity in the magnetic circuit gives

$$B_m A_m = B_g A_g \tag{2.1}$$

ii) Applying Amperes law to the magnetic circuit gives

$$-H_m L_m = H_g L_g + NI \tag{2.2}$$

iii) For a permanent magnet exhibiting a linear second quadrant demagnetization characteristic the B/H relationship can be expressed as

$$B_m = B_r + \mu_o \mu_r H_m \tag{2.3}$$

Thus, the open circuit airgap flux density, B_g, can be obtained by combining equations(2.1,2.2 and 2.3) and setting NI=0, giving:

$$B_g = \frac{B_r}{\frac{A_g}{A_m} + \mu_r \frac{L_g}{L_m}} \tag{2.4}$$

Alternatively, for devices where the magnet has the same cross sectional area A_m to that of the airgap A_g, such that the flux is neither focused nor defocused into the airgap, then the expression for B_g becomes:

$$B_g = \frac{B_r}{1 + \mu_r \frac{L_g}{L_m}} \tag{2.5}$$

The resulting excitation force acting upon a conductor in the airgap can be expressed by the Lorentz equation as:

$$F_e = B_g \, l_c \, I_c \tag{2.6}$$

Correspondingly, for a rotary motion device, the excitation torque:

$$T_e = B_g \; l_c \, I_c \, r_w \, p \tag{2.7}$$

where I_c is the current in the conductor,

l_c is the total length of conductor in the airgap magnetic field,

r_w is the average torque radius of the winding,

p is the number of poles

Hence for the linear system $F_e = \frac{B_r}{\frac{A_g}{A_m} + \mu_r \frac{L_g}{L_m}} \, l_c \, I_c$ (2.8)

In order to avoid demagnetization of the permanent magnet, caused by the armature reaction mmf of the excitation coil driving the magnet beyond the knee of its hysteresis loop, defined by the value H_{lim} shown in fig(A.3), the magnet must have a minimum magnet length $L_{m_{min}}$. This can be estimated by rearranging equations(2.1,2.2 and 2.3) and by setting $H_m = H_{lim}$ to give

$$L_{m_{min}} = -\frac{B_r A_m L_g}{\mu_o H_{lim} A_g} - \frac{\mu_r A_m L_g}{A_g} - \frac{NI}{H_{lim}} \tag{2.9}$$

In practice there will be some degree of saturation of the iron yokes, whilst some of the magnet flux will pass into leakage paths. To account for these departures from the ideal the above approach can be refined by introducing leakage and saturation factors K_1 and K_2 where:

$$K_1 = \text{leakage factor} = \frac{\textit{total flux in magnet}}{\textit{useful flux in the airgap}} \tag{2.10}$$

and $$K_2 = \text{saturation factor} = \frac{\textit{magnet mmf + mmf dropped in iron}}{\textit{mmf required for the airgap}} \tag{2.11}$$

giving: $$B_m A_m = K_1 B_g A_g \tag{2.12}$$

$$-H_m L_m = K_2 H_g L_g + NI \tag{2.13}$$

and hence $$L_{m_{min}} = -\frac{B_r A_m L_g K_2}{\mu_o H_{lim} A_g K_1} - \frac{\mu_r A_m L_g K_2}{A_g K_1} - \frac{NI}{H_{lim}} \tag{2.14}$$

K_1 and K_2 are dependent upon the topology of the device and the working point of the soft magnetic material. K_1 can be calculated from estimated values for the permeance of the predominant leakage paths[2.4,2.5,2.6,2.7] and appendix B gives expressions for the permeance of typical path geometries. With the judicious use of such permeances

and by estimating the level of saturation on an iterative basis the field distribution can be calculated with reasonable accuracy.

A typical procedure used for the first order design calculations of a voice-coil actuator as in fig(1.1) is as follows:

1) From the circuit geometry calculate the magnet working point (B_m,H_m) from equations (2.1,2.2 and 2.3) and the open circuit flux levels in the various parts of the device, i.e. the airgap, the magnet and the soft iron yoke assuming initially that $K_1 = K_2 = 1.0$.

2) Calculate the mmf dropped in the iron of the magnetic circuit from the first quadrant characteristic of the soft magnetic material and estimate values for the constants K_1 and K_2.

3) Recalculate the magnet working point.

4) Recalculate the circuit flux levels for the new value of magnet working point.

5) Compare the old and new values for the airgap flux density. If they are not within a pre-specified tolerance then recalculate the values of K_1 and K_2 and return to step 3. If the two values correspond to within the tolerance then proceed to the calculation of the force on the moving coil.

Experience is required by the design engineer to determine the principal and leakage flux paths in the electromagnetic circuits being analysed. Once established, the values of the lengths and cross-sectional areas for the reluctance elements have to be determined. This may be straightforward for most reluctances where the flux does not change direction, or for elements where there is no flux focusing or defocusing. The modelling of 'corner' effect or flux focusing in axisymmetric topologies can be performed using two alternative methods.

Method A) The length of the flux path is assumed to be through the mean length, i.e. the average of the longest and shortest lengths, and the area calculated at this position.

Method B) As illustrated in fig(2.2), determine an effective area for the reluctance from the average of the inward and outward faces of the reluctance element, i.e.

$$A_{eff} = \frac{A_1 + A_2}{2} \tag{2.15}$$

and the effective length calculated from the volume of the element

$$L_{eff} = \frac{V}{A_{eff}} \tag{2.16}$$

2.3 Automatic Lumped Parameter Network Solutions

If the magnetic circuit needs to be discretized into a complex network which becomes too cumbersome to be handled manually by the procedure established above, then an automatic solution is required. A lumped parameter field solution technique has been developed at the University of Sheffield into a CAD package 'MAGNET', the theory of which is presented in appendix C. This package has been employed in the design studies for the test models described in this chapter and throughout the thesis.

One criterion that is important to the applicability of any numerical field solution technique is the computational effort required. This is especially pertinent if the technique is to be combined with a computationally demanding optimization procedure. The lumped parameter solutions using 'MAGNET' were iterated until the levels of flux density and magnetization field in the non-linear elements correlated with the values from the non-linear material characteristic to within 0.1%, the solution was then assumed to have converged. Clearly, the number of iterations required before the field distribution

is computed to the necessary tolerance depends upon the initial conditions assigned to the network elements. Therefore, for consistency the initial conditions were, in all cases, B=0.0T, H=0.0A/m, mmf =0.0 A-turns and flux =0.0.Wb.

2.4 Finite Element Determination of the Field Distribution

Whilst a lumped parameter model can frequently be used in first order design, to obtain a more accurate evaluation of the field distribution a finite element solution is frequently performed. This requires no pre-conceived flux paths and can model the effects of flux leakage in the device as well as the non-linear properties of the materials and the permanent magnets. Essentially, the finite element technique reduces the solution of the field problem to the inversion of a matrix of finite order, which results in an approximation of the field. Therefore, the accuracy of the field solution increases as the number of equations(nodes or elements) increases. However, as the matrix becomes larger so does the numerical computation required to invert it and therefore, it usually becomes a trade-off between accuracy required of the field solution and execution speed.

A suite of finite element programs developed at Sheffield University is used to obtain the accurate finite element field solutions of all the actuators described in this thesis. 'MESHGEN' is a mesh generation package that allows a problem to be discretized into first order triangular elements, whilst 'MAGSTAT' solves the magnetostatic vector potential field solution for a two dimensional planar or axisymmetric problem.

2.5 Calculation of Forces in Non-Linear Systems

For some topologies of actuator, the static electromagnetic force produced cannot be accurately estimated using the Lorentz equation since the device may have a significant

component of saliency force. In these circumstances, and in order that comparisons can be made with the Lorentz equation results, alternative techniques have to be employed such as the change in stored energy with position or the Maxwell Stress method.

i) Change in Stored Energy

The force in a non-linear electromagnetic system can be determined using the principle of virtual work. That is, the stored energy is calculated from the static electromagnetic field solution, then the model of the device is altered to simulate a small movement of the system. If the system energies are calculated in both positions, the average force or torque during the move can be evaluated from the principle of conservation of energy. However, the energy must be calculated for a constant current displacement. For this to be possible, energy has to be supplied to the system to maintain a constant current.

Effectively $$\text{force} = \frac{d W_t}{dx} \text{ or torque} = \frac{dW_t}{d\theta} \tag{2.17}$$

and $$W_t = W_m - W_s \tag{2.18}$$

where

W_t = total energy,

W_m = stored magnetic energy,

W_s = supplied energy.

The energy supplied by the coils can be calculated by adapting Faraday's law governing the back-emf induced in a coil; i.e.

$$e = -\frac{N d\varphi}{dt} \tag{2.19}$$

Therefore the electrical power $P = ei = N\frac{d\varphi}{dt} I$ (2.20)

and the electrical input from the supply is given by

$$dW_s = \int_{t1}^{t2} ei\, dt = \int_{\varphi_1}^{\varphi_2} NI\, d\varphi \tag{2.21}$$

$$dW_s = NI\,(\varphi_1 - \varphi_2) \tag{2.22}$$

The stored magnetic energy can be separated into three distinct parts: associated with the airgaps, permanent magnets and the soft iron regions respectively.

The stored energy in the airgap permeances is represented by the shaded area in fig(2.3.a) and is given by

$$W_{m_p} = \frac{B_g^2}{2\mu_o} \tag{2.23}$$

The stored energy in the permanent magnet is represented by the shaded area in the second quadrant demagnetization characteristic of fig(2.3.b). For a material with a linear second quadrant, the energy in the magnet is given by:

$$W_{m_m} = \frac{(B_r - B_m)^2}{2\,\mu_o\,\mu_r} \tag{2.24}$$

The stored energy in the non-linear soft magnetic material, is represented by the shaded area in fig(2.3.c), and can be calculated from the expression

$$W_{m_{nl}} = \int_0^B H\, dB = BH - \int_0^H B\, dH \tag{2.25}$$

With the use of cubic splines to represent the non-linear material characteristics, as described in appendix C, equation(2.25) becomes

$$W_{m_{nl}} = \int_{H_n}^{H} B\,dH + \int_{H_{n-1}}^{H_n} B\,dH \ldots\ldots \int_{0}^{H_1} B\,dH \qquad (2.26)$$

And hence $$W_t = W_{m_{nl}} + W_{m_p} + W_{m_m} - W_s \qquad (2.27)$$

This technique can be used with either lumped reluctance or finite element field solutions, although with the finite element method the disadvantage that two separate field solutions are required to obtain a displacement of the rotor can be computationally demanding.

ii) Maxwell Stress Method

Another popular technique used in conjunction with the finite element method to calculate the force is the Maxwell Stress Integration. It has the advantage over the energy technique that only a single field solution is required to predict the force. However, the technique relies upon an accurate representation of the flux density distribution in the airgap of the device and can be erroneous if the flux density changes rapidly in this region[2.8]. It has also been reported[2.9] that the technique gives a greater accuracy for finer meshes in the airgap and if the triangular elements are equilateral in this region.

2.6 Validation of Modelling Techniques

2.6.1 Design of a Prototype Actuator

The methods described in this chapter were utilised in the design analysis of a linear voice-coil actuator illustrated in axisymmetric cross-section in fig(2.4). The actuator was designed to meet the specification given in table(2.1) and was undertaken in collaboration with British Aerospace plc, Electro-Optics division.

Parameter	Limit
Maximum O_d (mm)	40.0
Maximum W_s (mm)	44.0
Stroke (mm)	12.0
Maximum Copper loss (W)	20.0
Maximum Current Density ($A\ mm^{-2}$)	40.0
Force Required (N)	32.0

Table 2.1 Specification for a long stroke axisymmetric voice-coil actuator.

The major constraint on the design was the limited power supply available to the actuator which restricted the copper loss to be a maximum of 20 Watts at 20^o C. This specific topology of voice-coil actuator was chosen because a linear force/stroke profile was required. An axisymmetric(cylindrical) design was chosen so that the best coil utilisation factor could be obtained. Initially, an open-ended actuator, fig(2.5) designed by British Aerospace and similar to a disc drive voice-coil actuator, was analysed. This device was designed by trial-and-error techniques for the same force output specification, but the envelope dimensions O_d and W_s were constrained at 36.0mm and 24.0mm and the stroke length still being 12mm. However, the design is illustrative of this topology of actuator which proved to be unsuitable for this long stroke application as the device suffered from significant saliency forces due to the axial asymmetry of the soft magnetic circuit. The influence of this saliency force is illustrated in the force/displacement results given in fig(2.6). Therefore, a totally enclosed magnetic circuit design was chosen, to minimize the static magnetic circuit reluctance, thus leading to a higher airgap flux density. This necessitated the drilling of four small holes in the lid of the device so that the force

produced on the moving coil could be utilised. By altering the main dimensions and using the simple design strategy of section(2.2) many feasible designs were obtained from which the design of table(2.2) was selected to give the lowest estimate of the copper loss for the specified force and stroke. Fig(2.7) shows a photograph of the prototype actuator.

Parameter	Value
O_d (mm)	40.0
W_s (mm)	44.0
I_d (mm)	34.2
L_g (mm)	2.8
L_m (mm)	5.3
IY_d (mm)	18.0
H_{cu} (mm)	24.0
L_{cap} (mm)	4.0
Number of Turns	1885
Permanent Magnet Material	$Sm_2 Co_{17}$ $B_r = 1.07T$, $\mu_r = 1.1$
Soft Magnetic Material	Mild Steel
Copper Loss (W)	19.40
Resistance (Ω)	100.2
Full Load Current (Amps)	0.44

Table 2.2 Dimensions, material characteristics and predicted performance for the prototype voice-coil actuator.

2.6.2 Testing of the Prototype Actuator

Using a calibrated strain gauge and force transducer, the force acting on the moving coil was measured as a function of the winding current and displacement. The results are illustrated in fig(2.8), where it can be seen that a current of 0.46 Amps was required to produce the full load force of 32N, an increase of 4.5% over the design value. The force/displacement characteristic is greatly improved compared to the initial actuator design, this being due to the symmetry of the magnetic circuit. The average radial airgap flux density was measured using a search coil and integrating flux meter such that by moving the search coil axially in discrete step lengths and measuring the change in flux

linkages, the circumferential averaged airgap flux density profile could be determined as shown in fig(2.9). The figure shows that the measured flux density is some 6.7% lower than that predicted using the simple lumped parameter method described in section(2.2), which explains why the full-load current was higher by a similar margin of error.

During the modelling stage, a radially magnetized ring magnet was assumed, but in practice the magnet was fabricated from six diametrically magnetized 60^o magnet arc segments. In addition, the holes drilled in the endcap were not modelled. An estimate of the reduction in airgap flux density caused by the magnet segmentation was made by measuring the radial airgap flux density around the circumference of the airgap, at an axial plane corresponding to the centre of the stroke. However, since this was only possible using a Hall-probe and Gauss-meter, and due to the thickness of the Hall-probe, this required the removal of the soft magnetic end-plate. A new finite element field distribution was calculated assuming an ideally magnetized actuator but with the end-plate removed. Fig(2.10) compares the measured circumferential values with the value determined from the finite element solution, where it can be seen that the finite element value is greater than that measured, and that the measured value has an almost periodic nature every 60^o. For these test conditions the average reduction in the measured airgap flux density is 6.3% from the theoretical predictions which is a similar percentage to the average reduction noted above, suggesting that the magnet segmentation was the main reason for the discrepancy between test and predicted performance.

2.6.3 Comparison of Automatic Lumped Parameter and Finite Element Techniques with Measured Results

The non-linear lumped parameter technique was used to calculate the static field distribution of the voice-coil actuator and predict the force produced on the moving coil. The network used to predict the field solution was subjected to varying degrees of discretization, and figs(2.11 and 2.12) show the most complex networks considered and illustrate the flux paths modelled. As the actuator was totally enclosed, any external leakage was neglected. For the Lorentz force calculation, based on an open circuit flux density value, the symmetry about the axial length and central axis, required only one quarter of the actuator to be modelled as shown in fig(2.11). For the force calculation based on the rate of change of stored energy, the mmf sources due to the current in the conductors needed to be modelled and therefore the model of fig(2.12) was used, representing one half of the device. The Lorentz force was calculated initially for only elements 1-14 in the model and then including elements 15-22 in fig(2.11). For these cases the airgap flux density used in the Lorentz equation(2.6) was the average value for the flux density through the permeance elements under which the coil was situated. Increasing the model complexity reduced the average flux density and corresponding force prediction by some 3.2% as shown in table(2.3). For the energy method it was necessary to adjust the network to simulate small coil displacements over the central 5mm of the stroke length. From table(2.4) it can be seen again that increasing the model complexity reduced the average flux density calculated but increased the predicted force by 8.1%, this probably being caused by numerical errors in the calculation of the small energy differences.

Fig(2.13) shows the predicted and measured force as a function of excitation current. The Lorentz force equation, based on open-circuit flux calculations shows an overestimate compared with tests but the energy method underestimates and is much worse. Even when the number of lumped parameter elements was increased from 27 to 42, the force was still underestimated by some 24%.

Fig(2.13) and table(2.5) show that as the current is increased, the energy technique agrees more closely with the experimental results, whereas the Lorentz equation solutions, which do not account for the increased saturation of the iron due to the 'armature reaction' flux of the coil, overestimate the force on the moving coil. For example, at full load current the error in the prediction of the force was 6.1% and 23.8% for the Lorentz equation and energy techniques respectively. However, at 20% overload current these have changed to 9.7% and 22.8% respectively.

Tables(2.3 and 2.4) also compare the number of iterations required to achieve a 0.1% convergence criteria in the field solution for each model. It is evident that the energy method required a significantly greater number of iterations in comparison with the Lorentz equation, i.e. (14 compared to 70), to solve the corresponding network models. The main reasons for this are that firstly, the energy technique model requires two solutions to be able to estimate the force, and also that a greater number of reluctances were required in the model due to the modelling of the current sources. It would appear from tables(2.3, 2.4 and 2.5) that there is no significant advantage in either of the two methods for estimating the areas and lengths of the reluctances.

Fig(2.14) shows the force calculation determined from the stored energy and Maxwell Stress Integration techniques used in conjunction with the finite element method. The effect of the finite element mesh density was examined by increasing the number of finite elements and recalculating the stored energy, integrated over the whole mesh. Fig(2.15) shows that the mesh was sufficiently refined with 7220 elements. The results of the energy method are now in much closer agreement than those obtained from the lumped parameter model and again, the results become more accurate as the current in the conductors is increased with the error in the calculation being ~8% at full load current. The results from the Maxwell Stress Integration method were not quite as accurate as the energy technique but were still within 15% of the experimental measurements at full load.

Elements in Model	Areas and lengths calculated by method A. *			Areas and lengths calculated by method B. *.		
	B_g (T)	Force by Lorentz equation (N)	Number of iterations	B_g (T)	Force by Lorentz equation (N)	Number of iterations
1-14	0.63	33.0	11	0.65	34.1	11
1-21	0.61	32.0	14	0.63	33.0	14

Table 2.3 Number of solutions required and accuracy for the Lorentz equation method. The values quoted for the force are calculated for full-load current.

Elements in Model	Areas and lengths calculated by method A. *			Areas and lengths calculated by method B. *		
	B_g (T)	Force by energy method (N)	Number of iterations	B_g (T)	Force by energy method (N)	Number of iterations
1-27	0.60	22.3	54	0.59	22.9	54
1-33	0.58	22.8	62	0.58	23.4	62
1-42	0.57	24.1	70	0.56	24.4	70

Table 2.4 Force calculation results and number of solutions required from the stored energy technique at full-load current

Current (Amps)	Areas and lengths calculated by method A. *		Areas and lengths calculated by method B. *	
	Force by Lorentz (N)	Force by energy method (N)	Force by Lorentz (N)	Force by energy method (N)
0.1	7.6	4.4	7.4	4.6
0.2	15.2	9.8	15.1	10.1
0.3	22.8	15.3	22.8	15.8
0.4	30.4	21.6	30.7	21.8
0.5	38.0	29.1	38.5	29.4

Table 2.5 Comparison of the force calculation techniques for varying current level in the voice-coil actuator.
* See section(2.2) for details of the two methods of estimating lengths and areas.

2.7 Conclusions

It has been demonstrated that for the topology of actuator for which the lumped parameter solver MAGNET has been applied, the technique can calculate the field distribution with reasonable accuracy.

The accuracy in the calculation of the force by the method of rate of change of stored energy, with a lumped parameter technique is dependent upon the degree of discretization of the network model. However, it is notable from figs(2.13 and 2.14) that the method constantly underestimates the levels of force possible from the actuator. At full load current the best estimate using this technique is still 23.8% less then the measured value.

It is also evident that whenever possible the method based on the Lorentz equation should be used since not only does it produce greater accuracy in the calculation of the excitation force, but it also requires a significantly lower number of lumped reluctances in the network model and a reduced number of iterations in its solution.

The main conclusion from this study is that the lumped parameter method will be incorporated into the optimization procedures to be discussed in detail in chapter 3.

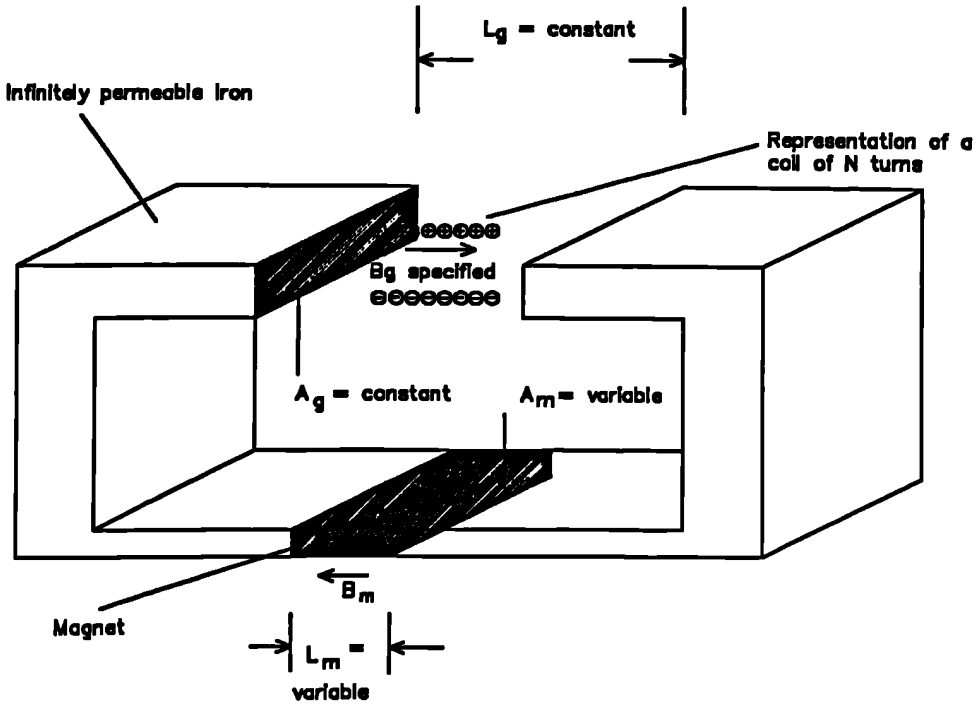

Fig 2.1 Infinitely permeable magnetic circuit.

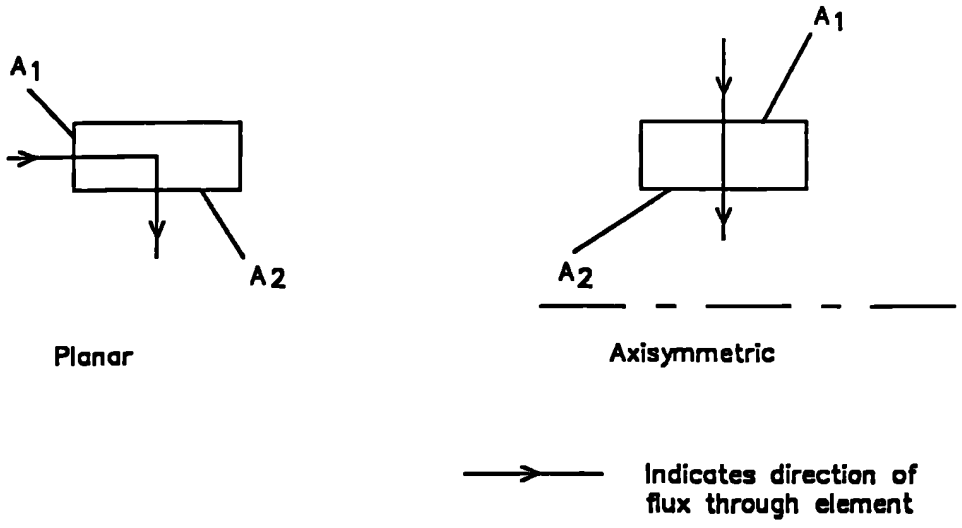

Fig 2.2 Lumped parameter reluctance elements with different inward and outward face areas.

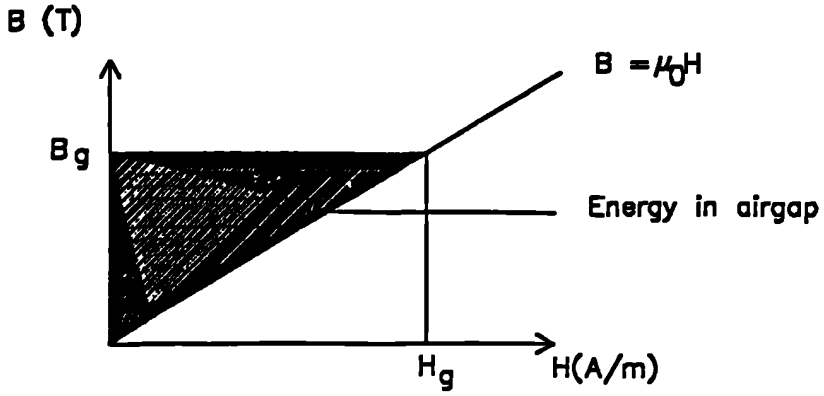

Fig 2.3.a Stored magnetic energy associated with the airgaps.

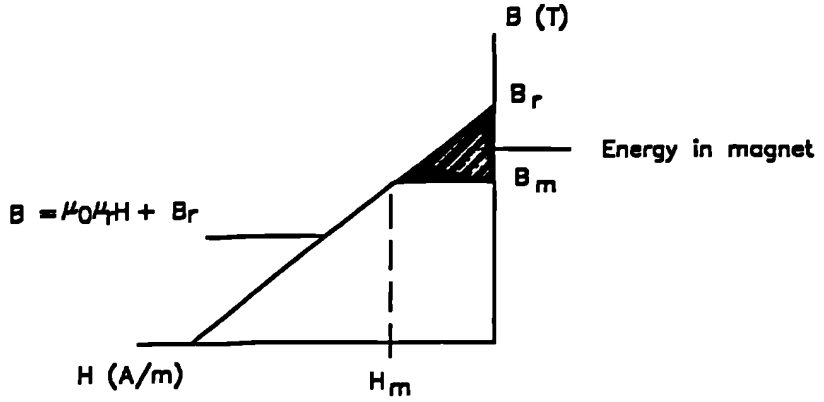

Fig 2.3.b Stored magnetic energy associated with the permanent magnets.

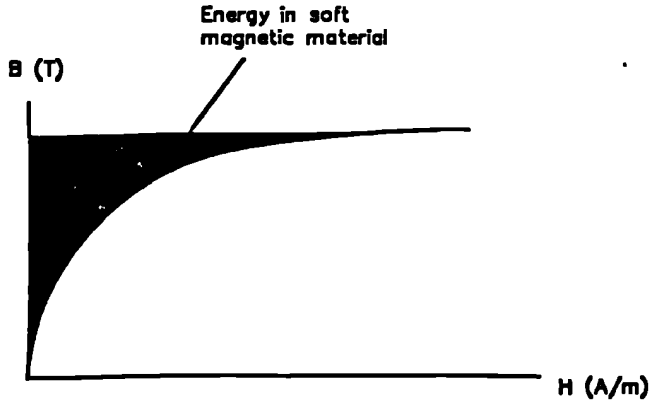

Fig 2.3.c Stored magnetic energy associated with the soft magnetic material.

Fig 2.3 Stored magnetic energies associated with the airgaps, permanent magnets and soft magnetic materials.

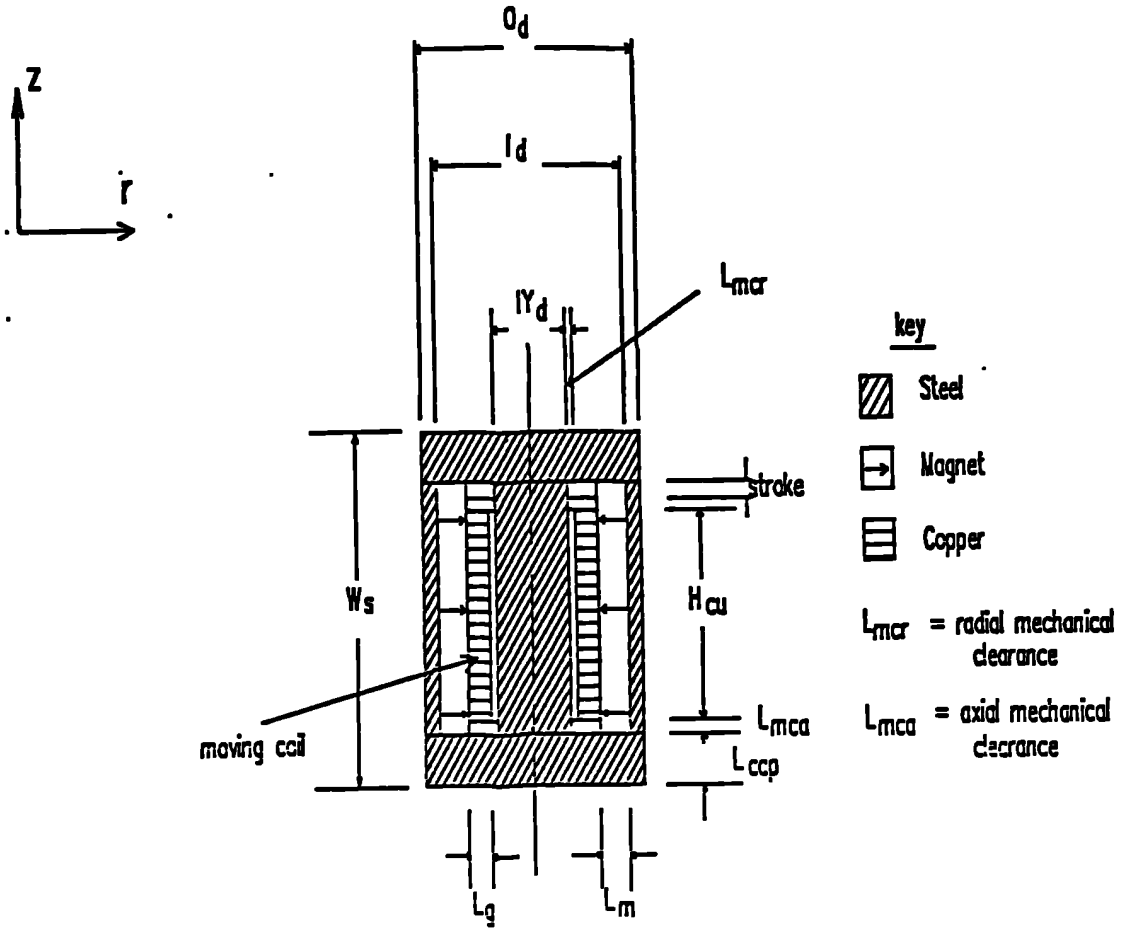

Fig 2.4 Axisymmetric cross-section of linear voice-coil actuator

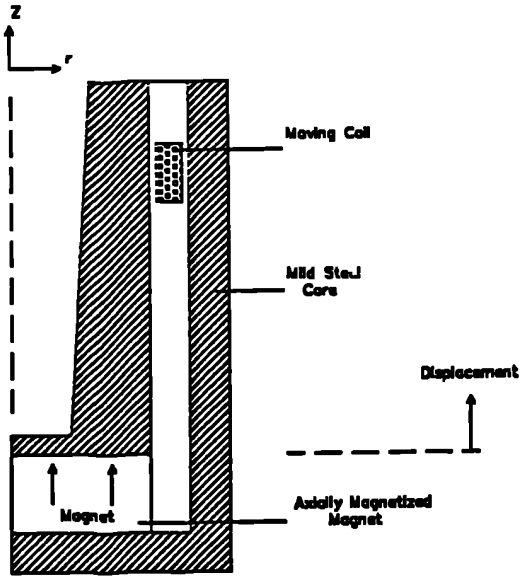

Fig 2.5 Schematic diagram of open ended voice-coil actuator topology

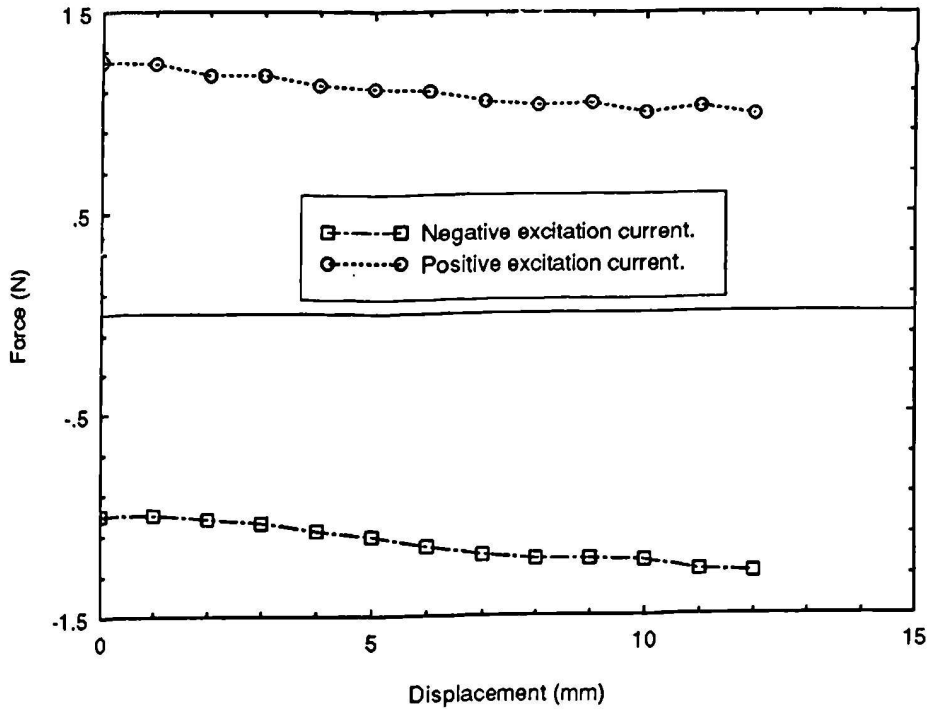

Fig 2.6 Measured force against displacement for an open ended actuator.

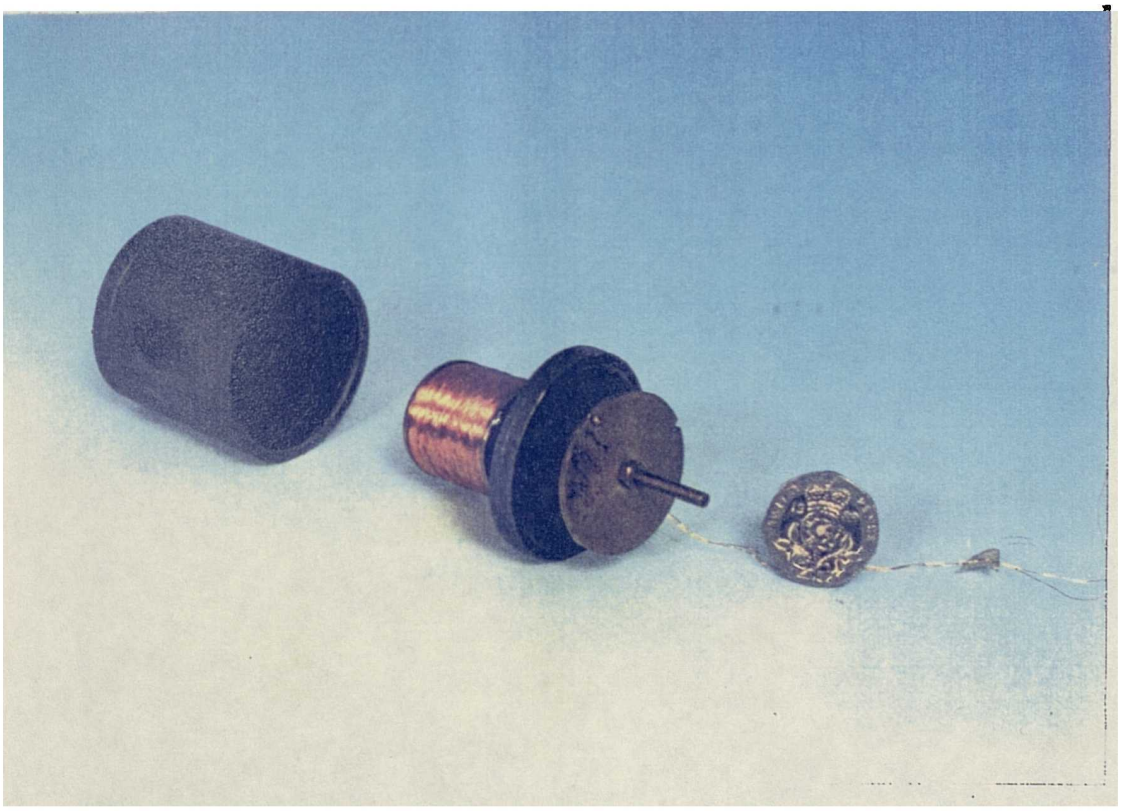

Fig 2.7 Photograph of prototype voice-coil actuator

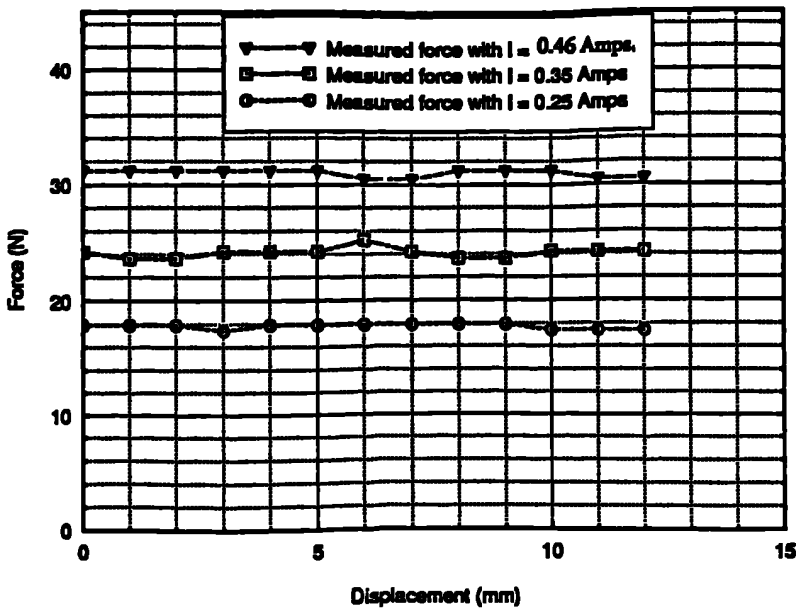

Fig 2.8 Measured force Vs. displacement and excitation current for the axisymmetric actuator.

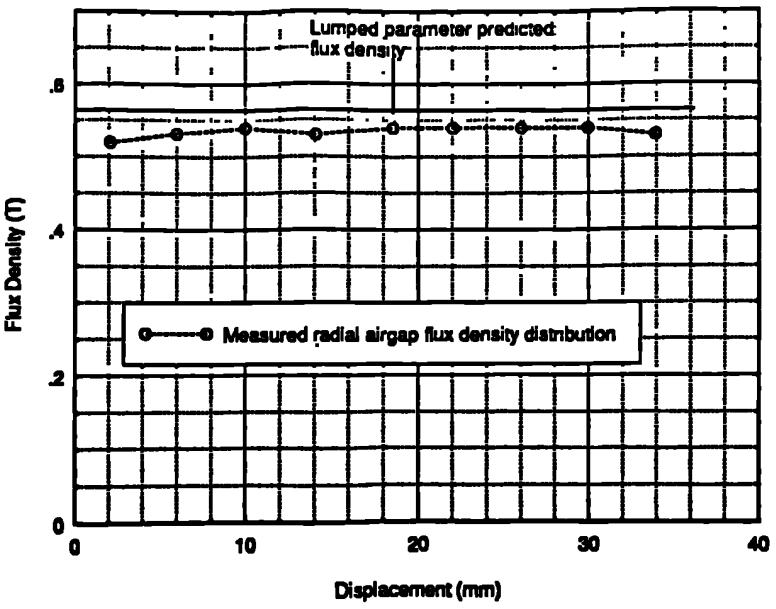

Fig 2.9 Measured and lumped parameter predicted radial airgap flux density.

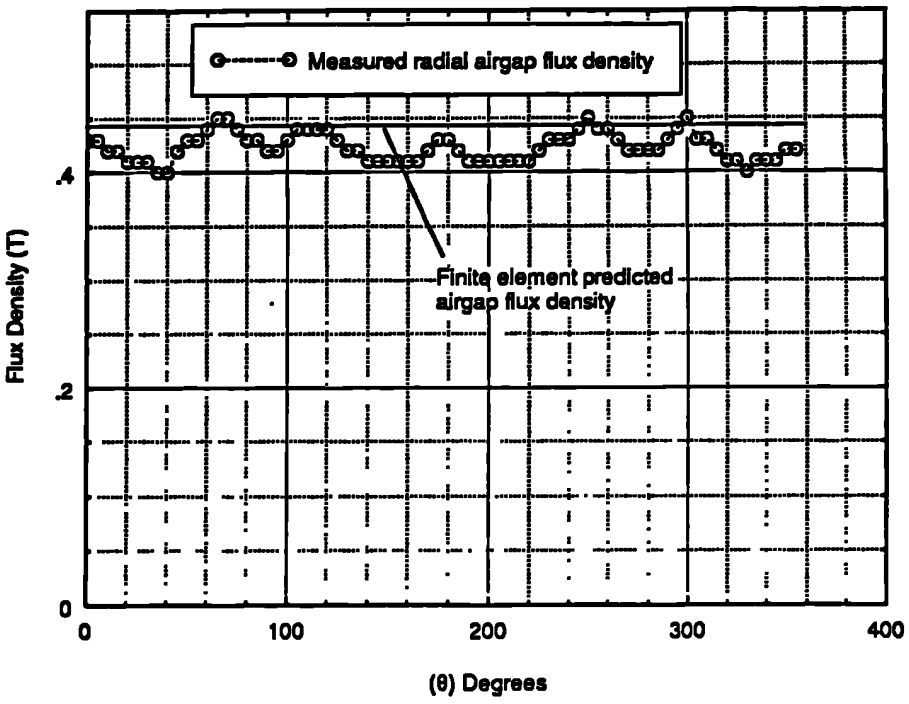

Fig 2.10 Measured and finite element predicted radial airgap flux density around the circumference of the airgap. (endcap removed).

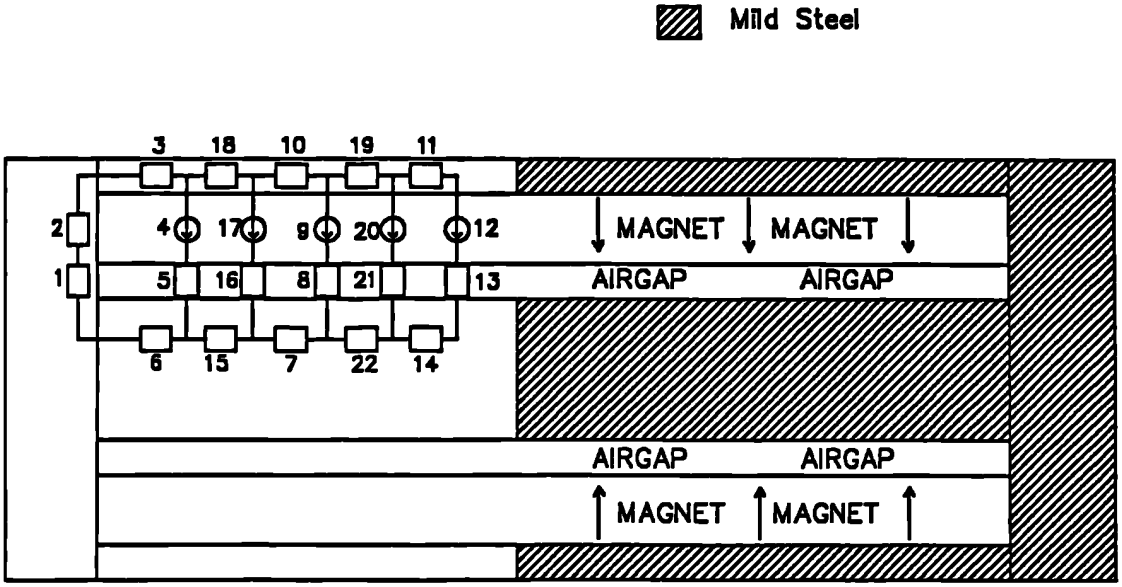

Lumped Reluctances

1) Endcap	12) Magnet
2) Endcap	13) Airgap
3)Outer Yoke	14) Inner Yoke
4) Magnet	15) Inner Yoke
5) Airgap	16) Airgap
6) Inner Yoke	17) Magnet
7) Inner Yoke	18) Outer Yoke
8) Airgap	19) Outer Yoke
9) Magnet	20) Magnet
10) Outer Yoke	21) Airgap
11) Outer Yoke.	22) Outer Yoke

Fig 2.11 Lumped reluctance network for prediction of field solution on open circuit

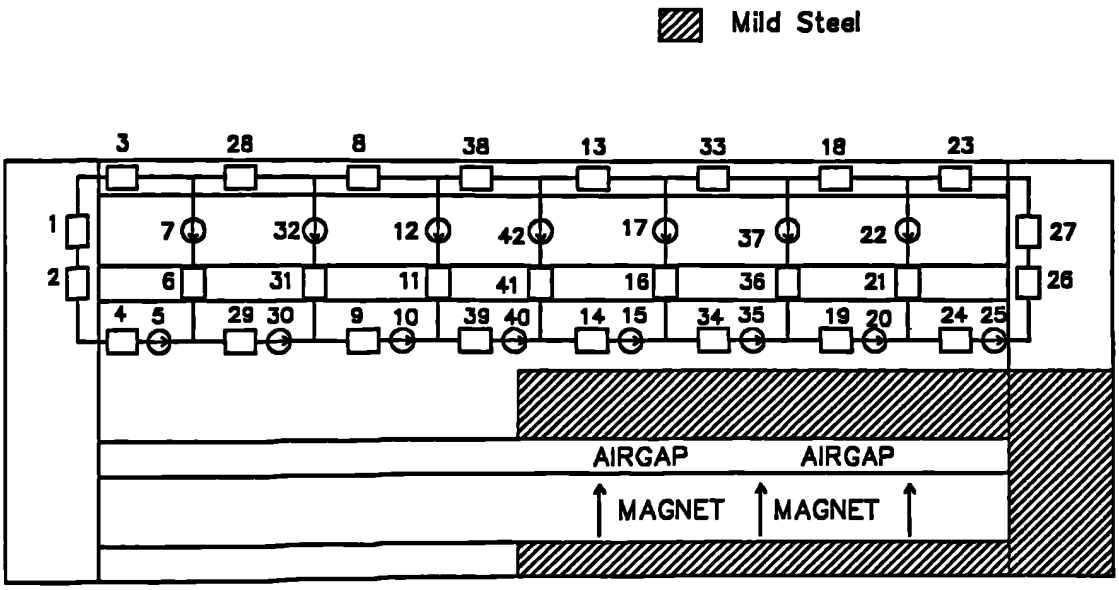

Lumped Reluctances

1) Endcap
2) Endcap
3) Outer Yoke
4) Inner Yoke
5) Coil Source
6) Airgap
7) Magnet
8) Outer Yoke
9)Inner Yoke
10) Coil Source
11) Airgap
12) Magnet
13) Outer Yoke
14) Inner Yoke
15) Coil Source
16) Airgap
17) Magnet
18) Outer Yoke
19) Inner Yoke
20) Coil Source
21) Airgap
22) Magnet
23) Outer Yoke
24) Inner Yoke
25) Coil Source
26) Endcap
27) Endcap
28) Outer Yoke
29) Inner Yoke
30) Coil Source
31) Airgap
32) Magnet
33) Outer Yoke
34) Inner Yoke
35) Coil Source
36) Airgap
37) Magnet
38) Outer Yoke
39) Inner Yoke
40) Coil Source
41) Airgap
42) Magnet

Fig 2.12 Lumped reluctance network for prediction of field solution with excitation current.

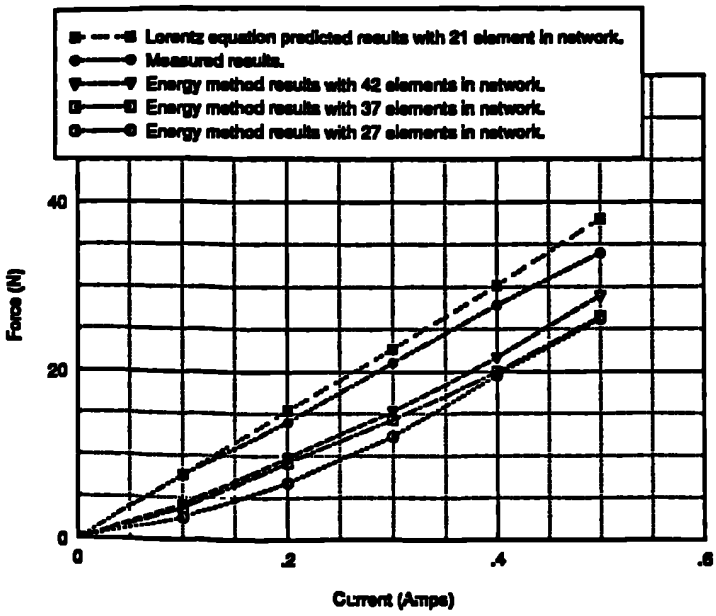

Fig 2.13 Lumped parameter model comparison of energy, Lorentz equation and measured Force Vs. current.
Coil in central stroke position.

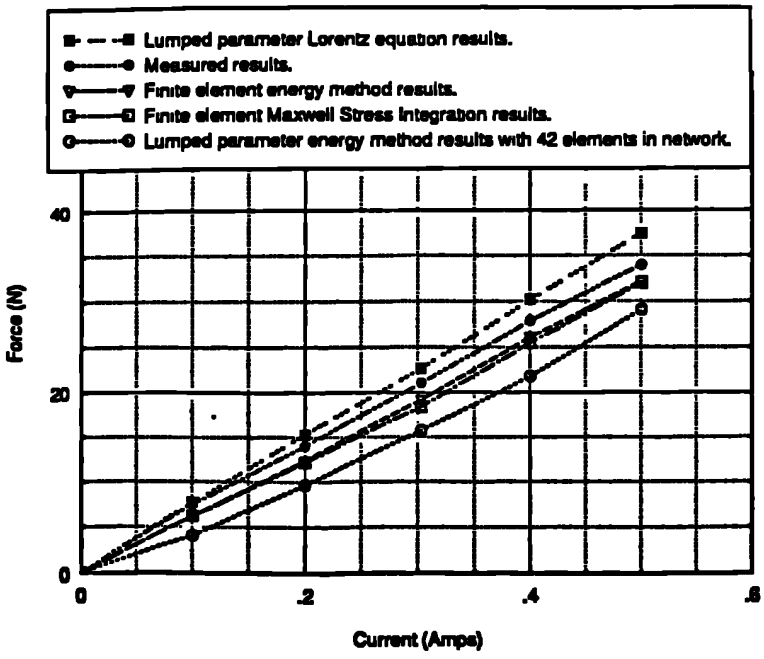

Fig 2.14 Comparison of force calculation results from lumped parameter and finite element models.
Coil in central stroke position.

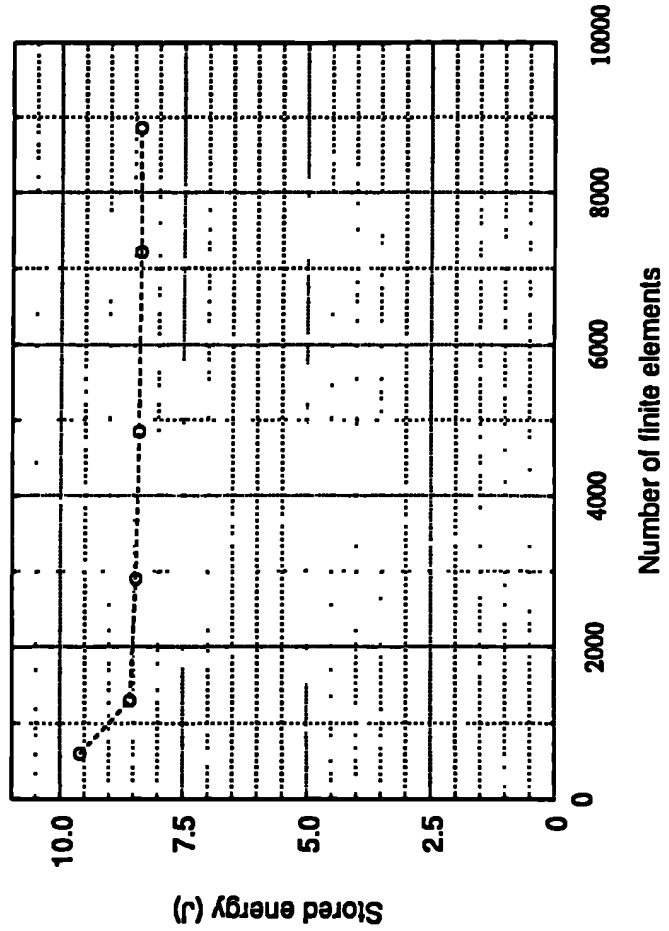

Fig 2.15 Variation of stored energy with discretization.

CHAPTER 3

SINGLE-CRITERION OPTIMIZATION

3.1 Introduction

Various approaches to the optimum design of an electromagnetic actuator will be discussed in this chapter, all of which involve explicitly formulating an objective function in terms of all the independent design variables, and mathematically minimizing this objective function. Therefore, as the value of the objective function decreases the quality of the design is improved. Single criterion optimization, as its name suggests, is the optimization of a specific performance objective which can be formulated in terms of the independent design variables.

There are numerous methods of unconstrained optimization which have proven to be applicable to various types of objective function[3.1-3.6]. The determination of the most suitable method for a particular optimization problem depends upon the specific requirements of the user. In general, however, the most powerful techniques are based upon gradient information, such as the Variable-Metric method developed by Davidon[3.1] and the Conjugate Gradient techniques of Fletcher-Reeves[3.2], in which the gradient information is calculated numerically. If these 'first-order' methods are capable of solving a specific objective function, they require fewer function evaluations before obtaining an optimum than the non-gradient methods[3.7]. For these gradient methods to be successful, however, the objective function must be differentiable with respect to every variable at every point to which the search moves. This has led to a significant failure rate of these methods[3.7], especially if some or all of the independent variables are either integer valued or discontinuous.

However, a second class of optimization algorithms exists which require function evaluations alone. Such 'zero-order' techniques are still used frequently in many engineering applications[3.8-3.10] due to their ease of implementation and the fact that they can still obtain a solution even if the objective function is discontinuous. Of the available 'zero-order' methods the Flexible Polyhedron - Flexible Tolerance method was selected for investigation over others, such as Powell's non-gradient[3.6] because it is robust and less prone to collapse at local optima[3.7].

A simple, accelerated alternating directions technique was then investigated both as a global optimization method in itself and also as a local search technique to be implemented in a Simulated Annealing schedule. This is because the method is liable to obtain only local optima, particularly when the objective function has many independent variables. However, as will be explained, it lends itself to a Simulated Annealing algorithm.

The application of constrained optimization techniques to engineering problems has increased significantly over the last decade as increased computational power has become available. Magnet design for NMR imaging systems pioneered the use of optimization techniques and more recently the field of medical physics has incorporated methods of solving combinatorial optimization problems for image reconstruction[3.11-3.15] In the area of electrical machines, the optimization of three-phase induction motors, permanent magnet brushless motors, linear force motors and design of electrical power equipment have all been the basis of recent studies[1.23-1.25,3.16].

Therefore, a constrained optimization procedure has been developed which involves obtaining a mathematical model of an actuator, followed by design/analysis and optimization stages. The device identified as the optimum was then subjected to detailed finite element analysis before being prototyped and tested.

In general an optimization problem can be stated as follows:

Minimize the objective function f(x) subject to gi(x) > 0 i=1,2,...p

hj(x) = 0 j=1,2,.....m

where $x = [x_1, x_2, \ldots\ldots\ldots x_n]^T$

n = number of variables

p = number of inequality constraints

m = number of equality constraints

In optimizing the design of actuators, equality constraints can be expressed in terms of the independent design variables. For example the axisymmetric moving coil actuator of fig (2.4):

$$I_d = IY_d + 2\,(L_g + L_{mcr} + L_m)$$

The effect of incorporating an equality constraint into an optimization problem is to reduce the order of the parameter space since one of the independent design variables can be expressed in terms of the constraints. Some methods such as the Flexible polyhedron technique to be discussed later in this chapter, explicitly reduce the parameter space, whilst other techniques can only incorporate equality constraints by replacing them with two inequality constraints.

For most objective functions a minimum is sought. However, if maximization of an objective function is required then it is performed by inverting the equation and minimizing it, i.e.

max(f) = min(1/f) for positive f.

Fig(3.1) illustrates the variation of an objective function to a single variable problem $f(x) = \frac{(x+2)(x-3)}{(x+1)}$ and illustrates how several maxima and minima can occur. Neglecting the constraints on the variable it can be seen that a global maximum and minimum occur at the singularities of the objective function as well as at $\pm\infty$. However, when the constraints are applied, i.e. the limits on the variable x, the minimum coincides with the lower bound on the variable.

In general, two heuristic approaches have been used to establish a global minimum; viz:

1) Find a set of local minima starting from a range of initial positions of the independent variables and choose the best of these results as the global optimum.

2) Once a local optimum has been located, take a finite step away from it and perform another optimization to establish if the routine returns to the original optimum.

However, more recently, the 'Simulated Annealing' techniques which use statistical methods to locate the global optimum directly have been developed. These and the constrained optimization techniques referred to earlier have been investigated.

3.2 Optimization Problems

3.2.1 Simple Magnetic Circuit

In the sections which follow a number of constrained optimization techniques will be introduced. To illustrate the methodology of these techniques, the minimization of a simple two variable objective function will be considered.

Fig(2.1) shows a simple permanent magnet/iron yoke arrangement in which saturation and flux leakage are neglected. The objective is to minimize the volume of magnet required to produce a specified value of flux density in the working airgap, whose length L_g and area A_g are fixed. This problem can be solved analytically, since :

neglecting flux leakage, then enforcing flux continuity, $B_g A_g = B_m A_m$ (3.1) and assuming infinitely permeable iron, $H_g L_g = - H_m L_m$ (3.2)

multiplying equations (3.1) (3.2) gives

$$B_g A_g H_g L_g = - B_m A_m H_m L_m \qquad (3.3)$$

$$\text{i.e.} \qquad |V_m| = \frac{B_g{}^2 V_g}{\mu_0 B_m H_m}$$

Where V_m is the volume of magnet
and V_g is the volume of the airgap.

Therefore, the minimum magnet volume is required if the magnet is working at its maximum energy product point. i.e. $B_m H_m$ has the maximum value. For a magnet having a linear second quadrant characteristic:

$$B_m = \frac{B_r}{2} \text{ and } H_m = \frac{H_{cn}}{2}$$

The following parameters were applied to the airgap:

$$A_g = 0.03\ m^2$$

$$L_g = 2.0\ \text{mm}$$

Therefore, the airgap permeance $\frac{\mu_o A_g}{L_g}$ = 1.89 e-5 Wb/NI

In addition, the following parameters were assumed for the magnet:

Remanence $B_r = 1.2\ \text{T}$

Normal Coercivity $H_{cn} = -770\ \text{KA/m}$

Finally, the required airgap flux density, B_g, was stipulated to be 1.0 T. Therefore, from equation(3.3) the minimum magnet volume is $V_m = 20669.5\ mm^3$. The corresponding values of A_m and L_m can be calculated from equations 3.1 and 3.2 and are 0.05 m^2 and 4.134 mm respectively.

3.2.2 Linear Voice-Coil Actuator

A second case study was undertaken, the objective being to minimize the copper loss in the voice-coil actuator described earlier in chapter 2. The major constraints applicable to this optimization problem were:

$$0.0 \le O_d \le 40.0$$

$$0.0 \le W_d \le 44.0$$

$$stroke = 12.0\ \text{mm}$$

$$I_d = IY_d + 2\,(L_g + L_{mrc} + L_m)$$

$$W_s = H_{cu} + stroke + 2\,(L_{mca} + L_{cap})$$

L_m > length of magnet required to avoid partial irreversible demagnetization of the magnet.

The copper loss was determined from the simple analytical equation

$$\text{copper loss} = I^2R$$

$$\text{copper loss} = \frac{force^2\, \rho_{cu}}{B_g{}^2\, V_g\, k_{pf}}$$

where k_{pf} is the winding packing factor
and ρ_{cu} is the resistivity of copper.

The permanent magnet has a linear second quadrant characteristic at 20^o C with $\mu_r = 1.1$ and B_r = 1.18 T and the soft magnetic yoke was a free cutting mild steel whose characteristic is given in fig(A.4).

The lumped parameter model of fig(2.11) was used to compute the field solution from which the average airgap flux density B_g was determined.

The two case studies were solved by the optimization techniques of Flexible Tolerance-Flexible Polyhedron, Alternating Directions and a combined Alternating Direction/Simulated Annealing algorithm.

3.3 Flexible Polyhedron-Flexible Tolerance Method

This method is based upon the unconstrained simplex technique proposed by Spendley, Hext and Himsworth[1.34] and subsequently updated by Nedler and Mead[3.17]. The method requires only objective function evaluations and not their derivatives. The

feasible region of 'hyperspace' needs to be specified by the use of equality and inequality constraints. However it is not very efficient in terms of the number of objective function evaluations that are required, compared with other optimization methods[3.7]. However, it is claimed to be a very robust technique that will almost certainly locate at least a local optimum if one exists[3.7]. The method has previously been implemented in applications where the computation time was small in comparison with the overall design effort[3.18]. Therefore, it is compatible with the requirements of this study.

3.3.1Unconstrained Optimization

A simplex is a polyhedron in the hyperspace determined by the independent variables. In the case of the first study under investigation these are L_m and A_m. A triangle is the lowest order of polyhedron which can be used as a simplex for such a 2-dimensional problem, since the method relies upon a vertex being reflected. Therefore, for a problem with less than three independent variables, a triangular simplex is automatically constructed.

If constraints exist on the variables, the initial starting position does not necessarily need to be within these constraints. However, as the test-cases of section(3.6) will show it does improve the rate of convergence of the solution. A method of choosing the initial position, as used by Nedler & Mead and Spendley, Hext and Himsworth is to form a regular polyhedron around a specified initial position. Assuming that the origin is one of the vertices then[3.7]:

$$D = \begin{pmatrix} 0 & d_1 & d_2 & d_2 & d_2 \\ 0 & d_2 & d_1 & d_2 & d_2 \\ 0 & d_2 & d_2 & d_1 & d_2 \\ 0 & d_2 & d_2 & d_2 & d_1 \end{pmatrix} \qquad \text{n * (n+1) matrix}$$

Where $$d_1 = \frac{t}{n\sqrt{2}} (\sqrt{(n+1)} + n - 1)$$

$$d_2 = \frac{t}{n\sqrt{2}} (\sqrt{n+1} - 1)$$

The columns in D represent the components of the vertices, numbered 1 to (n+1), and the rows represent the individual coordinates , 1 to n.

where t = distance between two vertices

and n = the number of variables.

Therefore, for a 2-variable, triangular simplex, having unit distance between the vertices, i.e. t = 1, and one of the vertices placed at the origin the initial simplex has the following coordinates:

$$D = \begin{pmatrix} 0 & 0.965 & 0.259 \\ 0 & 0.259 & 0.965 \end{pmatrix}$$

This initial simplex is illustrated in fig(3.2)

Once the positions of the vertices have been determined, the value of the objective function is calculated at each of the vertices. The vertices with the highest and lowest values of the objective function are then isolated:

$$f(x_h) = Max\{f(x_1), f(x_2) \ldots . f(x_{n+1})\}$$

$$f(x_l) = Min\{f(x_1), f(x_2) \ldots . f(x_{n+1})\}$$

The centroid of all the vertices excluding the vertex with the highest value of the objective function is then evaluated. For a triangular simplex, such as shown in fig(3.2), this point is simply the bisector of the line connecting the opposite two vertices. i.e.

$$x_{n+2} = \frac{1}{n}\{(\sum_{i=1}^{n+1}(x_i - x_h)\} \qquad i = 1, \ldots n \text{ where } i = \text{number of the vertex}$$

Four operations can then be used in an attempt to obtain a vertex with a lower value of the objective function.

1) Reflection of the Polyhedron

x_h is reflected through the centroid, giving

$$x_{n+3} = x_{n+2} + \alpha^*(x_{n+2} - x_h) \tag{3.4}$$

Where α is the reflection coefficient. The value of the objective function, $f(x_{n+3})$, is then calculated at the new vertex, and if at the new vertex x_{n+3}, gives a lower value of the objective function compared with x_h then it is accepted and x_h is discarded.

2) Expansion of the polyhedron

If the value of the objective function $f(x_{n+3})$ at the new vertex which is formed after the above reflection, is lower than $f(x_l)$ then a new vertex is obtained

$$x_{n+4} = x_{n+2} + \gamma^*(x_{n+3} - x_{n+2}) \tag{3.5}$$

where γ is the expansion coefficient which is used to accelerate the search when reflections are producing lower objective function vertices. This is shown by simplex (2) of fig(3.3). If $f(x_{n+4})$ is lower than $f(x_{n+3})$, then this step is accepted and a new reflection is made.

3) Contraction of the polyhedron

If $f(x_{n+3}) > f(x_i))$ after the reflection, for all i except x_h then a contracted vertex is obtained from,

$$x_{n+5} = x_{n+2} + \beta*(x_h - x_{n+2}) \tag{3.6}$$

where β is the contraction coefficient and accelerates the contraction of the polyhedron towards a minimum.

4) Reduction of the polyhedron

If $f(x_{n+3}) > f(x_h)$ after the reflection, then all the vertices are reduced by one half, i.e.

$$x_i = x_i - 0.5*(x_i) \tag{3.7}$$

In this way the flexible polyhedron adapts itself to the topography of the objective function, elongating along incline planes, changing direction in curving valleys and contracting in the neighbourhood of a minimum, as illustrated in fig(3.3). The termination criterion used for this method is to stop the routine when the average size for the sides of the polyhedron has contracted to be smaller then a preset convergence value ε, i.e.

$$\left[\frac{1}{(n+1)}\sum_{i=1}^{n+1}\left(f(x_i) - f(x_{n+2})\right)^2\right]^{1/2} \leq \varepsilon \tag{3.8}$$

Therefore the termination of the algorithm is dependent upon all the variables and can be dominated by any of these. This reduces the possibility of the search not terminating at a local minimum. Fig(3.3) illustrates the progress in going from two given starting positions towards an unconstrained optimum, corresponding to the minimum magnet volume, for the problem in section(3.2). For the sake of clarity the final contractions are not shown. For this unconstrained case the value of the magnet volume as a function of the iteration number, from both starting positions, is illustrated in fig(3.4). The value for the objective function is taken as the average of the values at the constituent vertices and normalised. Comparisons between analytical and numerically optimized results are presented in the case study of section(3.6).

3.3.2 Constrained Minimization Procedure

When constraints are incorporated into the problem the aim is now to,

$$\text{minimize } f(x) \qquad x = (x_1 \ldots\ldots x_n)^T$$

$$\text{subject to} \qquad h_j(x) = 0 \quad j = 1 \ldots\ldots m \text{ equality constraints}$$

$$g_i(x) \geq 0 \quad i = 1 \ldots\ldots p \text{ inequality constraints}$$

One possible method of incorporating such constraints into an unconstrained optimization solver, as used by Nedler & Mead[3.17] and Spendley, Hext and Himsworth[1.34], was to simply assume a large positive value for the objective function whenever an unfeasible vertex was obtained. However, Box[3.19] found that this approach usually caused the polyhedron to flatten itself against the constraint with the result that the size of the simplex quickly reduced to zero and collapsed at a false minimum. Himmelblau[3.7] proposed a more elaborate approach, which is as follows:

1) If the polyhedron is in a region where the constraints are not violated then minimize the objective function by the method of Nedler & Mead.

2) If the constraints are violated, set up a new objective function in terms of the violated constraints. This will inherently be an unconstrained objective function, and the aim is to minimize this function until it is less than a preset tolerance at this stage of the search. This is done by setting up a new simplex and following the procedure for unconstrained minimization as previously described. This is illustrated in fig(3.5) which shows a bounded version of fig(3.3), and has the unconstrained optimum in a violated position.

3) As the search proceeds, and nears a local optimum, the tolerance on the constraints and objective function is tightened until the polyhedron collapses on an optimum, at which point the tolerance is equal to the final convergence required from the search. i.e aim is to minimize f(x) subject to $\varphi - t(x) = 0$ (3.9)

where φ = value of the flexible tolerance criterion for feasibility which is reduced as the search nears an optimum value and is used as a termination criterion.

t(x) = positive functional of all the equality and/or inequality constraints.

The exact nature of the tolerance criterion, showing how it varies between different stages of the search, and how constraints are handled, is presented in detail in appendix D whilst appendix E also illustrates a method of quickly obtaining near-feasible points using the simplex method and uni-dimensional search techniques which can be used as a final resort if the flexible polyhedron is collapsing in a violated region.

3.4 Direct Search Method of Alternating Directions

A simple optimization technique which has been developed is based upon the alternating directions approach of Hooke & Jeeves'[1.35]. It involves changing one design variable at a time whilst keeping all the others constant in the search for the minimum. The algorithm consists of two separate parts, an exploratory search around an initial point, followed by an accelerating step in a direction selected for minimization as deduced from the results of the exploratory search. The user has to specify initial values for the independent variables and the value of the initial percentage incremental change of the variables Δx. The objective function is evaluated at the starting point and then each variable is changed in turn by incremental amounts until all the variables have been altered.

i.e $$x_1(0) = x_1(0) + \Delta x_{1(0)} \tag{3.10}$$

If this results in an improvement in the objective function then this is adopted as the new x_1 in the set of independent variables. If the value of the objective function has not been reduced then x_1 is changed by $-\Delta x_1$ (0)

i.e $$x_1(0) = x_{1(0)} - \Delta x_{1(0)} \tag{3.11}$$

If the value of the objective function is not improved by either of the changes then its value is left unchanged. Next, $x_2(0)$ is then changed by an amount Δx_2 (0) and so on until all the independent variables have been changed to complete one exploratory search. The optimum number of exploratory searches performed before the accelerating step, is dependent upon the topography of the objective function. However, in this investigation it was decided that two exploratory searches would be sufficient to obtain a direction of search non-parallel to either of the variable axes. At the end of these two searches the vector connecting the current and initial points is used to specify the magnitude and direction of the accelerating step. The success or failure of the accelerating step depends upon whether it reduces the value of the objective function. Following the accelerating step another exploratory search is implemented and so forth.

If the exploratory search fails to obtain a new direction then Δx is reduced until either one is established or the value of Δx is less than a preset tolerance, at which point the search is said to have collapsed onto a local optimum. Fig(3.6) illustrates the methodology for the 2-variable minimum magnet volume problem described in section(3.2.1). This method has advantages over the flexible polyhedron method when the problem has a large number of inequality constraints, where the latter technique can spend a large proportion of its execution time obtaining a feasible design.

3.4.1 Termination of the Algorithm

The termination of the algorithm is performed by two tests

1) If $$\frac{f(x^{(k+1)}) - f(x^{(k)})}{f(x^{(k)})} < \varepsilon \qquad (3.12)$$

However, if this test is used alone then a false minimum can be obtained if the objective function has a long constant slope as illustrated in one dimension in fig(3.7.a). Therefore, a second termination criterion is also used, viz:

2) If $$\frac{x^{(k+1)} - x^{(k)}}{x^{(k)}} < \varepsilon \qquad (3.13)$$

It will be noted that if this test was used alone then a false minimum could be obtained at a point with near-infinite slope in the objective function as illustrated in one dimension in fig(3.7.b). However, termination criterion 1) overcomes this possibility.

3.4.2 Advantages and Disadvantages of the Alternating Directions Method

The main advantage of the method is that it is extremely easy to implement and complex optimization problems can be solved in a comparatively short time. It can also obtain results for local minima quickly and therefore can be initiated a number of times from different starting positions so that the best of the local minima over the whole of the parameter space can be located.

An obvious disadvantage is that the method generally converges to local as opposed to global optima when applied to a multi-dimensional problem. Also, because the method rotates the variables in turn, the number of function evaluations can be large. In turn this can lead to excessive execution times, particularly if an iterative procedure is required each time the function has to be evaluated, as is the case when a non-linear lumped parameter model is used to compute the field solution of an electromagnetic problem, for example.

3.4.3 Penalty Function Methods of Dealing with Constraints

The Penalty function is the most commonly used method for incorporating constraints into an unconstrained optimization solver[3.20]. The Penalty function is added to the objective function, and is set to zero if the vector of the independent variables lies in the feasible region. However, if the problem becomes unfeasible then a positive Penalty function, which increases according to the violation of the constraints is added. The Penalty function should dominate the objective function if the vector is unfeasible, thus causing a rapid return to the feasible region. The following forms of Penalty function have been investigated because they all increase rapidly outside the feasible region, as shown in fig(3.8)

i) Linear Penalty Function

$$P(x) = f(x) + abs\left[\sum_{i=1}^{n} k\,(g_{i(x)})\right] \tag{3.14}$$

ii) Square Penalty Function

$$P(x) = f(x) + \sum_{i=1}^{n} k\,(g_i(x)^2) \tag{3.15}$$

iii) Exponential Penalty Function

$$P(x) = f(x) + \sum_{i=1}^{n} k\,[exp(abs\,(g_i(x))\,) - 1] \tag{3.16}$$

for i=1.....number of violated constraints

where $g_i(x)$ is the inequality constraints

and f(x) is the objective function

and k is the Penalty Function.

3.4.4 Interior and Exterior Penalty Functions

If there is sufficient information about the problem to be optimized to facilitate the selection of an initial point which is feasible then the values of the weighting factors should be orders of magnitude greater than the value of the maximum objective function in order to discourage the optimization algorithm from searching in unfeasible regions. This type of penalty function technique is known as an Interior Penalty function. As the name suggests it attempts to prevent the search from becoming unfeasible. This type of penalty function is often linear, as in equation(3.14), since as soon as the objective function is violated a large numerical value is assigned to $P(x)$. Thus, the search returns to the feasible region. Alternatively, if an initial point cannot be selected from the feasible region then the aim of the search is to return the variables to the feasible region as quickly as possible. In this case, it has been suggested[3.21] that a function which increases more rapidly than a linear function should be incorporated. Therefore, the squared and exponential penalty functions of equations(3.15 and 3.16) have been investigated and their applicability will be demonstrated with respect to the case studies of section(3.2). These are termed Exterior Penalty functions. It will be noted that the value of the constant, k, can be critical to the effectiveness of the Penalty functions, and needs to be investigated for each objective function to be minimized.

3.5 Simulated Annealing Technique

3.5.1 Introduction

The major drawback with the Alternating Direction technique described in section(3.4) is that the method is prone to converging to a local minima and therefore requires initialisation from many random starting positions within the variable space to establish the global optimum. Simulated Annealing algorithms[1.26] can be implemented to exploit the rapid identification of local minima by testing the probable benefits of each starting position. This technique has been implemented predominantly in the optimization of problems with a very large number of variables (typically > 100), such as the optimum arrangement of pins on an integrated circuit to minimize interference between the connecting wires[1.26], and the 'Travelling Salesman Problem', which involves the movement between a number of cities in the shortest possible distance[3.22-3.24], both of which were previously thought to be unrealisable in practice. The technique relies on the positional change of the variables to minimize the objective function, the acceptance or rejection of this positional change being dependent upon the value of the new objective function. However, in contrast with alternative optimization techniques a change in the position of the variables can be accepted even if the new objective function value is greater than the current best objective function value. The test performed to determine the acceptance of the move is of the form :

$$\gamma = \exp\left\{\frac{best\_f(x) - f(x)}{best\_f(x)*tfactor}\right\} \tag{3.17}$$

where $f(x)$ is the value of the objective function

$best\_f(x)$ is the current best objective function value.

and *tfactor* is a control variable which is altered throughout the optimization solution in response to improvements in the objective function, and to effect an acceleration of the search. As can be seen from equation(3.17) the value of γ lies in the interval 0 to 1, the exact value being dependent upon the current state of *tfactor* and the relative

difference of the objective function values. If a value of $f(x)$ is obtained which is lower than *best_f(x)*, then the move is always accepted.

The value of γ is then compared with a generated random number between 0 and 1. If $\gamma >$ the random number then the move is accepted, however, if $\gamma <$ the random number the move is rejected and a new position vector is sought by changing the next variable in rotation.

From equation(3.17), it can be seen that the value of *tfactor* is critical in determining whether the move is accepted or rejected. On commencement of the optimization a large positive value of tfactor, typically 200 is chosen so that almost all moves are acceptable in order that the magnitude of *best_f(x)* can be rapidly reduced. However, as the search progresses the value of *tfactor* is reduced such that the acceptable relative difference between the two objective functions is decreased.

The value of *tfactor* is decreased when one of the following conditions are met:
i) An improved *best_f(x)* is obtained.
ii) A pre-specified number of searches, N1, are performed without obtaining an improved *best_f(x)*.
iii) A pre-specified number of searches, N2, are rejected.

This decrease in *tfactor* is given by:

$$tfactor = k_{sim}\, tfactor \tag{3.18}$$

where typically $0.8 < k_{sim} < 0.95$.[3.25]

The shape of the curve representing the number of times an optimization is commenced as a function of *tfactor*, viz. the cooling schedule due to an analogy with the cooling rate applied to a hot body to bring about its minimum energy state[1.26], will be of the form illustrated in fig(3.9).

The application of the Simulated Annealing method is best highlighted by the use of a simple example: assuming that an objective function has a global minimum of 2.5, and that during the optimization the following positions are obtained.

1) At the start of the search

best_f(x) = 10 *f(x)* = 20 *tfactor* = 200

random number 0 -> 1

then from equation(3.17) γ= 0.995 and there is a 99.5% probabilityof this new vector being accepted.

Therefore, if the random number is 0.5 for example, then the search progresses along the same direction as the previous direction.

2) As the search progresses

best_f(x) = 3 *f(x)* = 5 *tfactor* = 1

random number 0 -> 1

then from equation(3.17) γ = 0.510 and there is only a 51.0% probability of this change in the position of the variables being accepted.

Therefore, if the random number is 0.5 for example, then the search progresses along the same direction as the previous direction.

3)As the optimization approaches the global optimum

best_f(x) = 2.55 *f(x)* = 2.9 *tfactor* = 0.05

random number 0 -> 1

then from equation(3.17) γ = 0.06. Hence there is only a 6% probability of this vector being accepted.

Therefore, if the random number is 0.5 for example, then the search progresses along the direction of the next variable.

3.5.2 Application of Simulated Annealing to Design Optimization of Permanent Magnet Actuators

In the optimization of the permanent magnet actuators in this study, the Simulated Annealing algorithm has been used to determine the probable benefits of commencing an Alternating Direction optimization solution from a randomly chosen starting position. Initially almost all randomly chosen starting positions can be made acceptable for optimization by selecting an initial value for *tfactor* of 200.

For example, if $f(x) = 140*best\_f(x)$ and *tfactor* = 200, $\gamma = 0.50$ and the probability of the value of $\gamma >$ generated random number is 50%. Hence almost all starting positions, of constrained, non-singular objective functions would be accepted.

The principal advantage of including the Simulated Annealing algorithm as opposed to the Alternating Direction technique initialized from a number of random positions, is particularly evident when *tfactor* is reduced and the optimization solution is numerically close to its global minimum value. The Simulated Annealing algorithm will only accept starting positions which have a value of $f(x)$ close to $best\_f(x)$, whereas the Alternating Direction technique will always perform the optimization. As examples, with *tfactor* = 1.0 in the search, and therefore the optimization should be near the global minimum:

Alternating Direction Technique

1) at starting position, when

$f(x) = 20$

$best\_f(x) = 6$

This starting position is accepted for optimization

2) at starting position, when

$f(x) = 7$

$best\_f(x) = 6$

This starting position is accepted for optimization

Simulated Annealing Technique

1) at starting position, when

$f(x) = 20$

$best\_f(x) = 6$

and *tfactor* = 1.0

from equation(3.17) $\gamma \sim 0.1$ and there is a 10% probability of an optimization commencing.

If random number < 0.1 an optimization solution is performed.

If random number > 0.1 a new starting position is sought.

2) at starting position, when

$f(x) = 7$

$best\_f(x) = 6$

and *tfactor* = 1.0

from equation(3.17) $\gamma \sim 0.85$ and there is a 85% probability of an optimization commencing.

If random number < 0.85 an optimization solution is performed.

If random number > 0.85 a new starting position is sought.

This illustrates that as the termination of the optimization is approached, the Simulated Annealing technique only allows optimizations to be performed if the relative difference between the objective functions is small.

In this study, the values of N1 and N2, which represent the number of times the optimization does not improve on the optimum and the number of allowed rejections, were selected to be 10 and 20 respectively. These values are typical of those used by a number of authors for problems with a similar number of variables[3.25-3.28].

3.6 Validation Problems

3.6.1 Determination of the Volume of Magnet Necessary to Produce a Required Level of Airgap Flux Density

The minimum magnet volume problem described in section(3.2.1) was used to identify optimum values of the constants used in the optimization methods discussed. These included the values of reflection, expansion, and contraction coefficients in the flexible polyhedron method, and values of initial step sizes for all the techniques. The Penalty function methods were used with various values for the numerical constant k and then compared with each other. The cooling rate for the Simulated Annealing algorithm was varied and the results will be presented. Fig(3.10) shows the contour of $B_g = 1.0$ T. and also illustrates the contours of equal magnet volume. The positions of interception of the two graphs correspond to feasible positions.

3.6.2 Results of Flexible Tolerance Method

As with other optimization techniques, the flexible tolerance method is not guaranteed to produce a solution. In addition, the results may not necessarily be repeatable for different starting positions. Therefore, tests were performed from three different random starting positions.

The first validation test was to vary the values of β and γ in equations (3.5 and 3.6) whilst the initial step size and tolerance were kept constant. The value for α was assumed to be 1.0 although for certain objective functions a slightly improved execution time might be obtained if $\alpha = 0.95$ [3.19]. From the results of Table(3.1) the lowest number of function evaluations occurred with $\beta = 0.1$ and $\gamma = 1.2$. However, the random pattern of the rest of the results does not highlight any trend towards an optimum value which

could be relied upon for all objective functions. For the following test the values of β and γ were set to 0.1 and 1.2 respectively.

γ	β	Number of Function Evaluations	Best Objective Function Value (mm^3)
1.2	0.05	37651	20666
1.2	0.1	35839	20665
1.2	0.3	39403	20666
1.2	0.5	40987	20665
1.2	0.7	39163	20663
1.2	0.9	46326	20664
1.4	0.1	49182	20662
1.4	0.3	54439	20661
1.4	0.5	50762	20663
1.4	0.7	49875	20663
1.4	0.9	54001	20667
1.6	0.1	74326	20664
1.6	0.3	88898	20664
1.6	0.5	64728	20663
1.6	0.7	81419	20658
1.6	0.9	76289	20663
1.8	0.1	74326	20662
1.8	0.3	82180	20664
1.8	0.5	76151	20661
1.8	0.7	80271	20668
1.8	0.9	82132	20663
2.0	0.1	44327	20663
2.0	0.3	76262	20662
2.0	0.5	52160	20665
2.0	0.7	52456	20662
2.0	0.9	56274	20665
2.2	0.1	84719	20664
2.2	0.3	99439	20667
2.2	0.5	83548	20664
2.2	0.7	79873	20669
2.2	0.9	87643	20664
2.4	0.1	67733	20663
2.4	0.3	64774	20664
2.4	0.5	81216	20663
2.4	0.7	67699	20663
2.5	0.9	71217	20661

Table 3.1 Effects of altering β and γ for the Flexible Tolerance method. $\alpha = 1.0$, convergence criterion= 0.0001 and initial step size = 0.5.

The next tests were performed to determine the optimum initial step size and the convergence criterion on the solution. As described in section(3.3), the number of degrees of freedom of the flexible tolerance method depends upon the difference between the number of independent variables and the number of equality constraints. Therefore, the test to determine the optimum convergence criterion value was performed with the value of the airgap flux density B_g set both as an equality constraint and as two inequality constraints. Table(3.2) shows that for all the convergence criterion values the number of function evaluations was reduced when the airgap flux density was set as an equality constraint. As anticipated, the number of function evaluations became less as the convergence criterion was increased. However, as the convergence criterion was increased the solution becomes less accurate and the effect of this was that the value of the optimum objective function was reduced because non-realistic designs were being generated since the algorithm reduced the value of the objective function as far as it could.

eg. With the convergence criterion =0.0001 Objective function = 20665.23 , B_g = 0.999898. The objective function has been calculated to within 0.02% of the analytical solution.

With the convergence criterion = 0.01 Objective function = 20065.50, B_g = 0.98528. The objective function has only been calculated to within 2.9% of the analytical solution.

Value of Convergence Criterion	Number of Function Evaluations With Equality Constraints	Number of Function Evaluations With Inequality Constraints	Value of B_g (T)	Value of B_m (T)	Best Objective Function Value (mm^3)
0.00001	56597	59993	0.9999899	0.599916	20668
0.00005	51210	54008	0.9999619	0.598548	20666
0.00010	35893	39433	0.9998980	0.599817	20665
0.00050	27244	28732	0.9991880	0.598548	20640
0.00100	24982	26630	0.9982850	0.604318	20599
0.00500	18044	19288	0.9922770	0.600832	20354
0.01000	16290	17664	0.9852800	0.598623	20065
0.05000	13806	14827	0.9333240	0.539569	18189

Table 3.2 Results of varying the convergence criterion on the solution for the Flexible Tolerance method. The results are presented for both inclusion and non-inclusion of equality constraints. α =1.0, β = 0.1, γ = 1.2 and initial step size = 0.5.

With the convergence criterion set to 0.0001, the value for the initial step size was investigated. Table(3.3) shows that a minimum occurred in the number of function evaluations when the step size was set to 0.5. A range of values, however, could have been used since the number of function evaluations is not sensitive to the step size apart from when either a very large or very small initial value is assigned.

Value of Initial Step Size	Number of Function Evaluations
0.0001	90810
0.0005	67813
0.0010	51039
0.0050	42361
0.0100	47023
0.0500	46947
0.1000	40720
0.5000	35893
1.0000	42361
5.0000	78369

Table 3.3 Results of varying the initial step size for the Flexible Tolerance method. α=1.0, β =0.1, γ=1.2 and convergence criterion = 0.0001.

Finally, the quadratic interpolation and Golden Section uni-dimensional searches described in appendix E were then compared with each other. Fig(3.11) shows the number of function evaluations for the two methods as the value of the convergence criterion was varied. It can be seen that at the higher values of convergence criterion, the quadratic interpolation method required significantly fewer number of function evaluations. However, as the convergence criterion was tightened the two curves intersected and the Golden Section method had a significant advantage at smaller convergence criterion values. In response to this result a composite uni-dimensional search was employed with the quadratic interpolation technique being used until the flexible tolerance was reduced below a specified value. After this point the Golden Section search method was used for any further uni-dimensional searches required. The result of this composite search is illustrated in fig(3.12), where it will be seen that a notable improvement of 9.3% was achieved over the Golden Section method when used by itself, when the cross-over value from the quadratic to Golden Section method was 0.0005 for a convergence criterion of 0.0001. This composite technique was therefore incorporated into the Flexible Tolerance method.

3.6.3 Results of Alternating Directions Method

For the Alternating Directions method it was decided to solve the optimization problem from 750 different starting positions so that the whole of the parameter space would be scanned. For the first two test results the squared penalty function method was used with the constant k in equation(3.15) set to 1000. The first test was to establish the accuracy required on the solution. Table(3.4) shows that, as with the flexible tolerance method, as the convergence criterion was reduced, the number of function evaluations increased significantly. With this technique, however, as the convergence criterion was reduced to a very small value the solution became less optimal in comparison with the analytical solution. i.e. with the convergence criterion set to 0.0001 the solution had only a 0.03% difference than the analytical solution as opposed to a 0.67% difference with a convergence criterion of 0.00001. This occurred because on some occasions the optimization was terminated, as described in section(3.4), before it could reach the required convergence criterion. Therefore, the value of tolerance was set to 0.0001 for the remainder of the validation tests.

Value of Convergence Criterion	Number of Objective Function Evaluations	Value of B_g (T)	Best Objective Function Value (mm^3)
0.00001	109681	0.99999904	20807
0.00005	104312	0.9999712	20729
0.00010	54364	0.9998972	20663
0.00050	49257	0.9991121	20684
0.00100	48753	0.9982762	20638
0.00500	35243	0.9932721	20478
0.01000	32981	0.9897392	20271
0.05000	23764	0.9473939	18656

Table 3.4 Results of varying the convergence criterion on the solution for the Alternating Directions method. A square Penalty Function with k=1000 has been used in these results and an initial step size = 0.01.

In the implementation of the Alternating Directions algorithm, if any of the independent variables were less than zero, the airgap flux density was not evaluated and the value of the objective function was set to a specified percentage greater than the previous value, effectively causing the search to move away from this position. This was implemented to protect the lumped parameter solver from attempting to solve unrealistic networks.

The value of the percentage increase was varied between 0-50 % so as to establish an optimum increase in the objective function. Table(3.5) shows the number of function evaluations required to obtain a solution within 0.03% of the analytical solution. It can be seen that there is a very shallow optimum around 5 -10 %. A 5% increase in the objective function was therefore implemented if the variables became negative. In order to determine the optimum value of the initial step size, both the number of function evaluations and the number of times the airgap flux density were not calculated was determined. Table(3.6) shows that as the value for the initial step size was decreased the number of function evaluations increased whilst the number of times the airgap flux density was not evaluated, increased significantly with increasing step size. As a consequence there appears to be no clear optimum value for the initial step for this test example.

Percentage Increase in Objective Function (%)	Number of Objective Function Evaluations
0.0	54633
5.0	54364
10.0	55112
15.0	56211
20.0	58262
25.0	61922
30.0	64252
35.0	67208
40.0	69083
45.0	71261
50.0	72989

Table 3.5 Results of varying the percentage increase in the objective function when variables are negative for the Alternating Directions method. A square Penalty Function with k = 1000 has been used in these results and a convergence criterion= 0.0001.

Value of Initial Step Size	Number of Objective Function Evaluations	Number of Times the Lumped Parameter was Rejected
0.0001	87923	0
0.0005	67320	0
0.0010	54364	16
0.0050	53098	763
0.0100	52387	2374
0.0500	49876	7874
0.1000	50932	10983
0.5000	47821	19273
1.0000	45373	32992
5.0000	46344	67522

Table 3.6 Results of varying the initial step size for the Alternating Directions method. A square Penalty Function with k = 1000 has been used in these results and a convergence criterion = 0.0001.

The penalty function equations(3.14, 3.15 and 3.16) were implemented into the algorithm to test if there was any obvious advantage in any one of them. With the convergence criterion = 0.0001 and the initial step size = 0.01, solutions were obtained until the value of the objective function was within 0.1% of the analytical solution. Table(3.7) illustrates that the minimum number of objective function evaluations was obtained with the value of k in excess of 1000 for all three types of penalty function. The number of evaluations did not alter as k was increased above this value but increased significantly as k was reduced. For the linear function and for values of $k < 0.1$ no solution could be obtained within the maximum number of evaluations, which was set at 10^6. These results do not give a conclusive answer as to the benefits of any of the Penalty functions.

Value of Constant	Number of Function Evaluation for Linear Penalty Function	Number of Function Evaluation for Square Penalty Function	Number of Function Evaluation for Exponential Penalty Function
0.00001	No Solution in 1.0e+06 Function Evaluations	676329	578622
0.00010	No Solution in 1.0e+06 Function Evaluations	514829	487632
0.00100	No Solution in 1.0e+06 Function Evaluations	412397	389131
0.01000	No Solution in 1.0e+06 Function Evaluations	307315	298420
0.10000	621001	243565	256429
1.00000	223448	216065	190013
10.0000	55416	163859	137866
100.0000	53668	57744	53987
1.0e+03	53681	54364	53636
1.0e+04	53681	54097	53681
1.0e+05	53681	53824	53681
1.0e+06	53681	53824	53681
1.0e+07	53681	53714	53681
1.0e+10	53681	53681	53681
1.0e+15	53681	53681	53681

Table 3.7 Results if varying the numerical constant in the Penalty Functions for the Alternating Directions method. Convergence criterion= 0.0001 and initial step size = 0.01.

3.6.4 Results of the Simulated Annealing Method

For the Simulated Annealing method, the recommendations deduced from the Alternating Directions technique were incorporated, viz:

convergence criterion = 0.0001, initial step size = 0.01 and a square penalty function method with k = 1000.

Various starting and termination values were chosen for *tfactor*, and the effect this had on both the optimum objective function and the number of function evaluations was determined. Table(3.8) summarises the results, and shows that, without compromising the value of the optimum objective function, the number of function evaluations can be reduced significantly from the Alternating Directions technique and is also lower than the average value for the flexible tolerance method. If the maximum value of *tfactor* is set too high, however, then the search is unnecessarily long since no further improvement

of the objective function can be achieved, whilst the minimum value of *tfactor* should be set as low as possible since this does not incur a significant increase in execution time, and yet gives the user greater confidence that no further searches are being made at these low values.

Value of *tfactor* max	Value of *tfactor* min	Number of Objective Function Evaluations	Best Objective Function Value (mm^3)
500	0.01	12345	20661
200	0.01	8764	20661
100	0.01	3752	20661
50	0.01	2985	20674
20	0.01	2876	20674
10	0.01	2676	20679
5	0.01	2547	20812
2	0.01	2239	20812
1	0.01	2016	20812
500	0.1	12345	20661
200	0.1	8764	20661
100	0.1	3752	20661
50	0.1	2985	20674
20	0.1	2718	20674
10	0.1	2537	20679
5	0.1	2466	20812
2	0.1	2180	20812
1	0.1	1987	21125
500	1	10763	20699
200	1	8152	20715
100	1	3129	20798
50	1	2539	20674
20	1	2412	20679
10	1	2299	20679
5	1	2101	20812
2	1	1985	21716
1	1	1712	28732

Table 3.8 Results of varying the upper and lower value of *tfactor* for the Simulated Annealing method. Convergence criterion = 0.0001, a square Penalty Function has been used with k = 1000 and an initial step size = 0.01.

3.6.5 Validation Problem 2 -Minimization of Copper Loss in a Linear Voice Coil Actuator

The minimization of the copper loss from the linear voice-coil actuator described in section(3.2.2) was investigated, in the hope that a more definitive guide might be obtained regarding the values of the constraints required to solve multi-variable problems.

3.6.6 Results of Optimization Methods

The series of numerical tests performed on the first test case were also applied to this problem. However, since it may not always be possible to establish a feasible initial starting vector for multi-variable problems, the three optimization techniques which were used to optimize the design so as to minimize the copper loss in the voice-coil actuator were initiated from both random feasible and non-feasible starting vectors.

For the flexible tolerance method it is notable from table(3.9) that the minimum number of function evaluations occurred at $\beta = 0.5$ and $\gamma = 2.0$ but varied by a maximum of 33% over the range of values investigated. These values for β and γ correspond to those obtained by Nedler and Mead[3.17] for the optimization problems which involve a large number of independent variables. The optimum objective function remained constant with a deviation of only 1.1% between the results. The number of function evaluations required when a non-feasible initial starting vector was supplied was on average 186% greater than when a feasible starting vector was available, but the value of the best objective functions remained largely insensitive and were within 0.04% of each other, as shown in table(3.10). Table(3.10) also shows that there is no improvement on the solution for a convergence criterion lower than 0.0001 whilst table(3.11) shows that the most appropriate value of step size is 0.5.

γ	β	Number of Objective Function Evaluations	Best Objective Function Value (W)
1.2	0.1	30304	18.02
1.2	0.3	30162	18.02
1.2	0.5	29578	18.01
1.2	0.7	30026	18.01
1.2	0.9	34042	18.01
1.4	0.1	28158	18.01
1.4	0.3	28204	18.01
1.4	0.5	27996	18.01
1.4	0.7	28184	18.01
1.4	0.9	29743	18.02
1.6	0.1	26442	18.01
1.6	0.3	26402	18.01
1.6	0.5	26014	18.01
1.6	0.7	26684	18.01
1.6	0.9	28038	18.01
1.8	0.1	29338	18.01
1.8	0.3	29174	18.01
1.8	0.5	27962	18.01
1.8	0.7	28650	18.01
1.8	0.9	30242	18.01
2.0	0.1	27992	18.01
2.0	0.3	26378	18.02
2.0	0.5	26342	18.02
2.0	0.7	27610	18.01
2.0	0.9	28620	18.01
2.2	0.1	29992	18.02
2.2	0.3	29750	18.04
2.2	0.5	29531	18.02
2.2	0.7	29797	18.05
2.2	0.9	38680	18.01
2.4	0.1	30871	18.12
2.4	0.3	32017	18.15
2.4	0.5	32020	18.02
2.4	0.7	33087	18.21
2.4	0.9	37941	18.16

Table 3.9 Results of varying β and γ for the Flexible Tolerance method. $\alpha = 1.0$, convergence criterion= 0.0001 and the initial step size = 0.5.

Value of Convergence Criterion	Number of Function Evaluation with Equality Constraints from Feasible Starting Position	Number of Function Evaluation with Inequality Constraints from Feasible Starting Position	Number of Function Evaluation with Equality Constraints from Non-Feasible Starting Position	Best Objective Function Value From Feasible Position (W)	Best Objective Function Value From Non-Feasible Position (W)
0.00001	65328	114620	119219	18.03	18.04
0.00005	28450	36850	58735	18.03	18.03
0.00010	26342	32820	49823	18.02	18.02
0.00050	23742	29191	45901	17.96	18.00
0.00100	18393	23844	43121	17.92	17.95
0.00500	15707	18897	39326	17.78	17.70
0.01000	12682	16007	36680	16.90	17.02
0.10000	1743	2193	1812	11.21	7.49

Table 3.10 Results of varying the convergence criterion on the solution for the FlexibleTolerance method. The results are presented for both the inclusion and the non-inclusion of equality constraints. $\alpha = 1.0, \beta = 0.5, \gamma = 2.0$ and the initial step size = 0.5.

Value of Initial Step Size	Number of Objective Function Evaluations
0.0001	42002
0.0010	36430
0.0100	34692
0.1000	28161
0.5000	26342
1.0000	27409
10.000	28711
100.00	29974
1000.0	31439

Table 3.11 Results of varying the initial step size for the Flexible Tolerance method. $\alpha = 1.0, \beta = 0.5, \gamma = 2.0$ and the convergence criterion = 0.0001.

For the Alternating Directions method it can be seen from table(3.12) that there is a smaller percentage difference between the number of function evaluations required from feasible and non-feasible starting positions Table(3.13) shows the dependence of the initial step size on the number of function evaluations required. The percentage increase in the objective function when a variable became negative was investigated again and table(3.14) shows that an increase of 5% produced a minimum number of function evaluations. Table(3.15) illustrates that for this specific objective function none of the Penalty function techniques offered a significant advantage, and that a large value should be assigned to the numerical constant.

Value of Convergence Criterion	Number of Objective Function Evaluations from Feasible Starting Position	Number of Objective Function Evaluations from Non-Feasible Starting Position	Best Objective Function Value from Feasible Starting Position (W)	Best Objective Function Value from Non-Feasible Starting Position (W)
0.00001	119083	139738	18.10	18.02
0.00005	48767	66923	18.22	18.02
0.00010	36480	57238	18.21	18.02
0.00050	30299	51132	17.99	17.81
0.00100	21871	46352	17.82	17.70
0.00500	21320	44119	17.72	17.70
0.01000	20125	36882	17.48	17.70
0.05000	8705	2019	6.32	1.21

Table 3.12 Results of varying the convergence criterion on the solution for the Alternating Direction method. A square Penalty Function with k = 100 has been used in these results and an initial step size = 0.5.

Value of Initial Step Size	Number of Objective Function Evaluations for Squared Penalty Function	Number of Times Lumped Parameter was Rejected
0.0001	358441	0
0.0010	172448	0
0.0100	141369	0
0.1000	40203	1448
0.5000	36480	4686
1.0000	32647	8645
10.000	26164	15120
100.00	26164	18008
1000.0	26164	44283
1e+04	26164	154684

Table 3.13 Results of varying the initial step size for the Alternating Direction method. A square Penalty Function has been used with k = 100 and a convergence criterion of 0.0001.

Percentage Increase in the Objective Function (%)	Number of Objective Function Evaluations
0.0	36766
5.0	36480
10.0	36983
15.0	37524
20.0	39003
25.0	41296
30.0	46292
35.0	49823
40.0	51294
45.0	53211
50.0	55922

Table 3.14 Results of varying the percentage increase in the objective function when the variables are negative for the Alternating Directions method. A square Penalty Function was used with k = 100 and a convergence criterion = 0.0001.

Value of Constant	Number of Objective Function Evaluations for Linear Penalty Function	Number of Objective Function Evaluations for squared Penalty Function	Number of Objective Function Evaluations for Exponential Penalty Function
0.00001	125403	113527	105246
0.00010	125408	109443	54840
0.00100	118441	71766	48243
0.01000	105480	42961	44883
0.10000	97447	45240	39728
1.00000	81366	36480	36480
10.0000	64088	36480	36480
100.000	48129	36480	36480
1.0e+03	36480	36480	36480
1.0e+04	36480	36480	36480
1.0e+05	36480	36480	36480
1.0e+06	36480	36480	36480
1.0e_07	36480	36480	36480
1.0e+10	36480	36480	36480
1.0e+15	36480	36480	36480

Table 3.15 Results of varying the value of the numerical constant in the Penalty Function for the Alternating Direction method. Convergence criterion= 0.0001 and an initial step size = 0.5.

For the Simulated Annealing method the value of the initial starting position, and hence the initial objective function, is crucial to the effectiveness of the technique. This is because, depending upon the numerical value of *tfactor*, the search is initiated only if the objective function value is within a certain percentage of the present best objective

function. Tables(3.16 and 3.17) show how the initial value of *tfactor, when a feasible* initial starting position was available was approximately an order of magnitude lower than when an initial feasible position was not available. This is due to the fact that a large penalty function is added to the initial non-feasible design. The number of function evaluations was also significantly affected, with an increase of approximately 410%.

Value of *tfactor* max	Value of *tfactor* min	Number of Objective Function Evaluations	Best Objective Function Value (W)
500	0.01	9839	18.02
200	0.01	6501	18.02
100	0.01	4377	18.02
50	0.01	3209	18.23
20	0.01	2710	18.24
10	0.01	2322	18.38
5	0.01	2091	18.38
2	0.01	1893	18.38
1	0.01	1781	18.38
500	0.10	9839	18.02
200	0.10	6501	18.02
100	0.10	4198	18.02
50	0.10	3176	18.23
20	0.10	2754	18.24
10	0.10	2298	18.38
5	0.10	1923	18.38
2	0.10	1818	18.38
1	0.10	1723	18.38
500	1.00	8145	18.02
200	1.00	5986	18.22
100	1.00	3874	18.30
50	1.00	2675	18.40
20	1.00	2213	18.40
10	1.00	1876	18.40
5	1.00	1465	18.46
2	1.00	1123	18.79
1	1.00	786	21.08

Table 3.16 Results of varying the upper and lower value of *tfactor* for the Simulated Annealing method for a feasible starting position. Convergence criterion = 0.0001, a squared Penalty Function has been used with k = 100 and an initial step size = 0.5.

Value of *tfactor* max	Value of *tfactor* min	Number of Objective Function Evaluations	Best Objective Function Value (W)
5000	0.01	21436	18.02
2000	0.01	19201	18.03
1000	0.01	17631	18.32
500	0.01	15983	18.65
200	0.01	15128	19.02
100	0.01	13217	19.10
50	0.01	12763	19.10
20	0.01	11210	21.29
10	0.01	9827	21.91
5000	0.10	21410	18.02
2000	0.10	19081	18.03
1000	0.10	16873	18.32
500	0.10	15762	18.65
200	0.10	15098	19.02
100	0.10	14563	19.10
50	0.10	11218	19.10
20	0.10	10982	21.29
10	0.10	8152	21.29
5000	1.00	19873	18.02
2000	1.00	16382	18.08
1000	1.00	14853	18.32
500	1.00	12998	18.65
200	1.00	11463	10.87
100	1.00	10742	24.99
50	1.00	9270	28.09
20	1.00	8571	32.09
10	1.00	7456	32.98

Table 3.17 Results of varying the upper and lower value of *tfactor* for the Simulated Annealing method for a non-feasible starting position.
Convergence criterion= 0.0001, a squared Penalty Function has been used with k = 100 and an initial step size = 0.5.

In this and the previous test case, the Simulated Annealing method, when used from a feasible starting position, required only 73.3% and 74.0% respectively of the function evaluation for the Flexible - Polyhedron, technique and 16.1% and 17.8% respectively of the number required by the Alternating Directions algorithm.

3.7 Conclusions

All the optimization methods investigated in this chapter have proven to be effective in locating an optimum value of objective function from either feasible or non-feasible starting vectors. However, it can be seen from the results presented that the method of Alternating Directions is inefficient in terms of the number of function evaluations required to obtain the optimum values. However, when used in conjunction with the Simulated Annealing technique it can be seen that the number of function evaluations can be reduced significantly without compromising the optimum. For the two test studies reported in this chapter the same cooling schedule could be applied. This can be considered a general property of this technique if a feasible initial starting vector can be chosen since :

With *tfactor* = 200 then if the initial objective function = 10.0* best objective function so far, then there is a 95.5% certainty of commencing an optimization run.

The Flexible Polyhedron/Flexible Tolerance method proved to be extremely reliable for both the test cases. Although it was commenced from three different initial positions, the maximum deviation between the optimum objective function obtained during one run and the best optimum objective function was only 9% for the first case study and 6% for the second. These results were obtained using convergence criterion levels $\leq 10^{-3}$ and lower. The composite uni-dimensional search strategy described in this chapter has been implemented with a convergence criterion value of 0.0005 assigned as the cross over point between the two methods.

If possible, a feasible starting vector should be applied to the variables for all three optimization methods. This is especially pertinent to the Simulated Annealing technique, since the initial objective function determines if an optimization is undertaken. From the results obtained it is notable that this requires an increased initial value of *tfactor*, thereby resulting in a larger number of function evaluations to obtain the same optimum objective function.

Comparison between the optimized actuator and the design obtained from the methods discussed in chapter 2 are presented in table(3.18), where it can be seen that the optimum design has a theoretical reduction in the copper loss of 7.1%.

Parameter	Design from Chapter 2	Optimum Design
O_d (mm)	40.0	40.0
W_g (mm)	44.0	44.0
IY_d (mm)	34.2	31.4
L_g (mm)	2.8	1.65
L_m (mm)	5.3	5.2
I_d (mm)	18.0	16.7
H_{cs} (mm)	24.0	21.2
L_{cap} (mm)	4.0	5.4
Number of Turns	1885	1885
Permanent Magnet Material	Sm_2Co_{17}(recoma 28) B_r = 1.07T, μ_r = 1.1	Sm_2Co_{17}(recoma 28) B_r = 1.07T, μ_r = 1.1
Soft Magnetic Material	Mild Steel	Mild Steel
Copper Loss (W)	19.40	18.02

Table 3.18 Comparison of design from chapter 2 and optimum design.

It is recommended that if feasible initial vectors can be determined, the Simulated Annealing method should be used as the optimization process, whilst the Flexible Polyhedron technique could be used as an alternative.

Fig(3.13) shows the run-time graphical display from the Simulated Annealing optimization technique. The eight windows at the top of the display correspond to the eight design variables, which are plotted as a function of *tfactor*, as is the objective function(bottom left). The values are plotted when an improved design is obtained. The number of iterations required at each value of *tfactor* is also plotted(bottom middle), the display being refreshed when *tfactor* is lowered so that the cooling schedule can be viewed, and if necessary adapted. In addition, each time an improved design is obtained, a schematic cross-section of the device is plotted(bottom right).

Fig(3.14) illustrates the 'history of optimization' for the voice-coil actuator. The worst and best ten feasible designs are plotted with the value of the copper loss. Thereby the improvements possible during optimization can be observed.

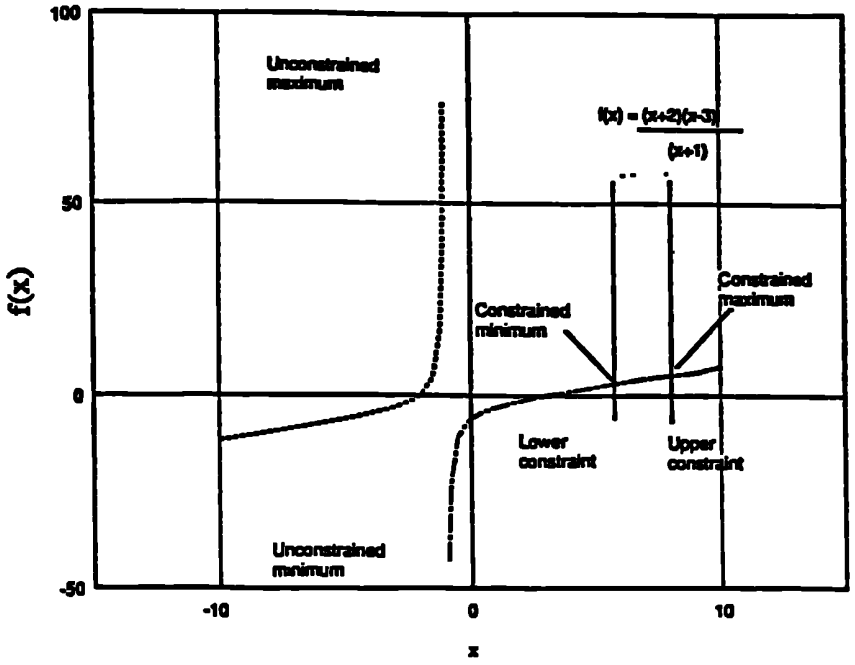

Fig 3.1 Optima possible for a single variable objective function.

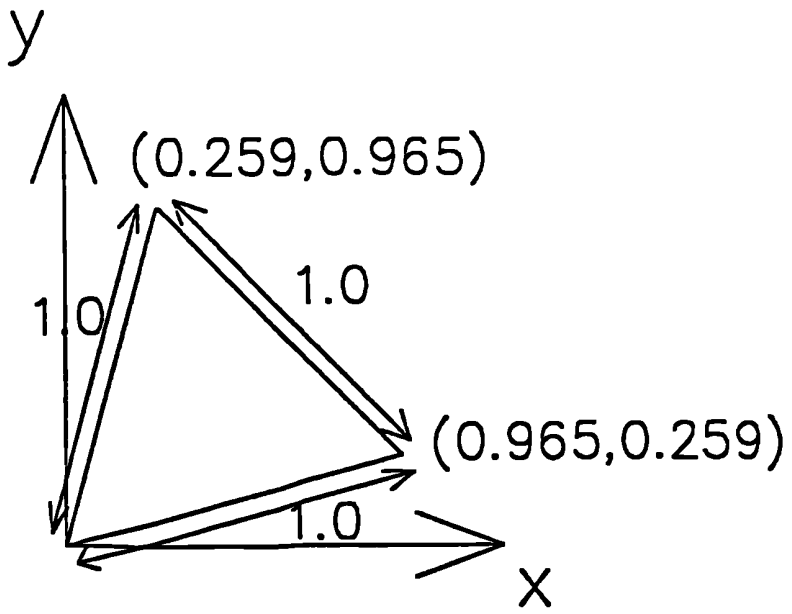

Fig 3.2 Initial starting triangular simplex

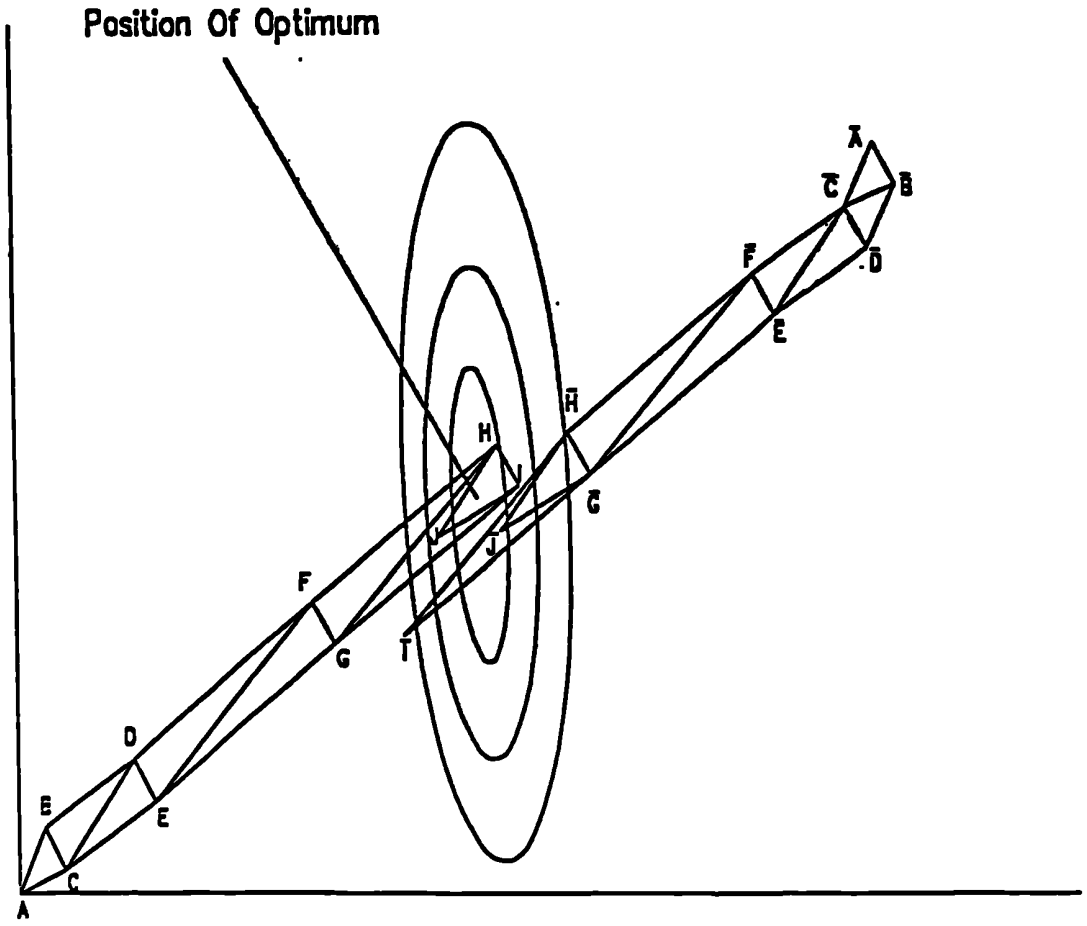

Starting from Position A	Search Starting From Position $\bar{A}$
Initial Simplex 1 ABC	Initial Simplex 1 $\bar{A}\bar{B}\bar{C}$
Expansion -> Simplex 2 BCD	Reflection -> Simplex $\bar{B}\bar{C}\bar{D}$
Reflection -> Simplex 3 CDE	Expansion -> Simplex $\bar{C}\bar{D}\bar{E}$
Expansion -> Simplex 4 DEF	Reflection -> Simplex $\bar{D}\bar{E}\bar{F}$
Reflection -> Simplex 5 EFG	Expansion -> Simplex $\bar{E}\bar{F}\bar{G}$
Reflection -> Simplex 6 FGH	Reflection -> Simplex $\bar{F}\bar{G}\bar{H}$
Reflection -> Simplex 7 GHI	Reflection -> Simplex $\bar{G}\bar{H}\bar{I}$
Contraction -> Simplex 8 HIJ	Contraction -> Simplex $\bar{G}\bar{H}\bar{J}$

Fig 3.3 Location of unconstrained optimum by flexible polyhedron/flexible tolerance method.

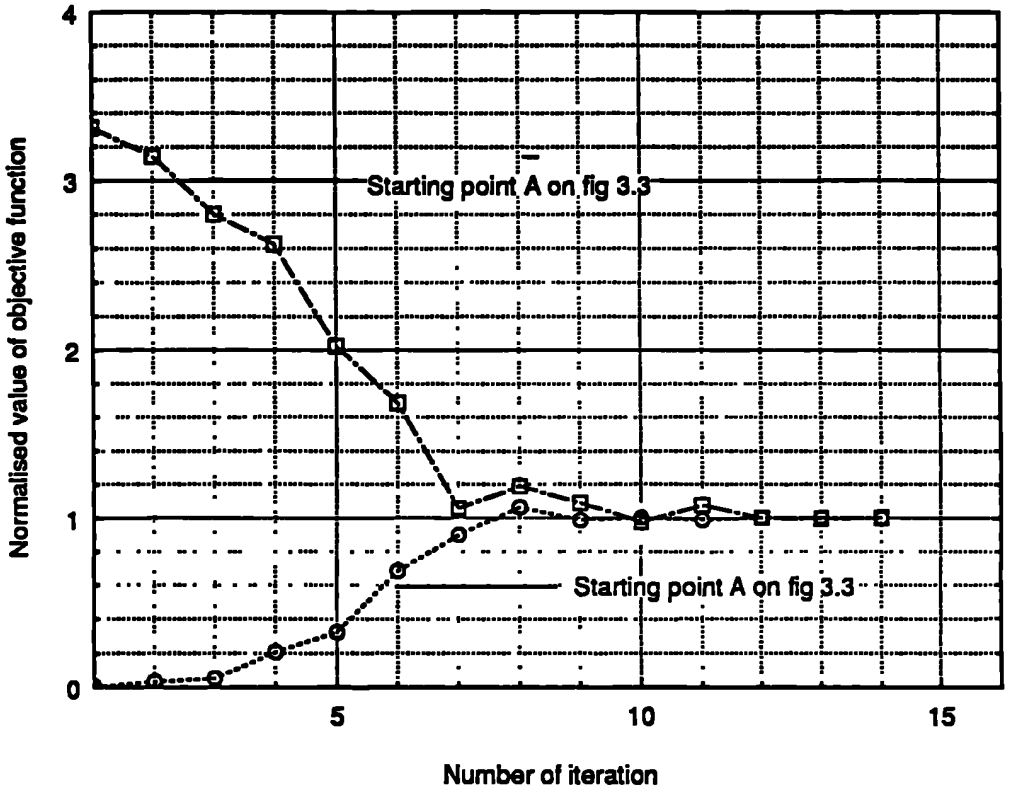

Fig 3.4 Progress of the flexible polyhedron/flexible tolerance method to the optimum solution.

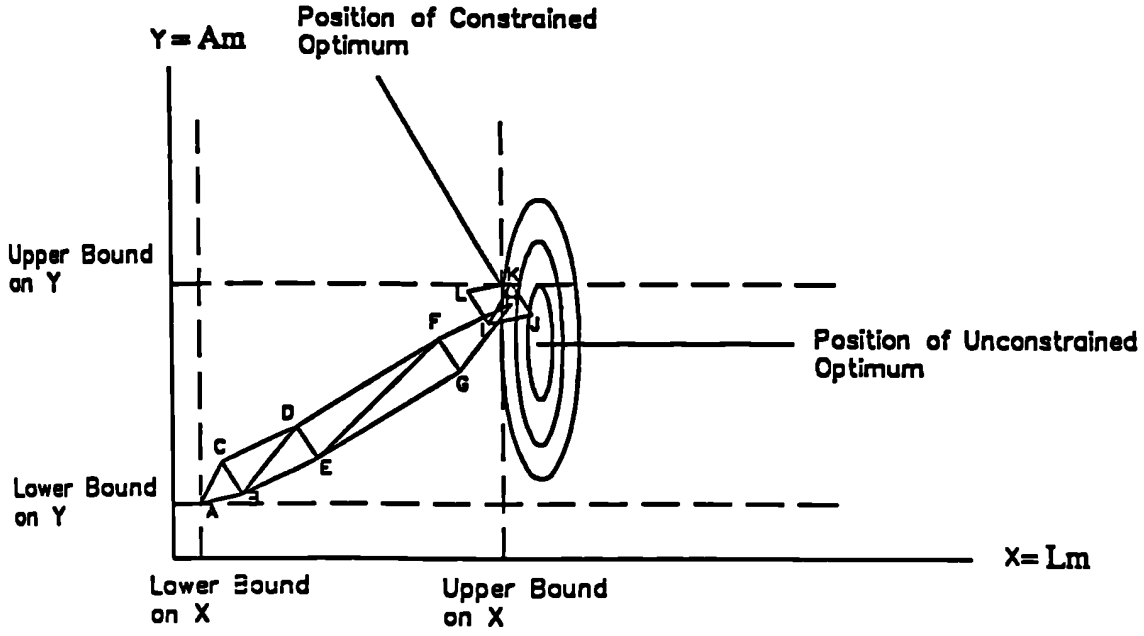

Initial Simplex	ABC
Expansion	BCD
Reflection	BDE
Expansion	DEF
Reflection	EFG
Contraction	FGH
New Simplex	IJK
Reflection	IKL

Fig 3.5 Location of the constrained optimum by the flexible polyhedron/flexible tolerance method.

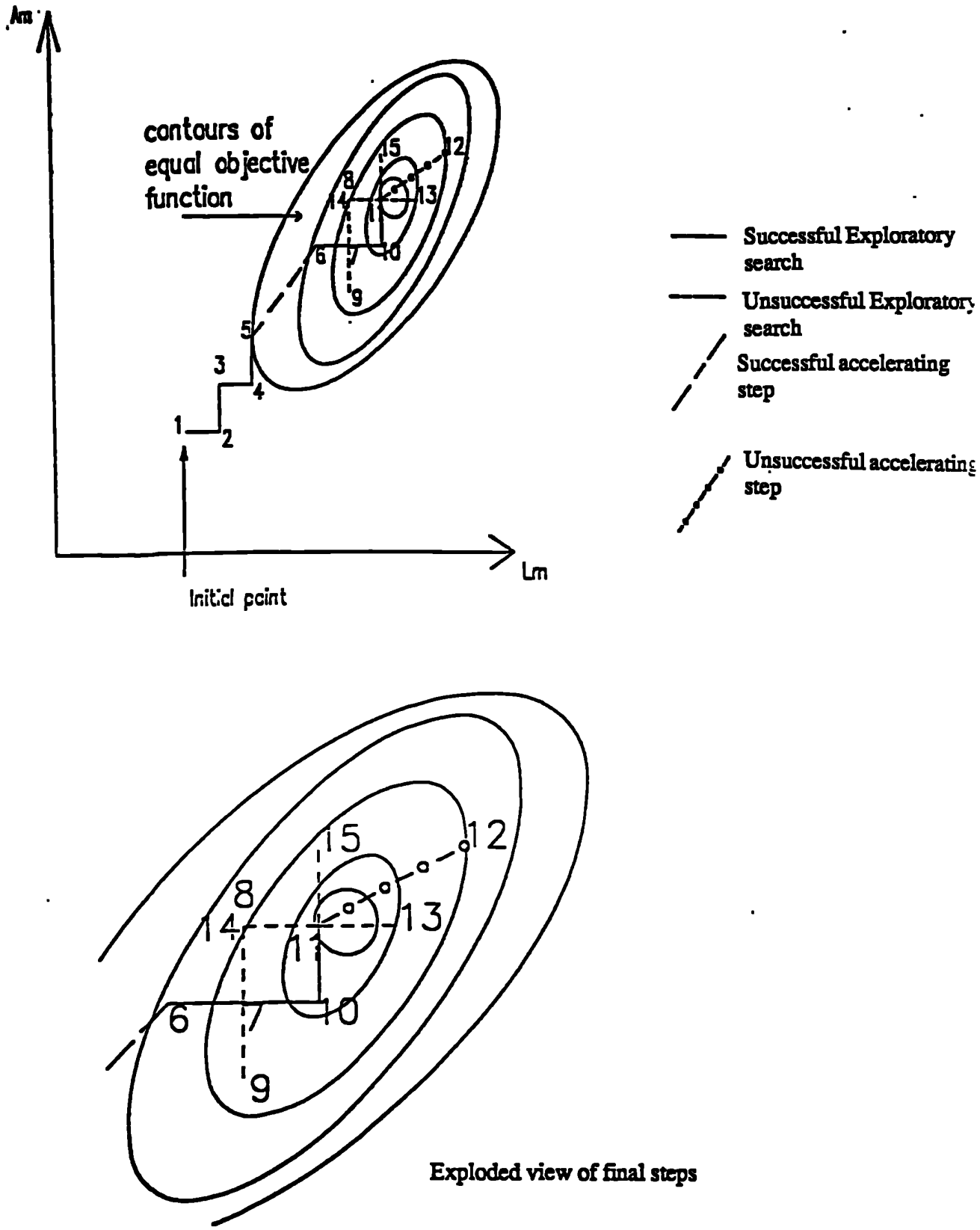

Fig 3.6 Alternating Directions technique in 2-dimensions

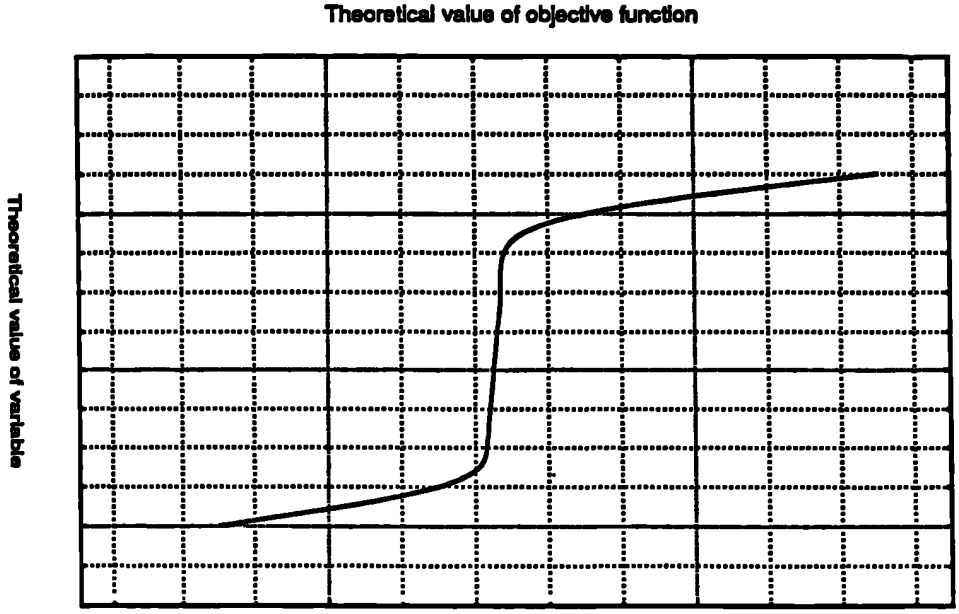

Fig 3.7.a Type of functional not catered for by criterion 1

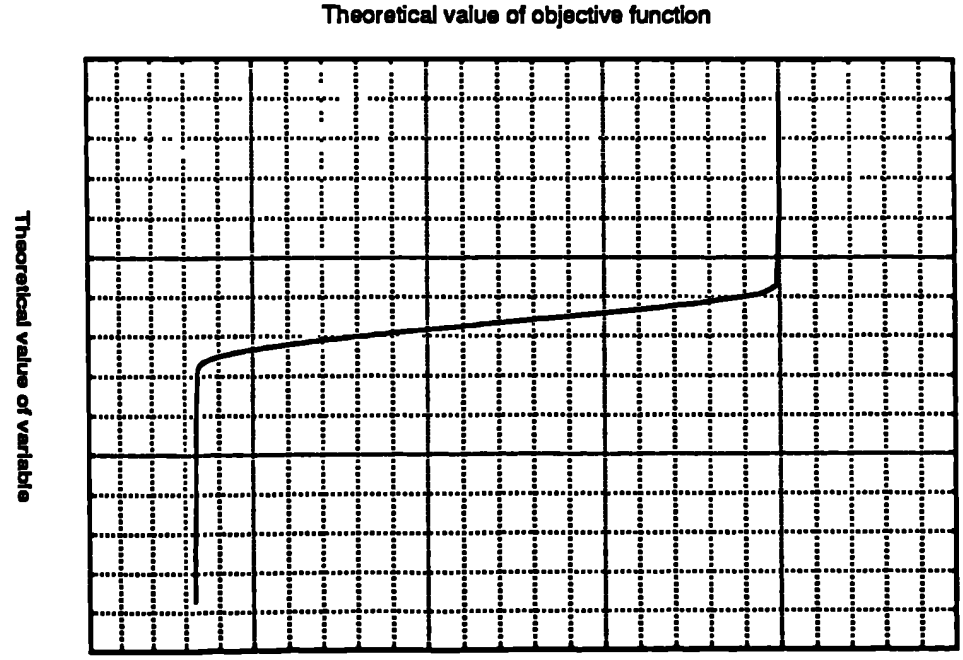

Fig 3.7.b Type of functional not catered for by criterion 2

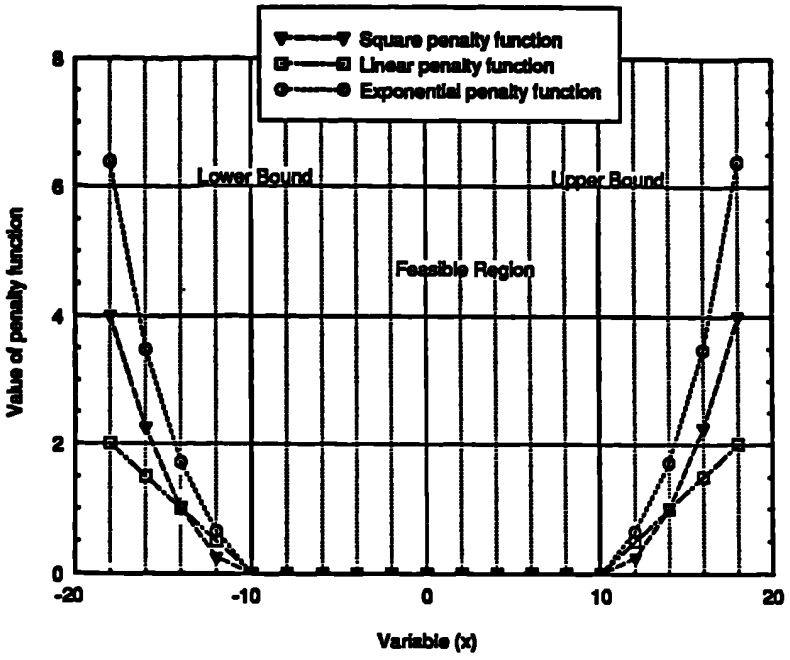

Fig 3.8 Comparison of Penalty functions

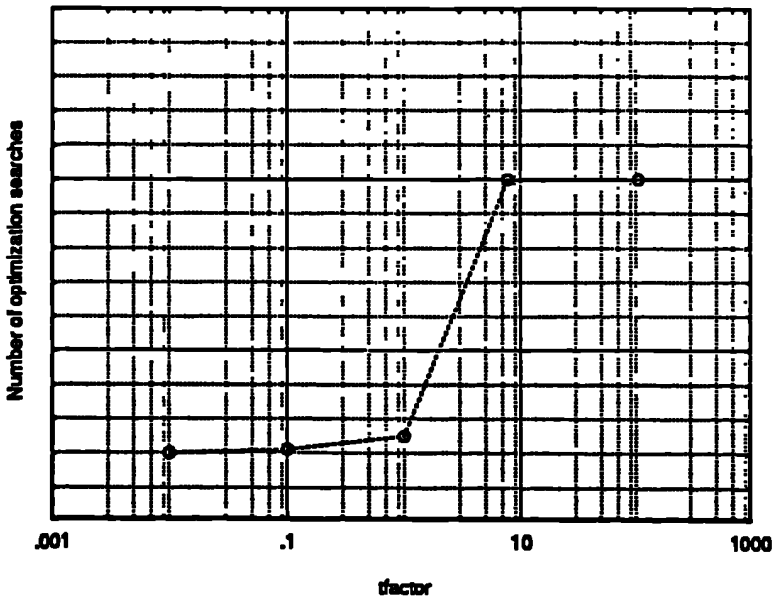

Fig 3.9 Theoretical optimum shape for *tfactor*

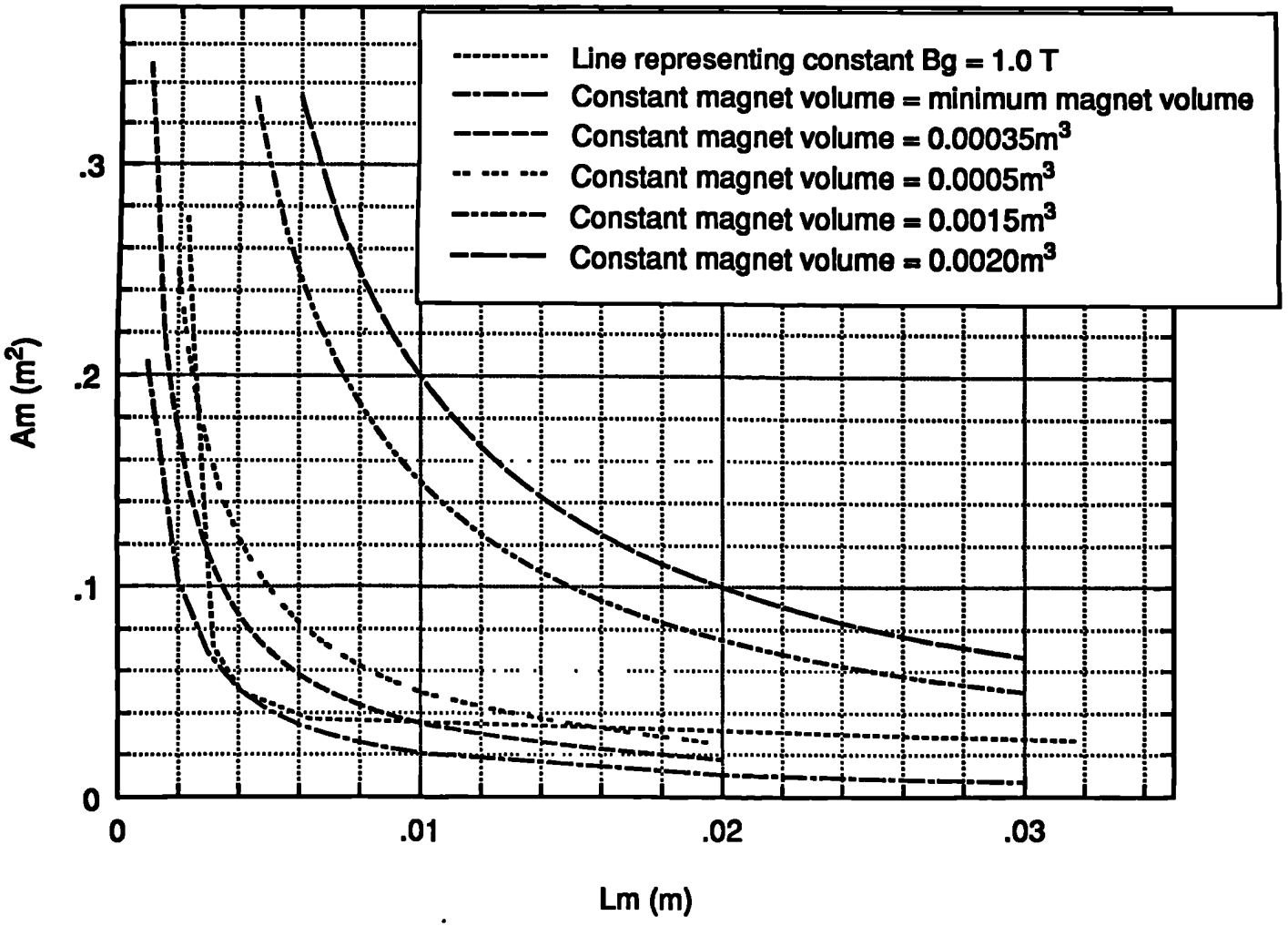

Fig 3.10 Contours of equal magnet volume and constant airgap flux density = 1.0 T.

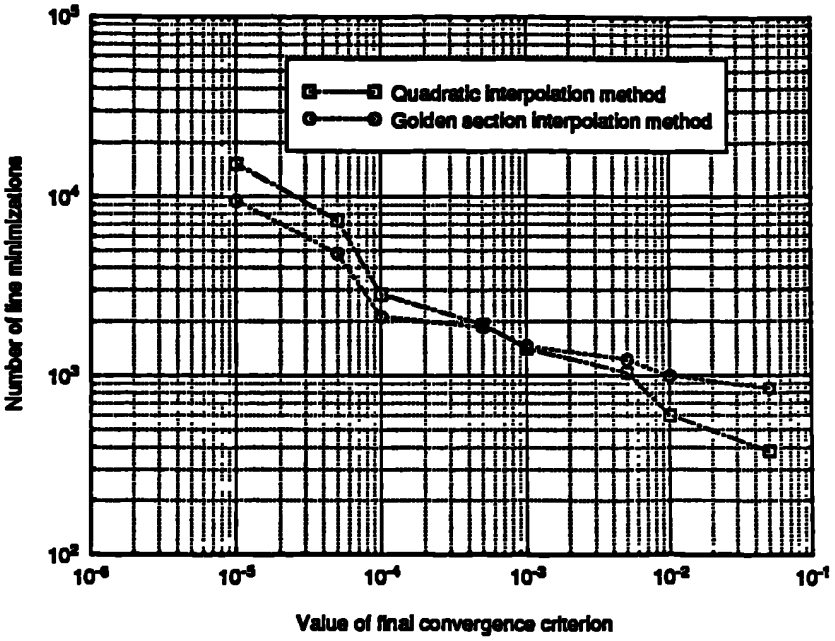

Fig 3.11 Comparison of interpolation methods as the convergence is varied.

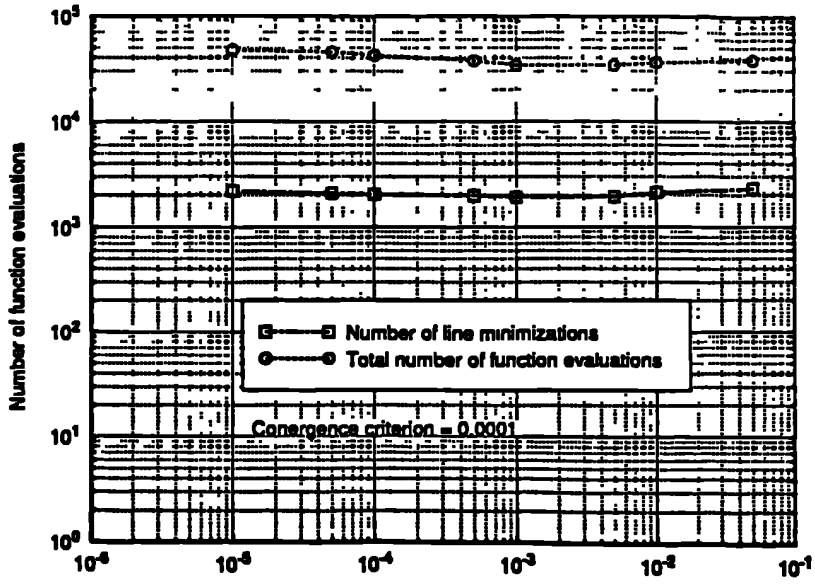

Fig 3.12 The variation of the number of line minimizations required before convergence with the value of the cross-over point from quadratic to golden section line minimization.

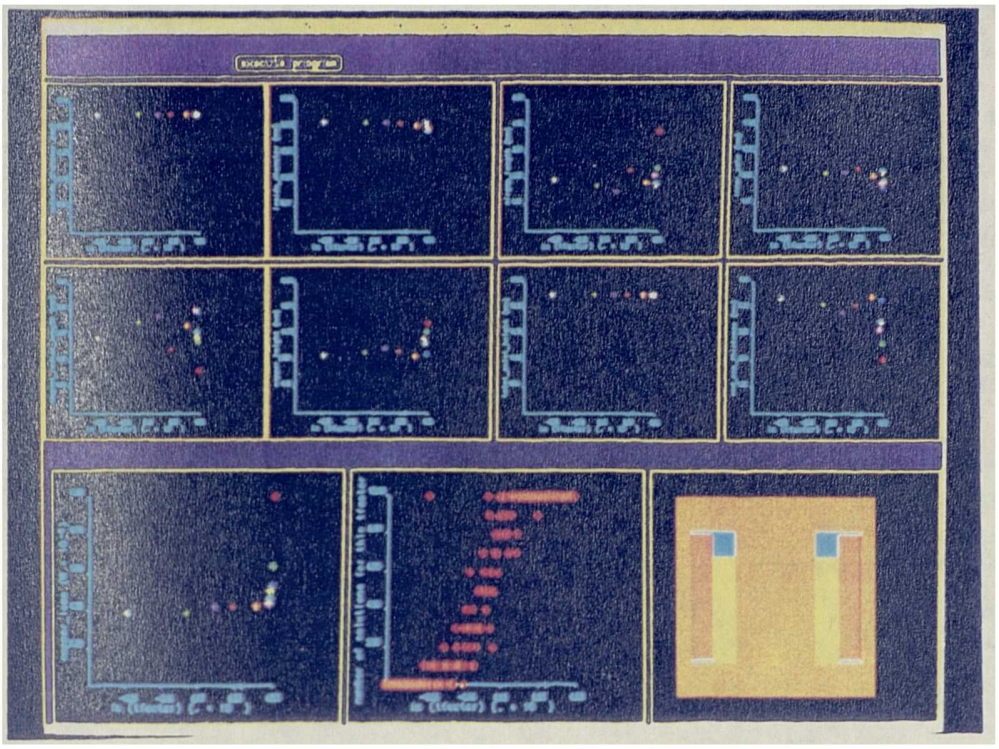

Fig 3.13 Run-time graphical display for the Simulated Annealing optimization technique

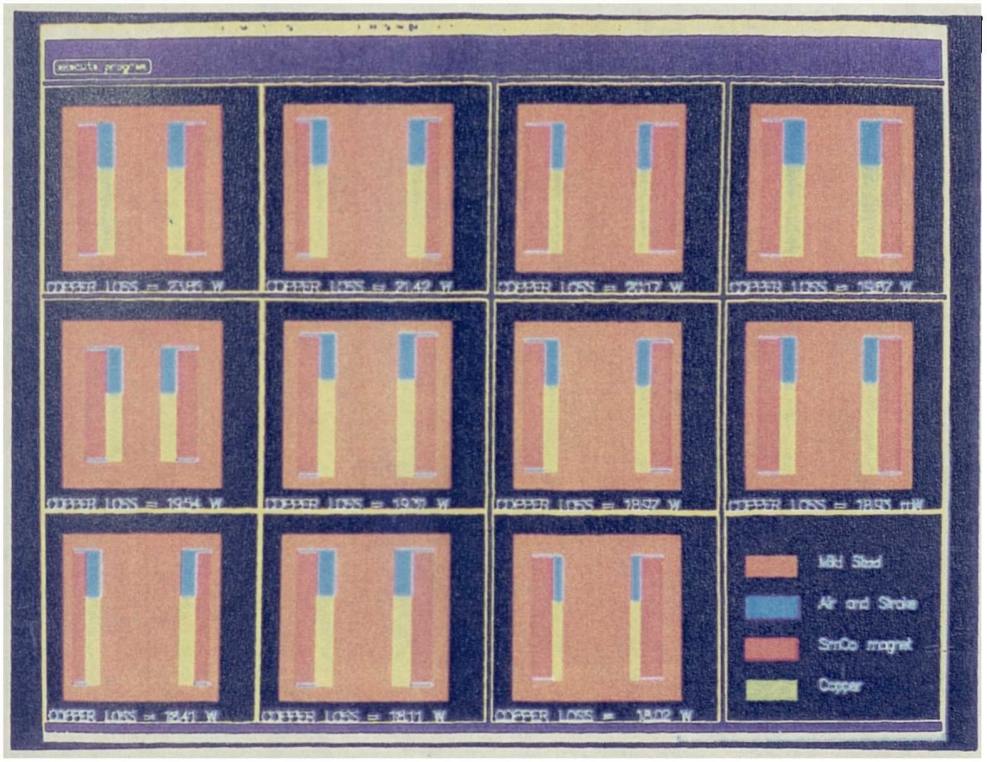

Fig 3.14 'History of optimization for the optimized voice-coil actuator.

CHAPTER 4

MULTI-CRITERION OPTIMIZATION

4.1 Introduction

In chapter 3 the case study, which was concerned with the optimization of a linear voice-coil actuator, was based explicitly upon one objective function, viz: the minimum copper loss. However, in many engineering problems there are often several performance criteria, which cannot be optimized independently, that have to be considered. In general, there will also be other objectives which are important, such as reducing the volume of the permanent magnet or minimizing the total materials cost. Also it is often the case that even if the optimum value of an objective function has been calculated, information regarding the sensitivity of the function about the optimum point would reveal a better compromise solution where a slight increase in the objective function would lead to a significant reduction of another factor. This situation can be formulated as a multi-criterion problem, which is often referred to as multi-objective or vector-optimization[4.1].

In recent years numerous techniques have been proposed to formulate and solve multi-criterion functions, and have been applied with varying degrees of success. In the field of electromagnetic device design, methods such as Lagrange Multiplier Estimation[4.2], Goal programming[4.3], and Hierarchial analysis[4.4] have been used. However, most of the methods obtain a single solution for any set of objective functions. The aim of this chapter is to evaluate the most appropriate method of formulating multi-criterion functions so as to enable the sensitivity of the objective function to be observed. The techniques considered are:

1) Scaling of the functionals by the application of weighting values so that the perceived relative importance of a specific objective function can easily be altered.

2) The use of all but one of the objective functions as flexible inequality constraints and subsequently minimizing the remaining objective function.

3) A technique, (Min-Max), in which a best compromise solution is obtained by considering all the criteria simultaneously, by the minimization of the relative increments of the objective functions from their values determined from individual single-criterion solutions.

Since the combined Alternating Directions/Simulated Annealing technique, which was described in chapter 3, proved to be the most successful in minimizing the number of function evaluations required for convergence, it has also been employed throughout this chapter to minimize the multi-criterion functions.

4.2 Application of Scalar Weighting Values to the Objective Functions

In this technique a multi-criterion objective function is formulated by the addition of the single-criterion functions using numerical values assigned as weighting functions to produce:

$$F_m = \frac{W_{(1)} f_{(1)}}{f_{(1)}} + \frac{W_{(2)} f_{(2)}}{f_{(2)}} + \ldots\ldots \frac{W_{(n)} f_{(n)}}{f_{(n)}} \qquad (4.1)$$

where F_m is the multi-criterion objective function.

$f_{(1)}, f_{(2)}$ and $f_{(n)}$ are the single-criterion objective functions.

$W_{(1)}, W_{(2)}$ and $W_{(n)}$ are scalar weighting values for the objective functions.

$\overline{f(1)}$, $\overline{f(2)}$, and $\overline{f(n)}$ are the normalizing factors.

n = number of objective functions.

Therefore, the vector of objective functions has been reduced to a scalar function which can be solved using any of the single-criterion optimization methods described in chapter 3.

The value of the normalizing factor is critical to the results obtained. Since the objective function F_m is evaluated for each design as it is generated, there is no prior knowledge of the optimum. Therefore, assigning normalizing factors can turn out to be quite arbitrary. Therefore, the procedure which has been adopted in this study is to pre-determine a value for the normalizing factors by performing single-criterion optimization solutions for each single-criterion objective function in turn. For example, to evaluate the normalizing factor, $\overline{f(1)}$, an initial single-criterion optimization would be performed with $W_{(1)}$ set to 1.0, whilst $W_{(2)}$ ..... $W_{(n)}$ are set to 0.0. The optimum value would then be used as the normalizing factor for the objective function $f_{(1)}$. This process would then be repeated until values for all $\overline{f(1)}$ to $\overline{f(n)}$ have been obtained.

Usually it has been assumed that[4.5]:

$$\sum_{i=1}^{n} W_{(i)} = 1 \tag{4.2}$$

Although this is an arbitrary rule, it has also been incorporated in this investigation so that when one of the weighting functions is set equal to unity, all the other objective functions become zero, and the minimum of the multi-criterion function should correspond to the solution of the single-criterion optimization for the corresponding function.

The main disadvantage with the scalar weighting method is that the value of the optimum can change rapidly as the weighting factors are varied, and in general there is no *a priori* knowledge of what values to assign to the weightings. Therefore, it requires a large number of multi-criterion solutions in order to obtain a comprehensive idea of the sensitivity of the optimum to the weightings, which is computationally inefficient, especially if more than two objective functions are involved in the multi-criterion solution, since a combinatorial increase in solutions is required.

4.3 Use of Objective Functions as Flexible Inequality Constraints

By far the most common technique of incorporating alternative parameters into an optimization problem is by assigning them as constraints to the minimization of the most important objective function. A second technique of solving multi-criterion problems which has been investigated in this study is to express all but one of the objective functions as inequality constraints and to minimize the remaining objective function. However, by allowing these inequality constraints to be incremented between subsequent optimization solutions, the sensitivity of the objective functions can be observed. The choice of function to be minimized depends upon its relative importance, since the least important objective function should be converted into flexible inequality constraints. A significant advantage of this technique is that it effectively reduces the available parameter space and therefore increases the computational efficiency of the solution. The units applied to the objective-function-constraints should be of the same order of magnitude as the bounds on the independent variables, so that they influence the convergence of the solution.

The values of the flexible inequality constraints are then increased by a fixed amount until they reach a pre-specified maximum. i.e.

$$f_{(i)} = f_{(i)} + \Delta f_{(i)} \qquad \text{for } i = 1,.....n \tag{4.3}$$

where $f_{(i)}$ = the i^{th} objective function,

$\Delta f_{(i)}$ = the increase in the i^{th} objective function

n = number of objective functions

4.4 Min-Max Multi-Criterion Optimization Technique

This technique of formulating multi-criterion objective functions, proposed by Jutler[4.6], involves the minimization of the sum of the relative increments from the results obtained from single-criterion optimization of the individual objective functions. That is, the multi-criterion objective function is formulated as follows:

i.e.
$$F_m = \sum_{i=1}^{n} \frac{|f_{(i)} - \overline{f_{(i)}}|}{|f_{(i)}|} \tag{4.4}$$

and is then minimized. A significant drawback with this technique is that it only provides one possible solution for a given set of objective functions and normalizing factors, and therefore no sensitivity of the objective function is available. Theoretically, this result is the optimum compromise of all the objective functions, since the sum of the relative deviations from the single-criterion results has been minimized, and the relative importance of each objective function is accounted for. However, if this design does not meet the required performance specification, the only recourse is to alter the values of the normalising factors. Therefore, although the computational requirements may be

significantly reduced in comparison to the Scalar Weighting technique, there is not the same quality of information available to the design engineer.

4.5 Global Criterion Methods

An extension to the Min-Max technique is to fit a curve to the vector of single-criterion minimized objective functions values and alter the order of the curve fit to test the sensitivity of the results[4.7,4.8].

The form of the multi-criterion function which was examined is:

$$F_m = \sum_{i=1}^{n} [(\frac{|\overline{f(i)} - f(i)|}{|\overline{f(i)}|})]^p \qquad (4.5)$$

where $f(i)$ is the value of the single-criterion minimum of the i^{th} objective function, p is the exponent of the equation.

The normalization of the functionals is again determined by the results of the single-criterion optimization of each objective function. Depending upon the topography of the objective function, the value of the exponent, p, could have a significant influence upon the results obtained, since it determines the degree of curve fitting assumed. For example, if p is set to 2, then the least square error between all the objective functions will be minimized.

The method was then extended to accommodate the curve fitting type.

$$F_m = \left(\sum_{i=1}^{n} \left(\frac{|\overline{f(i)} - f(i)|}{|\overline{f(i)}|} \right)^{1/p} \right)^p \qquad (4.6)$$

which also produces a 'measure of the closeness' of a multi-criterion solution to its ideal solution (1.29). An interesting consequence of this fitting technique is found by allowing p -> ∞. as then the Global Criterion method reverts to the Min-Max solution of equation(4.4) since:

$$F_m = \left(\sum_{i=1}^{n} \left(\frac{|\overline{f(i)} - f(i)|}{|\overline{f(i)}|} \right)^{1/\infty} \right)^{\infty} = \sum_{i=1}^{n} \frac{|\overline{f(i)} - f(i)|}{|f(i)|} \qquad (4.7)$$

Therefore, the specific case of the Min-Max optimization described in section(4.4) can be accommodated in the Global Criterion method. In order that the sensitivity of the optimum solution could be investigated, the practice adopted in this study was to alter the value of the exponent, p, and obtain a set of multi-criterion results which could then be examined.

It may be possible that a single combination of scalar weightings, a value for the flexible inequality constraint, or an exponent in the Global Criterion method would result in an acceptable design, and the computational requirements would be reduced significantly. However, one of the main criticisms of constrained optimization procedures is that they provide insufficient information so that an experienced design engineer can use his intuition to choose an appropriate design. By their very nature, the multi-criterion techniques described in this study are computationally demanding, since they also require the solution of the single-criterion objective functions. Therefore, for the test case to be presented, computational efficiency was a secondary consideration compared to the quality of information. Nevertheless, the number of function evaluations was monitored to determine which was the most efficient of the techniques investigated.

4.6 Test Case

The test case described in chapter 3 which required the minimization of the copper loss in a voice-coil actuator has been used by adding the objective functions of magnet volume and total volume to the copper loss to produce a multi-criterion objective function to be minimized using the Alternating Direction/Simulated Annealing method. For all the techniques for formulating the multi-criterion objective function, the total number of objective function evaluations required is used to indicate the computational effort required.

From the schematic diagram of fig(2.4) the objective functions can be formulated as:

$$f_{(1)} = \frac{\pi O_d^{\,2} W_s}{4} \tag{4.8}$$

$$f_{(2)} = \frac{force^{\,2} \rho_{cu}}{B_g^2 V_g k_{pf}} \tag{4.9}$$

$$f_{(3)} = L_m (H_{cu} + stroke + 2*L_{mca}) (I_d + 2*L_g + 2*L_{mcr} + L_m) \tag{4.10}$$

The constraints applied are the same as those assumed for the single-criterion optimization study in chapter 3.

The maximum value for the current density was constrained by British Aerospace due to temperature rise and power supply limitations such that $J \leq 40\ A/mm^2$.

The first step is to calculate values for the normalizing factors by performing single-criterion solutions for each of the two new objective functions. Implementing the recommendations of chapter 3 regarding the Simulated Annealing method, the actuators shown in fig(4.1) and whose dimensions are given in table(4.1), were obtained for the minimization of the total volume alone ($41840 mm^3$), the minimization of the copper loss alone (18.02 Watts) and the minimization of the magnet volume alone ($3590 mm^3$), all

of the actuators producing a force of 32.0N. Neither of the actuators optimized for total volume or magnet volume would have been applicable to the application in chapter 2 because their copper losses (38.23 W and 55.11 W) respectively, were far in excess of the specification. However, for alternative applications these devices may have provided the most appropriate design if either space or materials cost were critical.

Parameter	Actuator for Total Volume Minimum	Actuator for Copper Loss Minimum	Actuator for Magnet Volume Minimum
O_d (mm)	38.4	40.0	40.0
W_s (mm)	36.1	44.0	44.0
I_d (mm)	30.2	31.4	28.0
IY_d (mm)	16.3	16.7	18.0
L_g (mm)	1.77	1.65	2.07
L_m (mm)	4.75	5.20	2.38
H_{cs} (mm)	15.9	21.2	18.9
Stroke	12.0	12.0	12.0
L_{cap}	4.1	5.4	6.6

Table 4.1 Results of single-criterion optimization to obtain normalization factors.

The results from these single-criterion optimizations were then used as the normalizing values for the subsequent analyses.

4.6.1 Results of Weighting Method

The weighting values were varied in 0.2 increments from initial values of $W_{(2)} = 1.0$, $W_{(3)} = 0.0$ to $W_{(2)} = 0.0$, $W_{(3)} = 1.0$, with $W_{(1)}$ held constant at 0.0. The value of $W_{(1)}$ was then incremented and $W_{(2)} = 0.2$, and $W_{(3)}$ varied again and so on. Table(4.2) illustrates how the value of total volume objective function was the least sensitive to its assigned weighting, its value only changing by 32%. This was largely due to the maximum total volume being constrained by the bounds set upon the outside diameter and axial length. However, the magnet volume and copper loss varied considerably as the weightings were altered, varying by 312% and 437% respectively. It is notable that the copper loss increased significantly as the value of its weighting factor changed having

a larger value when the weighting of the magnet volume objective function was increased compared with when the value of the weighting of the total volume objective function was increased, again illustrating that these were the sensitive objective functions. Fig(4.2) schematically illustrates some of the multi-criterion solutions in axisymmetric cross-section.

The principal benefit of this technique is that a wide range of optimized designs are made available and the most appropriate for any specific application may be chosen. However, this benefit is somewhat counteracted by the fact that an enormous number of function evaluations are required to produce these results.

$W_{(1)}$	$W_{(2)}$	$W_{(3)}$	Total Volume *e-06 (m^3)	Copper Loss (W)	Magnet Volume *e-06 (m^3)	F_m
0.0	1.0	0.0	55.29	18.02	11.23	1.00
0.0	0.8	0.2	55.29	19.87	8.11	1.33
0.0	0.6	0.4	55.29	23.83	6.56	1.52
0.0	0.4	0.6	55.29	30.42	4.34	1.40
0.0	0.2	0.8	55.29	42.54	3.66	1.29
0.0	0.0	1.0	55.29	57.11	3.59	1.00
0.2	0.8	0.0	54.19	18.20	10.23	1.07
0.2	0.6	0.2	53.65	22.77	7.30	1.42
0.2	0.4	0.4	50.96	34.06	4.86	1.54
0.2	0.2	0.6	53.65	52.82	3.67	1.46
0.2	0.0	0.8	53.61	78.81	3.64	1.07
0.4	0.6	0.0	52.56	18.80	9.87	1.13
0.4	0.4	0.2	50.95	23.43	7.46	1.42
0.4	0.2	0.4	51.50	40.01	3.72	1.35
0.4	0.0	0.6	53.64	58.81	3.67	1.13
0.6	0.4	0.0	45.79	22.76	9.02	1.16
0.6	0.2	0.2	45.79	31.53	5.67	1.32
0.6	0.0	0.4	53.64	60.35	3.74	1.19
0.8	0.2	0.0	42.82	27.46	9.14	1.12
0.8	0.0	0.2	45.79	75.55	5.75	1.20
1.0	0.0	0.0	41.84	38.23	6.02	1.00

Table 4.2 Results of weighted scaling. The total number of function evaluations required to obtain these results was 134309.

4.6.2 Results of Incorporating Objective Functions as Flexible Inequality Constraints

The magnet and total volume functions were incorporated into the optimization problem as flexible inequality constraints. Initially, the value for the magnet constraint was set equal to its single-criterion optimization solution, whilst the total volume objective function was set to its maximum value throughout the whole of the study because of its insensitivity in the weighted scaling results

i.e.

$$f(1) = 55290\, e^{-9} m^3$$

$$f(3) = 3590\, e^{-9}\, m^3$$

The magnet volume was then allowed to increase from its initial value in 10% increments, i.e.

$$f(3) = 3590\, e^{-9} + 0.1\, f(3)$$

Table(4.3) shows the results from these solutions, which exhibit a similar trend to those obtained for the scalar weighting technique. In both techniques the copper loss increases rapidly as the constraint on the magnet volume approaches its single-criterion value. However, the copper loss has a smaller increase at higher values of the magnet volume. For example, with a magnet volume of twice its single-criterion value the copper loss increases only by 25% of its optimum value. In addition, when the magnet volume is increased to above 10.25*e-06 m^3 there is no further decrease in the copper loss, since this is the same solution as the single-criterion optimization for copper loss, and therefore, cannot be improved upon. The number of $\frac{function\ evaluations}{optimization\ solutions}$ for this technique is only approximately 70% of that required by the weighted scaling method, which is a

direct result of the reduction in the parameter space by the incorporation of the extra inequality constraint.

Objective -Function-Constraint Magnet Volume *e-06 (m^3)	Objective Function Copper Loss (W)
3.59	57.11
3.95	36.28
4.34	30.42
4.78	29.01
5.26	28.15
5.78	27.15
6.36	24.14
7.00	21.12
7.70	19.54
8.47	18.74
9.37	18.52
10.25	18.11
11.27	18.02
12.40	18.02

Table 4.3 Results obtained by incorporating the magnet volume objective function as a constraint into the solution of the copper loss objective function. The total number of objective function evaluations required to obtain these results was 63216.

4.6.3 Results of Global Criterion Method

Finally, the Global Criterion method was implemented incorporating both types of curve fitting functions established in equation(4.5 and 4.6), for a range of exponent values. To simulate the Min-Max optimization case in which the exponent $\rightarrow \infty$, the value was set equal to 100. The results are presented in table(4.4) which shows that the value of the objective functions were similar for all the exponent values. The reason for this is that the copper loss and magnet volume objective functions are extremely sensitive and either of these would increase rapidly if the reduction of the other from the multi-criterion optimal point was demanded. Consequently, it is possible to obtain the multi-criterion optimum very efficiently. However, in contrast to the scaling weighting technique which produces several multi-criterion optimum designs, from which a specific design may be

chosen, if the design evaluated by the Global Criterion technique is not acceptable to the engineer, an alternative multi-criterion methodology has to be implemented. It is therefore, advised that the Global Criterion technique is used as the first multi-criterion technique with a single value of exponent, for example p=2, and if this does not produce an acceptable design, then continue with the alternative exponent values and then alternative multi-criterion methods.

In comparison with the Scalar Weighting method, the results closely match the case where $W_{(2)} = W_{(3)} = 0.4$ and $W_{(1)} = 0.2$. This may be anticipated since the copper loss and magnet volume objective functions are the most sensitive and have a more pronounced effect on the value of the multi-criterion solution, whilst the total volume is largely insensitive to its weighting.

Exponent Value	Total Volume *e-06 (m^3)	Copper Loss (W)	Magnet Volume *e-06 (m^3)
1	51.45	31.69	5.63
2	52.61	31.37	5.64
3	53.15	31.27	5.65
4	54.17	31.19	5.66
5	54.41	31.10	5.69
10	54.41	31.10	5.69

Table 4.4 Results from Global Criterion method with the functional form as in equation (4.5). The total number of objective function evaluations required to obtain these results was 36624.

Exponent Value	Total Volume *e-06 (m^3)	Copper Loss (W)	Magnet Volume *e-06 (m^3)
1	53.64	49.97	3.83
2	50.95	47.08	3.92
3	53.59	51.15	3.72
4	53.55	53.30	3.70
5	53.49	52.39	3.81
10	54.73	50.14	3.82
100	55.29	49.02	3.19

Table 4.5 Results from Global Criterion method with the function form as in equation(4.6). The total number of objective function evaluations required to obtain these results was 43218.

4.7 Conclusions

The multi-criterion optimization results which have been investigated in this chapter increase the information available to the design engineer in attempting to identify an optimum design. The Scalar Weighting method, although computationally demanding, gives an insight into the sensitivity of the objective functions. In practice this would usually be applied in an iterative manner, with large increments in the weighting values being applied initially, these becoming refined as the user selects a 'region of interest', for which the increments on the weightings would be reduced. The results allow the user to select a design which is a compromise between all the objective functions according to their perceived relative importance for a specific application. However, the major limiting constraint with this method is the increase in the number of objective function evaluations required as the number of objectives is increased.

The results for the technique in which the objective functions are incorporated into the optimization problem as flexible inequality constraints are easy to analyse. The design engineer would quickly be able to identify a design from table(4.3) which is acceptable for his specific application. However, it has similar problems to the Scalar Weighting technique in that it becomes very cumbersome if more than two objective functions are to be incorporated. It is likely that the objective function would then be applied simply as constraints and not incremented, the value of the constraint being equivalent to the highest value acceptable for the parameter. For example, in this study the problem would have been formulated as follows

Magnet Volume $\leq$ constraint[1]

Total Volume $\leq$ constraint[2]

Objective function = copper loss.

and assuming that a feasible design was obtained, it would automatically suit the engineer.

The Global Criterion technique is very powerful and can obtain a design, which is the best compromise between the single-criterion solutions, very quickly. However, as experienced in this study the solution with varying exponents did not span the whole range of values for the objective functions as was possible with the scaling technique. The results obtained therefore, might not satisfy the needs of the user and a second alternative technique must be employed to determine the sensitivity of the objective functions. The principal advantage of the method is that even as extra objective functions are considered the computational requirements do not become excessive.

It has been shown in this study that if the design engineer requires an optimum design then one can be computed very quickly which will be a compromise between the functionals. In addition, it is also possible to present a number of alternative optimum designs from which he may wish to use his experience to select an appropriate design for a specific application. Finally, although the number of function evaluations can become enormous, for example 134309 required for the scalar weighting method in this chapter, this can be evaluated in approximately 2 hours on a 'SUN 386' workstation and still represents a more effective approach to obtaining an optimum design than 'trial and error' techniques.

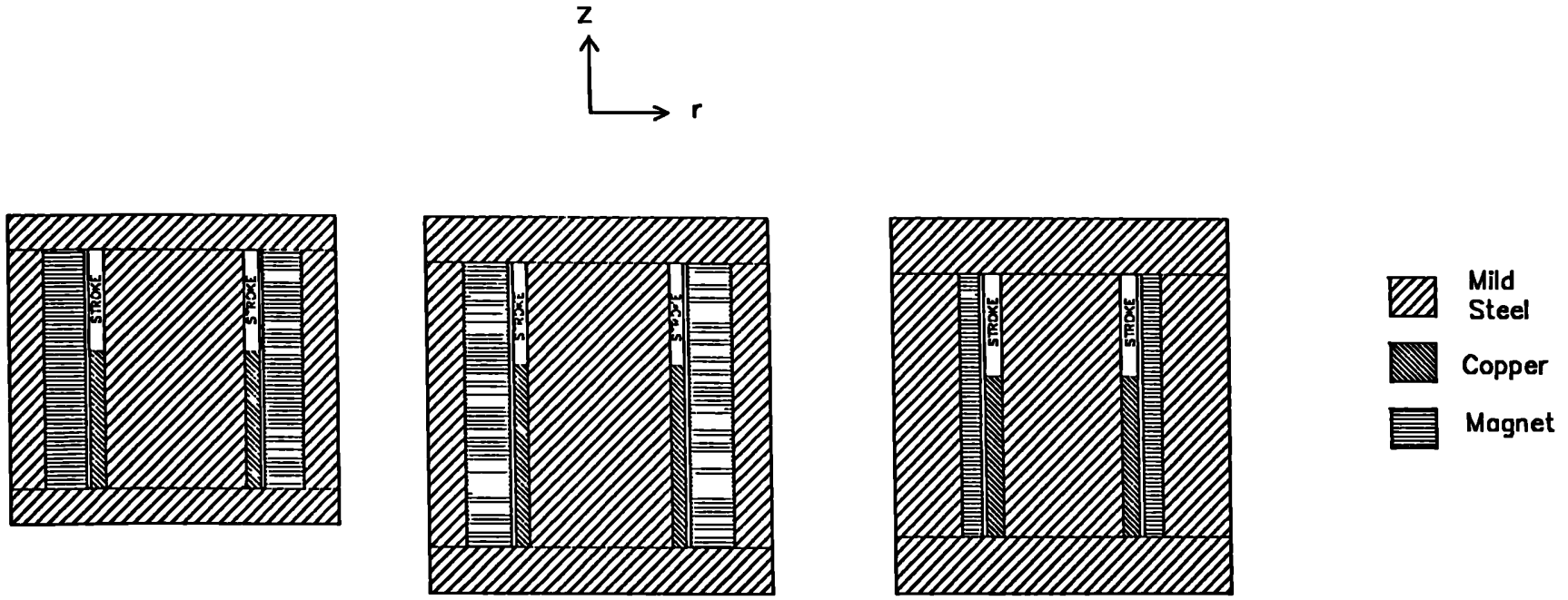

a) Minimum Total Volume ($41840\ mm^3$)

b) Minimum Copper Loss (18.02 W)

c) Minimum Magnet Volume ($3590\ mm^3$)

Fig 4.1 Single-Criterion optimization solutions

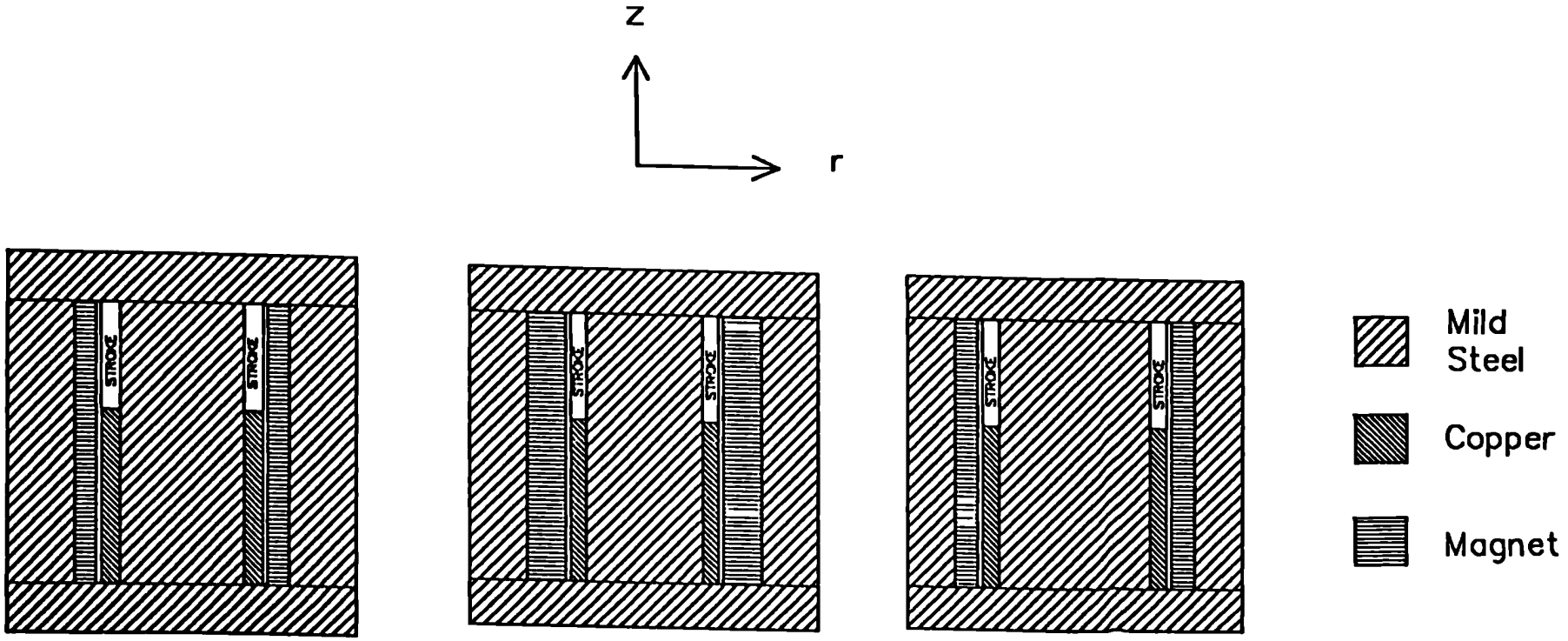

Fig 4.2 Multi-criterion optimized actuators for different weighting values.

CHAPTER 5

DESIGN OPTIMIZATION OF PERMANENT MAGNET TOROIDALLY WOUND ACTUATORS

5.1 Introduction

A permanent magnet toroidally wound actuator or Limited Angle Torquer usually consists of an internal permanent magnet rotor and a toroidal (Gramme ring) winding in either a slotted or slotless stator, as illustrated in figs(5.1) and (5.2). Reported design studies have resulted in the development of actuators with torque levels ranging from 10mNm up to 1.6Nm[5.1,5.2], but in general for larger devices, (typically > 1Nm), lower material costs appear to make the wound rotor, doubly-excited type, as illustrated in fig(5.3), more economic. This view is supported by the fact that none of the major actuator manufacturers[5.3,5.4,5.5] make permanent magnet actuators with torque levels in excess of 1Nm. In lower torque devices the simpler rotor construction and absence of rotor copper loss make the permanent magnet rotor the preferred topology and result in higher electrical efficiency and better power to weight ratio devices. Traditionally, one-piece alloy-magnet rotors such as Alnicos were popular because of their ease of construction, low material costs and easy in-situ magnetization. However, these types are more readily demagnetized when exposed to armature reaction fields, which drive the magnet working point of these non-linear magnet materials beyond the knee of their second quadrant BH characteristic. More recently, sintered and polymer-bonded rare-earth magnet materials, with linear second quadrant characteristics have been used. In these devices the magnets are usually mounted on a steel rotor core, although for two pole designs, a one piece rotor may still be employed[5.3].

The slotted winding stator gives an improved torque constant, better efficiency and a higher torque to weight ratio than the slotless toroidally wound types because the proportion of copper exposed to the magnetic field is higher, and the magnetic field intensity is increased due to the smaller effective airgap. In addition, heat conduction from the windings is superior because of the relatively large area of surface contact within the slots. The slotless actuator however, has extremely low torque ripple and the smooth stator suffers less from local armature reaction saturation effects, thus giving a more linear torque-current characteristic and making it a predominantly thermal rather than magnetically constrained device, capable of withstanding very high, short-term overload currents.

Typical LAT applications include closed loop high quality optical and infra-red scanning devices, stabilized platforms, material handling and positioning systems[5.6]. The actuators could also be used in lower precision open loop systems but because of the shape of the torque/angle characteristic, i.e. ideally flat top, they would require the use of a return spring for stable position control. They would then be in direct competition with iron-vane, Laws' Relay type devices[5.7] which, due to the high saturation density of the moving iron-vane, will almost certainly outperform the LAT on the basis of torque/inertia, but which have much more non-linear torque-current characteristics.

The theoretical maximum angular displacement 'β' which can be produced by the LAT is given by:

$$\beta = \frac{\pi}{2p}(\text{rad}) \qquad \text{or } \beta = \frac{180}{2p} \text{ (degrees)} \tag{5.1}$$

where p = number of poles.

In practice, the torque is nominally constant over only a limited range of the maximum displacement angle due to regions where the magnet poles do not fully overlap the windings. Typically, for the slotless version, this results in a trapezoidal

torque-displacement characteristic, known as the 'torque-motor' characteristic, as illustrated in fig(5.4) for a 2-pole device.

The study reported in this chapter was undertaken in collaboration with Automatic Systems Laboratories and relates to a fast response, large angular displacement, limited-angle, toroidally-wound actuator, required for use in an Infra-red 'Lasertrace' scanning system for precision displacement measurements. Two high resolution LAT devices were required to control the angular position of two mirrors forming part of the optical system.

Typical commercial devices could not produce the required speed of response, since most are designed to maximize either $\frac{torque}{\sqrt{copperloss}}$ or torque/amp ratios, and less emphasis is placed on their torque/inertia ratios, resulting in relatively low values of maximum rotor acceleration.

Thus, the following study was undertaken with the objective of designing a number of actuators, based on the typical commercial device specification given in table(5.1) with alternative constraints and to meet alternative performance criteria.

Basically two groups of designs were considered:

i) LAT1, with the same fixed envelope dimensions, O_d and W_s, material characteristics, temperature rise and torque as the commercial device.

ii) LAT2, with the same overall envelope volume, $\frac{\pi O_d^2 W_s}{4}$, material characteristics, temperature rise and torque as the commercial device.

Within these two categories each was designed using the three alternative techniques of constrained single-criterion and multi-criterion optimization to maximize the two

objective functions of torque/inertia and torque/amp. In addition, a more direct 'parameter scanning' technique was used as described in section(5.5). Before the designs were carried out it was necessary to determine the detailed specification of the typical commercial device.

O_d (mm)	W_g (mm)	Voltage(V)	Current (Amps)	Torque (mNm)	Torque/Amp (mNm/A)	Torque/ inertia ($Nm/K_g m^2$)	θ
38.1	16.5	8.5	1.00	32.0	32.0	17500	±35

Table 5.1 Specification of a typical commercial actuator.

5.2 Analysis Of The Commercial Actuator

Only the performance specification and dimensions of the commercial actuator were known and the design parameters of the actuator were deduced from its specification and from test measurements. In common with most commercial actuators the winding was encapsulated, thus the exact number of turns could not be established, and this was estimated from the measured winding resistance assuming a packing factor, k_{pf}, of 0.5. In addition, the manufacturers information only stated that the permanent magnet was an unspecified grade of samarium cobalt. Hence, repeated analyses were performed using typical characteristics for a number of grades of samarium cobalt ranging from $SmCo_5$ with $B_r = 0.85$T and $H_{cn} = -625$ kA/m to a high grade Sm_2Co_{17} with $B_r = 1.07$T and $H_{cn} = -750$ kA/m. The results, given in fig(5.5), suggest that the specified peak torque of 32.0 mNm could be obtained using a material with the second quadrant demagnetization characteristic given in fig(5.6), which is that of a commercial grade of material, Vacomax 225HR.

PARAMETER RESULTS	
SPECIFICATION DETAILS	
Peak Torque (Nm)	0.032
Maximum Excursion (± degrees)	35.0
Axial Length (mm)	16.5
Number of Poles	2
Total Airgap Length (mm)	1.63
Winding Temperature (° C)	236
Ambient Temperature (° C)	20
Torque Constant ($Nm\,A^{-1}$)	0.032
Torque/inertia Ratio (N/kgm)	1.75e+04
ELECTRICAL DETAILS	
Voltage (V)	8.02
Current (A)	1.00
Current Density (Am^{-1})	18.1
Total Resistance (Ω) at 25°C	8.0
Inductance (mH)	4.0
Copper Loss (W)	8.0
STATOR DIMENSIONS	
Material Type	Mild Steel
Axial Length (mm)	16.5
ROTOR DIMENSIONS	
Axial Length (mm)	13.7
Pole arc/Pole pitch ratio	0.33
MOMENTS OF INERTIA	
Rotor Moment of Inertia (kgm^2)	7.18e-07
Magnet Moment of Inertia (kgm^2)	1.11e-06
Total Moment of Inertia (kgm^2)	1.82e-06
WINDING DESIGN	
Number of Turns	720
Packing Factor	0.5
Wire Copper Diameter (mm^2)	0.265
Winding C.S.A (mm^2)	59.3
Total Winding Length (m)	13.0
Winding Pole Arc	130.0
MAGNET DESIGN	
Remanence (T)	1.07
Normal Coercivity ($kA\,m^{-1}$)	-750
Airgap Flux Density	0.57
Thickness (mm)	4.38
Minimum Thickness for Demag (mm) $L_{m_{min}}$ (mm)	0.26
Pole Arc	60.0

Table 5.2 Results of the analysis of the commercial actuator.

A non-linear lumped reluctance model was used to calculate the open circuit flux density within the LAT. In a similar investigation to that performed in chapter 2 for the linear voice-coil actuator, the discretization of the lumped reluctance network was varied and the effect upon the calculated airgap flux density established. Figs(5.7.a and 5.7.b) illustrate the two lumped reluctance networks utilised in the calculation, whilst table(5.3) shows the effect upon the value of the airgap flux density and the number of iterations required before the lumped reluctance solver 'MAGNET' converged. Since the difference in the calculated airgap flux density was minimal(< 2%), and the difference in the number of iterations was significant(> 93%), the less discretized of the two lumped reluctance networks, fig(5.7.a) was utilised for the predictions of the airgap flux density to be presented in this chapter.

Elements in Model	B_g (T)	Number of Iterations
1-8	0.57	16
1-14	0.56	31

Table 5.3 Comparison of the calculated airgap flux density and number of iterations required from lumped reluctance networks figs(5.7.a and 5.7.b)

The B/H characteristic for the soft iron stator core was obtained using a 50 turn excitation coil and a second toroidal search coil to measure the core flux density. From these, a series of B/H loops such as shown in fig(5.8) were obtained and when compared to published curves showed that the core material was magnetically similar to mild steel. The complete analysis output file shown in table(5.2) gives the best estimate of the actuator parameters. The dimensions, etc. are not identical with those in table(5.1) for the commercial device but are considered to be sufficiently close to make them a valid basis for development of the three new designs.

5.3 Temperature Rise Prediction of Toroidally Wound Actuators

The specifications of commercial toroidally wound actuators are given at room temperature(293K), with the magnet working point assumed to be on its major B/H

characteristic. Therefore, in the design optimization of LAT's in this study a simple technique for the comparison of the temperature rise of designed and commercial devices was performed. This involved simply determining the copper loss, the iron loss being neglected as commercial devices are specified at standstill, and assuming that the power loss is dissipated into ambient. The temperautre of the winding could then be quickly evaluated and compared with the commercial actuator, being dependent upon the surface area of the toroid $A_{s_{cu}}$ and the thermal dissipation factor.

$$\theta = ambient + \frac{I^2 R}{H_{cu} A_{s_{cu}}} \tag{5.2}$$

i.e $$\theta = ambient + \frac{2 I^2 N \rho_{cu}}{H_{cu} A_{s_{cu}} A_{cu}} \left(W_s + \left(\frac{O_d - IT_d}{2}\right)\right)$$

where ρ_{cu} is the resistivity of copper.

$A_{s_{cu}}$ is the surface area of the toroid winding.

A_{cu} is the cross-sectional area of the winding.

and H_{cu} is the thermal dissipation factor.

i.e

$$A_{s_{cu}} = \pi (O_d + 2 L_g) W_s + \pi (IT_d - 2 L_g) W_s +$$

$$2\left\{\left(\frac{O_d + 2 L_g}{2}\right)^2 - \left(\frac{IT_d - 2 L_g}{2}\right)^2\right\}$$

(5.3)

Therefore, the temperature rise prediction is dependent upon accurate values for the thermal dissipation H_{cu}. In the optimization of the actuators the value for the temperature

rise was not to exceed that of the commercial device. Therefore, the temperature rise for the commercial device was measured and compared with predictions, varying H_{cu} in 0.5 $W/m^2 K$ increments. The actuator was tested with the rotor held stationary at one of the null points on its torque characteristic. Fig(5.9) shows the measured winding temperature as a function of time for two current levels together with the predicted steady state temperatures. The temperature was measured with the actuator held both horizontally and vertically but the results for the actuator in the vertical position, i.e. with the rotational axis vertical, are shown, since in practice the temperatures were virtually identical for both cases. The results show that the agreement between the theoretical and measured steady state temperatures were closest with H_{cu} =12.0 $W/m^2 K$ and hence this value was assumed in the thermal model for the optimization studies, since the aspect ratios of the devices were anticipated to be reasonably similar.

5.4 Estimation of the Winding Inductance

The winding inductance was calculated using the analytical expression determined by Dawson for permanent magnet limited angle actuators, and is given in appendix F[5.1].

5.5 Parameter Scanning Optimization

In addition to the single and multi-criterion optimization techniques, described in chapters 3 and 4, for the design of the LAT actuators, a much simpler approach has been adopted in which the design variables are incremented in discrete steps between pre-specified limits, feasible designs being produced for many possible combinations of the variables. Any performance parameters of interest are then evaluated for the feasible designs and are available for graphical display, plotted against any of the design variables. The principal disadvantage of this approach is the possibility of a

'combinatorial explosion' when the number of candidate designs becomes too enormous to view by graphical techniques, as might occur when;

i) the number of input variables being scanned is too large,

ii) the range of values for each variable is too large,

iii) the increments on the scanned variables are set too fine.

Therefore, for this method to be successful a degree of *a priori* knowledge of the likely design constraints and variable interactions is required, in order to avoid a 'combinatorial explosion' on the one hand whilst not missing an optimum design on the other.

5.6 Maximization of Torque/Inertia and Torque/Amps ratios

Both scanning and constrained optimization techniques were utilised to maximize the torque/inertia and torque/amp ratios of the actuator. It was therefore necessary to obtain the objective function form of these two parameters. The Lorentz torque equation was utilised for predicting the torque from slotless, toroidally wound actuators, giving

$$Torque = B_g\, i\, l\, r_w\, p$$

$$\text{or} \qquad Torque = (B_g\, N\, [W_s - 2\, L_g]\, r_w\, p\, \frac{\psi_r}{\psi_s})\, i \qquad (5.4)$$

Where the term in oval brackets is the torque constant $K_t\ (Nm\, A^{-1})$

From the schematic diagram of fig(5.10) and the leading dimensions of a typical LAT the effective torque radius is given by:

$$r_w = \frac{I_d + 2\,(L_m + L_{mc}) + L_g}{2} \qquad (5.5)$$

Therefore:

$$\text{Functional 1} = F_1 = \frac{(B_g N [W_s - 2L_g] \left(\frac{I_d + 2(L_m + L_{mc}) + L_g}{2} \right) p \frac{\psi_r}{\psi_s}) i}{J} \qquad (5.6)$$

where J is the rotor inertia. A radial sided magnet topology was used for the design, as this topology is preferable for large angular displacement, low pole number LAT's. The rotor inertias for both a radial magnet rotor and a slab type construction rotor are presented in appendix G, from which equation(5.6) can be expressed as:

$$F_1 = \frac{(B_g N [W_s - 2L_g] \left(\frac{I_d + 2(L_m + L_{mc}) + L_g}{2} \right) p \frac{\psi_r}{\psi_s}) i}{\pi \frac{[W_s - 2L_g] \sigma_{steel} (\frac{I_d}{2})^4}{2} + \frac{\sigma_{mag} [W_s - 2L_g] p \psi_r ((\frac{I_d + 2L_m}{2})^4 - (\frac{I_d}{2})^4)}{4}} \qquad (5.7)$$

The torque/amp can also be expressed as:

$$\text{Functional 2} = F_2 = (B_g N [W_s - 2L_g] \left(\frac{I_d + 2(L_m + L_{mc}) + L_g}{2} \right) p \frac{\psi_r}{\psi_s}) \qquad (5.8)$$

Table(5.4) illustrates the constraints applied for each of the design considerations, LAT1 and LAT2.

	LAT1	LAT2
Torque	32.0	32.0
Inequality Constraints		
i)Max O_d (*mm*)	= 38.1	≤ 100.0
ii)Max W_s (*mm*)	= 16.52	≤ 100.0
iii)Max Volume (mm^3)	= 18834	= 18834
iv)Max θ_{max} (^oC)	≤ 236	≤ 236
v)Min $L_{m_{min}}$ (mm)	> demag length	> demag length
vi)Max ψ_r (degrees)	≤ 60.0	≤ 60.0
Equality Constraints		
i) $IT_d = I_d + 2(L_m + L_g + L_{mc})$	yes	yes
ii) $W_s = W_r + 2L_g$	yes	yes
Variables		
i) O_d	no	yes
ii) W_s	no	yes
iii) IT_d	yes	yes
iv) L_g	yes	yes
v) L_m	yes	yes
vi) I_d	yes	yes
vii) ψ_r	yes	yes

Table 5.4 The torque required, the constraints applied and the active variables for LAT1 and LAT2 actuator optimization.

The value of the mechanical clearance, Lmc, was given as that used in the analysis of the commercial actuator, and advised by our industrial collaborators, i.e. Lmc = 0.23mm.

5.7 Results Of The Single-Criterion Optimization Techniques

5.7.1 Scanning technique

The scanning method of optimization was used in three stages, firstly, a coarse scan with large incremental values of the variables was used to identify the 'region of interest'

followed by two finer scans to converge to the optimized design. This is illustrated by the scan of torque/inertia with magnet thickness given in figs(5.11.a and 5.11.b), for LAT1, for the following incremental ranges:

1) 5 increments over the whole of the parameter range for the 7 variables (Fig 5.11.a).

2) 5 increments over a restricted range for the 7 variables (not illustrated).

3) 5 increments over a further restricted range for the 7 variables (Fig 5.11.b).

Hence the total number of objective function evaluations was 234375. This could be significantly reduced by using a coarser initial scan but this runs the risk of not identifying the correct region. One of the major benefits of the scanning technique is illustrated in fig(5.11) which highlights the enormous number of similar, feasible designs all of which have greater values for the torque/inertia ratio than the commercial device.

As a result of this exercise for both LAT1 and LAT2 the designs shown in tables(5.5 and 5.6) were selected.

PARAMETER RESULTS	
SPECIFICATION DETAILS	
Peak Torque (Nm)	0.032
Maximum Excursion (± degrees)	35.0
Axial Length (mm)	16.5
Number of Poles	2
Total Airgap Length (mm)	2.74
Winding Temperature (° C)	236
Ambient Temperature (° C)	20
Torque Constant ($Nm\,A^{-1}$)	0.032
Torque/inertia Ratio (N/kgm)	4.59e+04
ELECTRICAL DETAILS	
Voltage (V)	8.18
Current (A)	1.01
Current Density (Am^{-1})	*14.3*
Total Resistance (Ω) at 25°C	8.10
Inductance (mH)	7.0
Copper Loss (W)	8.26
STATOR DIMENSIONS	
Material Type	Mild Steel
Axial Length (mm)	16.5
ROTOR DIMENSIONS	
Axial Length (mm)	11.5
Pole arc/Pole pitch ratio	0.33
MOMENTS OF INERTIA	
Rotor Moment of Inertia (kgm^2)	2.29e-08
Magnet Moment of Inertia (kgm^2)	6.45e-07
Total Moment of Inertia (kgm^2)	6.68e-07
WINDING DESIGN	
Number of Turns	974
Packing Factor	0.5
Wire Copper Diameter (mm^2)	0.330
Winding C.S.A (mm^2)	68.9
Total Winding Length (m)	16.9
Winding Pole Arc	130.0
MAGNET DESIGN	
Remanence (T)	1.07
Normal Coercivity ($kA\,m^{-1}$)	-750
Airgap Flux Density	0.50
Thickness (mm)	7.20
Minimum Thickness for Demag $L_{m_{min}}$ (mm)	0.15
Pole Arc	60.0

Table 5.5 Results of the scanning optimization for the LAT1 actuator.

PARAMETER RESULTS	
SPECIFICATION DETAILS	
Peak Torque (Nm)	0.032
Maximum Excursion (± degrees)	35.0
Axial Length (mm)	35.9
Number of Poles	2
Total Airgap Length (mm)	2.60
Winding Temperature (° C)	234
Ambient Temperature (° C)	20
Torque Constant ($Nm\,A^{-1}$)	0.032
Torque/inertia Ratio (N/kgm)	1.08e+05
ELECTRICAL DETAILS	
Voltage (V)	8.44
Current (A)	1.00
Current Density (Am^{-1})	14.1
Total Resistance (Ω) at 25°C	10.5
Inductance (mH)	5.25
Copper Loss (W)	10.5
STATOR DIMENSIONS	
Material Type	Mild Steel
Axial Length (mm)	35.9
ROTOR DIMENSIONS	
Axial Length (mm)	31.2
Pole arc/Pole pitch ratio	0.33
MOMENTS OF INERTIA	
Rotor Moment of Inertia (kgm^2)	1.13e-08
Magnet Moment of Inertia (kgm^2)	2.84e-07
Total Moment of Inertia (kgm^2)	2.96e-07
WINDING DESIGN	
Number of Turns	618
Packing Factor	0.5
Wire Copper Diameter (mm^2)	0.270
Winding C.S.A (mm^2)	35.4
Total Winding Length (m)	21.8
Winding Pole Arc	130.0
MAGNET DESIGN	
Remanence (T)	1.07
Normal Coercivity ($kA\,m^{-1}$)	-750
Airgap Flux Density	0.44
Thickness (mm)	4.44
Minimum Thickness for Demag $L_{m_{min}}$ (mm)	0.20
Pole Arc	60.0

Table 5.6 Results of the scanning optimization for the LAT2 actuator.

5.7.2 Constrained Techniques

The objective functions were individually optimized using all three of the constrained methods described in chapter 3. The 'history of optimization' for the constrained optimization of LAT2, optimized for maximum torque/inertia is illustrated in fig(5.12) where it can be seen that the inertia of the rotor is reduced significantly as the axial length is increased with a subsequent decrease in the overall diameter. The number of function evaluations and the minimum objective function for each of the three constrained optimization techniques is illustrated in table(5.7) for LAT1. It can be seen that the Simulated Annealing technique requires the fewest number of function evaluations to obtain the global optimum, which is consistent with the results obtained in chapter 3.

Optimization Method	Maximum Torque/Inertia $*10^4$ (N/Kgm)	Number of Function Evaluations	Maximum Torque/amp $*$ 10^{-3} (Nm/A^{-1})	Number of Function Evaluations
Flexible Polyhedron	4.83	4375	46.9	7536
Alternating Directions	4.79	7972	47.0	12345
Simulated Annealing	4.79	2178	47.0	2997

Table 5.7 Comparison of the number of function evaluations for the LAT1 actuator.

5.7.3 Comparison of Scanning and Constrained Techniques

Comparisons of the dimensions and performance of the optimized devices LAT1 and LAT2 from both scanning and constrained optimization and the commercial device are given in table(5.8), where it can be seen that scanning and constrained methods have produced slightly different results. This is probably due to the choice of 'region of interest' and the level of increment on the variable during the final fine scan. Both techniques however, suggest that it is possible for LAT1 to obtain improvements of 47% and 175% for the torque/amp and torque/inertia ratios respectively, compared to the commercial device. These improvements are increased for LAT2 for which it is possible to predict improvements of 61% and 517% in torque/amp and torque/inertia. Such improvements in the torque/inertia are not unexpected since, as described in section(5.1),

toroidally wound actuators are seldom designed to optimize this parameter and the inertia can be rapidly reduced as it is dependent upon $((\frac{I_d + 2L_m}{2})^4 - (\frac{I_d}{2})^4)$. The improvements in the torque/amp ratio however, show the extent to which the optimization techniques can lead to significant benefits over heuristic design methodologies, since the torque/amp is a parameter to which commercial LAT manufacturers pay great attention. One possible disadvantage with the LAT2 actuator, from its shape, is that the device could be more difficult to manufacture because of the long axial dimension, causing problems in the magnet cutting.

In terms of the number of function evaluations required, the Simulated Annealing constrained optimization method is far more efficient than the scanning technique, e.g. for LAT1 the comparison is 9375:2178, with the constrained method also obtaining a design which has a 4.4% improved torque/inertia.

	Optimization Technique	Parameter	Optimum	O_d (mm)	W_s (mm)	L_m (mm)	L_g (mm)	I_d (mm)
Commercial		Torque/inertia	$1.74 * 10^4$	38.1	16.5	4.38	1.65	15.0
		Torque/amp	$32.0 * 10^{-3}$	38.1	16.5	4.38	1.65	15.0
LAT1	Constrained	Torque/inertia	$4.79 * 10^4$	38.1	16.5	7.10	2.74	7.08
	Scanning	Torque/inertia	$4.59 * 10^4$	38.1	16.5	7.20	2.76	6.80
	Constrained	Torque/amp	$47.0 * 10^{-3}$	38.1	16.5	5.82	2.49	12.4
	Scanning	Torque/amp	$46.9 * 10^{-3}$	38.1	16.5	5.80	2.50	12.4
LAT2	Constrained	Torque/inertia	$10.8 * 10^4$	25.8	35.9	4.45	2.60	4.68
	Scanning	Torque/inertia	$10.4 * 10^4$	29.1	28.3	4.75	3.00	5.34
	Constrained	Torque/amp	$51.5 * 10^{-3}$	40.6	14.6	5.76	2.51	14.7
	Scanning	Torque/amp	$49.7 * 10^{-3}$	40.8	14.4	5.28	2.48	16.1

Table 5.8 Comparison of commercial, scanning and constrained optimization results for torque/inertia and torque/amp objective functions.

5.8 Results of Multi-Criterion Optimization

The results from the single-criterion optimization studies showed that large improvements in both torque/inertia and torque/amp could be obtained in comparison with the commercial device specification. On many occasions however, the most appropriate design is one that has not been optimized to any single functional but has adequate values for a number of parameters.

The multi-criterion optimization methods described in chapter 4 were used to test the sensitivity of the objective functions using the results of the single-criterion optimizations as the normalizing factors. Again both LAT1 and LAT2 conditions were investigated.

5.8.1 Scalar Weighting Technique

The weighted multi-criterion objective function is formulated as:

$$F_m = \frac{W_1\ torque/inertia}{\bar{f}1} + \frac{W_2\ torque/amp}{\bar{f}2} \qquad (5.9)$$

where $\bar{f}1$ and $\bar{f}2$ are the single-criterion optimum solutions for torque/inertia and torque/amp respectively.

Tables(5.9 and 5.10) illustrate the results as the weightings are varied between 0.0 and 1.0 for each functional. For LAT1 the results are almost independent of the weightings, this being due to the fact that the inertia varies in proportion to $((\frac{I_d + 2L_m}{2})^4 - (\frac{I_d}{2})^4)$ and is extremely sensitive to the value of these variables. Therefore the multi-criterion functional is dominated by the torque/inertia part until the value of the weighting assigned to the torque/amp approaches unity. These trends are

diluted in the case of LAT2 but still prefer to lie towards the single-criterion torque/inertia optimized design. The 'history of optimization' for LAT2 case is given in fig(5.13) as the weightings are varied.

W_1	W_2	$F_1\,(N/Kgm)*10^4$	$F_2\,(NmA^{-1})*10^{-3}$
1.0	0.0	4.79	32.0
0.8	0.20	4.65	32.8
0.6	0.40	4.63	33.2
0.4	0.60	4.53	33.4
0.2	0.80	4.46	33.7
0.1	0.90	4.23	34.3
0.05	0.95	2.54	44.3
0.0	1.0	2.21	47.0

Table 5.9 Results of Scalar Weighted Multi-Criterion optimization for LAT1 actuator

W_1	W_2	$F_1\,(N/Kgm)*10^4$	$F_2\,(NmA^{-1})*10^{-3}$
1.0	0.0	10.80	32.0
0.8	0.2	9.96	36.5
0.6	0.4	6.50	42.4
0.4	0.6	5.63	48.4
0.2	0.8	4.94	50.8
0.0	1.0	1.89	51.6

Table 5.10 Results of Scalar Weighted Multi-Criterion optimization for LAT2 actuator

5.8.2 Global Criterion Technique

Using the equation fitting techniques described in chapter 4 to obtain best compromise solutions, tables(5.11 and 5.12) were obtained for LAT1 and LAT2 respectively, from the multi-criterion functional

$$F_m = \left(\left(\frac{(\bar{f}_1 - f_1)}{\bar{f}_1} \right)^p + \left(\frac{(\bar{f}_2 - f_2)}{\bar{f}_2} \right)^p \right)^{1/p}. \qquad (5.10)$$

where $\bar{f}_1$ and $\bar{f}_2$ are the normalising factors for the torque/inertia and torque/amp objective functions respectively.

The main inference from these results is that there is little difference in the optimized design for any of the exponential values. For both LAT1 and LAT2 the values of the torque/inertia are very close to their single-criterion solutions, showing how this objective function again dominates the multi-criterion functional.

Exponential Value	$F_1\,(N/Kgm)*10^4$	$F_2\,(Nm/A^{-1})*10^{-3}$
1	4.63	33.2
2	4.54	33.5
3	4.52	33.6
4	4.47	33.8
5	4.47	33.8
10	4.47	33.8

Table 5.11 Results of Global Criterion optimization for LAT1.

Exponential Value	$F_1\,(N/Kgm)*10^4$	$F_2\,(Nm/A^{-1})*10^{-3}$
1	8.87	37.3
2	8.69	38.5
3	8.56	38.8
4	8.40	39.9
5	8.23	41.2
10	7.98	41.8

Table 5.12 Results of Global Criterion optimization for LAT2.

5.8.3 Flexible Inequality Constraints Technique

The torque/amp objective function was incorporated as a flexible inequality constraint and the torque/inertia ratio maximized. The results for the LAT1 actuators given in tables(5.13 and 5.14) show similar trends to the previous multi-criterion methods in that the torque/inertia is very sensitive to the value of the torque/amp assigned as a constraint. As the torque/amp is increased from its base value of 32.0mNm the torque/inertia is

reduced rapidly. The reduction is not as severe for the LAT2 actuators, with the torque/inertia only falling below $5.0*10^4$ (N/Kgm) when the torque/amp ratio is increased to $46.6*10^{-3}$ (Nm/A^{-1}).

Objective-Function-Constraints Torque/amp $*10^{-3}$ (Nm/A^{-1})	Objective Function Torque/inertia $*10^4$ (N/Kgm)
32.0	4.79
34.4	4.27
36.9	3.43
41.8	2.66
44.2	2.54
46.6	2.27

Table 5.13 Results of incorporation of torque/amp objective function as a flexible inequality constraint for LAT1.

Objective-Function-Constraints Torque/amp $*10^{-3}$ (Nm/A^{-1})	Objective Function Torque/inertia$*10^4$ (N/Kgm)
32.0	10.8
34.4	10.6
36.9	9.83
39.3	8.43
41.8	7.98
44.2	5.84
46.6	3.03
49.1	2.74
51.5	2.56

Table 5.14 Results of incorporation of torque/amp objective function as a flexible inequality constraint for LAT2.

5.8.4 Comments on Multi-Criterion Optimization Results

The predominant inference from the multi-criterion optimization results is that the torque/inertia ratio is dominant over the torque/amp objective function for both LAT1 and LAT2 actuators, although the trends are diluted for the LAT2 actuator. In addition, the results show that there exist several designs, of LAT1 and LAT2 with improved

values of both objective functions, in comparison with the commercial device. All the designs optimized using the Global Criterion technique have improved values for both the objective functions.

5.9 Finite Element Analysis of Optimized Torque/Inertia and Commercial Actuators

The two single-criterion optimized torque/inertia actuators LAT1 and LAT2 of tables(5.5 and 5.6) were selected for further investigation and prototyping, since improved rotor maximum acceleration was the primary requirement.

5.9.1 Open Circuit Flux Density Calculation

Following selection of the optimized toroidal actuators, LAT1 and LAT2, as described above, and in order that a more accurate evaluation of the average radial airgap flux density could be made, LAT1, LAT2 and the commercial actuator were analysed using the finite element technique, taking full account of the effects of saturation of the iron circuit and leakage flux. Meshes representing a cross-section of each actuator were selected so that in each case the magnet was modelled by a number of elements which could be effectively rotated $\pm 45^{o}$ about the central line. Open circuit field solutions were obtained and fig(5.14) shows the resulting flux plots for each of the three designs. It can be seen for all the devices that slight leakage occurred from the edges of the magnet poles which was unaccounted for in the lumped parameter solutions. Fig(5.15) illustrates the values of the average radial airgap flux density and compares them with their predicted lumped parameter values. It is notable that all the finite element results are slightly lower than their lumped parameter counterparts and assuming the FE solutions to be more accurate, then to achieve the specified torque/amp of $32.0 mNm\,A^{-1}$ a better

coil packing factor than that assumed at the design stage would be necessary. A stronger magnet was considered but since Vacomax 225HR is a 2:17 grade of Samarium Cobalt with as high an energy-product at room temperature as is currently available, this was not a viable alternative. A revised value of the packing factor was therefore calculated to compensate for the predicted reduction in the airgap flux density of the commercial actuator:

$$K_{pfnew} = K_{pfold}\left(\frac{B_{gave}\,Lumped\,parameter}{B_{gave}\,Finite\,Element}\right) \tag{5.11}$$

5.9.2 Demagnetization

Full load field calculations were made and fig(5.16) shows field plots for twice overload conditions and fig(5.17) shows the corresponding magnet working points. Even at overload currents of five times rated current, the permanent magnet did not become irreversibly demagnetized. The reason for this is the large magnet thicknesses required for such torque/inertia optimized actuators.

5.9.3 Torque Calculation

The predicted torque was calculated using both Maxwell Stress Integration and stored energy methods as described in chapter 2. For the energy method the stored energy was calculated for all three actuators, using an increasingly refined mesh and fig(5.18) shows how the predicted energy varies slightly with meshing density. In each case it was established that a mesh of 7858 elements was adequate to calculate the stored energy to the required precision. For the Maxwell Stress Integration the number of layers of elements in the airgap was varied between one and nine, and the value of torque

calculated for each case. Figs(5.19, 5.20 and 5.21) compare the torque for each actuator at full load current as calculated by the two numerical techniques and by the lumped parameter method. All three methods show quite a good agreement, both on the peak torque and on the shape of the torque/θ characteristic. The best agreement between the Maxwell Stress, stored energy and lumped parameter results occurs when there are 3 layers of finite elements in the airgap, and less accuracy was obtained for 1 and 5 layers respectively. The probable reason for this is that only the case of the three airgap layers produced good equilateral elements which is an important factor in the calculation accuracy as described in chapter 2. The agreement between the numerical methods and the linearly scaled lumped parameter results became worse as the current in the winding was increased as illustrated in fig(5.22) and table(5.15) which gives the average and minimum percentage differences between the numerical techniques and the lumped parameter results for the LAT1 actuator.

Current (Amps)	Lumped Parameter Torque (mNm)	Minimum Percentage Error for Energy Method %	Average Percentage Error for Energy Method % *	*Minimum* Percentage Error for Maxwell Stress Method %	*Average* Percentage Error for Maxwell Stress Method% *
0.8	25.6	0.4	1.4	1.5	3.7
1.0	32.0	1.6	4.7	5.3	5.8
1.4	44.8	0.8	4.2	4.1	6.1
2.0	89.6	4.3	4.9	6.3	8.4

Table 5.15 Comparison of the torque calculations methods applied to LAT1. * Taken over ± 37.5 degrees range of angles.

5.10 Prototyping the Maximized Torque/Inertia Actuators

The two actuators LAT1 and LAT2 optimized for maximum torque/inertia were prototyped. However, due to practical constraints a few departures were made from the theoretical designs.

5.10.1 Prototype Construction

5.10.1.a Stator Core

In addition to the relatively poor torque/inertia ratio of commercial devices, they also exhibited a considerable rotor drag torque caused by induced eddy currents in the solid iron stator core. The opportunity was therefore taken to reduce this drag torque in the optimized devices by designing the core using 0.35mm Silicon steel laminations (Transil 330-30-A5) rather than a solid mild steel core. Fig(5.23) compares the first quadrant B/H characteristic for the Transil material and mild steel from which it can be seen that the two materials are magnetically similar. The ring laminations were punched out of a single sheet and annealed after burrs were removed from the edges.

5.10.1.b Rotor Magnets

Radially anisotropic 60^{o} magnet arc segments assumed in the design were not available and three diametrically magnetized segments were used as illustrated in fig(5.24). Fig(5.25) compares the finite element predicted airgap flux density distribution for LAT1 and LAT2 for the two rotor magnet arrangements. A small reduction of approximately 0.4% in the airgap flux density is predicted at the joints between the magnet segments, caused by the slight reduction in the thickness at these points.

The second quadrant demagnetization characteristic of the magnet used for the actuators was measured using a permeameter. Comparisons between figs(5.6 and 5.26) show good agreement between the measured curve and that of Vacomax 225HR used in the design.

5.10.1.c Stator Design

The modified values of packing factor calculated following the finite element analysis as described in section(5.9) could not be achieved with hand-winding. This was a problem for the LAT2 actuator with its long axial length, but this should easily be remedied in production with use of a toroidal winding machine. Consequently a thinner gauge of wire had to be used for the prototype actuators, in order that the correct number of turns could be accommodated. Table(5.16) compares the resistance and copper diameters for the new windings with that predicted in the model. It can be seen that the LAT2 actuator in particular has a much higher resistance and, as a consequence, a much higher copper loss was anticipated. Fig(5.27) shows a photograph of the prototype actuators.

Prototype	Designed Resistance (Ω)	Designed Copper Diameter(mm)	Actual Resistance (Ω)	Actual Copper Diameter(mm)
LAT1	8.13	0.300	14.8	0.22
LAT2	10.7	0.270	20.0	0.20

Table 5.16 Predicted and actual winding resistances and copper diameters for the prototype actuators.

5.10.2 Prototype Testing

5.10.2.a Open Circuit Airgap Flux Density Measurements

A calibrated Hall probe and integrating flux meter were used to measure the average airgap flux density of the commercial and prototype actuators. Fig(5.28) illustrates the results obtained as the Hall probe was rotated through 180^o around the airgap. The measured and predicted values agreed to within 4%, with the dips in the airgap flux density being caused by the reduction in magnet thickness at the magnet joints, although the dips were not as pronounced for the prototype devices as in the theoretical predictions

For clarity, fig(5.28) only shows the measured values but these can be compared with the predictions in fig(5.25).

5.10.2.b Static Torque-Displacement and Torque-Amp Measurements

The experimental test rig of fig(5.29) was used to measure the static torque against both displacement and current. The torque was measured using a strain gauge and calibrated torque transducer, which measured the reaction torque on the rotor shaft. Fig(5.30) shows the results obtained at full load current, illustrating a close agreement between measured and predicted results for all three actuators. Table(5.17) compares the peak values for the prototype devices with the theoretical peak torque. All the actuators performed within 0.7% of the specified theoretical peak torque value. The torque-current characteristics for each device, for $\theta = 0^o$, are shown in fig(5.31) where it can be seen that the characteristics are affected by the saturation of the iron at approximately 1.5 to 2 times the full load current. However, if required, high short-term overload torques in excess of 100mNm could be achieved without magnet demagnetization.

Device	Theoretical Peak Torque (mNm)	Experimental Peak Torque (mNm)	Error %
LAT1	32.0	31.8	-0.63
LAT2	32.0	32.1	+0.31
Commercial	32.0	32.0	+0.0

Table 5.17 Comparison of prototype and commercial actuators for maximum peak torque at full load current.

5.10.2.c Temperature Rise Measurements

As previously described in section(5.3), the temperature rise was measured using thermocouples located at the surface of the winding. Since the actuators were naturally cooled and previous tests described in section(5.3) showed that the cooling was

independent of the orientation of the device, the measurements shown fig(5.32) are for the actuators in the vertical position only. Due to the increase in winding resistance caused by the use of a thinner wire gauge a lower current had to be used so as not to thermally demagnetize the permanent magnet. The horizontal lines on fig(5.32) represent the predicted steady state temperatures for these new current levels. Clearly the empirical choice of $H_{cu} = 12.0\ W\,m^{-2}\,K^{-1}$ based on the commercial actuator results in section(5.3), is accurate for LAT1 but not quite as accurate for LAT2 which has a very different aspect ratio. However, even for this case the results are within 13.5% of the predictions.

5.10.2.d Dynamic Drag Torque Measurements

The experimental test rig of fig(5.33) was used to measure the drag torque as a function of rotor speed. The rig consisted of a brushed dc motor used to rotate the actuator continuously with the reaction torque on the shaft being measured on the torque transducer. The results of fig(5.34) highlight the improvements that are possible by simply laminating the stator core. The LAT2 actuator produced a slightly higher drag torque than that of LAT1, which is probably due its aspect ratio, LAT2 required a very thin radial lamination thickness which necessitated significant deburring before final annealing. This led to the removal of some parts of the lamination varnish probably resulting in some shorting out of the laminations.

5.11 Conclusions

From the results obtained in this test case, the following conclusions can be drawn:

1) The use of both scanning and constrained optimization techniques have led to a possible 517% increase in the torque/inertia ratio and 61% in the torque/amp ratio for

the toroidally wound actuators investigated. The multi-criterion optimization has also shown that significant improvements in these parameters over the commercial device can occur simultaneously. For example it is possible to obtain a 40% improvement in the torque/amp and a 290% improvement in the torque/inertia within the single design. Therefore the actuators can be designed both for a specific application and also for a demanding overall specification. However, it must be emphasised that these improvements do not consider their ultimate cost which for the commercial device would be of great significance.

2) The use of the Lorentz formula of equation(5.4) has proven to be satisfactory in determining the peak torques levels developed, as can be seen by the close agreement between the lumped parameter and experimental results throughout this study.

3) The results of the parameter scanning and constrained optimization techniques are similar in the value of the optimum obtained. One significant advantage the scanning technique has over the constrained methods is that a much greater number of candidate designs are available to the designer. The constrained methods however, require far fewer function evaluations to obtain the optimum design and considering the time usually required to manufacture prototype devices it is worthwhile to pursue both optimization methods.

4) If multi-criterion optimization is required, in which more than two objective functions are considered, then the parameter scanning method becomes more attractive in terms of the number of function evaluations required.

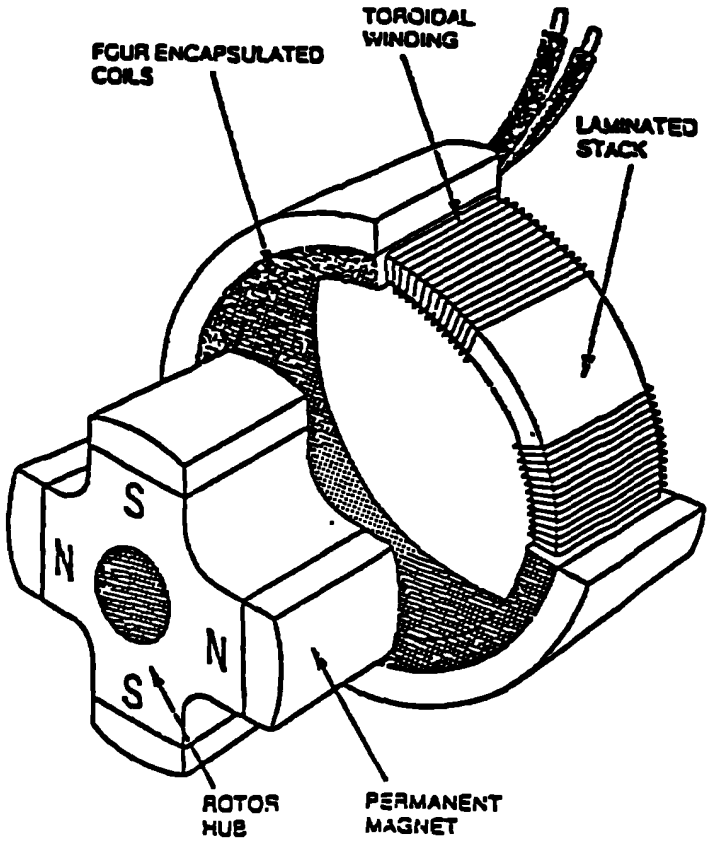

Fig 5.1 Slotless 4-pole Limited Angle Torque motor with Gramme ring winding.

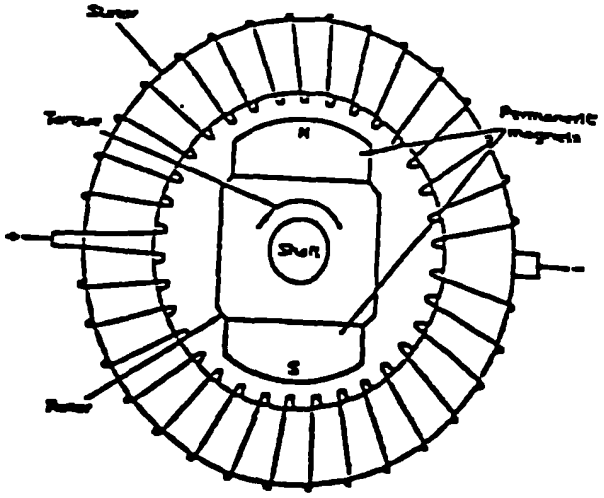

Fig 5.2 Slotless 2-pole Limited Angle Torque motor with Gramme ring winding.

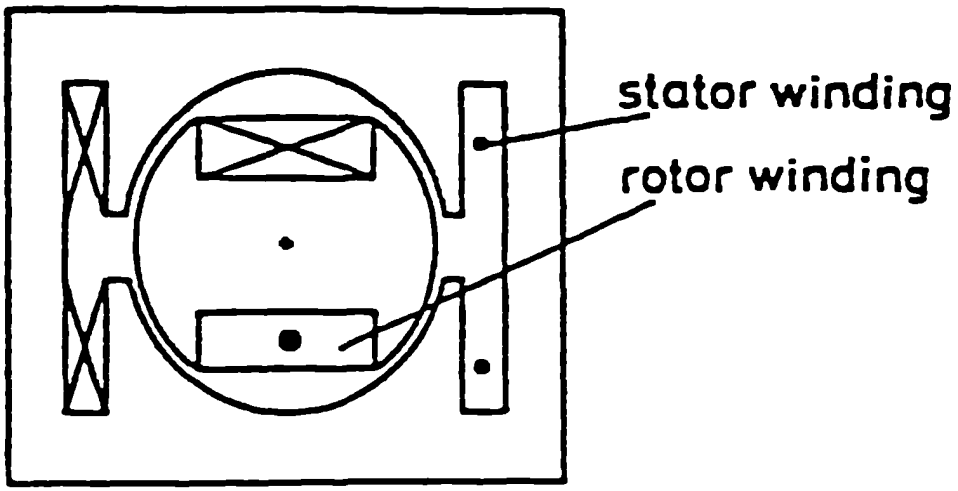

Fig 5.3 Doubly-excited wound rotor Limited Angle Torque motor.

Fig 5.4 Typical Torque characteristic for a 2-pole LAT2.

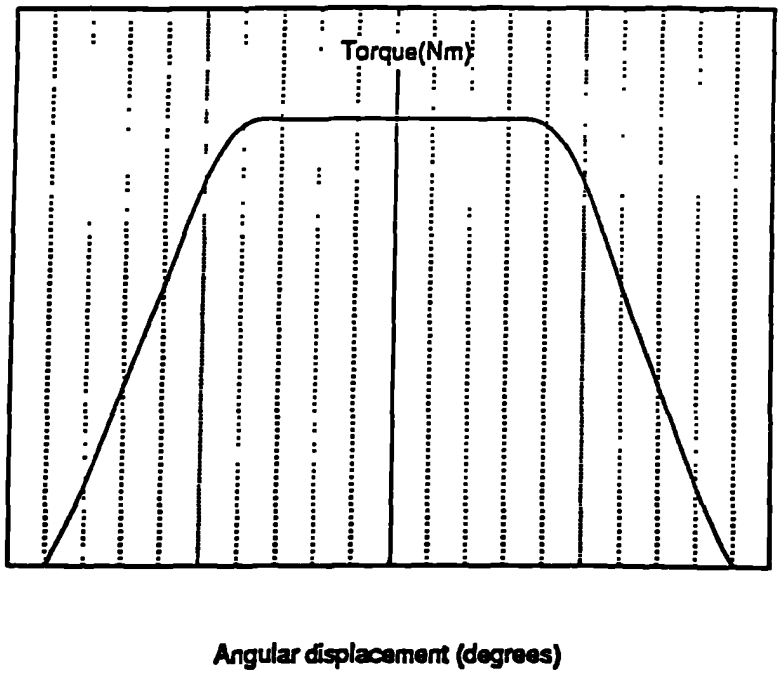

Fig 5.5 Variation of torque with magnet remanence for a range of SmCo grade magnets.

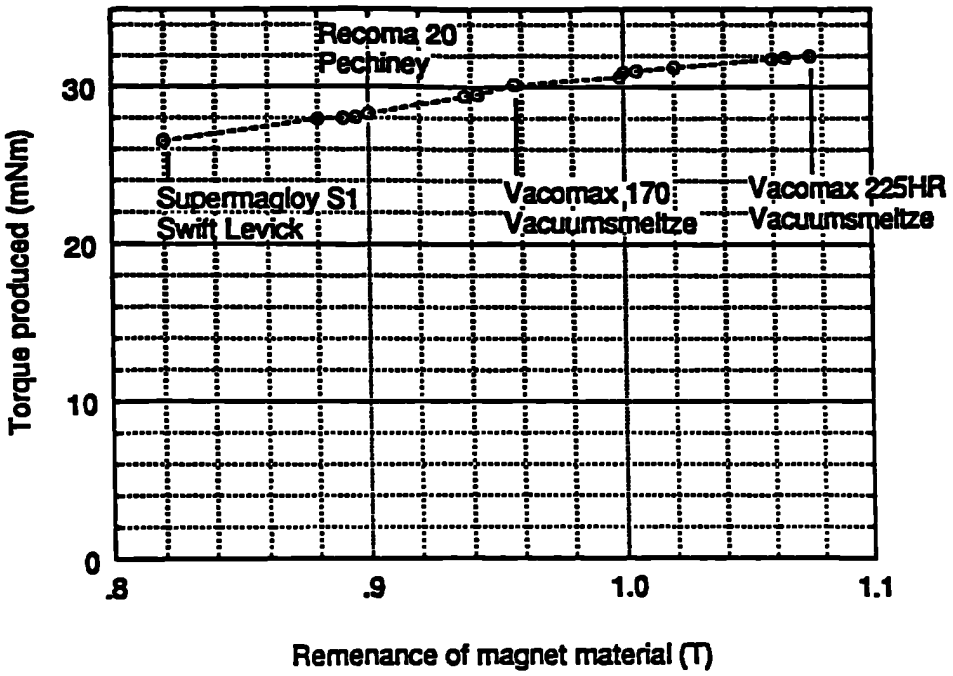

Fig 5.6 Demagnetization characteristic for Vacomax 225 HR.

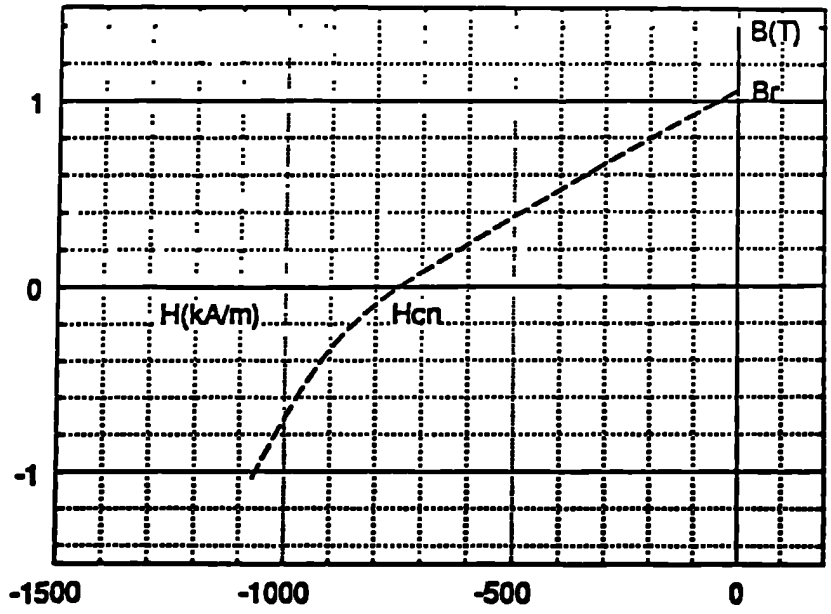

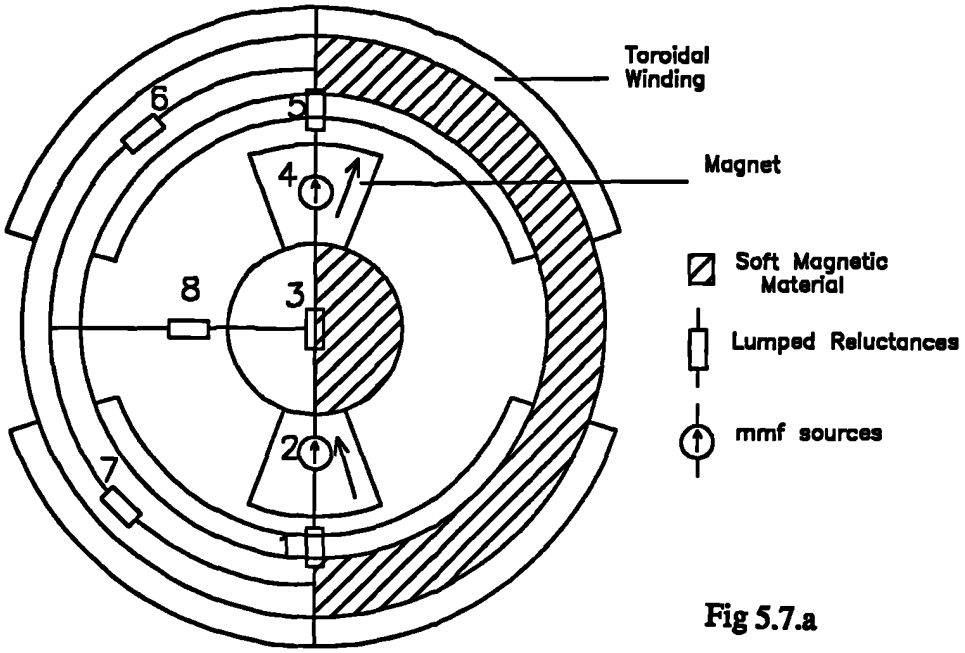

Fig 5.7.a

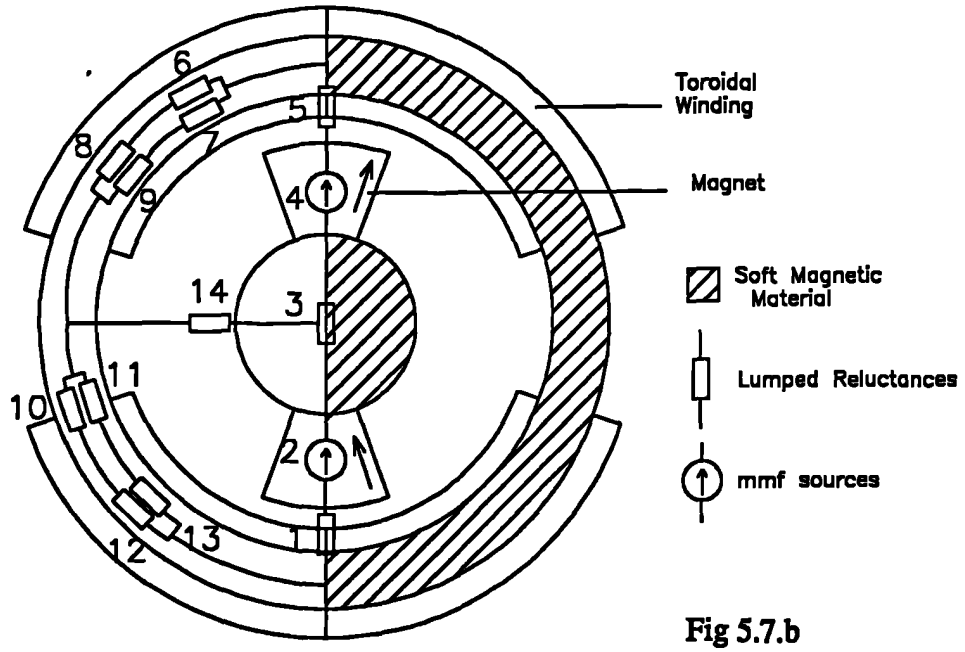

Fig 5.7.b

Fig 5.7 Lumped reluctance networks used to determine the airgap flux density for the commercial actuator.

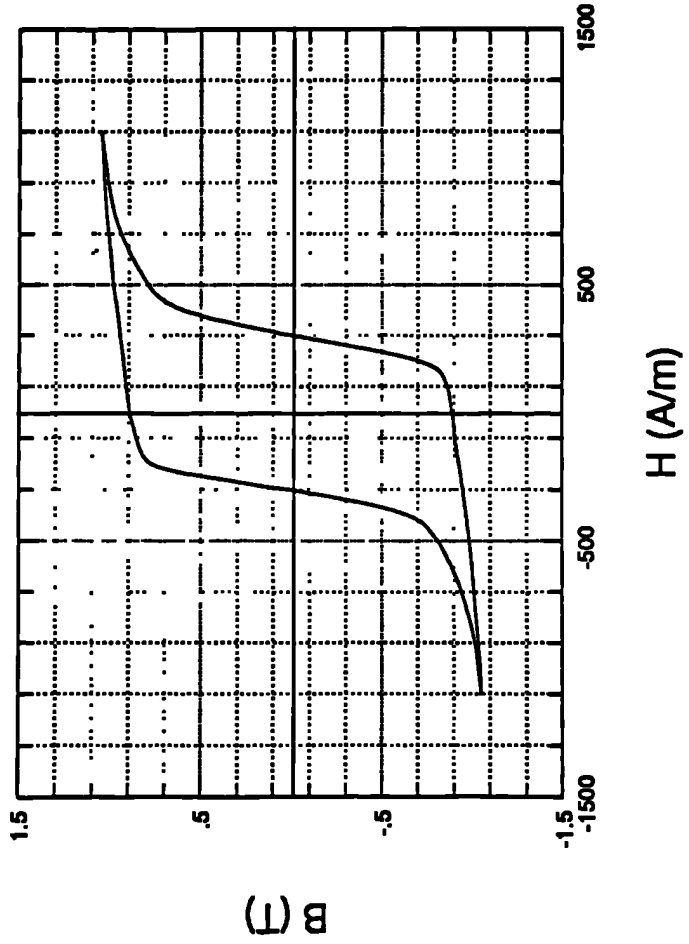

Fig 5.8 Measured B/H loop of soft iron stator.

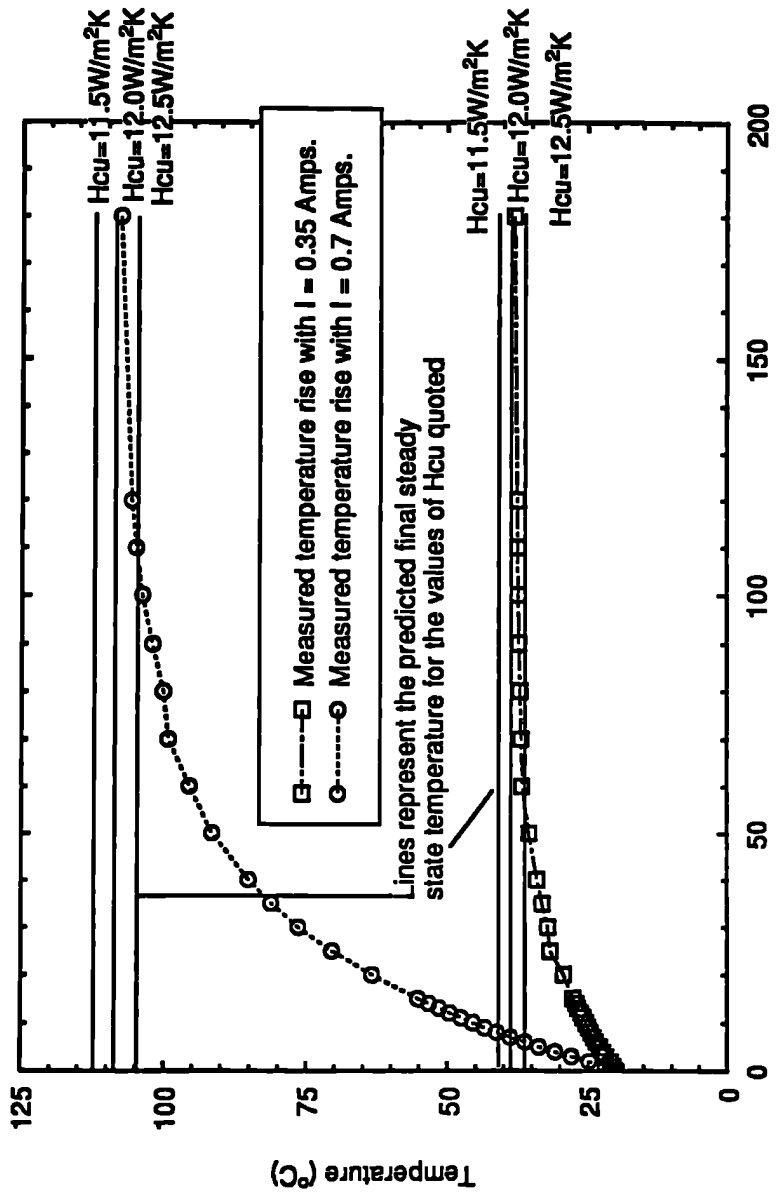

Fig 5.9 Measured and predicted steady-state temperatures for the commercial actuator.

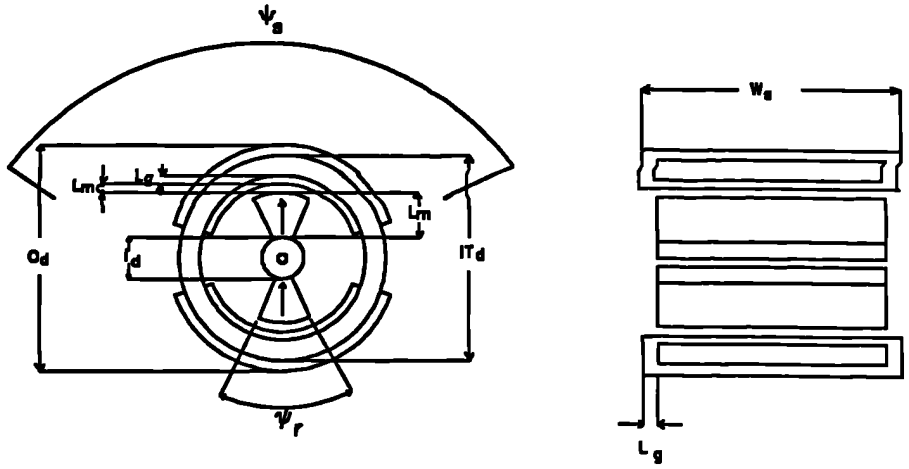

Fig 5.10 Schematic diagram and leading dimensions of a LAT.

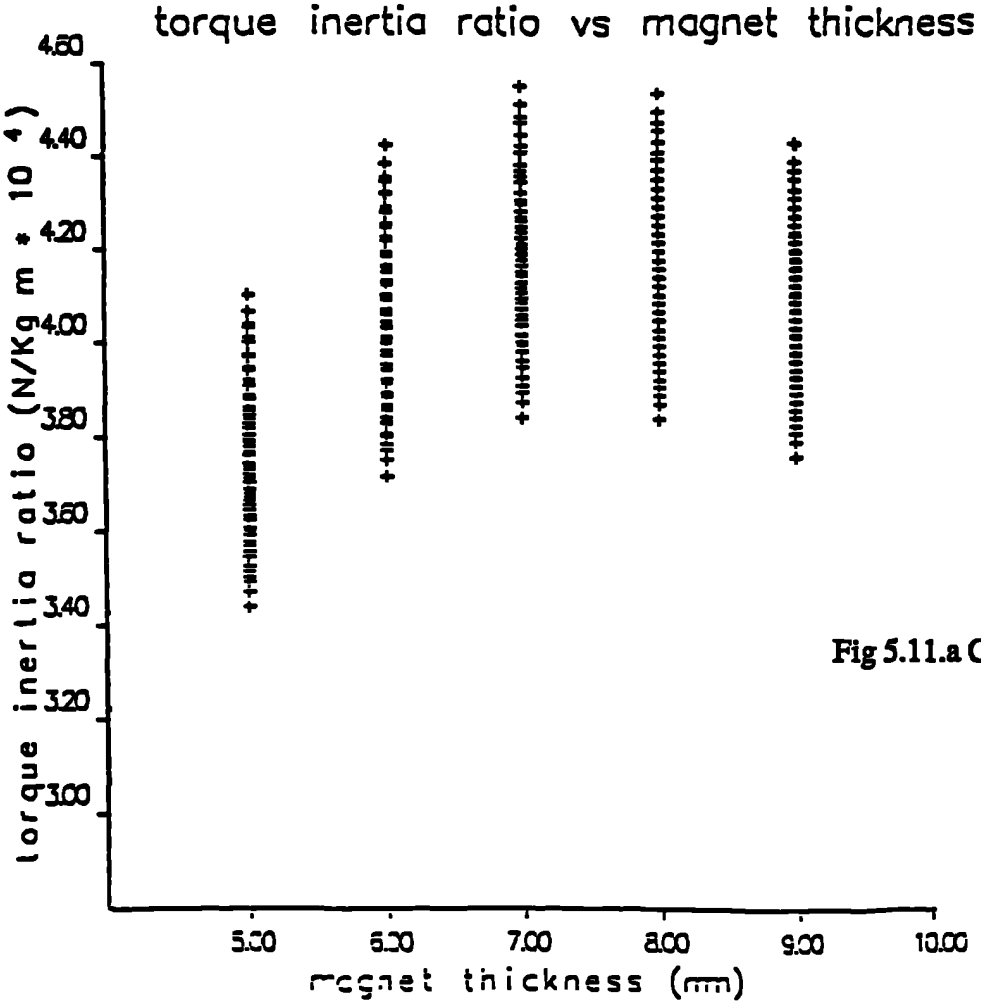

Fig 5.11.a Coarse scan.

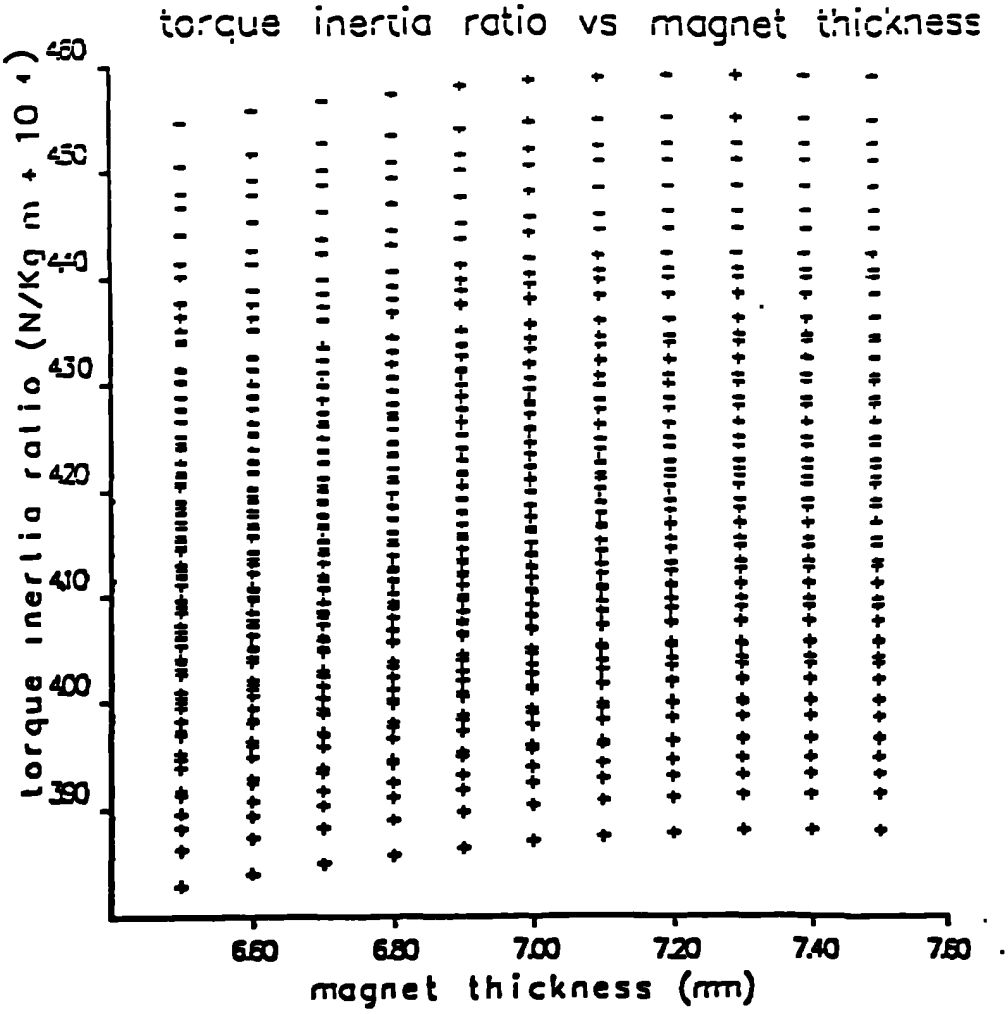

Fig 5.11.b Fine scan

Fig 5.11 Results of the variation of torque/inertia with magnet thickness for the scanning optimization.

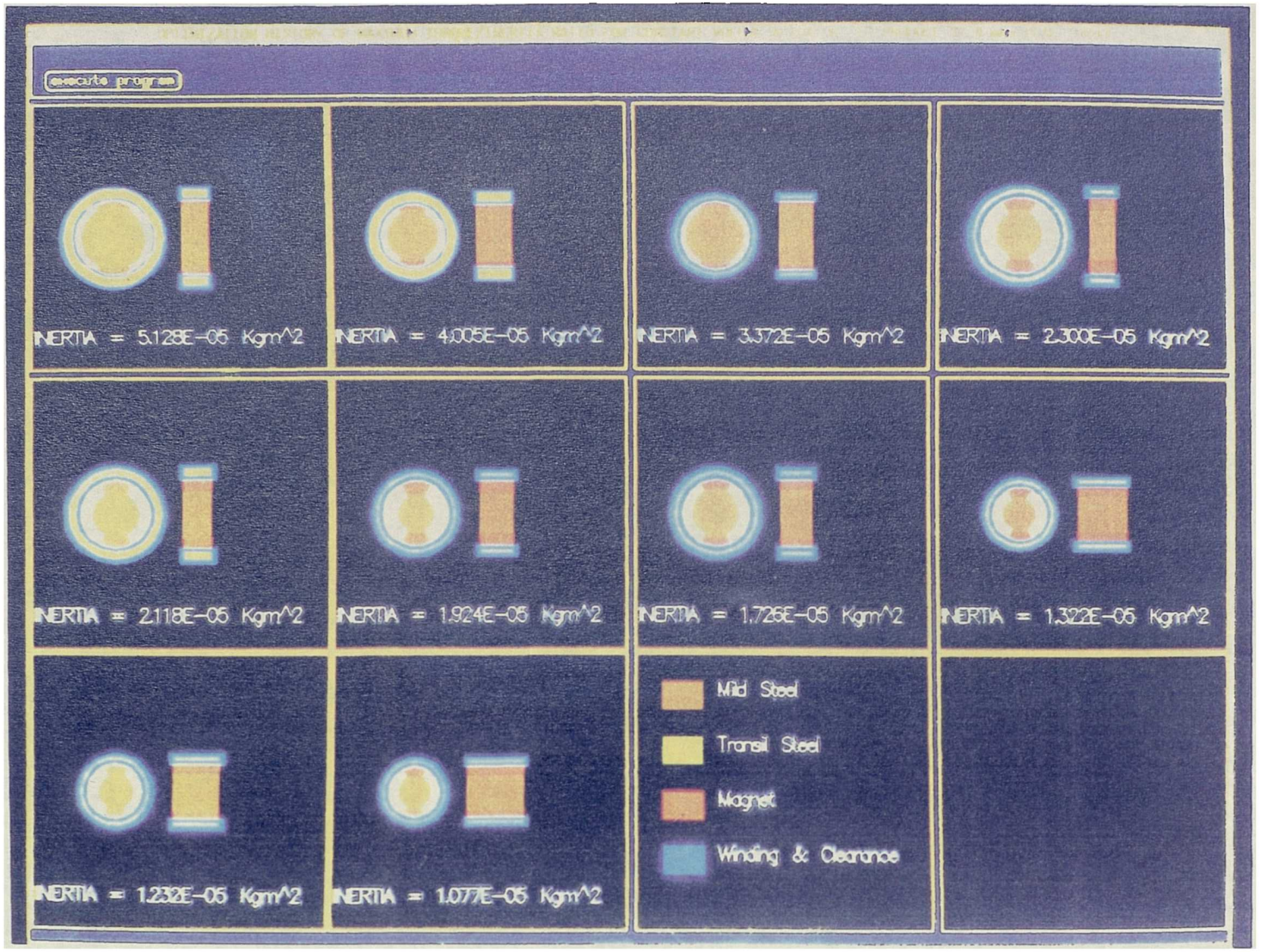

Fig 5.12 Constrained sinlge-criterion optimization 'history of optimization' for LAT2 actuator.

Fig 5.13 Constrained multi-criterion 'history of optimization' for LAT2 actuator.

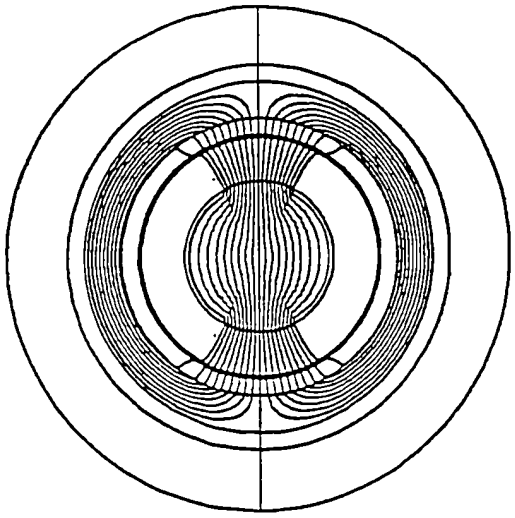

Fig 5.14.a commercial actuator .

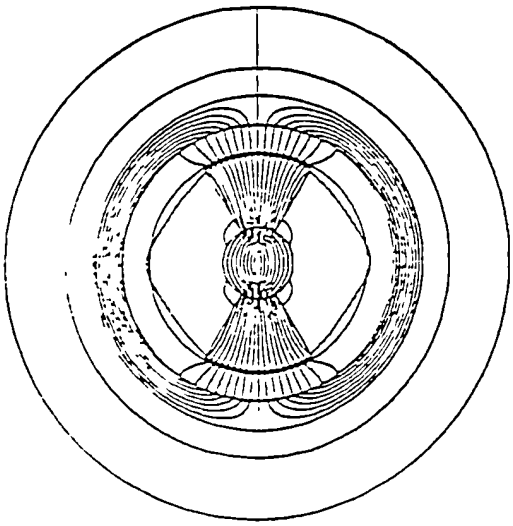

Fig 5.14.b LAT1 actuator .

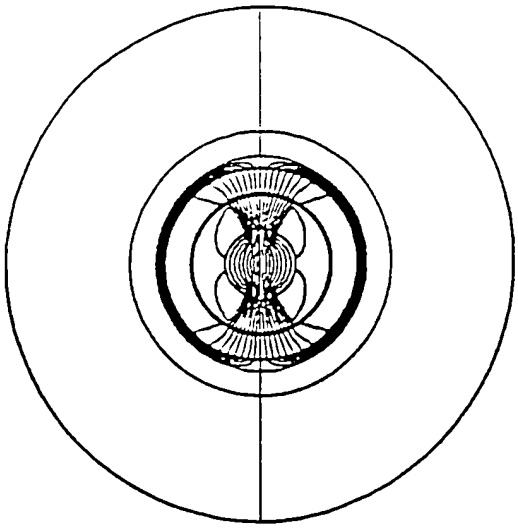

Fig 5.14.c LAT2 actuator .

Fig 5.14 Finite element solution open circuit flux plots.

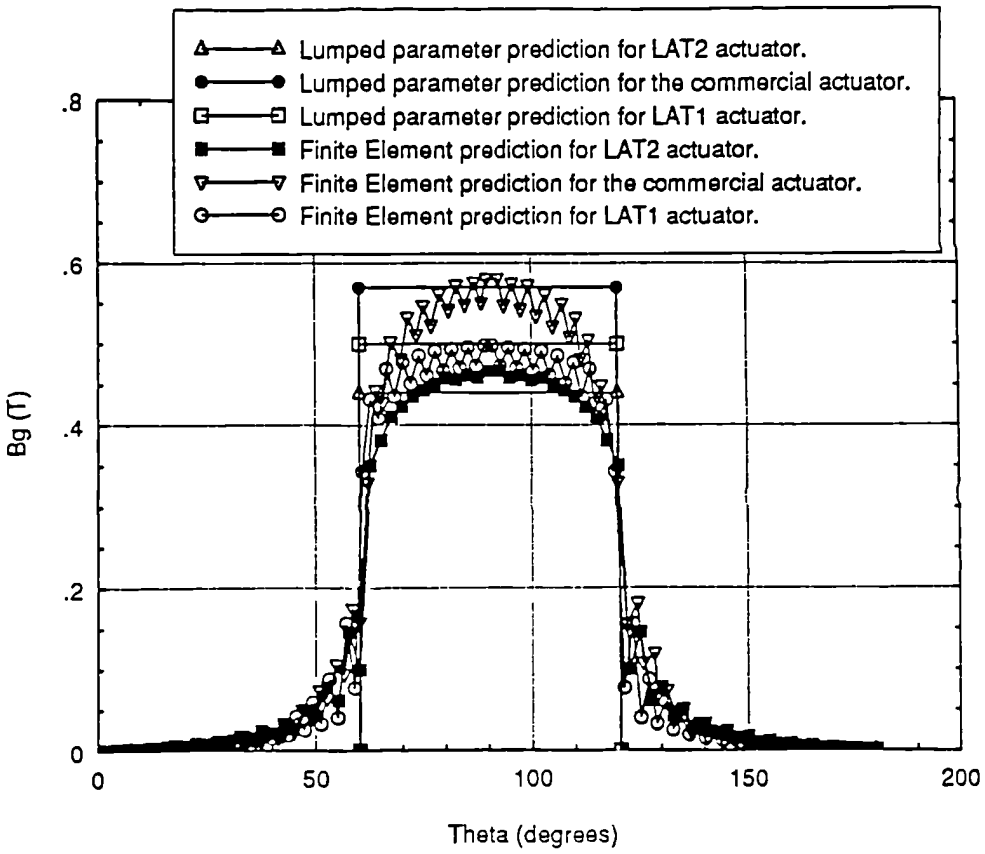

Fig 5.15 Comparisons of the lumped parameter and the finite element predictions of the radial airgap flux densities in LAT1, LAT2 and the commercial actuators.

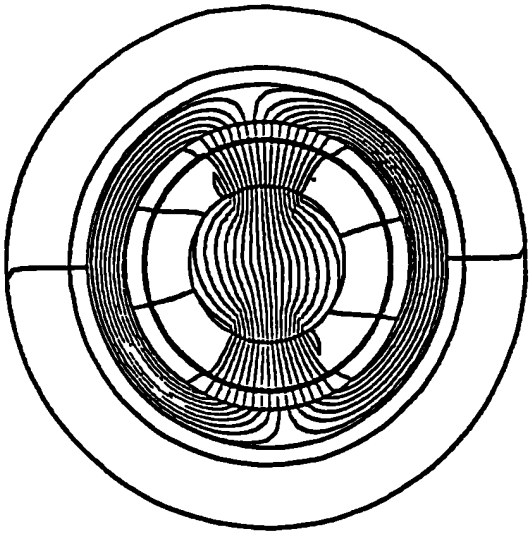

Fig 5.16.a Commercial actuator.

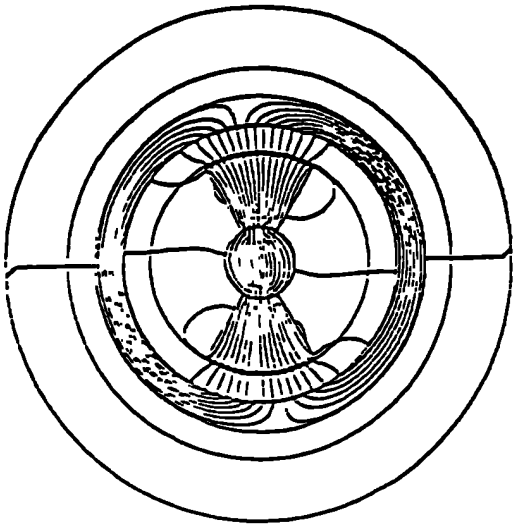

Fig 5.16.b LAT1 actuator.

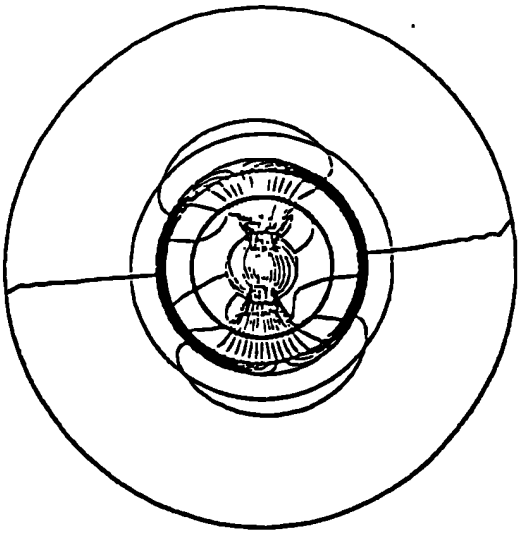

Fig 5.16.c LAT2 actuator.

Fig 5.16 Finite element solution,twice full load open circuit flux plot.

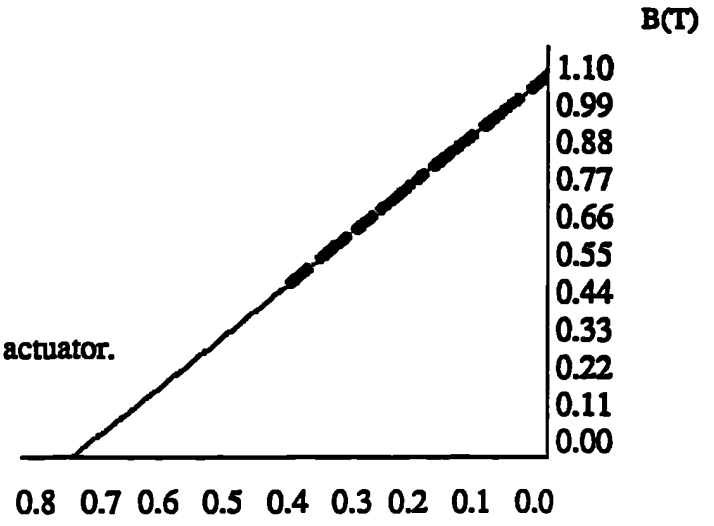

Fig 5.17.a commercial actuator.

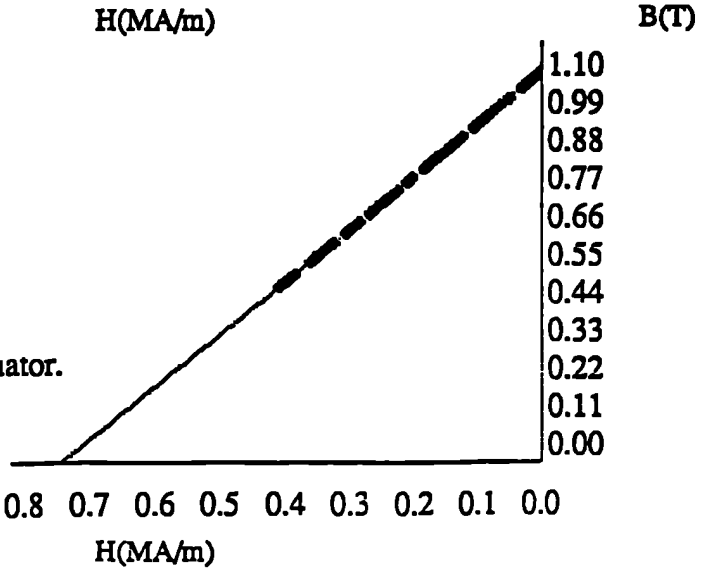

Fig 5.17.b LAT1 actuator.

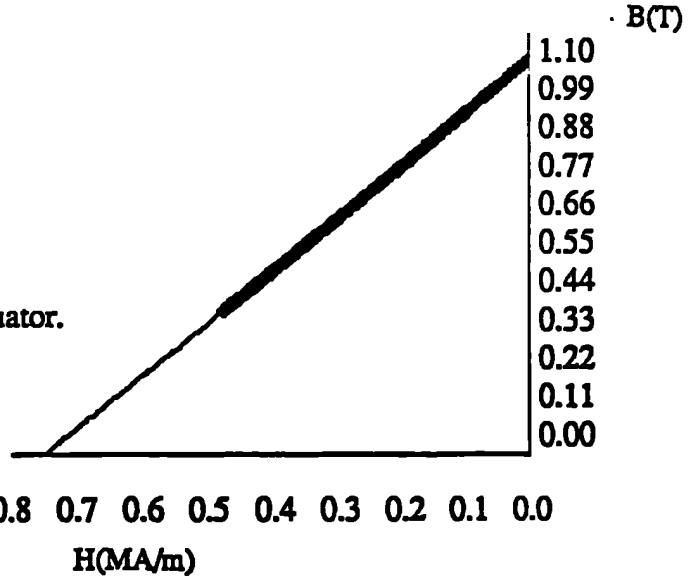

Fig 5.17.c LAT2 actuator.

Fig 5.17 Twice full-load current predicted magnet working points.

Fig 5.18 Variation of the stored energy with meshing density.

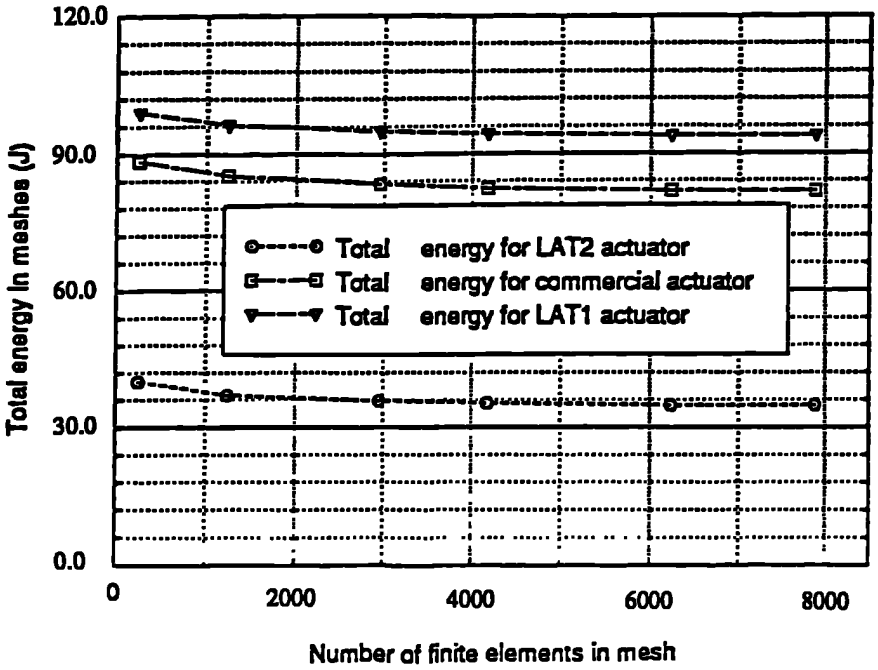

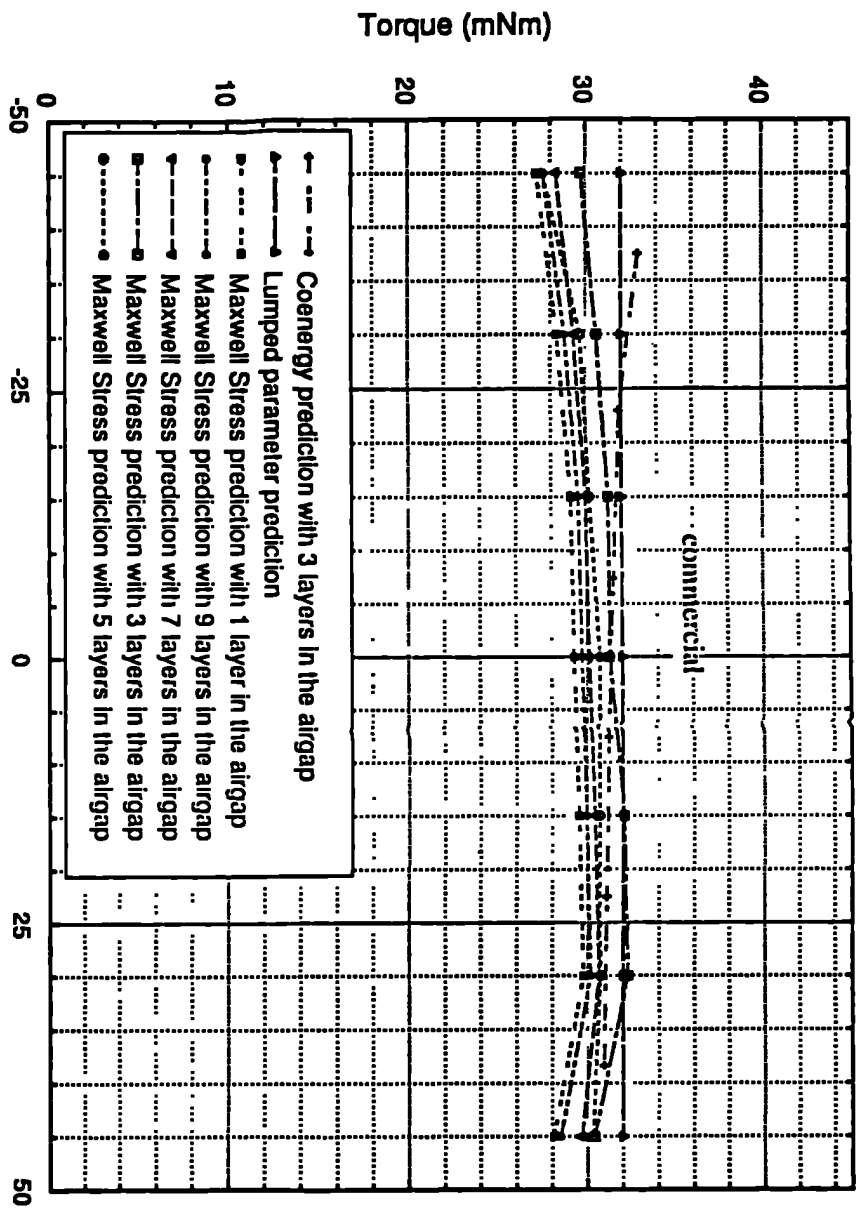

Fig 5.19 Maxwell Stress and energy method predicted torque Vs. θ for the commercial actuator. I = 1.0 Amps.

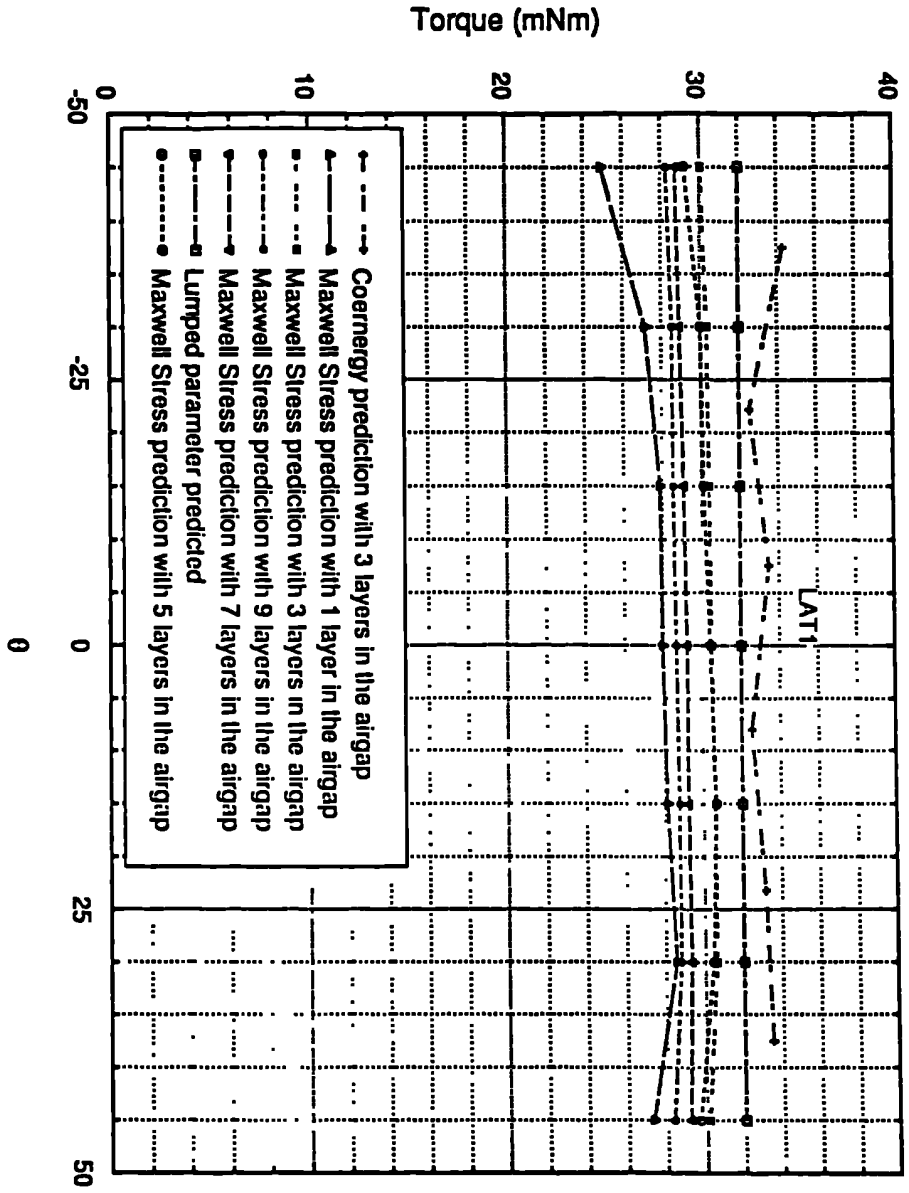

Fig 5.20 Maxwell Stress and energy method predicted torque Vs. θ for LAT 1.
I = 1.0 Amps.

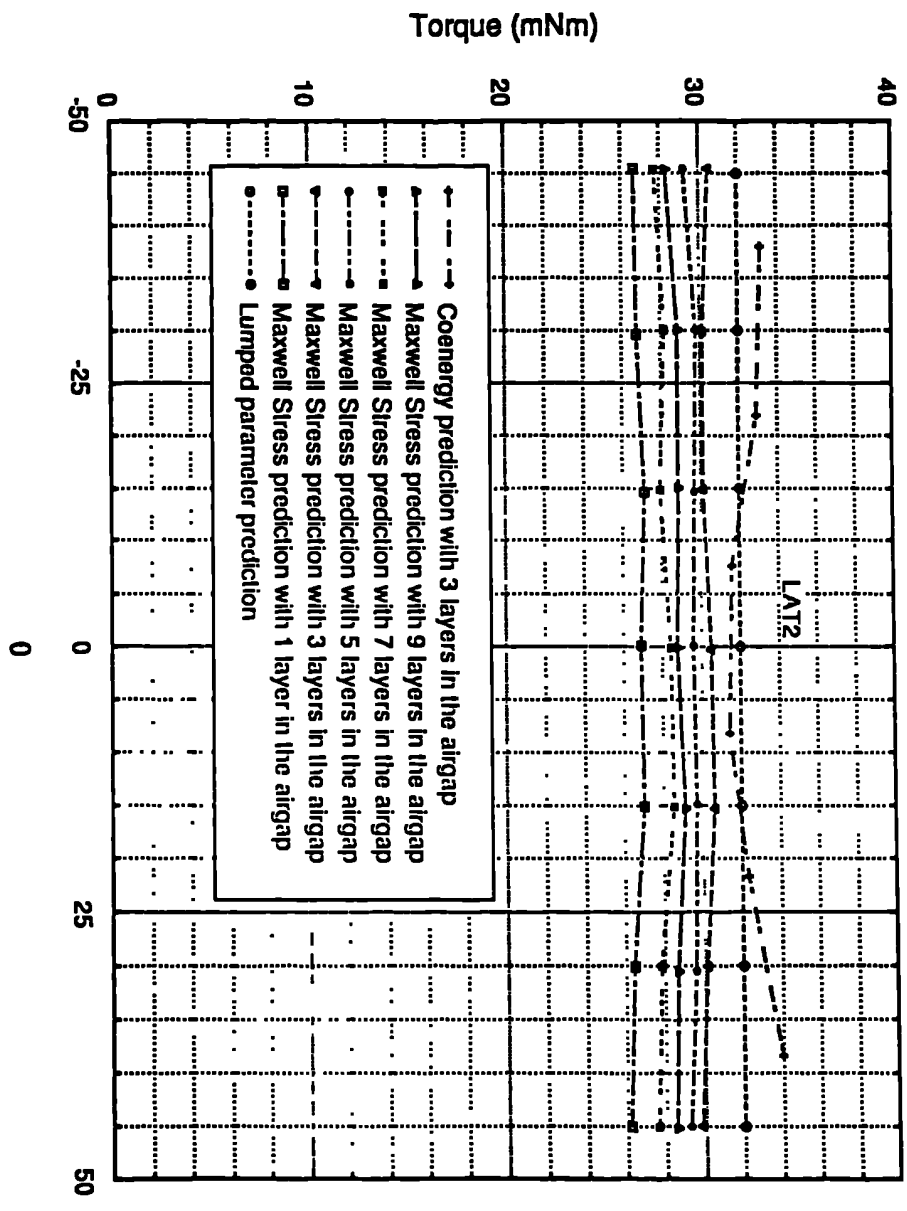

Fig 5.21 Maxwell Stress and energy method predicted torque Vs. θ for LAT 2. I = 1.0 Amps.

Fig 5.22 Finite element torque calculation at θ= 0 degrees for LAT1.

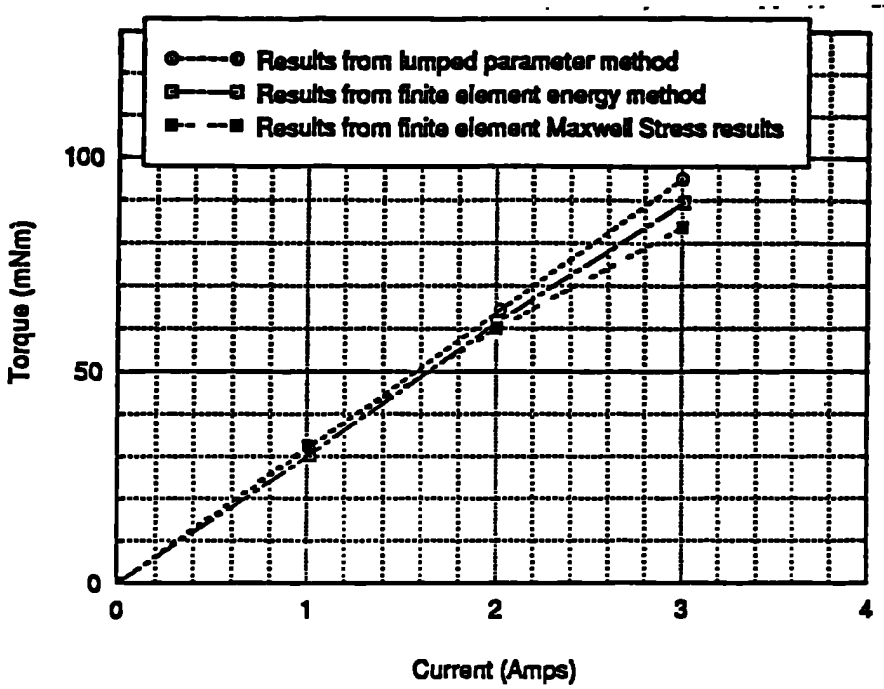

Fig 5.23 Comparison of the first quadrant magnetization characteristics for Transil 335 and mild steel.

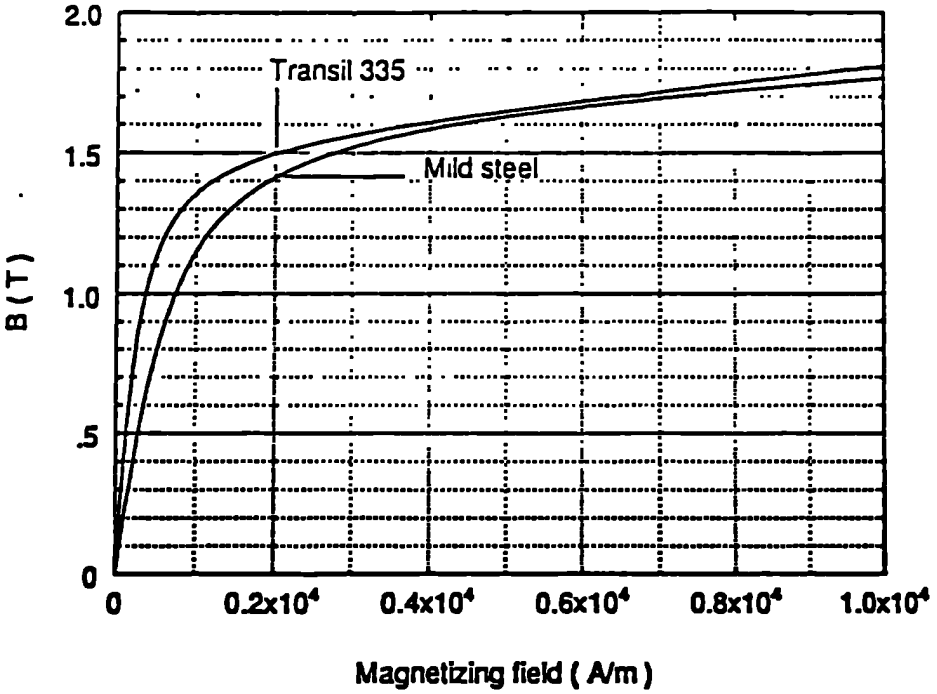

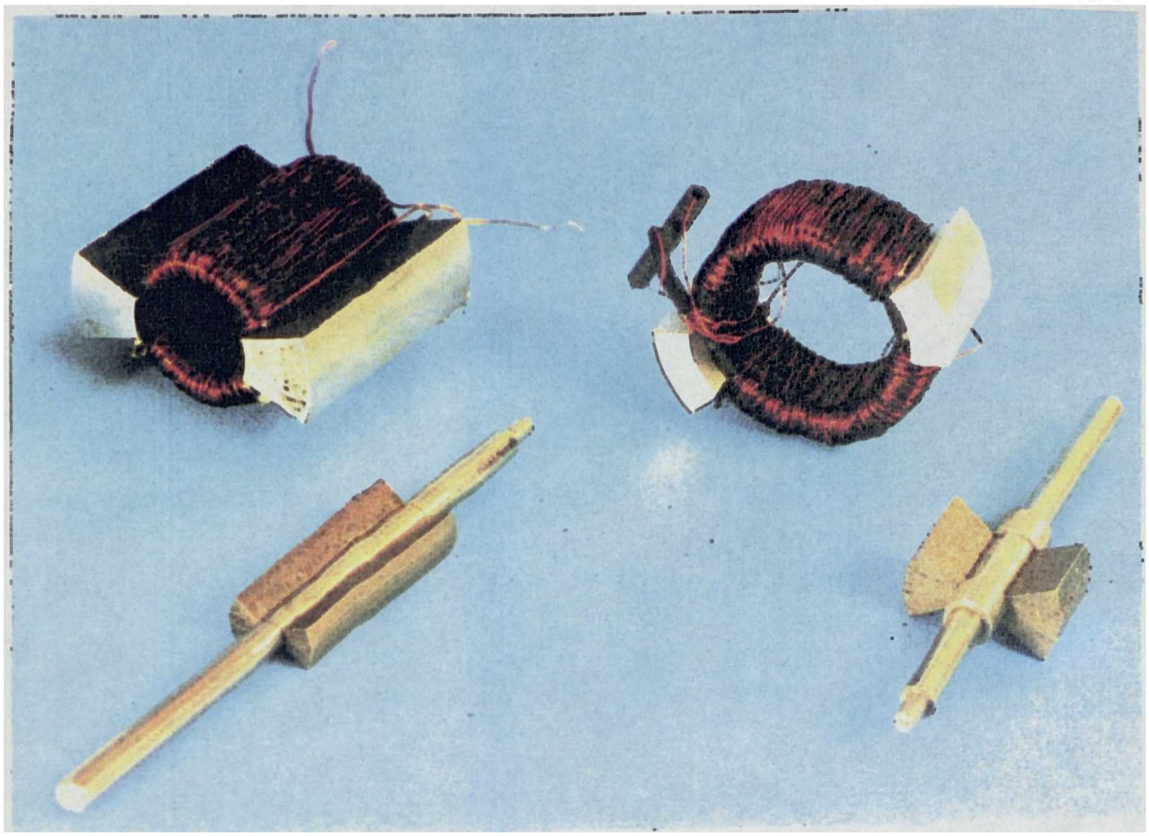

LAT2 LAT1

Fig 5.24 The two LAT actuators showing stator and rotor constructions.

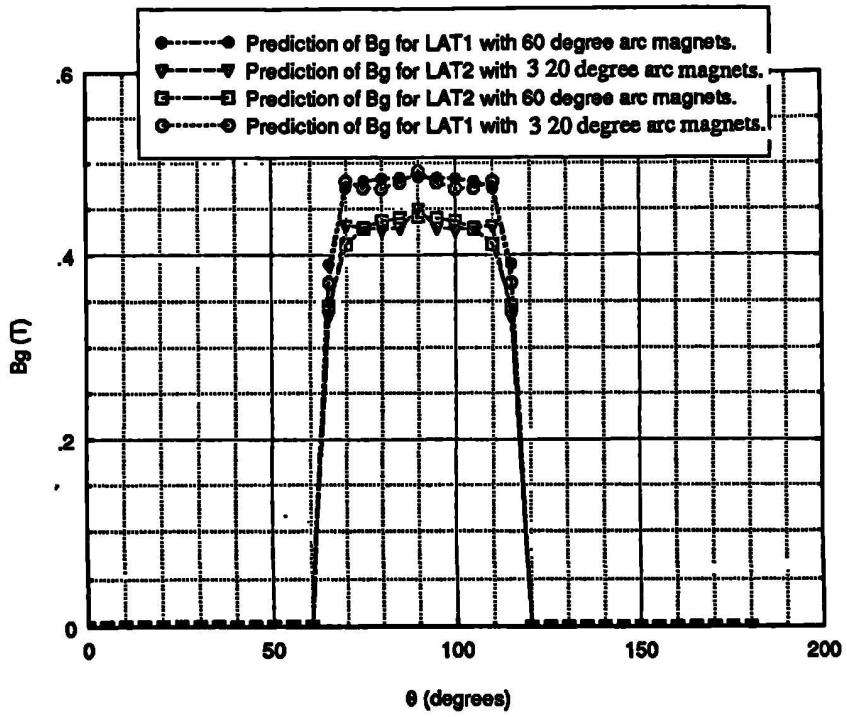

Fig 5.25 Finite element predictions of the radial airgap flux densities with 60 and 20 degree magnet arc segments for LAT1 and LAT2 actuators.

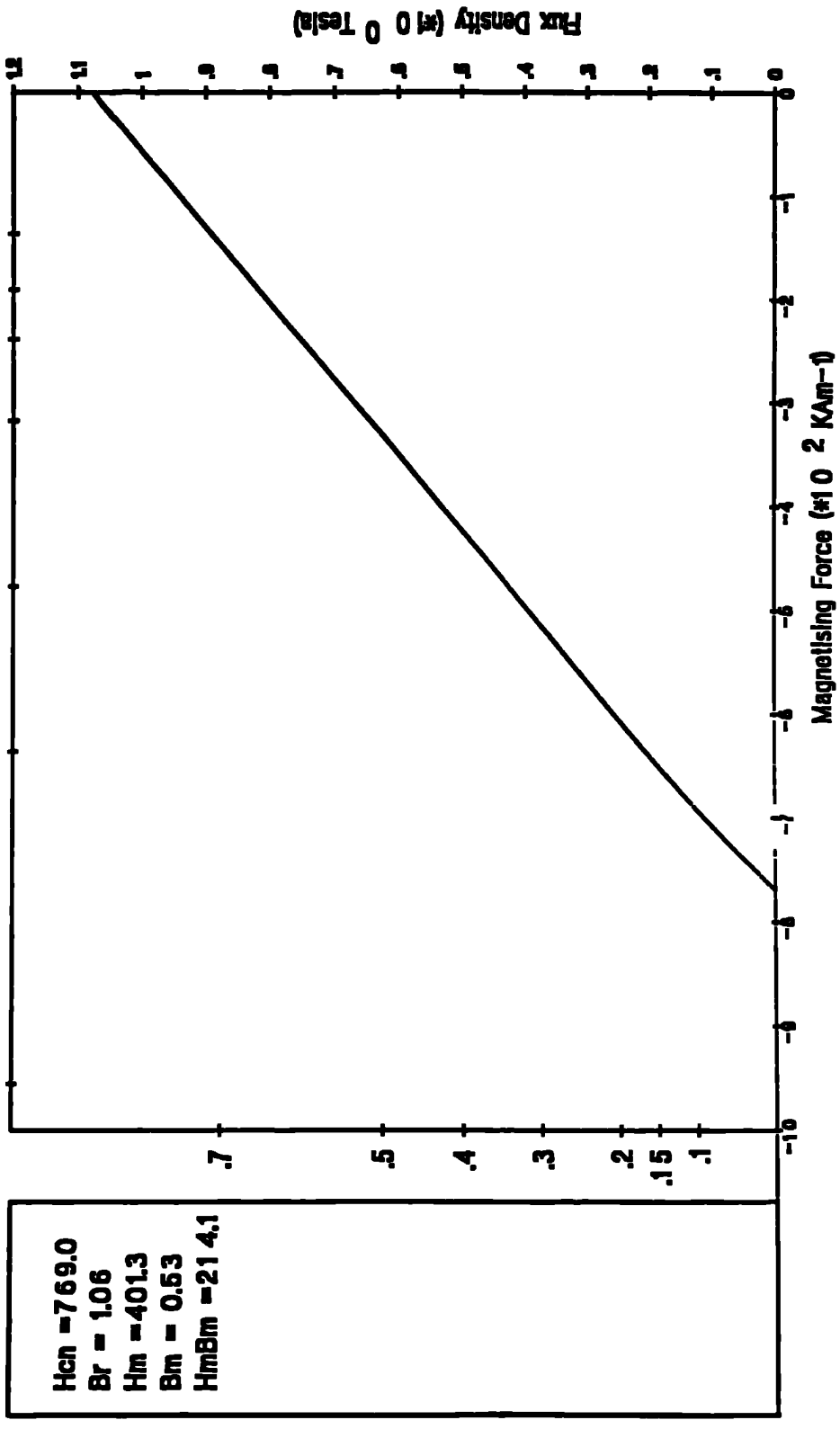

Fig 5.26 Measurement of the demagnetization characteristic of the prototype magnet.

Fig 5.27 Photograph of prototype actuators.

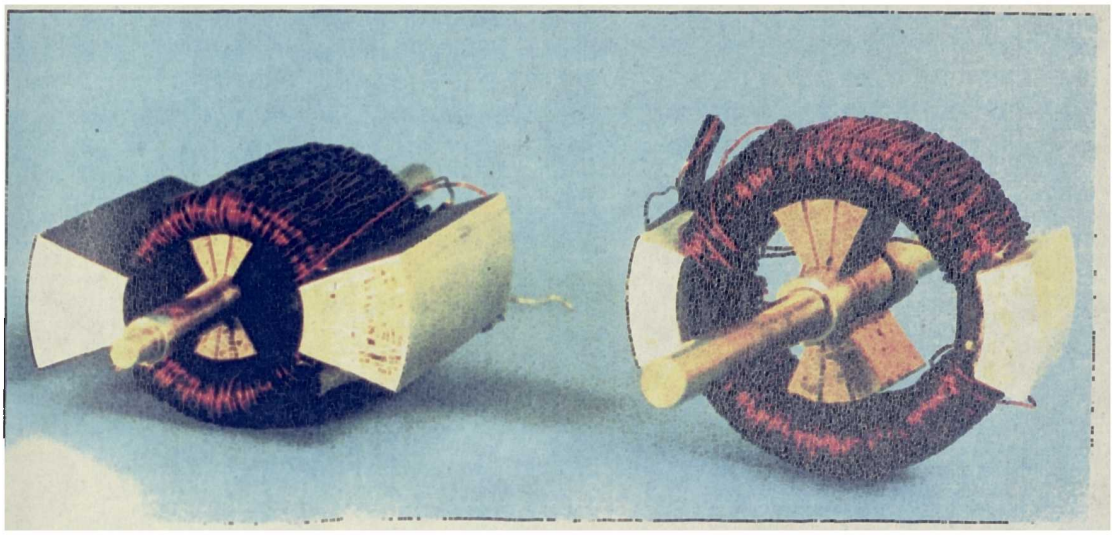

LAT2 LAT1

F'g 5.28 Measured airgap flux densites for LAT1, LAT2 and commercial actuators.

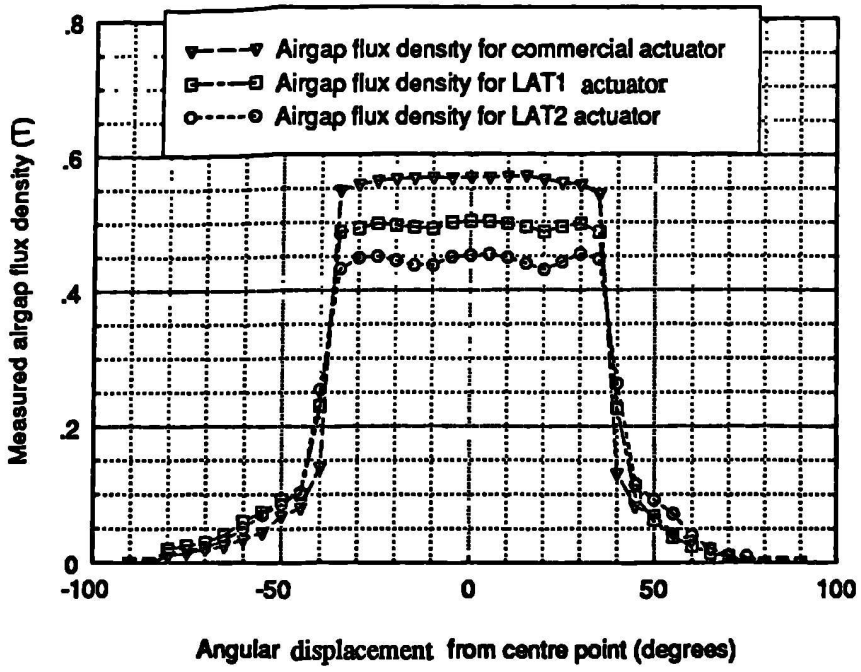

Fig 5.29 Experimental test rig for the static torque/angular displacement measurement.

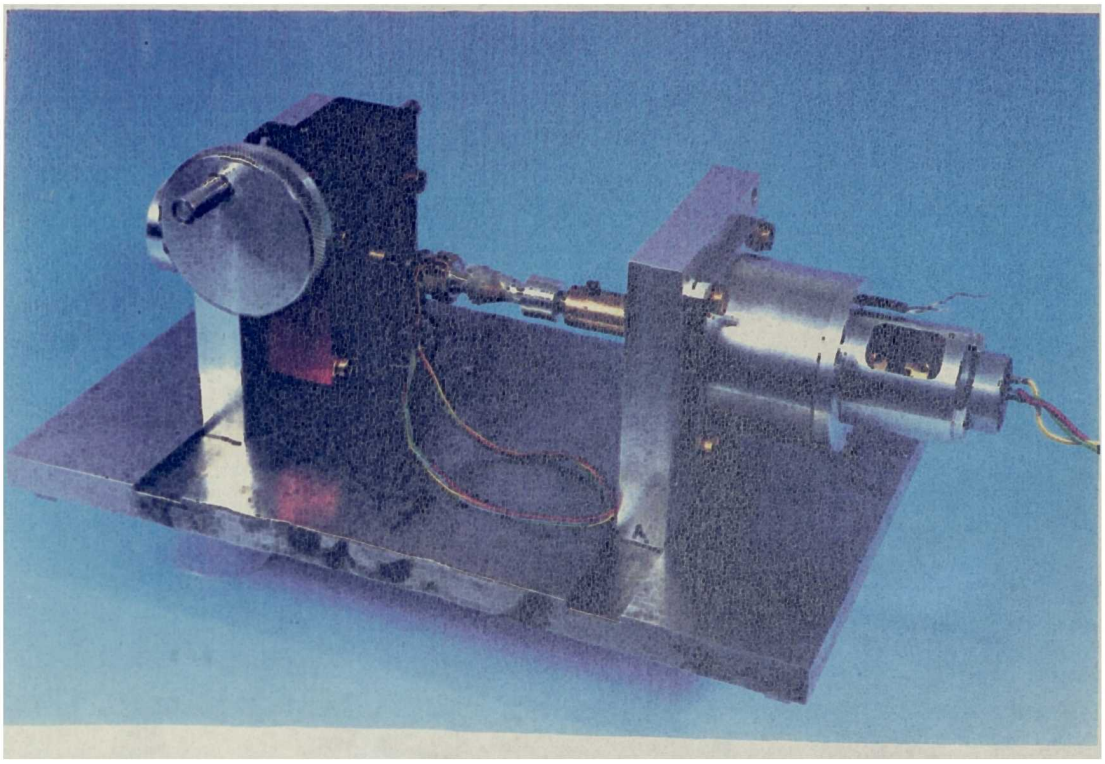

Fig 5.30 Measured full-load torque characteristics for LAT1, LAT2 and commercial actuators.

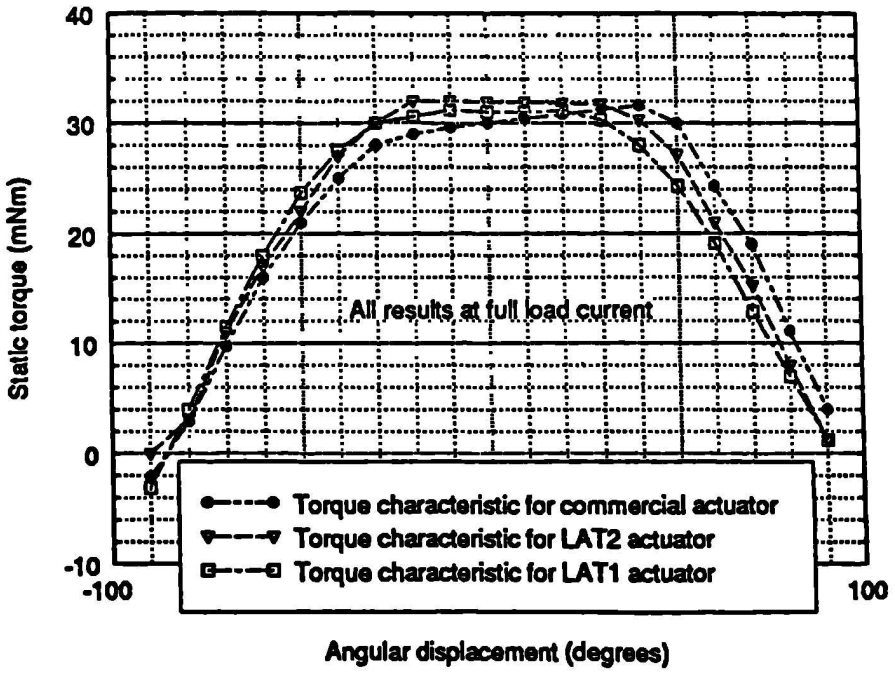

Fig 5.31 Measured Torque Vs. current for LAT1,LAT2 and commercial actuators Measured in centre of angular displacement ($\theta = 0$ degrees).

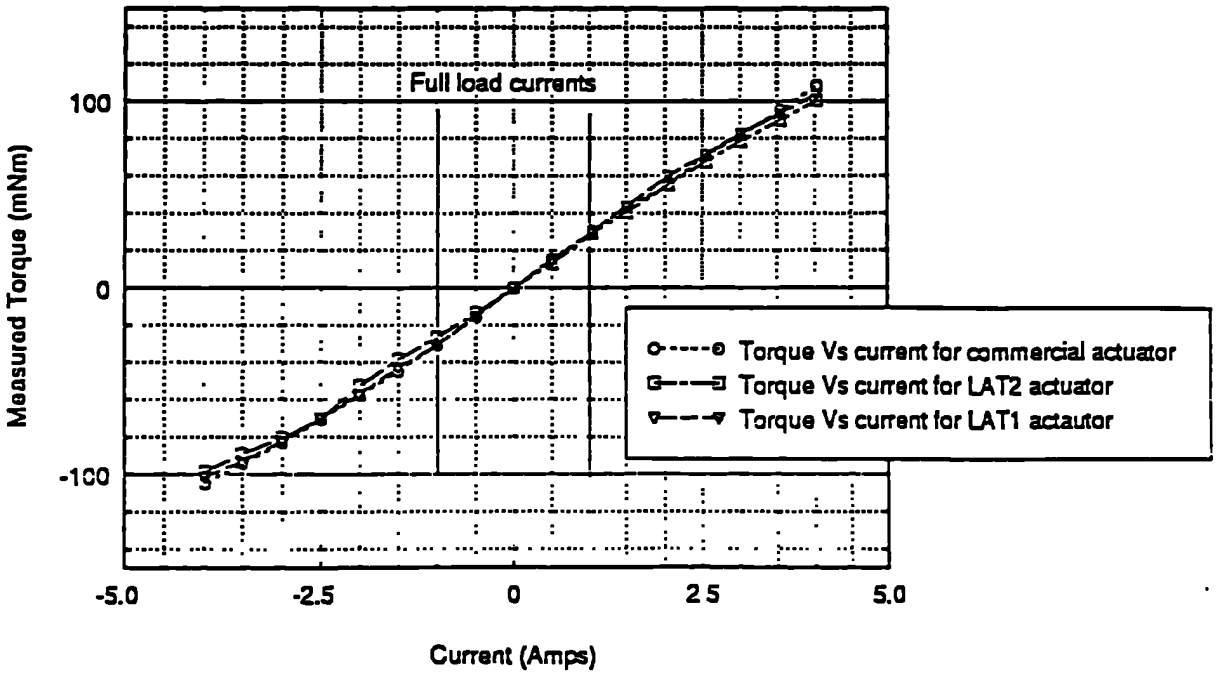

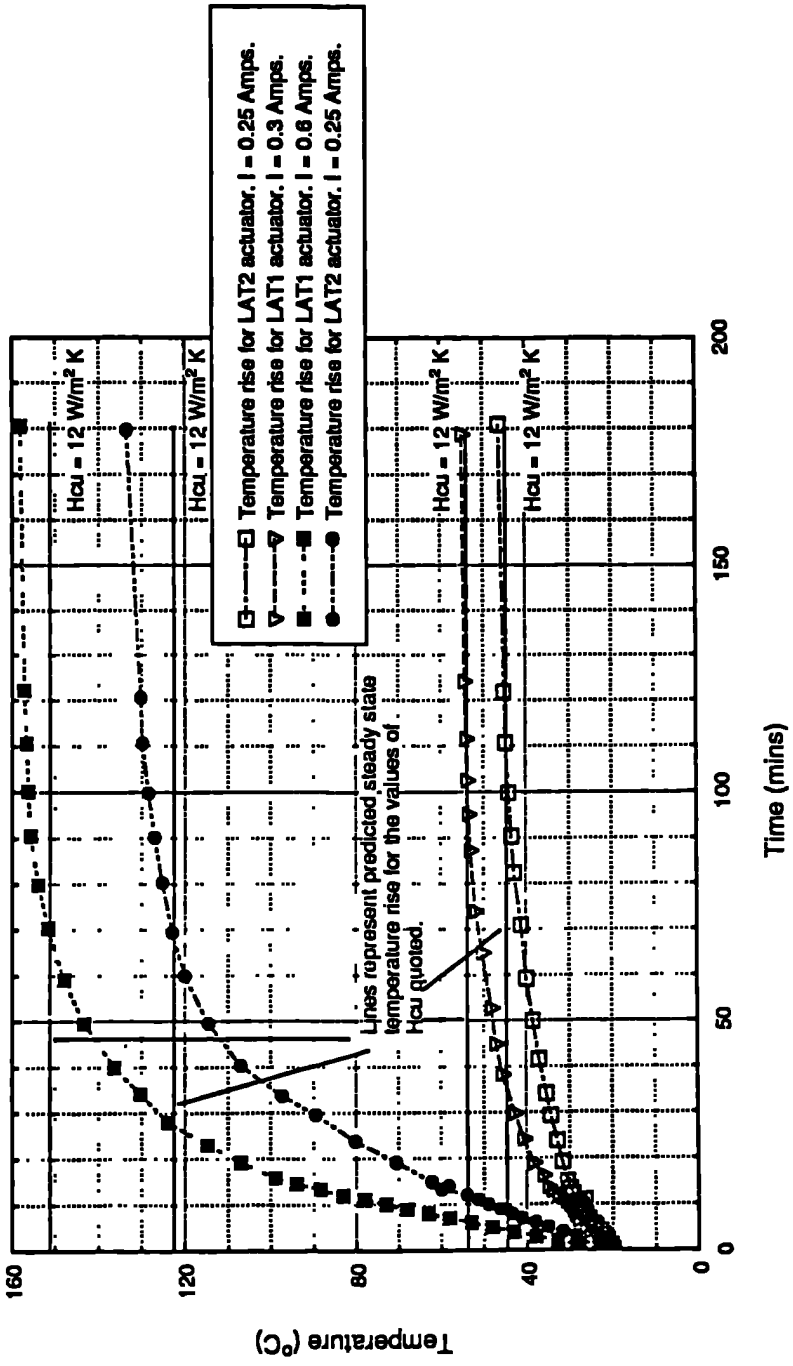

Fig 5.32 Comparisons of the measured and predicted steady state temperatures for the prototype actuators.

Fig 5.33 Experimental test rig for drag torque measurements.

F'g 5.34 Measured drag torques for LAT1, LAT2 and commercial actuators.

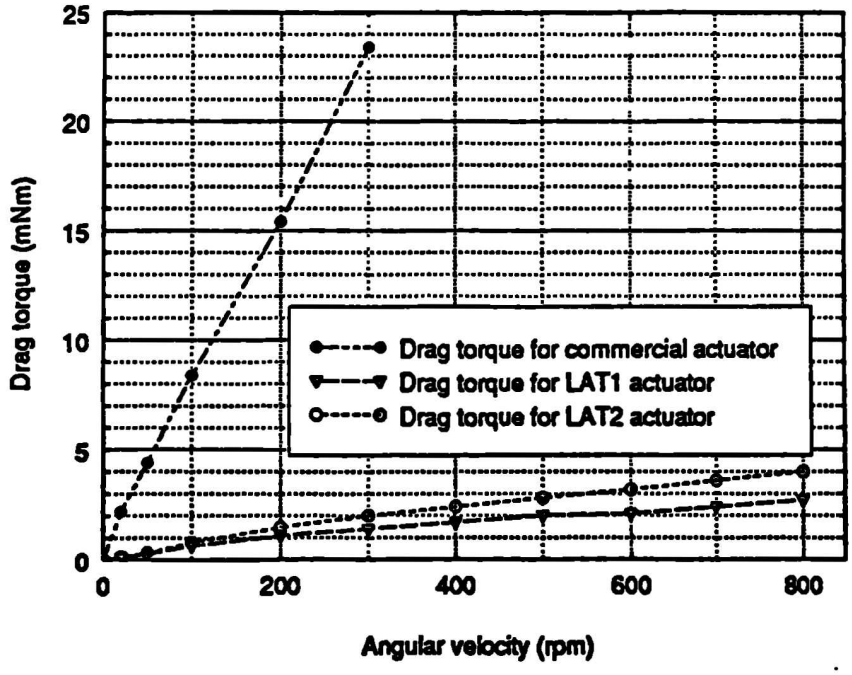

CHAPTER 6

DESIGN OPTIMIZATION OF A SHORT STROKE LINEAR VOICE-COIL ACTUATOR

6.1 Introduction

The aim of this study was the design optimization of a linear voice-coil actuator, capable of producing a near-constant 1.4N force over a ±0.5mm stroke whilst dissipating less than 0.5mW copper loss when operating at 4.2 Kelvin. This project has been conducted in collaboration with the Perkin Elmer Corporation of Connecticutt and the Advanced Materials Corporation, Carnegie Mellon University, Pittsburgh, who performed the permanent magnet materials investigation. The actuator is to be a part of NASA's Great Observatory Program, Space Infrared Telescope Facility(SIRTF), which is scheduled to be launched at the end of the 1990's.

In the telescope fixture, a mirror assembly is driven about its combined centre of mass using a pivot and a four actuator control system, feedback being provided by pairs of differential position sensors. The actuators are mounted on a second pivoted mass which isolates the telescope from vibrationally induced disturbances. When the actuators are activated, either individually or in combination, the mirror can be moved with six degrees of freedom.

To maximize the signal-to-noise ratio from the telescope, in order to observe longer wavelengths than was previously possible, the SIRTF system will be operated at the lowest possible temperature. Therefore, the telescope assembly is to be immersed in tanks of liquid helium, He^4 at 4.2K. However, the finite thermal conductance between the assembly and the helium requires minimal power dissipation to the secondary mirror

assembly in order to maximize the cryogenic lifetime. Calculations performed by the Perkin Elmer Corporation[6.1] show that for a copper loss of 0.5mW per actuator the telescope has a predicted lifespan of ten years. Hence, even small improvements on the target copper loss specification can result in the lifespan being extended by months. The specification and constraints on the actuator are given in table(6.1).

Parameter	Requirements
Force (N)	1.4
Stroke (mm)	± 0.5
Max O_d (mm)	25.4
Max W_s (mm)	25.4
Max Total mass (g)	113.6
Max Moving mass (g)	46.2
Max frequency (Hz)	5.0
Operating frequency (Hz)	4.2
Max Copper loss (mW)	0.5

Table 6.1 Specification of the voice-coil actuator.

6.2 Actuator Material Properties

Although the use of rare-earth permanent magnets such as neodymium iron boron and samarium cobalt is increasing, their performance and utilisation at cryogenic temperatures was relatively unknown, possibly due to a previous lack of commercial interest required to motivate the necessary research. SmCo, NdFe and praseodymium iron boron(PrFeB) magnets all have negative temperature coefficients of both remanence and coercivity, and therefore their energy-products should increase as the temperature is lowered. However, as the temperature is reduced below that of liquid nitrogen (77K), relatively PrFeB increases to a greater extent compared with NdFeB and SmCo. Table(6.2) compares the magnetic properties of SmCo, NdFeB and PrFeB magnets at different temperatures, whilst figs(6.1.a and 6.1.b) show the temperature dependence of the remanence and maximum energy-product respectively for PrFeB.

Like NdFeB, PrFeB magnets can also be doped with transition metal elements such as dysprosium and terbium which increase the intrinsic coercivity[1.33], so as to make them less prone to irreversible demagnetization. However, a slight reduction in the remanence and maximum energy-product results, and therefore doping was not utilised for this application.

Magnet Material	300 K			77 K			4.2 K		
	B_r (T)	H_{cn} (kA/m)	BH_{max} (kJ/m^3)	B_r (T)	H_{cn} (kA/m)	BH_{max} (kJ/m^3)	B_r (T)	H_{cn} (kA/m)	BH_{max} (kJ/m^3)
Sm_2Co_{17}	1.08	-800	219.6	1.12	-870	243.4	1.13	-870	246.6
$Nd_2Fe_{14}B$	1.25	-800	249.8	1.36	-850	288.0	1.35	-872	294.4
$Pr_2Fe_{14}B$	1.26	-850	270.5	1.41	-1026	362.0	1.45	-1098	390.0

Table 6.2 Parameters of $Sm_2\,Co_{17}\,Nd_2\,Fe_{14}\,B$ and $Pr_2\,Fe_{14}\,B$ at different temperatures.

As a further contribution to reducing losses, the conductors of the moving coil were to be manufactured from high purity, cold worked copper, which has a resistivity at 4.2K of $0.8*10^{-10}$ Ωm[1.33].

The soft magnetic material for the yoke was assumed to be a high saturation cobalt iron, such as Permendur 49 or Vacoflux 50, in order to extract maximum benefit from the use of the high energy permanent magnet. Since a magnetization characteristic for cobalt iron at 4.2K was not available, the room temperature characteristic of fig(A.4) was assumed in the design and optimization studies.

6.3 Actuator Topologies

Since the maximum specified frequency was only 5Hz, and the connected inertia was relatively high, the dynamic performance of the actuator was not particularly sensitive to the value of the coil inductance. Furthermore, at such a low frequency it was considered acceptable to manufacture the device using a solid rather than a laminated

yoke, whilst the iron loss component was considered to be negligible in comparison with the copper loss and was therefore neglected.

Because the minimization of the copper loss was the prime objective, a single-criterion optimization design procedure was followed, with other considerations such as the reduction of cost or magnet volume, which can be paramount in many industrial applications, being relatively unimportant. However, before the problem could be decomposed into a form where mathematical analyses could be applied, a topology of actuator had to be specified which would be the most appropriate for the minimization of the copper loss and yet produce a near-constant force over the required stroke. An airgap winding was selected so as to eliminate any reluctance force which could be significant in comparison with the required excitation force of 1.4N.

Attention was focussed on the two topologies of actuator shown in axisymmetric cross-section in fig(6.2). In topology 1 the flux is focussed from the magnet into the airgap, as it is at a greater radius, so that possibly $B_g > B_r$ depending upon the relative airgap and magnet lengths. This is also possible in topology 2 with a judicious choice of H_{m1} and H_{cu}. However, in topology 1 the whole of the axial length, apart from the stroke and mechanical clearances, is available for the winding, and therefore this is probably a more appropriate choice. However, the soft magnetic endcaps will short-circuit the magnetic flux causing a significant proportion of flux to pass with a tangential component, and thus not producing any axial force, towards the ends of the device. Both topology 1 and 2 were subjected to a single-criterion optimization to investigate which arrangement would produce the minimum copper loss.

6.4 Objective Function and Constraints

Basically two groups were considered:

i) VC1, with the same fixed envelope dimensions, O_d and W_s as the specification.

ii) VC2, with the same overall envelope volume, $\frac{\pi O_d^2 W_s}{4}$ as the specification. This investigation was undertaken to test the sensitivity of the copper loss to the envelope dimensions.

Within these two categories, both topologies 1 and 2 were designed using the alternative constrained single-criterion optimization techniques. The objective function to be incorporated into the optimization procedures was the minimization of the copper loss

i.e. $$\text{copper loss} = I^2 R \tag{6.1}$$

and since $$\text{force} = B_g I_c l_c \tag{6.2}$$

where B_g is the average radial airgap flux density,

I_c is the current in the conductor

l_c is the length of the conductor in the magnetic field.

$$\text{copper loss} = \frac{force^2 \rho_{cu}}{B_g^2 V_{ag} k_{pf}} \tag{6.3}$$

where ρ_{cu} = resistivity of copper

V_{ag} = volume of airgap

k_{pf} = winding packing factor.

The moving and total masses, which were constrained in this application were then evaluated, for example, for topology1:

$$M_{total} = \frac{\pi (O_d^2 - I_d^2)(H_{cu} + L_{mmca} + stroke)\,\sigma_{vaco}}{4} + \frac{\pi IY_d^2 (H_{cu} + L_{mmca} + stroke)\,\sigma_{vaco}}{4} + \frac{2\pi O_d^2 L_{cap}\,\sigma_{vaco}}{4} + \frac{\pi\left\{(IY_d + 2L_{mcr} + 2L_g)^2 - (IY_d + 2L_{mcr})^2\right\} H_{cu}\,\sigma_{cu}\,kpf}{4} + \frac{\pi\left\{(IY_d + 2L_{mcr} + 2L_g + 2L_m)^2 - (IY_d + 2L_{mcr} + 2L_g)^2\right\} H_{cu}\,\sigma_{mag}}{4} + \frac{\pi\left\{(IY_d + 2L_{mcr})^2 - (IY_d)^2\right\} H_{cu}\,\sigma_{brass}}{4} + \frac{2\pi\left\{(IY_d + 2L_{mcr} + 2L_g)^2 - (IY_d)^2\right\} L_{mca}\,\sigma_{brass}}{4}$$

(6.4)

$$M_{mov} = \frac{\pi\left\{(IY_d + 2L_{mcr} + 2L_g)^2 - (IY_d + 2L_{mcr})^2\right\} H_{cu}\,\sigma_{cu}\,kpf}{4} + \frac{\pi\left\{(IY_d + 2L_{mcr})^2 - (IY_d)^2\right\} H_{cu}\,\sigma_{brass}}{4} + \frac{2\pi\left\{(IY_d + 2L_{mcr} + 2L_g)^2 - (IY_d)^2\right\} L_{mca}\,\sigma_{brass}}{4}$$

(6.5)

where σ_c is the density of copper = 8930 kg/m^3

σ_{vaco} is the density of the cobalt iron = 8250 kg/m^3

σ_{mag} is the density of PrFeB = 7400 kg/m^3

σ_{brass} is the density of brass = 8100 kg/m^3

Table(6.3) illustrates the constraints applied for each design consideration, VC1 and VC2.

	VC1		VC2	
	Topology 1	Topology 2	Topology 1	Topology 2
Force (N)	1.4	1.4	1.4	1.4
Inequality Constraints				
i) Max O_d (mm)	25.4	25.4	100.0	100.0
ii) Max W_s (mm)	25.4	25.4	100.0	100.0
iii) Min L_m (mm)	> demag length	> demag length	> demag length	> demag length
iv) Max Volume (mm^3)	12870.4	12870.4	12870.4	12870.4
v) Stroke (mm)	± 0.5	± 0.5	± 0.5	± 0.5
vi) Max Total mass (g)	113.6	113.6	113.6	113.6
vii) Max Moving mass (g)	46.2	46.2	46.2	46.2
Equality Constraints				
i) $I_d = IY_d + 2(L_m + L_{mcr} + L_g)$	yes	no	yes	no
ii) $I_d = D_{m2} + 2L_{m1}$	no	yes	no	yes
iii) $W_s = H_{cu} + 2(L_{mca} + L_{cap})$	yes	no	yes	no
iv) $W_s = H_{m1} + L_{mca} + H_{cu} + L_{cap}$	no	yes	no	yes
v) $D_{m2} = IY_d$	no	yes	no	yes
vi) $L_g = L_{m1}$	no	yes	no	yes
Variables				
i) O_d (mm)	no	no	yes	yes
ii) W_s (mm)	no	no	yes	yes
iii) L_m (mm)	yes	no	yes	
iv) IY_d (mm)	yes	yes	yes	yes
v) L_g (mm)	yes	yes	yes	yes
vi) H_{cu} (mm)	yes	yes	yes	yes
vii) L_{cap} (mm)	yes	yes	yes	yes
viii) H_{m1} (mm)	no	yes	no	yes
ix) L_{m2} (mm)	no	yes	no	yes

Table 6.3 The force required, the constraints and the active variables for the VC1 and VC2 actuator optimization.

Thermal analyses were not required since the liquid helium maintained the entire secondary mirror assembly, including the actuators, at a constant temperature of 4.2K. Furthermore, in accordance with recommendations from AMC/Perkin Elmer, realistic values for the mechanical tolerances: Lmca and Lmcr, and the packing factor k_{pf} are:

Lmca = 1.00mm, Lmcr = 0.70mm and K_{pf} = 0.720

Although the above value of packing factor would normally be regarded as exceptionally high, it was achievable in this application, as was demonstrated in coil winding trials undertaken by Perkin Elmer. In accordance with the findings of chapter 2, the lumped reluctance networks shown in figs(6.3.a and 6.3.b) were used to compute the open-circuit field distribution of the actuators, topology 1 requiring only 1/4 of the device to be modelled on open circuit, and topology 2 requiring 1/2 of the actuator to be modelled, due to the asymmetry caused by the removal of the soft magnetic endcap. The value of B_g was determined from the average of the flux densities in the permeances in the networks, and implemented in equation(6.3).

6.5 Results of Single-Criterion Optimization Techniques

The three constrained optimization techniques which were described in chapter 3 were used to obtain the minimum copper loss for VC1 and VC2 designs. Table(6.4) compares the number of objective function evaluations required for each technique before convergence to a global optimum for VC1, topology 1, from which it is evident that the Simulated Annealing technique is the most efficient. However, the advantage over the Flexible-Tolerance/Flexible-Polyhedron approach is not as pronounced as that reported in chapter 5 for the toroidally wound actuator. This is somewhat surprising as the Simulated Annealing technique was envisaged to become increasingly superior as the number of independent design variables was increased. However, the reason this occurred may be that fewer local optima existed in the 'design space'. Nevertheless, the results represent a 43% reduction in function evaluations compared to that required by the Flexible-Tolerance/Flexible-Polyhedron approach in converging to the solution.

Table(6.5) shows the minimum copper loss for each topology for the VC1, in which the envelope dimensions were fixed, from which it is evident that topology 1 is capable of

producing the 1.4 N force with only 75% of the copper loss compared with topology 2, even though the average airgap flux density is some 23% lower. However, both actuator topologies are predicted to satisfy the copper loss specification given in table(6.1). Table(6.5) also illustrates that with a slight relaxation in the envelope dimensions constraints, as in VC2, a further reduction of 5.4% in the copper loss can be achieved. Unfortunately, the alterations to the envelope dimensions could not be incorporated in this application due to the specification set by Perkin Elmer. The 'history of optimization' for topology 1 is illustrated in fig(6.4), where it can be seen that a number of designs will, in theory, meet the specification.

In conclusion, the actuator of topology 1 has been shown to be capable of producing the required force with a lower loss than that of topology 2, and can easily meet the specification of table(6.1).

Optimization Method	Minimum Objective Function(mW)	Number of Function Evaluations
Flexible Polyhedron	0.373	7621
Alternating Directions	0.371	15271
Simulated Annealing	0.371	4372

Table 6.4 Comparison of the number of function evaluations required to achieve the global optimum for topology 1.

	Topology	L_m (mm)	L_g (mm)	O_d (mm)	W_s (mm)	IY_d (mm)	H_{cu} (mm)	H_{m1} (mm)	H_{m2} (mm)	L_{cap} (mm)	B_g (T)	Copper loss(mW)	M_{total} (g)	M_{mov} (g)
VC1	1	2.66	2.52	25.4	25.4	9.74	16.60	N/A	N/A	2.88	0.551	0.371	93.6	13.6
VC1	2	4.71	4.01	25.4	25.4	14.06	4.48	2.86	13.90	0.86	0.745	0.498	93.1	5.8
VC2	1	4.63	2.51	28.3	20.47	10.97	8.02	N/A	N/A	3.01	0.670	0.351	86.6	12.4
VC2	2	3.43	2.73	26.2	23.96	14.52	5.04	2.97	12.06	0.89	0.731	0.465	101.4	8.8

Table 6.5 Results of constrained optimization for the Simulated Annealing method for both topologies of voice coil actuator investigated. N/A indicates not applicable.

6.6 Finite Element Analysis To Estimate The Radial Aigap Flux Density

In order to predict the average radial airgap flux density more accurately, the magnetic field was analysed by finite elements. Field solutions were obtained for operation at both 4.2K and 293K, the higher temperature prediction being performed to permit subsequent experimental validation. Fig(6.5) is typical for topology 1 of VC1, it is at 4.2K, and shows that the flux does not cross the airgap perfectly radially since the soft magnetic yoke short-circuits the flux at both ends of the magnet and leads to a significant leakage flux. The relatively large spread of magnet working points is exacerbated since flux is being focussed towards the working airgap. Fig(6.6) shows the flux plot and corresponding magnet working points when a full-load current density is applied to the finite elements representing the coil. It confirms that partial irreversible demagnetization of the magnet will not occur. The value of the current density set in the finite elements representing the winding, for any specific level of force was calculated from equation (6.2).

i.e
$$J = \frac{force}{B_g V_{ag} k_{pf}} \qquad (6.6)$$

In the finite element mesh of the cross-section of the actuator, the area of the elements representing the winding was identical to its physical dimensions, and therefore equation(6.6) does not need to be modified by a distribution factor.

Airgap flux density profiles for different radii are shown in fig(6.7) and confirm that because of flux leakage at each end of the magnet the flux density is greatest at the centre, and because of flux focusing, it increases as the inner core is approached. The flux density at the geometric average diameter of the working airgap:

i.e.
$$\frac{\sqrt{(IY_d + 2L_{mcr})^2 + (IY_d + 2(L_{mcr} + L_g))^2}}{2}$$

has been averaged from the corresponding finite element results. Table(6.6) gives a comparison with predictions from the lumped parameter model for both VC1 and VC2 actuators. Clearly the results from the finite element analyses are lower than those estimated from the lumped parameter technique, due in part to the more refined discretization of the finite element analyses and hence more accurate representation of localised saturation as well as its ability to account for radial and tangential components of flux density. However, the actuators of topology 1 for both VC1 and VC2 are still anticipated to satisfy the copper loss specification of 0.5mW at 4.2K.

	Topology	B_g (T) LP *	B_g (T) FE *	Copper loss (mW) LP *	Copper loss (mW) FE *
VC1	1	0.58	0.55	0.371	0.404
VC1	2	0.67	0.64	0.351	0.384
VC2	1	0.75	0.72	0.498	0.553
VC2	2	0.73	0.70	0.465	0.501

Table 6.6 Comparisons of lumped parameter and finite element B_g and copper loss prediction.

* LP denotes lumped parameter analysis. FE denotes finite element analysis.

6.7 Numerical Methods Of Force Calculation

The force calculation, based upon the rate of change of energy with coil displacement which was described in chapter 2, was used to estimate the force acting on the moving coil in order to check the earlier calculation method and to establish whether saturation effects at rated load current would influence the force. Fig(6.8) shows how the energy, integrated over all the finite elements used to discretize a cross-section of the actuator, varies with the number of elements in the mesh. It indicates that a mesh of 8900 elements is likely to be suitable to calculate the energy to the required precision. The incremental displacement of the coil was selected to be 0.1mm with the average force calculated assumed to be acting at the centre of the displacement. Fig(6.9) shows the calculated force/displacement characteristic as a function of the current density in the finite element calculations, and compares the results with the force estimated from equation(6.2) with

the value of airgap flux density, calculated by finite element as described in section(6.6). The results from the energy method, at rated current density, are only some 5.8% lower than that predicted from equation(6.2). These results represent a close correlation between the two methods of force calculation considering the small displacements and change in stored energy.

The armature reaction effects and increased saturation were shown to be negligible, as confirmed by the linearity of the predicted force/current density characteristic of fig(6.10) for currents well in excess of the specified full-load current.

6.8 Alternative Directions Of Magnetization

From the flux plot of fig(6.5) it can be seen that there was significant leakage flux towards the end of the PrFeB magnet, caused by the short-circuiting effect of the soft magnetic endcaps. An approach to ensure that more of the main magnet flux passes in a more radial direction across the working airgap, is to vary the magnetization of the ring magnet along its axial length. In order to quantify the benefits from such a design, it was simulated in the finite element model by discrete changes in the angle of magnetization along the axial length of the ring, as illustrated in fig(6.11). The axial centre of the magnet was assigned a perfectly radial magnetization, with the angle of magnetization varied in discrete steps on either side of the centre. Fig(6.12) shows the variation in the average airgap flux density, calculated by the finite element technique, and the estimated copper loss as a function of the change in magnetization angle. It can be seen that an optimum exists, when the change in magnetization is $\pm 40^{o}$ from the perfectly radial, where there is a reduction in the copper loss of 5.7%.

Unfortunately, this realisation of a varying preferred direction of magnetization is a significant practical problem, and so was not pursued further. Table(6.7) compares the results with the VC1 optimized actuator.

Change in Angle of Magnetization	B_g (T)	Copper loss (mW)
$\pm 0^o$ i.e. VC1	0.551	0.404
$\pm 15^o$	0.559	0.393
$\pm 40^o$	0.565	0.384
$\pm 60^o$	0.555	0.398

Table 6.7 Comparison of B_g and copper loss with change in angle of magnetization.

6.9 Prototyping of Minimized Copper Loss VC1 Actuator

The actuator optimized for minimum copper loss, which meets the specification of table(6.1) was prototyped. However, due to practical constraints a few departures were made from the theoretical design.

6.9.1 Prototype Construction

6.9.1.a Soft Magnetic Yoke

The yoke of the actuator was made from a (50%) cobalt steel, Vacoflux 50, supplied and finally annealed after machining by Vacuumsmeltze AG. The accuracy of any published soft magnetic material characteristics is questionable especially after annealing. Therefore, the initial B/H magnetization characteristic of the cobalt steel used for the yoke of the prototype actuator was measured using an 180-turn excitation coil and a close-fitting toroidal search coil wound around an annulus of the material and is illustrated in fig(6.13). It can be seen that the measured characteristic is slightly lower than the published characteristic, especially at low values of flux density, possibly due

to a partial loss in the magnetization which was not subsequently recovered by annealing and possibly due to experimental errors.

6.9.1.b Permanent Magnets

The anisotropic PrFeB magnets were manufactured by the Advanced Materials Corporation(AMC). Radially anisotropic 360^o ring magnets assumed in the design are not currently available although a 360^o ring is still thought possible for a final prototype by the mid 1990's. Therefore, six diametrically magnetized 60^o arc segments were supplied as illustrated in fig(6.14). Unfortunately, they did not exactly match the sizes required from table(6.5) and therefore the design was altered to accomodate this factor. Table(6.8) compares the optimized design, VC1, with the prototype, the new theoretical values of B_g and copper loss being evaluated from a finite element analysis of the prototype actuator with the initial B/H characteristic for the cobalt iron as measured in fig(6.13).

Parameter	Optimized Actuator	Prototype Actuator
O_d (mm)	25.4	25.4
W_s (mm)	25.4	25.4
I_d (mm)	21.52	21.10
IY_d (mm)	9.74	9.62
L_m (mm)	2.66	2.55
L_g (mm)	2.52	2.54
H_{cs} (mm)	16.63	16.69
L_{cap} (mm)	2.89	2.70
B_g (T) at 293 K	0.424	0.399
Copper loss at 293 K	150	168

Table 6.8 Comparison of optimized and prototype actuators.

6.9.1.c Winding Design

At this stage in the development of a prototype device the choice of wire diameter was made in order to maximize the packing factor. A conventional grade of copper was used with a resistivity of $1.78*10^{-8}$ Ωm at 293 K. After repeated attempts, a packing factor of 0.72 was achieved with a winding of 122 turns of 0.50mm copper diameter wire, resulting in a winding resistance of 0.508Ω, measured using a Cambridge precision decade resistance bridge. Fig(6.15) shows the prototype actuator. The former was machined from brass.

6.9.2 Prototype Testing

6.9.2.a Open Circuit Airgap Flux Density Measurement

The circumferentially averaged airgap flux density distribution along the axial length of the airgap was measured in the same way as the British Aerospace voice-coil actuator described in section(2.5.2), using a search coil/integrating flux meter, and by moving the search coil axially in discrete steps and measuring the change in flux linkage. Due to the axial length of the search coil, there existed a 'dead-space' for which the airgap flux density could not be measured. Therefore, in this region the flux density was assumed to exhibit the same percentage reduction as the finite element results. The results of fig(6.16) show that the measured open circuit flux density was only approximately 63% of the value obtained from the finite element prediction at 293 K.

The possible reasons for this reduction are:

1) The magnets were not fully magnetized.

2) The use of diametrically magnetized arc segments as opposed to a full 360^{o}.

3) A reduction in magnetization caused by stress, induced from surface grinding to produce the arc segments.

To test the level of magnetization of the arc segments, they were remagnetized in discrete 20% full voltage steps from 0-100%, using a 14.2kJ, 42500μF capacitor discharge magnetizer illustrated in fig(6.17). The flux from each segment was measured using a Helmholtz coil/integrating flux meter. Fig(6.18) and table(6.9) show that none of the segments were initially fully magnetized, the average improvement upon remagnetization being 28.3%. In addition, it would appear from fig(6.18) that upon remagnetization the segments were subsequently fully magnetized as the curve had saturated by 100% full voltage. However, there still exists a significant variation in the measured flux from segments 4 and 6 of 9.1%, so that improvements in the material should be possible.

Magnet Segment	Flux measurement (mWb-Turns) prior to remagnetization	Flux measurement (mWb-Turns) at 20% full voltage	Flux measurement (mWb-Turns) at 40% full voltage	Flux measurement (mWb-Turns) at 60% full voltage	Flux measurement (mWb-Turns) at 80% full voltage	Flux measurement (mWb-Turns) at 100% full voltage
1	58.7	60.7	70.6	84.9	86.3	86.6
2	69.0	72.1	76.4	83.9	87.9	88.8
3	63.5	66.0	72.8	87.1	87.9	88.0
4	68.7	70.7	75.0	85.3	90.6	90.9
5	58.4	60.6	66.2	83.0	84.6	84.8
6	55.9	57.9	65.3	81.3	83.3	83.3

Table 6.9 Measurement of the flux from the magnet segments in air by Helmholtz coil/integrating flux meter.

Fig(6.19) shows the results from the remeasurement of the open circuit flux density, which shows that the average airgap flux density was now 0.355T, which is ~92% of the theoretical prediction. However, this still represents a significant anomaly of approximately 8% and therefore, the current required to produce rated force is 0.575 Amps, as determined from equation(6.2).

To estimate the reduction in the airgap flux density caused by the magnet segmentation, the radial airgap flux density was measured around the circumference of the airgap at an

axial plane corresponding to the centre of the axial length of the magnet, using a Hall-probe/Gauss-meter, with the removal of the soft magnetic endcap. The results presented in fig(6.20) are compared with a new finite element prediction of the airgap flux density assuming an ideally magnetized magnet but with the endcap removed. Similar to the British Aerospace design of section(2.5.2), the measured value was approximately periodic every 60^o. For these test conditions the average reduction in the measured airgap flux density was ~4.2% from the peak flux density measured at the centre of magnet arc segment 4. As described in section(6.9.1.b) a 360^o ring magnet is expected to be available for a final prototype.

The remaining ~3.8% reduction in airgap flux density could possibly be caused by stress induced from surface grinding of the PrFeB magnet. Previous designs based on surface ground PrFeB have led to reductions of up to 25.0% in open circuit flux density measurements compared to theoretical predictions[6.2]. This could possibly be an explanation for the 9.1% variation of the measured flux from magnet segments 4 and 6.

6.2.9.b Static Force-Displacement and Force-Amp Measurements

Using a calibrated strain gauge and force transducer, the force acting on the moving coil was measured as a function of the winding displacement and current. Initially there was a significant friction force between the brass former and the inner yoke. This was reduced by shaving the inside of the former, reducing its thickness from 0.7mm to ~0.5mm. However, it still required 0.06 Amps to displace the coil. With this value of friction force remaining constant with applied current it would represent an increase from 0.575 A to 0.635 A for the current required to produce rated output force, corresponding to an increase in rated copper loss of ~36 mW.

The force on the coil was measured at 0.1mm increments in position, and fig(6.21) shows that for each current level the force was significantly lower towards the ends of the stroke,

caused by the reduction in the airgap flux density in these regions. As might be expected, the reduction in force was diluted in comparison to the flux density/displacement characteristic of fig(6.19) since most of the moving coil was situated in the region of high flux density away from the endcaps.

The force/current characteristic presented in fig(6.22), in which the coil is in the centre of its stroke, shows that not only is there a delay in the measurement of a force, due to the friction force, but the gradient of the characteristic is also lower than the results predicted from a linearly scaled Lorentz equation using the value of flux density determined from the finite element analysis, and assuming an ideally magnetized magnet. The current required to produce rated force was 0.70 A, corresponding to a copper loss of 249mW. However, neglecting the friction force, which should be significantly reduced in a final, manufactured prototype, the rated current and copper loss would be reduced to 0.64 A and 208 mW respectively, representing an increase over the theoretical copper loss prediction of ~24%.

Assuming that the reduction in flux density, caused by magnet segmentation can be overcome, thereby increasing the flux density by 4.2%, then the copper loss would be reduced to approximately 188 mW.

It is also notable from fig(6.22) that the measured force/current characteristic shows little saturation due to the armature reaction current. This would be anticipated at room temperature, especially as the total magnet flux has been reduced.

Unfortunately, measurements at reduced temperatures were not possible. However, assuming a reduction in the copper resistivity to $0.8*10^{-10}\Omega m$ and an increase in the airgap flux density in the ratio $\frac{0.551}{0.424}$, as predicted from the results of tables(6.5 and 6.8), then the copper loss would be reduced to 0.501 mW.

It is therefore essential that the reduction in magnetic performance, possibly due to the surface grinding of the PrFeB magnet material must be overcome before the final prototyping of the actuator in the mid 1990's.

6.10 Conclusions

The optimum design established from this study, VC1, will theoretically meet the specification of producing a force of 1.4N whilst dissapating less than 0.5 mW copper loss. However, problems caused by material manufacture must be overcome to produce the best possible actuator. Table(6.10) shows the values of airgap flux density and copper loss assuming that the problems of friction force and magnet segmentation are overcome.

State of the design	B_g (T)	Copper loss (mW)
Measured	0.355	249
Measured Neglecting Friction Force	0.355	208
Measured, Neglecting Friction Force and Assuming 360° radial magnetized magnet	0.375	188

Table 6.10 The measured and assumed values for the airgap flux density and copper loss assuming various material complications are overcome.

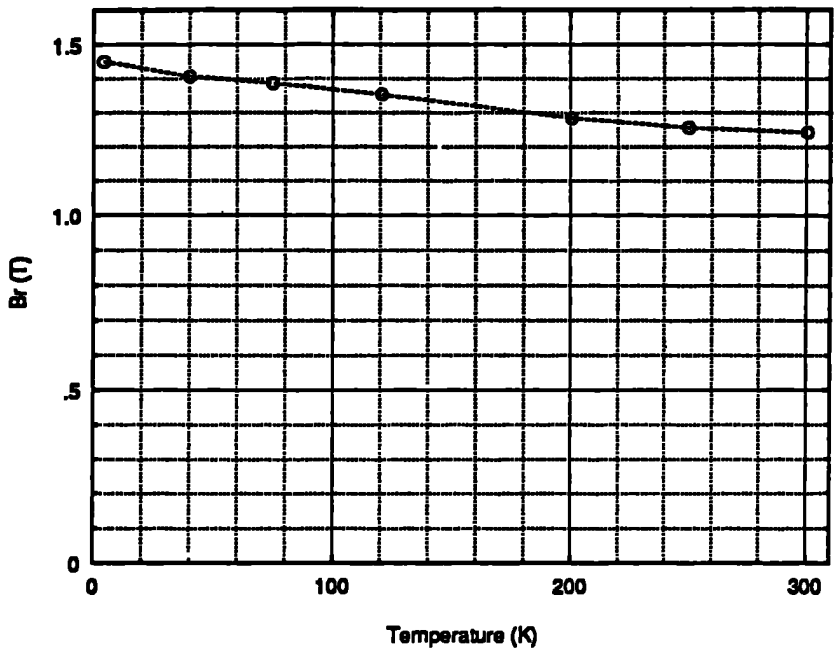

Fig 6.1.a Temperature dependence of remanence for PrFeB.

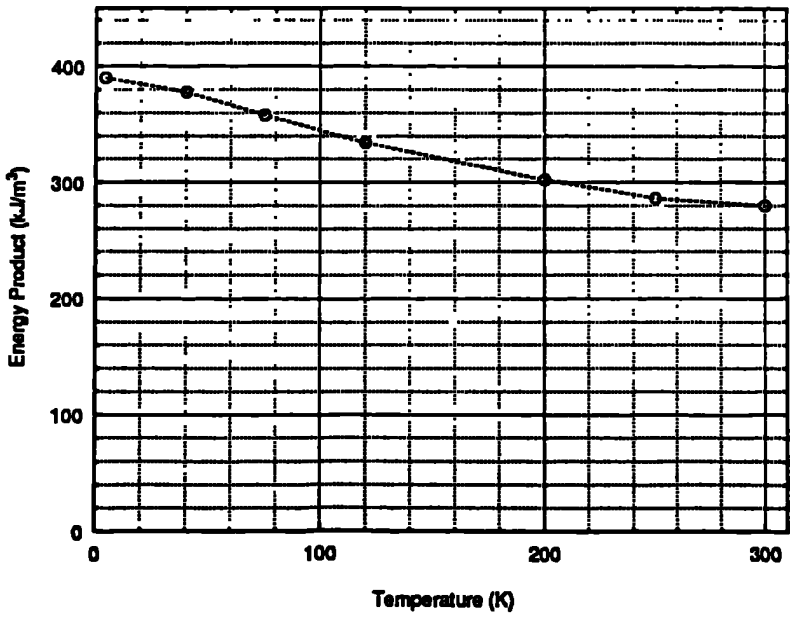

Fig 6.1.b Temperature dependence of the maximum energy product for PrFeB.

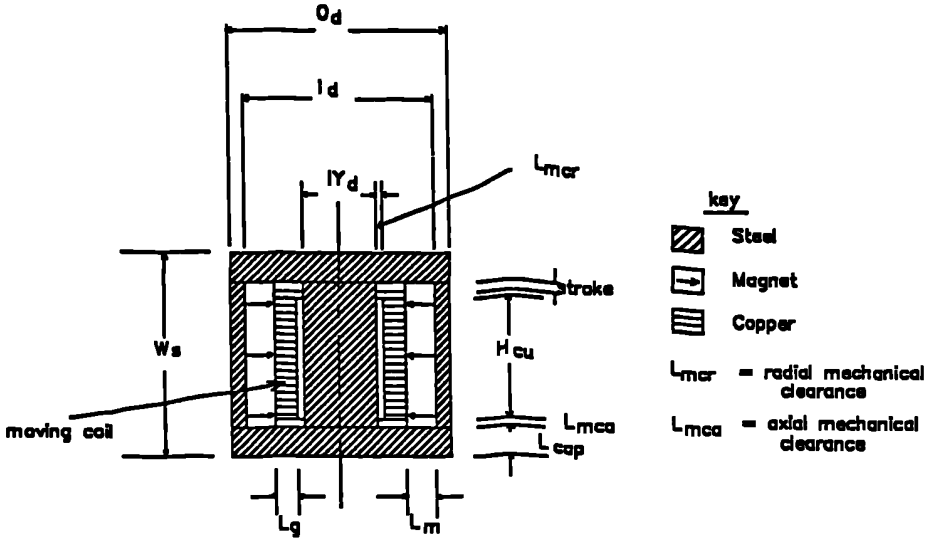

Fig 6.2.a Topology 1 - Fully enclosed actuator.

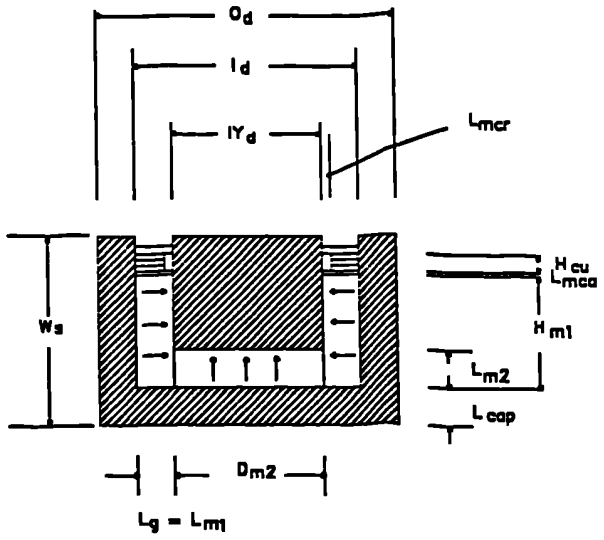

Fig 6.2.b Topology 2 - Open-ended actuator.

Fig 6.2 Topologies of voice-coil actuator investigated.

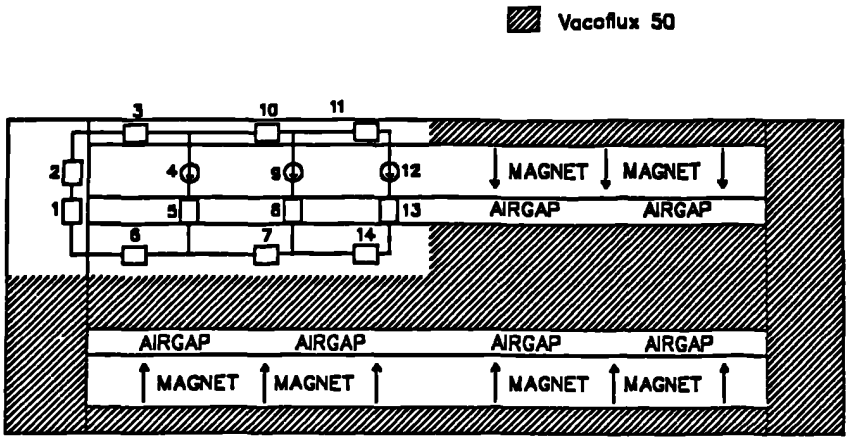

Fig 6.3.a Schematic diagram of the lumped parameter network used to calculate the open circuit flux density of topology 1.

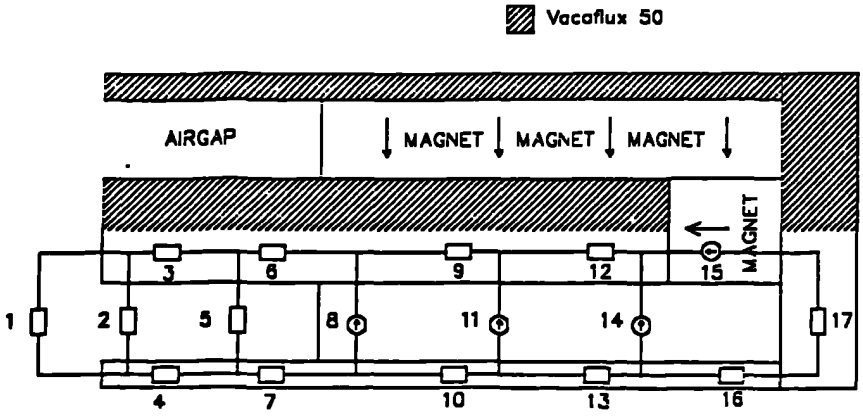

Fig6.3.b Schematic diagram of the lumped parameter network used to calculate the open circuit flux density of topology 2.

Fig 6.3 Lumped parameter models used in the open circuit airgap flux density calculation

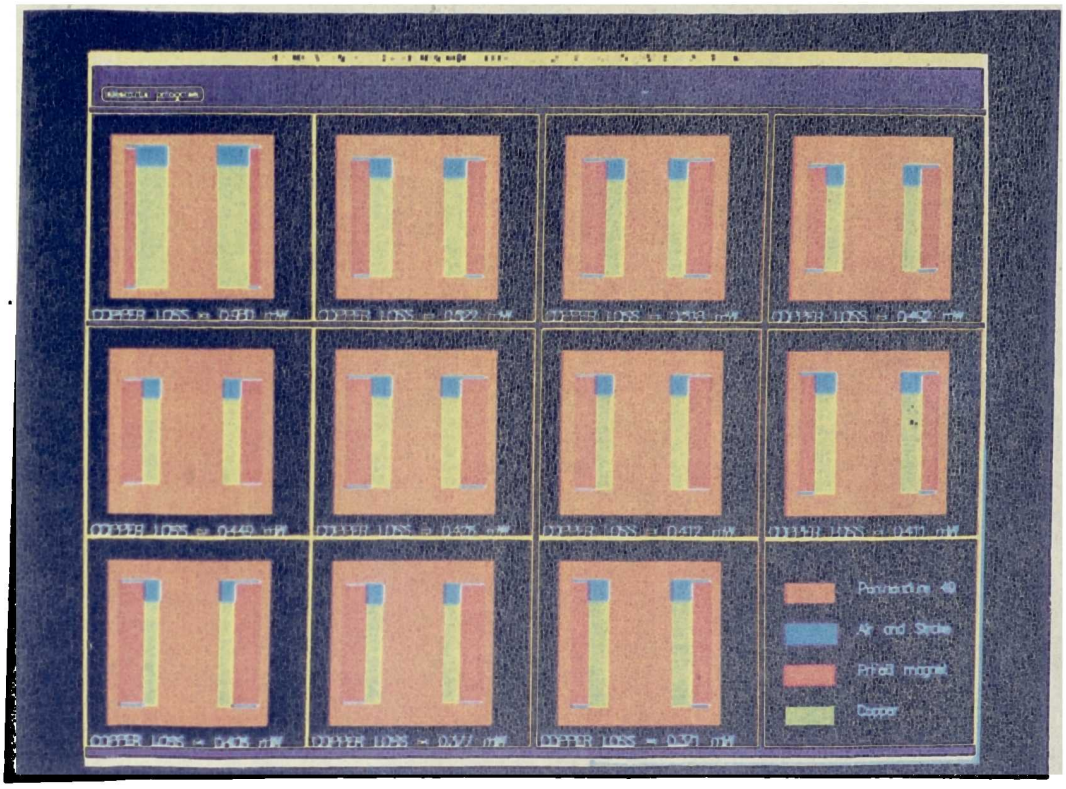

Fig 6.4 'History of optimization' for VC1, topology 1 actuator.

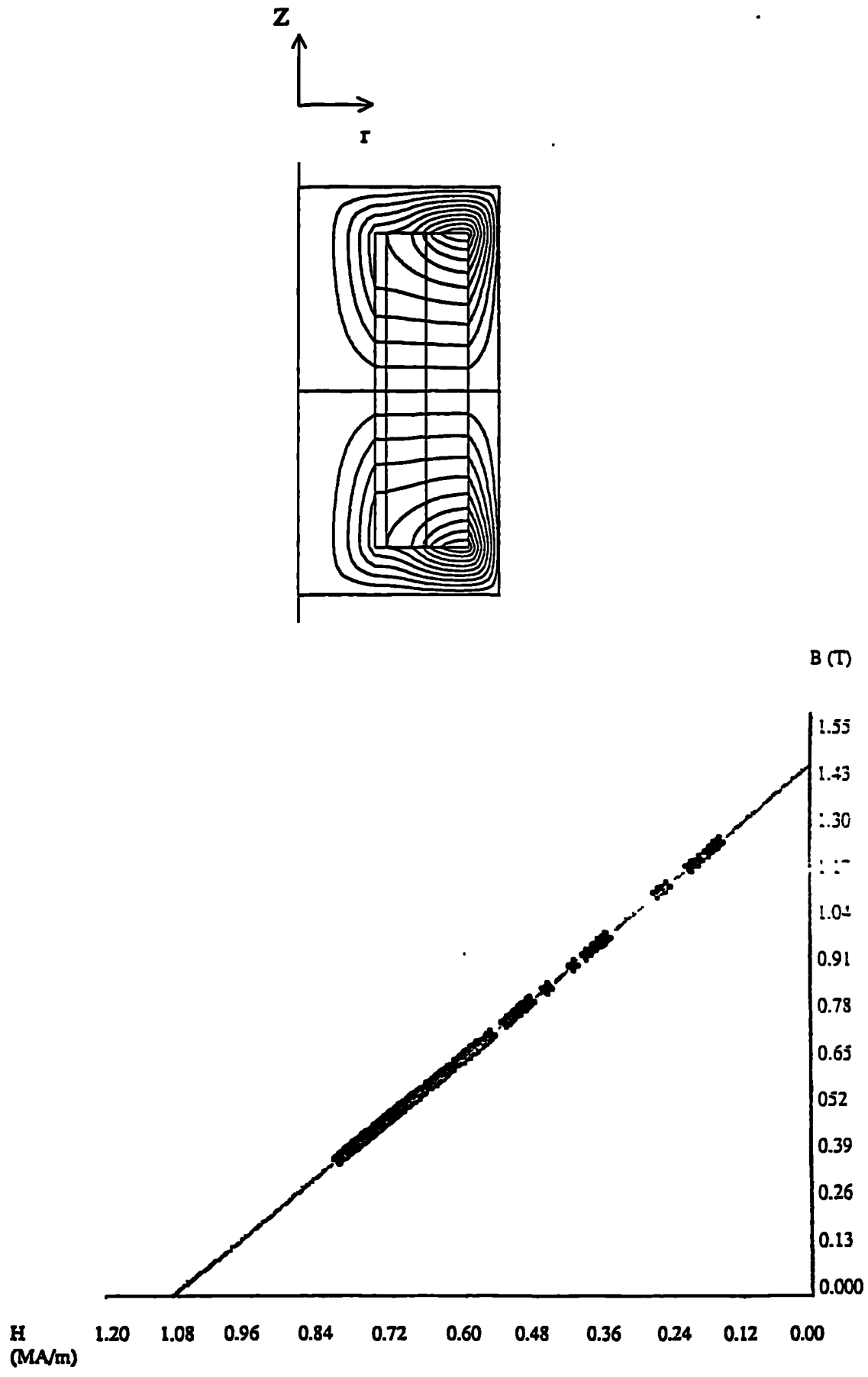

Fig 6.5 Flux plot and magnet working points on open circuit.

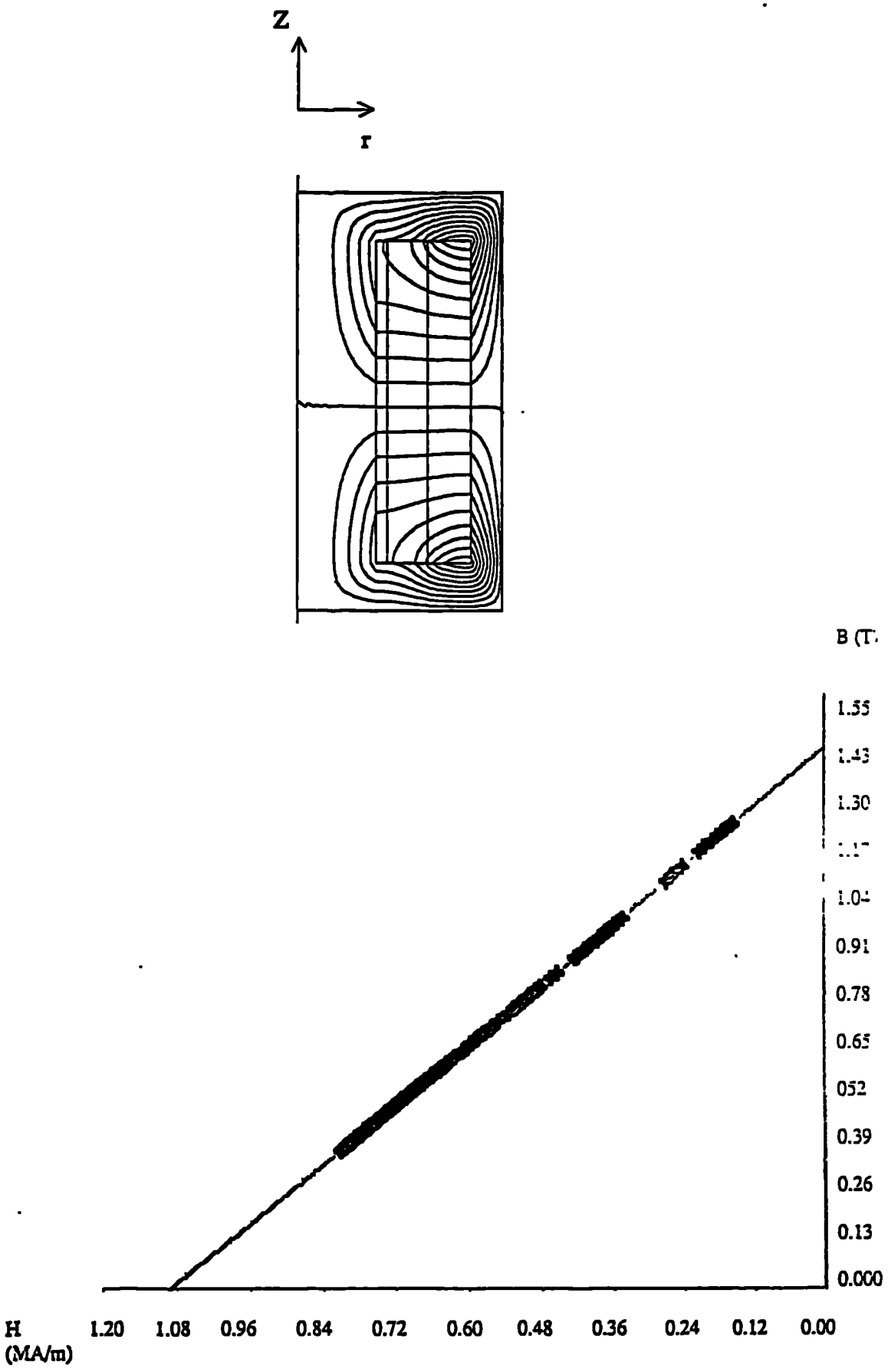

Fig 6.6 Flux plot and magnet working points for full load current.

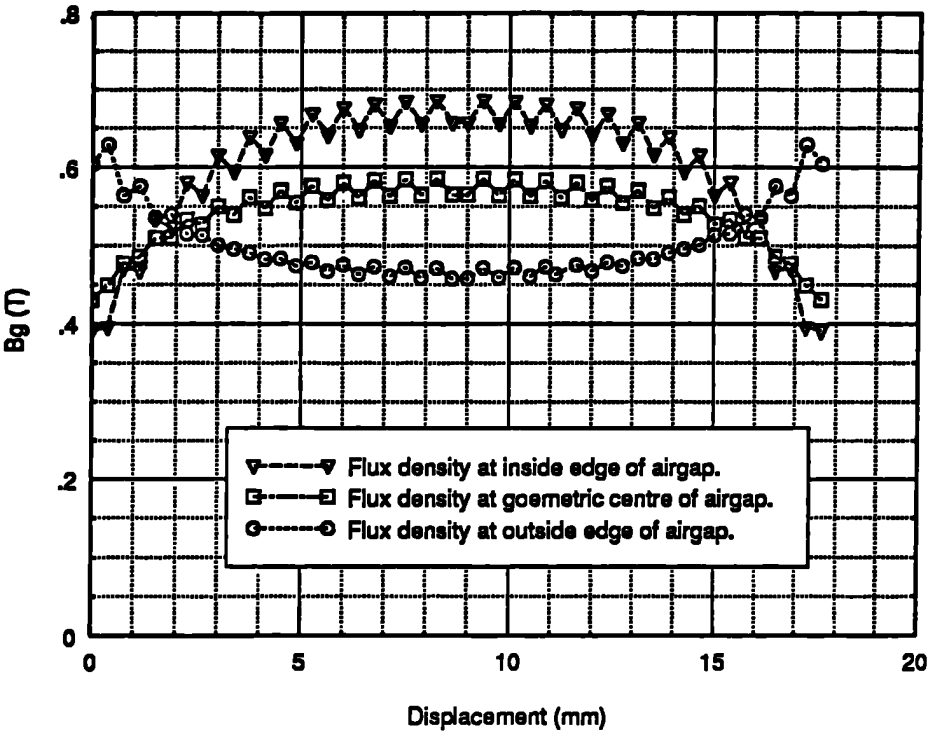

Fig 6.7 Variation of the radial airgap flux density in the axial direction.

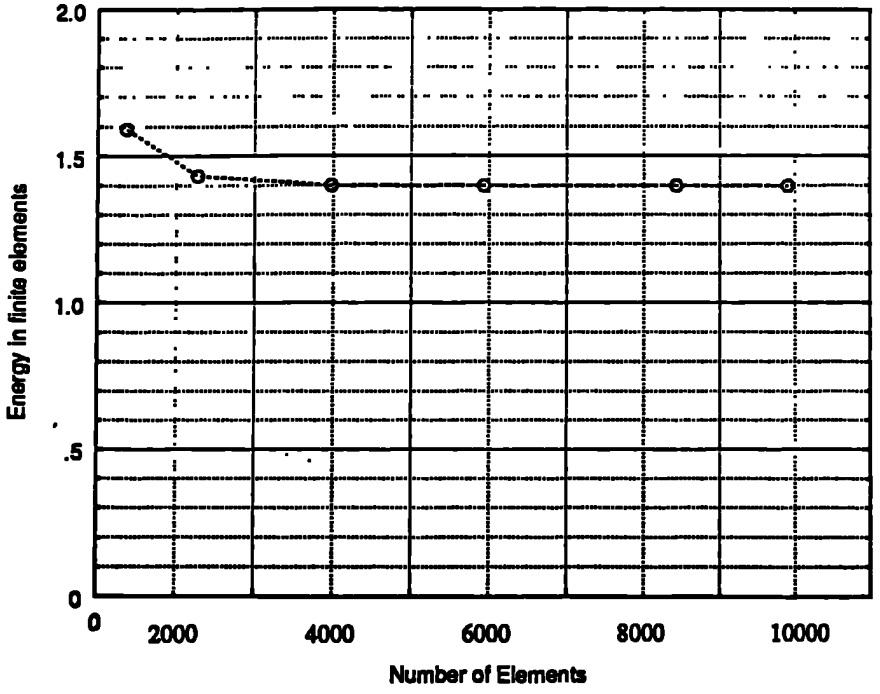

Fig 6.8 Variation of the mesh energy with the number of finite elements at rated current density.

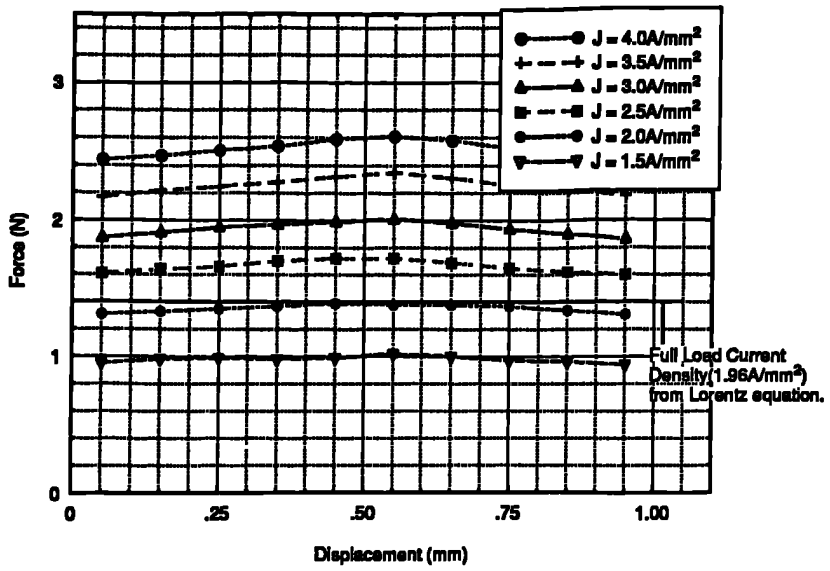

Fig 6.9 Comparison of the energy method and Lorentz equation force/displacement characteristics at different winding current densities for VC1 actuator.

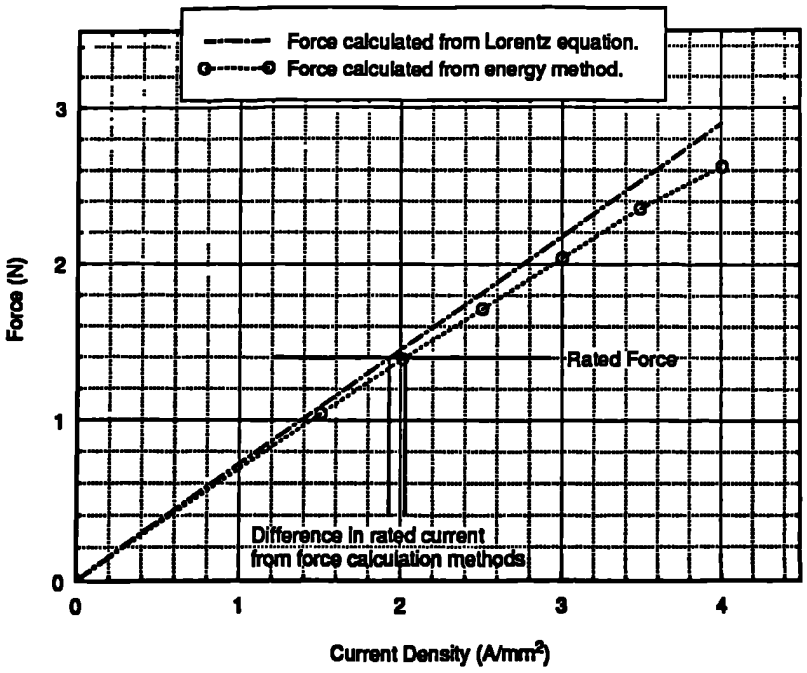

Fig 6.10 Comparison of the energy method and Lorentz equation force/current characteristics for VC1 actuator. Results are for the central stroke position.

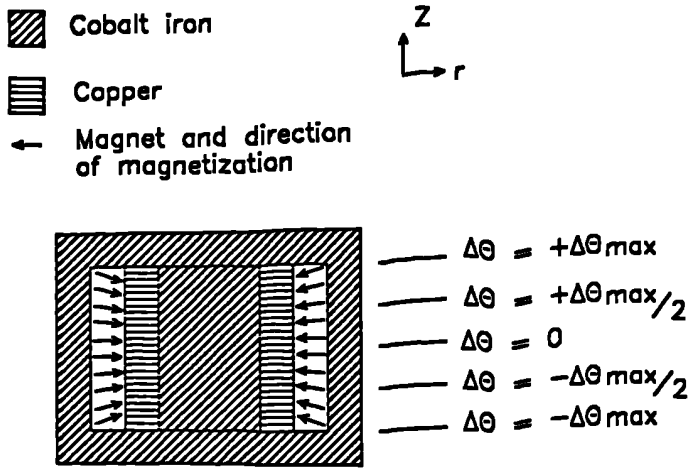

Fig 6.11 Schematic representation of the angular deviations from perfectly radial magnetization.

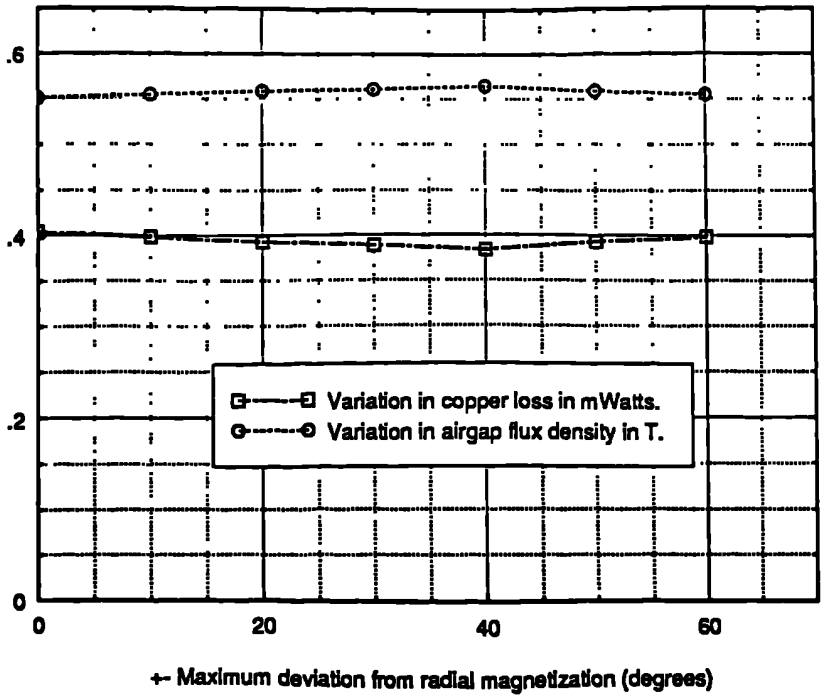

Fig 6.12 Variation of B_g and copper loss with maximum deviation from perfectly radial magnetization.

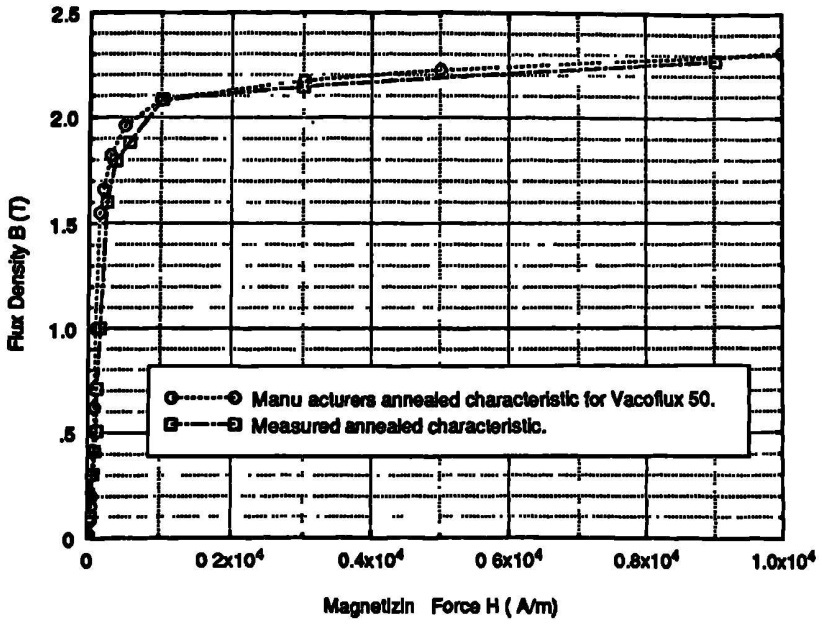

Fig 6.13 Measured a p b ed inı al B/H characteristics of Vacoflux 50 cobalt steel. An 180-turn excıtation c l was used to obtain the measured ch cteris c.

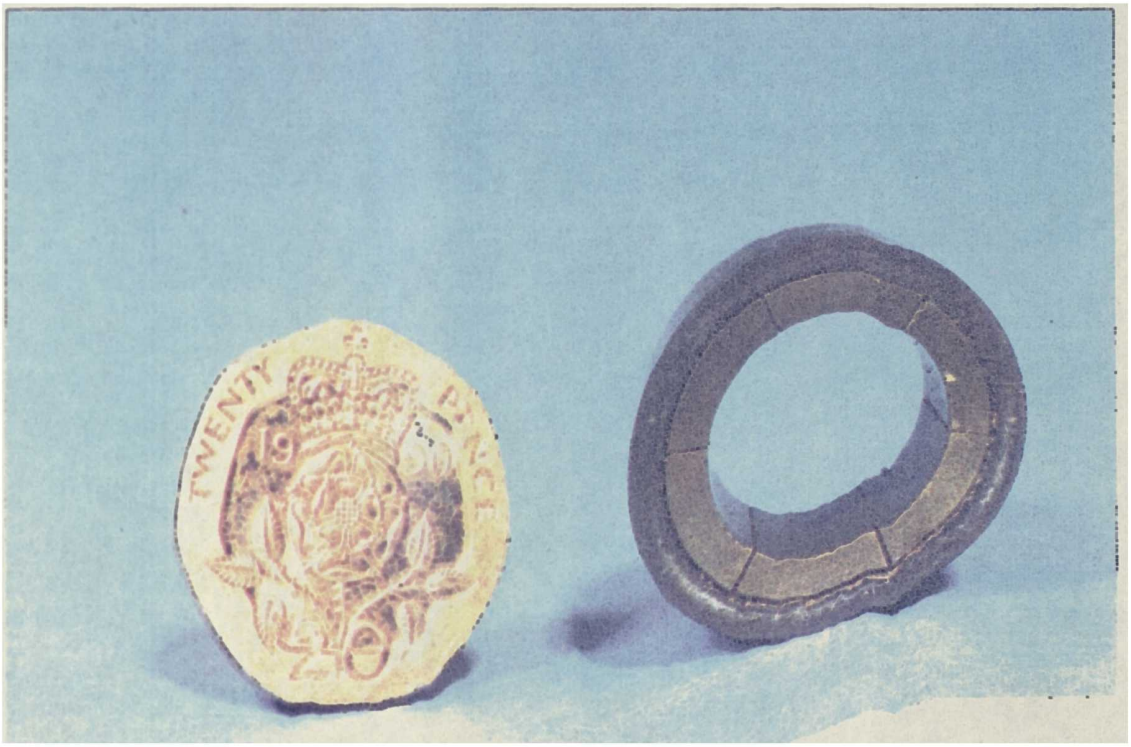

Fig 6.14 Photograph of the magnet segments used in the prototype actuator.

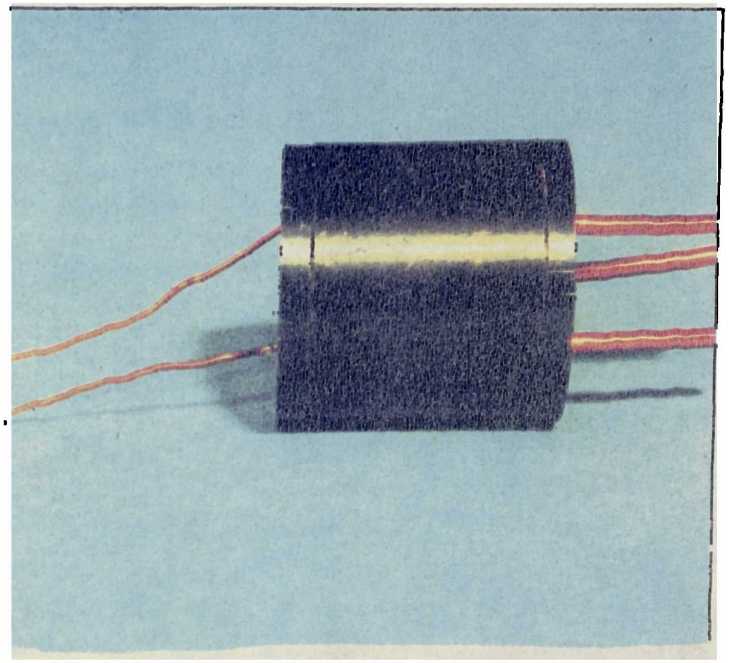

Fig 6.15 Photograph of the prototype actuator.

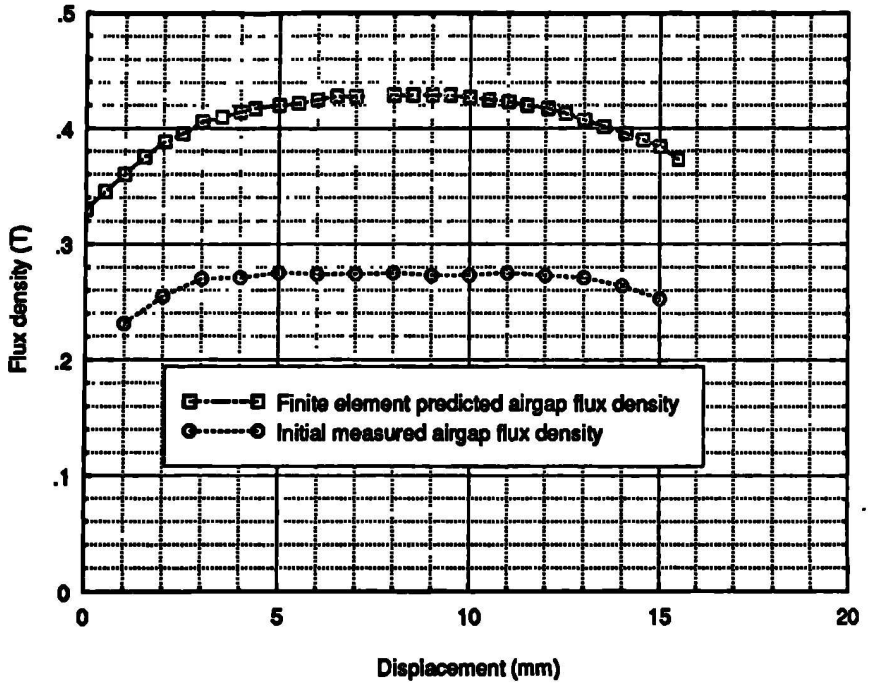

Fig 6.16 Comparison of the measured and predicted radial airgap flux density/displacement characteristics.

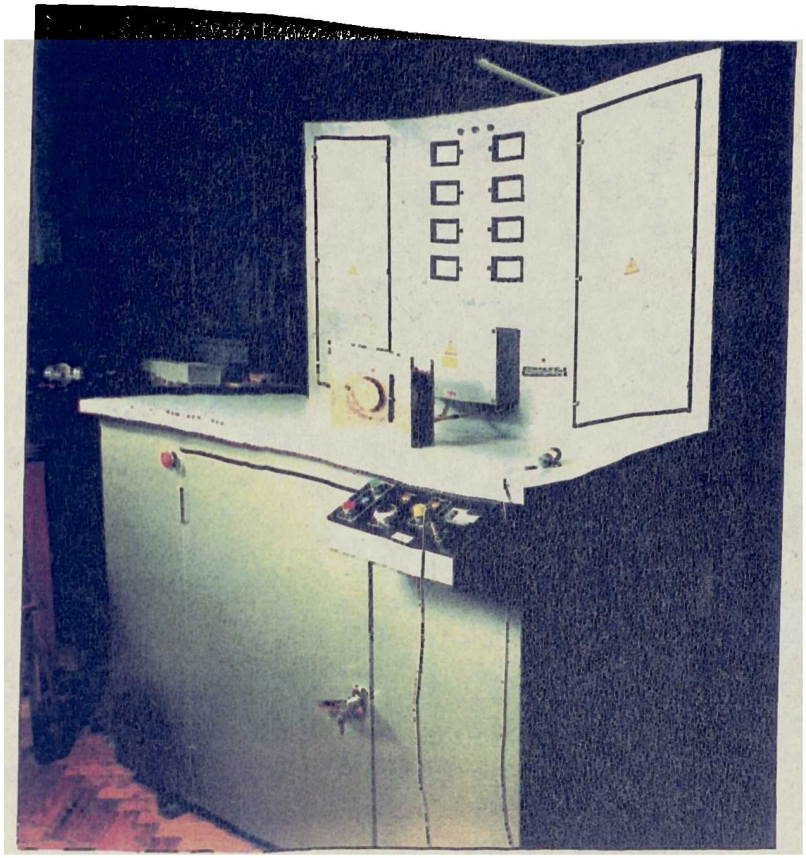

Fig 6.17 Photograph of the 14.2 kJ, 42500μF capacitor discharge magnetizer.

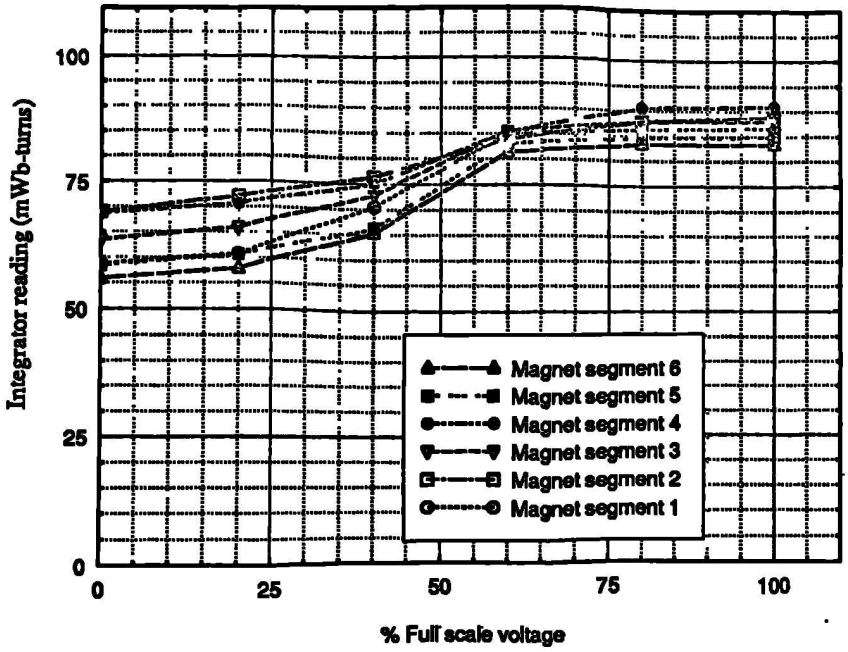

Fig 6.18 Helmholtz coil measurement of the flux from the magnet segments as as function of the magnetizing voltage.

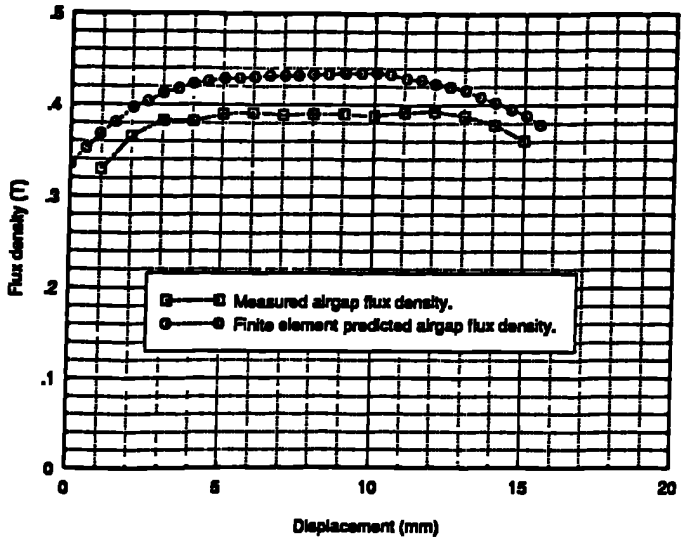

Fig 6.19 Measurement of the airgap flux density after remagnetization of the magnet segments

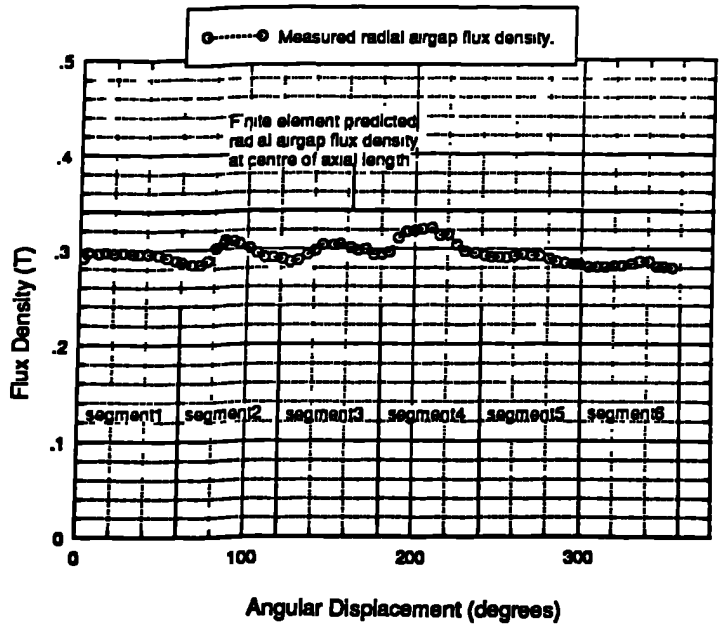

Fig 6.20 Measured and finite element predicted radial airgap flux density around the circumference of the airgap.

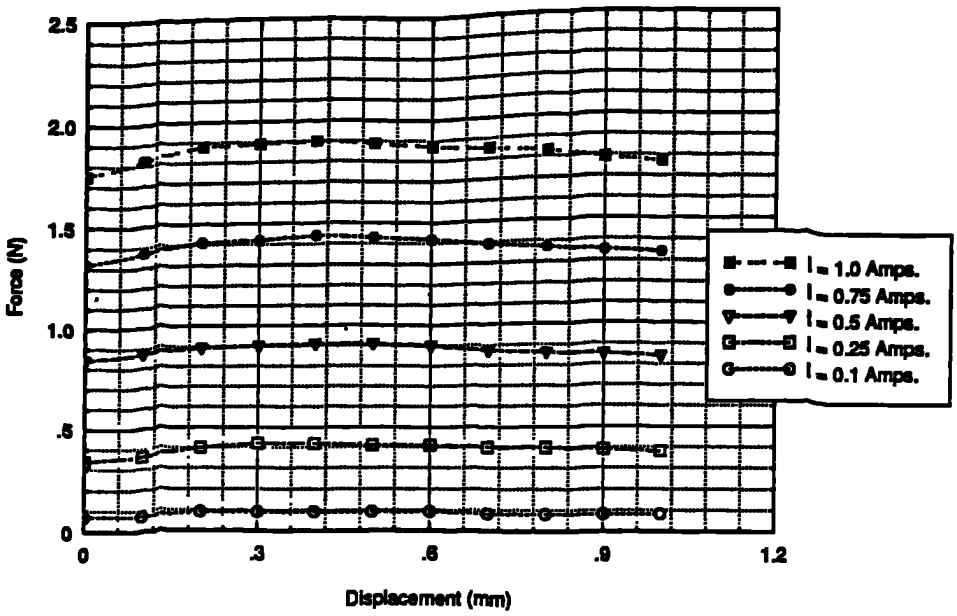

Fig 6.21 Comparison of the measured and finite element predicted force/displacement characteristics for different winding currents

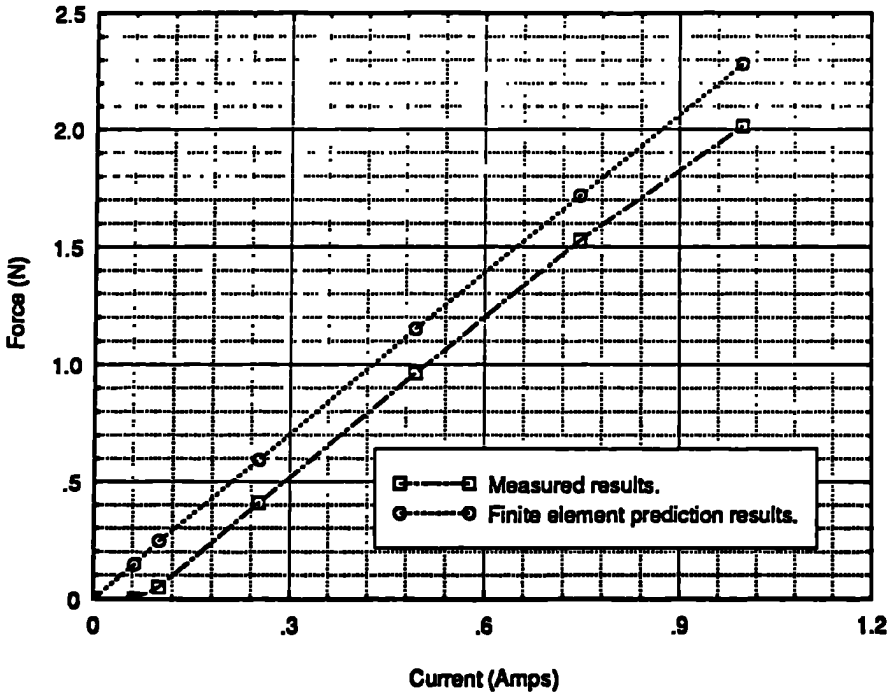

Fig 6.22 Comparison of the measured and finite element predicted force/current characteristics. The force was measured at the centre of the stroke.

CHAPTER 7

CONCLUSIONS

7.1 General Conclusions

Constrained and parameter scanning, single and multi-criterion optimization techniques have been utilised throughout this thesis for the design optimization of permanent magnet actuators, encompassing an automated lumped parameter field solution technique and graphical post-processing techniques. The lumped parameter technique has proven to be of sufficient accuracy to be applied to both the voice-coil and toroidally wound actuator topologies. One of the primary problems associated with the combination of iterative numerical lumped parameter techniques and optimization methods, that of obtaining solutions when there are negative values for the design variables, was overcome by not solving the network and subsequently increasing the value of the objective function by 5%, causing a departure from this non-feasible position. This specific increase in the objective function was determined, from the case study of chapter 3, to be the optimum in terms of the number of function evaluations.

Of the constrained optimization techniques developed in this thesis, the method which combined a Simulated Annealing algorithm to determine the usefulness of the initial starting position for the Alternating Directions method proved to be the most successful. This novel technique offers the robustness of the Flexible-Polyhedron/Flexible-Tolerance technique but requires far fewer objective function evaluations before converging on the global minimum.

The multi-criterion techniques investigated in chapter 4 improve the quality of information available to the design engineer when more than one objective function requires consideration. Although all the methods are computationally demanding, their use still offers a reduction in effort and expense in comparison with 'trial-and-error' design methods. All the multi-criterion techniques discussed have their advantages and disadvantages, depending upon the number and sensitivity of the objective functions. However, if there are more than two objective functions of interest, then it is advised that the Global-Criterion method be used, as this may obtain an acceptable design in the shortest possible computation time and that the scalar weighting technique be used for two objective functions with all the others incorporated as flexible inequality constraints. The results from these two investigations should produce an optimum design for any combination of the weightings required on the functions.

The optimization of the toroidally wound rotating magnet actuators of chapter 5 illustrated the effectiveness of the optimization procedures, since all the techniques obtained significant improvements compared with the commercial specification for both the maximization of the torque/inertia and torque/amp ratios. For example within a single design it was possible to obtain improvements of 271% and 33% for the torque/inertia and torque/amp respectively. The experimental results showed that the calculation of the excitation torque using the Lorentz equation, using the averaged airgap flux density obtained from the lumped parameter solutions, was of sufficient accuracy to predict the global parameters of the device.

In chapter 6 the optimization of a voice-coil actuator for minimum copper loss was required to meet a demanding specification. The preferred use of PrFeB at liquid helium temperature was demonstrated, since the material, in contrast with SmCo and NdFeB, did not suffer from a spin reorientation to reduce its maximum energy-product. The optimization studies illustrated that a closed magnetic circuit topology was preferred for this application since the minimization of the circuit reluctance resulted in high radial airgap flux densities and hence lower copper losses. In addition, with improved materials technology, it may be possible to further reduce the copper loss by using ring magnets

with angles of magnetization away from the preferred radial direction. Theoretically, this has been shown to produce a 5.7% reduction in the copper loss when producing a force of 1.4N. Nevertheless, before the device can meet the specification the reduction in the magnetization of the material, probably caused by surface grinding, must be overcome.

7.2 Further Work

This thesis has demonstrated the utility of both constrained and parameter scanning optimization, used in conjunction with a non-linear field solution technique, to aid the design of limited motion actuators. The techniques developed have been applied to two actuator topologies for which a number of single-criterion and multi-criterion optimized designs have been produced which either meet or substantially improve existing specifications. To date however, only the magnetostatic performance has been considered, its calculation being performed by algebraic, lumped parameter and finite element techniques. Further work in this area should concentrate on a coupled system simulation/optimization program, since for many applications it is the dynamic performance at the system level which is of the most relevance. For actuator topologies such as impacting solenoids, the static optimum design often has to be sacrificed for one with a superior dynamic performance.

Further, the use of coupled lumped parameter/finite element techniques to obtain the field solution requires investigation, since for some applications the use of lumped parameter models alone does not give sufficiently accurate results. For example the Law's Relay is a device whose performance under severe saturation requires accurate analysis if optimization is to be performed upon the topology.

In this thesis it has been necessary to employ comparitive temperature rise predictions. Absolute temperature rise predictions, encompassing the required dynamic performance and iron loss mechanisms needs further detailed investigation.

REFERENCES

1.1) Wolber W.G, 'An overview of automotive control actuators', Soc. Automotive Engineers, Paper 840306, 1984.

1.2) Bulton D.J, ' A loudspeaker motor structure for very high power handling and high excursion' Journal of Audio Engineering Society, Vol 36, No. 10, 1988.

1.3) Pembridge P, Anayi F.J., and Basak A., 'DC linear stepping motors', Proc. of the 25th Universities Power Engineering Conference, Aberdeen, Sept. 1990.

1.4) Yamada H, Nirei M, Ota M, Kawakatsu K, Nakajima T, Yamamoto Y, Karita M and Maruyama T, 'Development of a linear electromagnetic actuator for implantable artificial heart', I.E.E.E. Translational Journal on Magnetics in Japan, Vol 4, No. 9, 1989.

1.5) Brosens P.J, 'Fast response optical scanning', Electro-optical Systems Design, April 1971.

1.6) Warring R H, 'Hydraulic Handbook - 8th edition', Trade and Technical Press.

1.7) 'The piezoelectric travelling wave motor', Design Engineer, pp 36-40, Jan 1991.

1.8) 'The Micro-push Motor', 2nd Symposium on Electrical Drives, Sept. 1991, Philips Research Laboratories, Eindhoven.

1.9) Aksinin V.I, Apollonov V.V, Borodin V.I, Brynskikh A.S, Chetkin S.A, Murav'ev S.V, Ostanin V.V, and Vdovin G.V, 'Spring type magnetostriction actuator based on the Wiedemann effect', Sensors and Actuators, A21-A23, 1990, pp 236-42.

1.10) Bullough W.A., Firoozian R.G, Johnson A.R., Sianaki A.H, and Makin J, 'The elector-rheological catch/latch/clutch', Proc. I.Mech.E., Eurotech, June 1991.

1.11) Lequesne B, 'Fast-acting, long stroke bistable solenoids with moving permanent magnets', I.E.E.E Trans. on Industry Applications, Vol 26, No. 3, 1990.

1.12) Seilly A.H, 'Helenoid actuators - A new concept in extremely fast acting solenoids', Soc. Automotive Engineers, Paper 790119, 1979.

1.13) Westbrook M H, 'Future developments in automotive sensors and their systems', Journal Phys. E. Sci. Instum., Vol 22, No 9, pp 693-699, 1989

1.14) Chitayat A, and Tal J, 'Linear actuators provide fast and precise motion', Proceedings of MOTOR-CON, Sept. 1987.

1.15) Widdowson G.P., 'The analysis and synthesis of linear voice-coil actuators', Internal report, Dec. 1989.

1.16) Wagner J.A, 'The shorted turn in the linear actuator of a high performance disc drive', I.E.E.E. Trans. on Magnetics, Vol 18, No. 6, 1982.

1.17) Cory B.J, 'Expert systems for power applications', I.E.E.E. Review, April 1988.

1.18) Appelbaum J, Khan I.A and Fuchs E.F, 'Optimization of three-phase induction motor design. Part ii: The efficiency and cost of an optimal design', I.E.E.E. Trans. on Energy Conversion, Vol 2, No. 3, 1987.

1.19) Appelbaum J, Fuchs E.F and White J.C, 'Optimization of three-phase induction motor design. Part i: Formulation of the optimization technique', I.E.E.E. Trans. on Energy Conversion, Vol 2, No. 3, 1987.

1.20) Menzies R.W. and Neal G.W, ' Optimization program for large-induction-motor design', Proc. I.E.E.E. Vol 122, No. 6, 1975.

1.21) Nurdin M, Poloujadoff M and Faure A, 'Synthesis of squirrel cage motors: A key to optimization', I.E.E.E. Trans. on Energy Conversion, Vol6, No.2, 1991.

1.22) Erlicki M.S. and Appelbaum J, 'Optimized parameter analysis of an induction motor', I.E.E.E. Trans. on Power Apparatus and Systems, Vol 84, No 11, 1965.

1.23) Watterson P A., Zhu J.G and Ramsden V.S, 'Optimization of permanent magnet motors using field computations of increasing precision.', I.E.E.E. Trans. on Magnetics, Vol 28, No. 2, 1992.

1.24) Leu M.C, Scorza E.V and Bartel D.L, 'Characteristics and design of variable airgap linear force motors', I.E.E. Proc. B. Vol 135, No. 6, 1988.

1.25) Anderson O.W., 'Optimized design of electrical power equipment', Trans. I.E.E.E. Computer Applications in Power, Jan 1991.

1.26) Kirkpatrick S, Gellat Jr. C.D, and Vecchi M.P, 'Optimization by Simulated Annealing', Science, Vol 220, No. 4598, pp 671-680, 1983.

1.27) Jinguan G.L, 'Multiple-objective problems: Pareto optimal solutions by method of proper equality constraints', I.E.E.E. Trans. on Automatic Control, Vol 21, No. 5, 1976.

1.28) Korhonen P, and Soisomaa M, 'An interactive multiple criterion approach to ranking alternatives, Journal Opl. Research Society, Vol 32, pp 577-585, 1981.

1.29) Osyczka A, 'An approach to multicriterion optimization problems for engineering design', Computational Methods in Applied Mechnanics and Engineering, Vol 15, pp 309-333, 1978.

1.30) Nyce A.C., 'State of the Industry', Proceedings of the Gorham Advanced Materials Institute Permanent Magnet Design Short-Course and Exhibition, Rosemont, Illinois, May-June, 1992.

1.31) Steinhirstt M, Ederling G, Oberste-Ufer G, and Eggert H, 'Improved NdFeB alloys via the R/D route developed by Th. Goldschmidt', Proceedings of the Gorham Advanced Materilas Institute Technical Conference and Exhibition on Reassessing the Business oppotunity, Markets and Technology for Neodymium Iron Boron Permanent Magnets, Orlando, Florida, Feb 16-19, 1992.

1.32) Takeshita T, 'Preparation of NdFeB anisotropic magnet powders produced by HDDR process and bonded magnets made from them', Proceedings of the Gorham Advanced Materilas Institute Technical Conference and Exhibition on Reassessing the Business oppotunity, Markets and Technology for Neodymium Iron Boron Permanent Magnets, Orlando, Florida, Feb 16-19, 1992.

1.33) Boltich E.B, Sankar S.G, 'Lightweight permanent magnet actuators and manipulators', Final report on contract number NAS8-38044, July 1989.

1.34) Himsworth F R, Spendley W, and Hext G R, 'The sequential application of simplex designs in optimization and evolutionary operation', Technometrics, Vol 4, 1962.

1.35) Hooke R and Jeeves T.A, 'Direct search solution of numerical and statistical problems', J. Assoc. Comp. Mach., 8, 221-230.

2.1) Smith A.C. and Appel L.C, 'Determining the maximum thrust of a permanent-magnet linear actuator', Proc. Third Int. Conf. on Electrical Machines, 1987.

2.2) Gottvald A, 'Global optimization methods for computational electromagnetics', I.E.E.E. Trans. on Magnetics, Vol 28, No. 2 1992.

2.3) Marienescu M and Marienescu N, 'Numerical computation of torques in permanent magnet motors by Maxwell Stress and energy method', I.E.E.E. Trans. on Magnetics, Vol 24, No. 1, 1988.

2.4) Rotors H.C., 'Electromagnetic Devices', 3rd Edition, New York, Wiley, 1967.

2.5) Parker R.J and Studders R.J., 'Permanent magnets and their application', Wiley and Sons, New York, 1962.

2.6) Honds S.L, and Meyer K.H, 'A linear D.C. motor with permanent magnets' Phillips Techical Review, 40, 329-337, 1982

2.7) Chai H.D, 'Permeance based step motor model revisited', MOTION, March/April 1986 pp14-28

2.8) Mizia J, Admaik K A, Eastham A R, and Dawson G E, 'Finite element force calculation comparisons of methods for electrical machines', I.E.E.E. Trans. on Magnetics, Vol 24, No. 1, 1988.

2.9) McFee J, and Lowther D A, 'Towards accurate and consistent force calculation in finite element based computational magnetostatics', I.E.E.E. Trans. on Magnetic, Vol 23, No. 5, 1987.

3.1) Davidon W.C, 'Variable metric method for minimization', A.E.C. Research and Development Report, ANL-5990, 1959.

3.2) Fletcher R. and Reeves C.M, 'Function minimization by conjugate gradients', The Computer Journal, No. 10, 1968.

3.3) Rosenbrock H, 'An automatic method for finding the greatest or least value of a function', The Computer Journal, Vol 3, 1960.

3.4) Fletcher R and Powell M.J.D, 'A rapidly convergent descent method for minimization' The Computer Journal, Vol 6, 1963.

3.5) Aarts E. and Korst , 'Simulated Annealing and Boltzmann machines', Wiley ans Sons, 1989.

3.6) Powell M.J.D, 'An efficient method of finding the minimum of a functional of several variables without calculating derivatives', The Computer Journal, Vol 7, 1964.

3.7) Himmelblau D.M, 'Applied nonlinear programming', McGraw-Hill, New York, 1973.

3.8) Widdowson G.P, Howe D. and Evison P.R, 'Computer aided optimization of rare earth permanent magnet actuators', Proc. I.E.E. Computation in Electromagnetics, Publication No. 350, 1991.

3.9) Boules N, 'Design optimization of permanent magnet DC motors', I.E.E.E. Trans. on Industry Applications, Vol 26, No. 4, 1990.

3.10) Juffner M, and Heine G, 'Linear DC motor optimization used in disc drives. Proc. of 15th Annual Symposium on Incremental Motion Control Systems and Devices.

3.11) Drago G, Manella A, Nervi M, Repetto M, and Secondo G, 'A combined strategy for optimization in non-linear magnetic problems using Simulated Annealing and search techniques', I.E.E.E. Trans on Magnetics, Vol 28, No2. 1992.

3.12) Friedland N. and Adam D, 'Automatic ventricular cavity boundary detection from sequential ultrasound images using Simulated Annealing', I.E.E.E. Trans. on Medical Imaging, Vol 8, No. 4, 1989.

3.13) Kearfott K.J. and Hill S.E, 'Simulated Annealing image reconstruction method for a Pinhole Single Photon Emission computed tomography (S.P.E.C.T.)', I.E.E.E. Trans. on Medical Imaging, Vol 9, No. 2, 1990.

3.14) Smith W E, Paxman R G, andd Barrett H H, 'Application of Simulated Annealing to coded-aperture design and tomographic reconstruction', I.E.E.E. Trans. on Nucl. Sci., Vol 32, pp 758-761, 1985.

3.15) Trussell H J, Orun-Ozturk H, and Cirvanlar M R, 'Errors in re-projection methods in computerized tomography', I.E.E.E. Trans. on Medical Imaging, Vol 6, pp 220-227, 1987.

3.16) Apostolov R and Petkov N, 'Approaches fpr optimal design of brushless DC motors', Scientific Session of HEMI, Sofia, 1989.

3.17) Nedler J.A. and Mead R, 'A Simplex method for function minimization', The Computer Journal, Vol 7, 1965.

3.18) Subrahmanyam M.B, 'An extension of the Simplex method to constrained nonlinear optimization', Journal of Optimization Theory and Applications, Vol 62, No. 2, 1989.

3.19) Box M.J, 'A new method of constrained optimization and a comparison with other methods', The Computer Journal, Vol 8, 1965.

3.20) Press W.H, Flennery B.P, Teukolsky S.A and Vetterling W.T, 'Numerical Recipes in C', Cambridge, Cambridge University Press, 1986.

3.21) Dimarogonas A, 'Computer aided machine design', Prentice-Hall, 1989.

3.22) Greene J.W, and Supowit K.J, 'Simulated Annealing without rejected moves', I.E.E.E Trans. on Computer Aided Design, Vol CAD-5, No1, 1986.

3.23) Cerny V, 'Thermodynamic approach to the Travelling Salesman problem: An efficient Simulated Annealing algorithm', Journal of Optimization Theory and Applications, Vol 45, No1, 1985.

3.24) Feller W, 'An introduction to probability theory and applications', J.Willey, 3rd Edition, 1970.

3.25) Szu H. and Hartley R, 'Fast Simulated Annealing', Physics Letters A, Vol 122, No. 3,4, 1987.

3.26) Romeo F, Snagiovanni-Venentelli A. and Sechen C, 'Research on Simulated Annealing at Berkley', I.E.E.E. Comput. SOc. Press 1984, pp 652-657.

3.27) White S.R, 'Concepts of scale in Simulated Annealing', I.E.E.E. Comput. Soc. 1984 pp 646-651.

3.28) Huang M.D, Romeo F. and Sangiovanni-Vincentelli A, 'An efficient general cooling schedule for Simulted Annealing', I.E.E.E. Comput. Soc. Press, Nov 1986, pp 381-384.

4.1) Osyczka A. 'Multicriterion optimization in science and engineering', Prentice-Hall, 1989

4.2) Russenchuk S, 'Application of Lagrange Multiplier estimation to the design optimization of permanent magnet synchronous machines', I.E.E.E. Trans. on Magnetics, Vol 28, No. 2, 1992.

4.3) Lee S.M, 'Goal programming methods for decision analysis', Auerbach Publishers, Philadelphia, Pennsylvania.

4.4) Walz F.M, 'An engineering approach: Hierarchial optimization criteria', I.E.E.E. Trans. on Automatic Control, AC-12, 1967.

4.5) Zionts S and Wallenius J, 'An iterative programming method for solving the multiple criteria problem', Mgmt. Sci., 22, 6, 632-663.

4.6) Jutler H, 'Linear model with several objective functions', Ekonomika i Matematiceckije Metody, Vol 3, No. 3, 1967.

4.7) Boychuk L.M and Ovchannikov V.O, 'Principal methods of solution: Multicriterion optimization problems (survey)' Journal of Soviet Automatic Control, 6-1-4, 1973.

5.1) Dawson C and Bolton H.R, 'Limited motion rotary actuators of the toroidal-stator, permanent magnet rotor type', I.E.E. Proc. B, Vol 129, No.4 1982.

5.2) Dawson C and Bolton H.R, 'Design of a class of wide-angle limited-rotation rotary actuators', I.E.E. Proc. B, Vol 126, No. 4, 1979.

5.3) Hightech Components Limited, 'Advanced servocomponents for British industry' (Sales literature).

5.4) Bowmar/Harowe, 'Brushless torque motors for limited angle applications' (Sales literature).

5.5) Inland Motor, 'Speciality products division' (Sales literature).

5.6) Fleisher W A, 'Brushless motors for limited rotation', Machine Design, Dec. 1989.

5.7) Bolton H.R and Shakweh Y, 'Performance prediction of Law's relay actuator', Proc. I.E.E. B, V 137, No. 1, 1990.

6.1) Stier M, Duffy M, Gullapalli S, Rockwell R, Sileo F and Krim M, 'I.E.E.E. Trans. Nucl. Sci, 36, 903, 1989.

6.2) Simizu S, Personal Communications.

A.1) Vacuumsmeltze, Gruner Weg, Hannau, Germany 'Soft Magnetic Material', (Sales Literature).

A.2) Telcon, Napier Way, Crawley, West Sussex, 'Speciality Alloys and Components - Cobalt iron Alloys'. (Sales Literature).

A.3) Metglass, Parsippany, New Jersey, USA, 'Magnetic Alloys, Technically Superior' (Sales Literature).

Appendix A

GLOSSARY OF TERMS

A.1 Permanent Magnets

The potential usefulness of a permanent magnet material can be judged on the basis of a number of criteria related to its hysteresis loop. The normal and intrinsic hysteresis loops of a permanent magnet are shown in fig(A.1). The normal characteristic shows the total flux density B as a function of the magnetizing field strength H, where B is the resultant of the intrinsic polarization J and the applied field(self-demagnetization plus applied field).

The important features are:

Saturation - The value of magnetizing force required to fully align the domains of a permanent magnet corresponding to point A on fig(A.5). The increase in flux density, when a higher magnetizing force is applied, is equal to the increase which could be obtained in air.

Remanence, B_r - After the magnet has been fully magnetized to saturation its working point follows the hysteresis loop and the remanent flux density, when the field strength is zero, is point B on fig(A.5).

Normal Coercivity, H_{cn} - This is the value of the magnetic field strength at which the flux density is zero, and is point C on fig(A.5).

Intrinsic Coercivity, H_{ci} - This is the value of the magnetic field strength at which the polarization is zero and is point D in fig(A.5).

Maximum Energy-Product BH_{max}- This is the working point on the second quadrant of the major hysteresis loop at which the BH product is a maximum. For a magnet having a linear second quadrant characteristic the maximum energy-product corresponds to the point $\frac{B_r}{2}$, $\frac{H_{cn}}{2}$. Table (A.1) gives values for the remanence, normal coercivity and maximum energy-product for a range of permanent magnet materials.

Recoil Permeability μ_r- The slope of the major hysteresis loop at remanence is given by $\mu_o \mu_r$, . For a magnet which exhibits a linear demagnetization characteristic μ_r is the slope of the characteristic, and varies between 1.05 -> 1.20 for the rare-earths and ferrite materials.

Temperature coefficients , τ_b , τ_{hci} - Two temperature coefficients are usually quoted, for the remanence and coercivity. NdFeB has relatively high temperature coefficients and fig(A.2) shows the effect that increasing the temperature has on the intrinsic and normal characteristics of a typical commercial grade of NdFeB. Due to the reduction in the magnetic performance, especially the value of the intrinsic coercivity, and increased likelihood of irreversible demagnetization, NdFeB is not suitable for applications above 150 ^{o} C. SmCo, on the other hand has low values for both *temperature coefficients, as* shown in table(A.1), and is therefore suitable for high temperature applications.

Curie temperature - This is the temperature to which the permanent magnet can be raised before becoming non-magnetic. NdFeB has a comparatively low Curie temperature of ~ 310^oC whilst the Curie temperature for $Sm_2 Co_5$ is much higher at ~700^o C. Table(A.1) shows the values for a range of materials.

Armature Reaction Effects - In permanent magnet devices there may be a reversible or irreversible loss of flux due to external applied fields caused by'armature reaction' effects as illustrated in fig(A.3). On open-circuit, all parts of a magnet may be assumed to be operating at a single working point, A, although this is strictly true only for elliptical

magnet geometries. If the magnet is exposed to an armature reaction field, then parts of it will be subjected to a demagnetizing component of mmf, which drives its working point down the major magnetization curve, to point B for example, whilst other parts will be subjected to a pro-magnetizing mmf, which may drive its working point into the first quadrant, to point C, for example, If the maximum demagnetization field to which the magnet is subjected is sufficiently high to drive some of the working points beyond the linear portion of the demagnetization curve then when the mmf is then removed, different parts of the magnet will recoil along minor recoil loops which can be approximated by recoil lines parallel to the major hysteresis loop at B_r. Thus parts of the magnet whose working point did not leave the linear section of the demagnetization curve during exposure to the armature reaction field, will essentially recoil to the original working point A, whilst parts whose working point was driven beyond the linear section will recoil from a point such as B to a point $\overline{A}$, which is within the major characteristic. As a result the total flux from the magnet will have been reduced, and can only be recovered by remagnetization of the magnet. However, irreversible demagnetization can be prevented by the judicious choice of magnet material and leading dimensions, particularly the thickness of the magnet L_m. It will also be seén from fig(A.3) that temperature effects can severely reduce the maximum demagnetization mmf which a magnet can withstand before the onset of irreversible demagnetization. For high coercivity rare-earth magnets having a linear second quadrant demagnetization characteristic a smaller length of magnet in the direction of magnetization is required to avoid irreversible demagnetization.

Property	Hard Ferrite	*SmCo5*	NdFeB	AlNiCo-8
Remanence (T)	0.4	0.92	1.2	0.82
Coercivity (kA/m)	-250	-700	-900	-160
Energy-Product (kJ/m^3)	25.0	161.0	270.0	20.6
Rev. Temp. Coeff τ_b .(%K)	-0.20	-0.04	-0.10	-0.013
Rev. Temp. Coeff τ_{hci} .(%K)	+0.35 -> +0.4	-0.05	-0.3 -> -0.6	-0.02
T_{max} Cont. ($^\circ C$)	150-200	250	100-200	520
Curie Temp ($^\circ C$)	450	700	310	890
Density (Kgm^{-3})	4500	8300	7500	7260

Table A.1 Characteristic properties of permanent magnet materials.

A.2 The Use of Soft Magnetic Steels

Special magnetic steels, with a high saturation flux density and/or a low hysteresis loss, can often be used to extract greater leverage from high energy-product rare-earth magnets. Fig(A.4) shows the first quadrant magnetization characteristics for various magnetic materials including mild steel[A.1-A.3]. A major drawback to the widespread use of the highest grade materials is their relatively high cost and poor machinability which generally restricts them only to applications having the most demanding specifications. Most steel alloys require annealing after being machined or ground, usually in a high temperature vacuum or hydrogen atmosphere, in order to obtain their full magnetic properties, which can be both expensive and time consuming.

A.3 Optimization

Objective Function, f(x) is a parameter to be minimized which is made up of the independent variables.

Equality Constraint, h(x) is a constraint in the optimization when one or more variables are equal to a specific value.

Inquality Constraint, g(x) is a constraint in the optimization when one or more variables are greater or less then to a specific value.

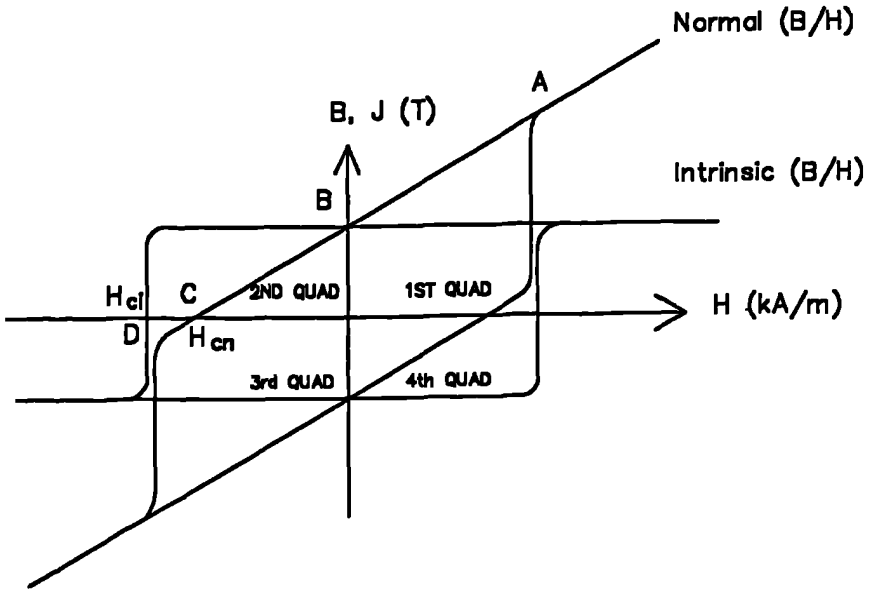

A.1 Typical normal and intrinsic permanent magnet characteristics.

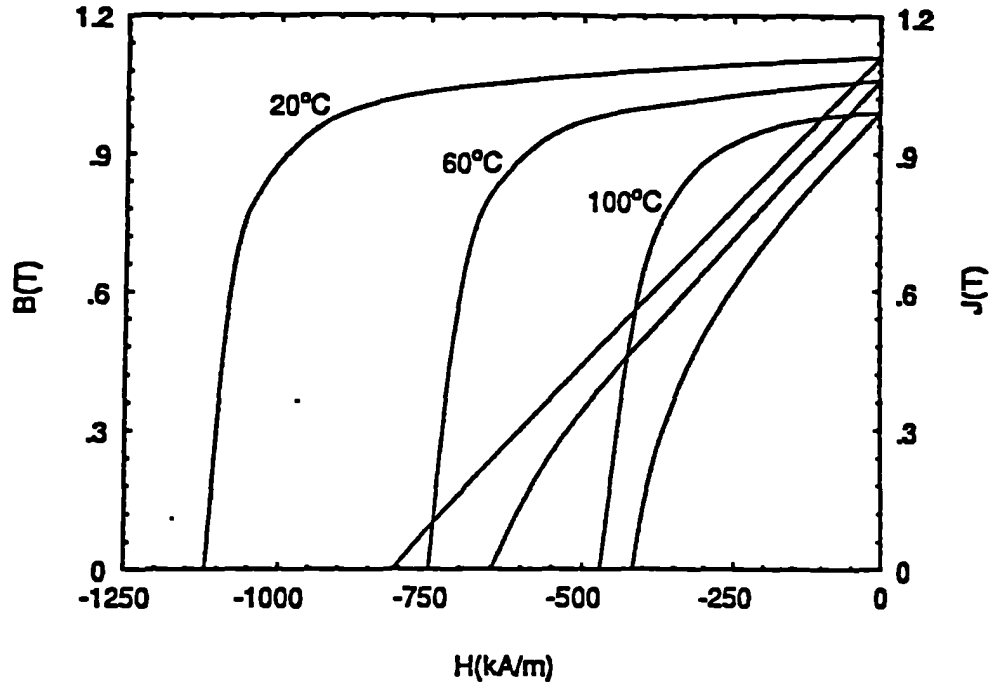

A.2 Effect of temperature on the demagnetization characteristic of sintered NdFeB.

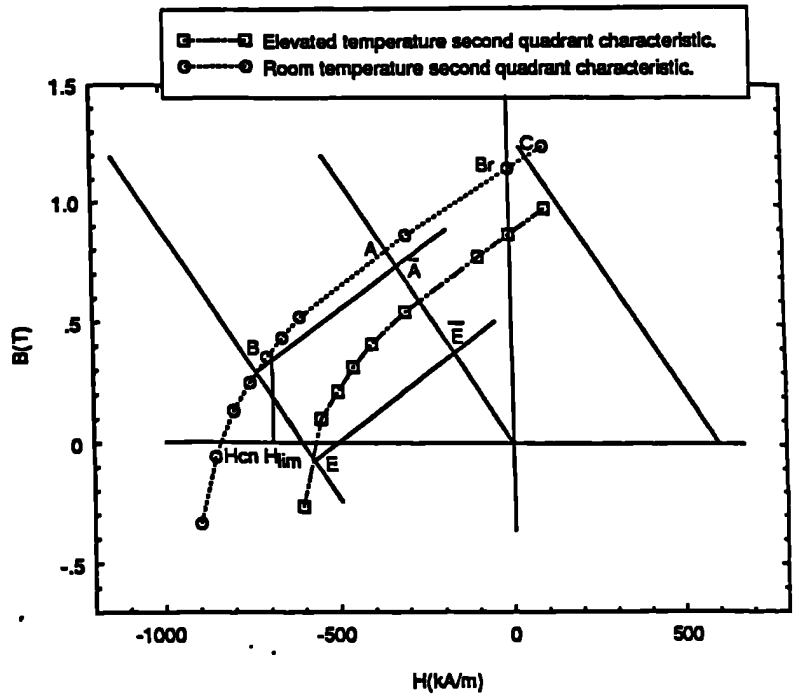

A.3 'Armature reaction' effects on demagnetization.

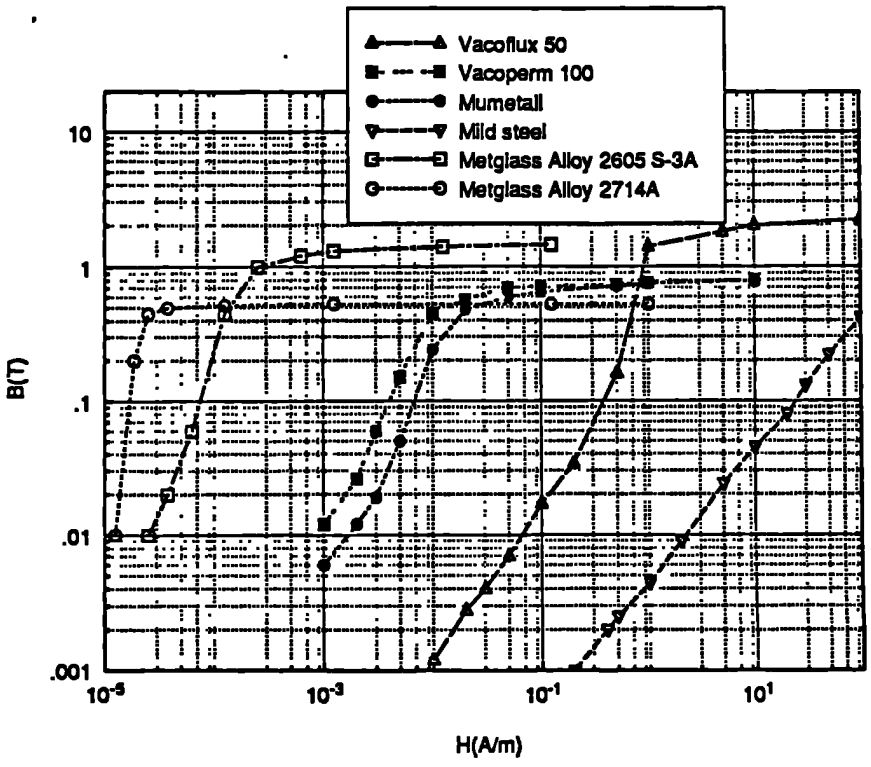

A.4 Initial magnetizing B/H characteristics for soft magnetic steels.

APPENDIX B

PERMEANCES OF PREDOMINANT FLUX PATHS

Fig (B.1) illustrates some of the predominant flux paths in electrical machines

Permeance of fig(B.1.1)

$$\Phi = \int\int B\,dA = \int_0^x\int_0^y = B\,x\,y$$

$$B = \frac{\Phi}{x\,y}$$

$$F = \int H.\,dl = \int_o^g H\,dl = \int_0^g \frac{B}{\mu_0}\,dl = \int_o^g \frac{\Phi}{\mu_0\,x\,y}\,dl = \frac{\Phi\,g}{\mu_0\,x\,y}$$

$$P = \frac{\Phi}{F} = \frac{\mu_0\,x\,y}{g}$$

Permeance of fig(B.1.2)

$$F = \int H.\,dl = \int_0^{\pi} Hr\,d\theta = H\,r\,\pi$$

$$H = \frac{F}{r\,\pi}$$

$$\Phi = \int\int B\,dA = \int_o^y \int_{\frac{g}{2}}^{\frac{g}{2}+w} B\,dx\,dr = \int_0^y \int_{\frac{g}{2}}^{\frac{g}{2}+w} \mu_0 H\,dx\,dy = \frac{\mu_0 y}{F}\int_o^y \int_{\frac{g}{2}}^{\frac{g}{2}+w} \frac{dx\,dr}{r}$$

$$= \frac{\mu_0\,y\,F}{\pi}\left[ln\,(r)\right]_{\frac{g}{2}}^{\frac{g}{2}+w} = \mu_0\,y\,F\left[\ln\left(1+\frac{2w}{g}\right)\right]$$

$$P = \frac{\Phi}{F} = \frac{\mu_0\,y}{\pi}\left[ln\left(1+\frac{2w}{g}\right)\right]$$

Permeance of fig(B.1.3)

$$Vol = \frac{1}{4}\frac{\pi g^2 y}{4} = \frac{\pi g^2 y}{16}$$

As before $A_{mean} = \frac{g y}{\pi}$

Therefore $l_{mean} = \frac{Vol}{A}mean = \frac{\pi g^2 y}{\pi}\frac{\pi}{g y} = \frac{\pi^2 g}{16}$

$$p = \frac{\mu_0 A_{mean}}{l_{mean}} = \frac{\mu_0 g y}{\pi}\frac{16}{\pi^2 g} = 0.516\,\mu_0 y$$

Permeance of fig(B.1.4)

$$\Phi = \int\int B\,dA = \int_0^{r}\int_0^{L} B\,\alpha\,dr\,dx = B\,\alpha\,r\,L$$

$$B = \frac{\Phi}{\alpha\,r\,L}$$

$$F = \int H.\,dl = \int_{r_i}^{r_o} H\,dr = \int_{r_i}^{r_o}\frac{B}{\mu_0}br = \frac{\Phi}{\mu_0\,\alpha\,L}\int_{r_i}^{r_o}\frac{1}{r}dr$$

$$= \frac{\Phi}{\mu_o\,\alpha\,L}[\ln(r)]_{r_i}^{r_o} = \frac{\Phi}{\mu_0\,\alpha\,L}[\ln(\frac{r_o}{r_i})]$$

$$p = \frac{F}{\Phi} = \frac{\mu_0\,\alpha\,L}{\ln(\frac{r_o}{r_i})}$$

Permeance of fig(B.1.5)

with $\alpha = 2\pi$

$$P = \frac{2\pi\mu_o L}{\ln(\frac{do}{di})}$$

Permeance of fig(B.1.6)

$$F = \int H.\,dl = \int_0^g H\,dl = H\,g$$

$$H = \frac{F}{g}$$

$$\varphi = \int\int B\,dA = E_0 \frac{p}{2} \int_0^{2\pi} B\,r\,d\theta\,dr = \frac{\mu_0 F}{g} \int_{2o}^{p\int_0^{2\pi} r\,dr\,d\theta}$$

$$= \frac{\mu_0 \pi d^2}{4g}$$

$$P = \frac{\Phi}{F} = \frac{\mu_0 \pi d^2}{4g}$$

APPENDIX C

SOLUTION OF NON-LINEAR MAGNETIC CIRCUITS

C.1 Non Linear Lumped Reluctance Modelling

In many devices in which the flux may be divided into fairly homogeneous regions it should be possible to develop an equivalent circuit consisting of mmf sources and reluctances as illustrated in fig(C.1). Each reluctance may be calculated from an associated area and length and material characteristic.

i.e. $$R_n = \frac{L_n}{\mu_n A_n} \qquad \text{(C.1)}$$

where μ_n is the permeability of the particular reluctance.

In the case of a non-linear material the permeability will be a function of the flux passing through the reluctance. Such an equivalent circuit may be described by a set of simultaneous equations as shown in fig(C.1), which for a linear device may be solved by Gaussian Elimination, for example, to give the flux in each element

i.e. $$[\Phi] = [R]^{-1}\,[F] \qquad \text{(C.2)}$$

For a non-linear device, an initial permeability may be assigned to each reluctance so that its value may be calculated. Then after solving the network equations the flux density and field intensity in each reluctance are given by

$$B_n = \frac{\Phi_{Rn}}{A_n} \tag{C.3}$$

$$H_n = \frac{\Phi_{Rn}}{\mu_n A_n} \tag{C.4}$$

where Φ_{Rn} is the flux passing through the reluctance.

The working point of each reluctance may then be compared with its material characteristic as shown in fig(C.2), and a new estimate of the permeability obtained. After having recalculated the value of each reluctance the set of simultaneous equations is then solved again, the iterative procedure being repeated until the required accuracy for the flux density and field intensity in each reluctance is acheived.

Several different algorithms for estimating updated values for the permeability may be used including Newton-Raphson techniques. However, the simplest, if not most economical, deduces the permeability from:

$$\mu_n' = \frac{B_n'}{H_n} \tag{C.5}$$

where B_n' is the flux density in the material characteristic corresponding to the calculated field intensity H_n, as shown in fig(C.2).

C.2 Cubic Spline Curve Fits

In order to solve non-linear problems it is necessary to represent the non-linearities by some form of curve fit. For most solvers it is imperative that the curve fit be continuous,

even up to the 2nd derivative, and also that the curve be monotonic. Also for the energy calculations it is a requirement that the curve be easily integrable.

Whilst numerical functions are available for modelling specific characteristics, a general approach which has been found to fulfil all the above requirements is to employ a cubic spline fit, in which each interval between successive data points are modelled by a cubic function of the form shown in fig(C.3).

For n data points the required 3(n-1) coefficients can be found by generating 3(n-1) independent equations from various constraints, viz:

i) the curve is continuous, (n-1) equations

$$y_{n+1} = A_n (x_{n+1} - x_n)^3 + B_n (x_{n+1} - x_n)^2 + C_n (x_{n+1} - x_n) + y_n \qquad (C.6)$$

ii) the first derivative of the curve is continuous, (n-2) equations,

$$C_{n+1} = 3 A_n (x_{n+1} - x_n)^2 + 2 B_n (x_{n+1} - x_n) + C_n \qquad (C.7)$$

iii) the second derivative of the curve is continuous, (n-2) equations

$$2 B_{n+1} = 6 A_n (x_{n+1} - x_n) + 2 B_n \qquad (C.8)$$

iv) the two additional constraints which define the end conditions of the curve where dy/dx = some specified gradient.

The 3(n-1) equations may be solved to give the required 3(n-1) coefficients.

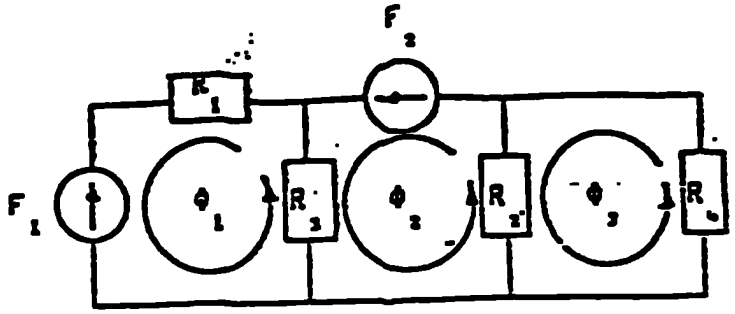

$$-F_1 = \Phi_1 (R_1 + R_3) - \Phi_2 (R_3) + \Phi_3 (0)$$

$$F_2 = \Phi_1 (R_3) - \Phi_2 (R_2 + R_3) + \Phi_3 (-R_2)$$

$$0 = \Phi_1 (0) + \Phi_2 (-R_2) + \Phi_3 (R_2 + R_4)$$

Fig C.1 Equivalent electromagnetic circuit

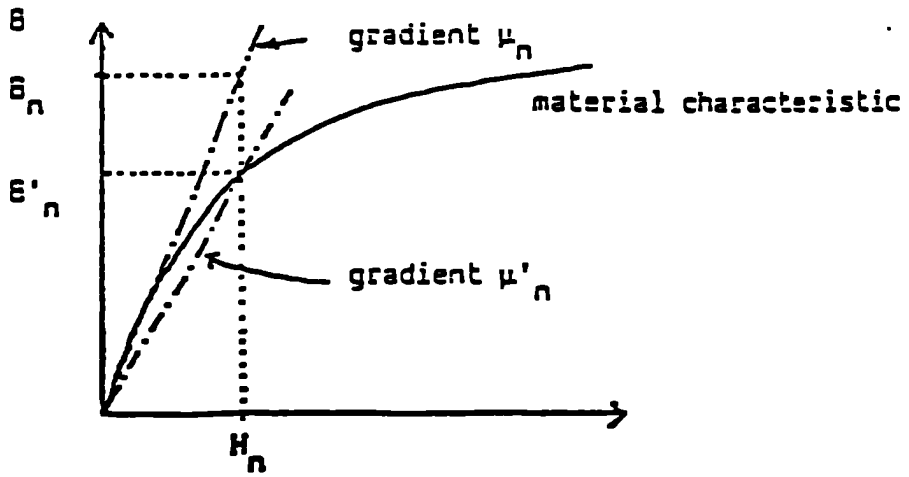

Fig C.2 Estimination of permeability

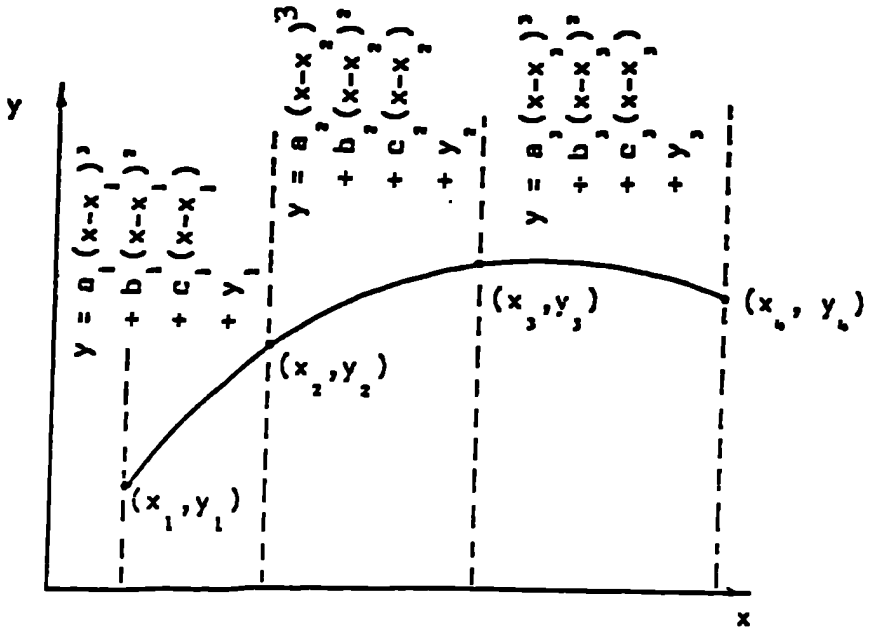

Fig C.3 Cubic spline curve fit

APPENDIX D

UNCONSTRAINED OPTIMIZATION BY THE FLEXIBLE TOLERANCE TECHNIQUE

It was described in chapter 3 that the search for a feasible vector of the independent variables is complete when the violation of the constraints t(x) is less than the current value for the tolerance φ. φ acts as a tolerance criterion for constaints violation throughout the search, and is also used as a termination value.

If the constraints are violated and $t(x) > \varphi$, then a new vector has to be established before an unconstrained search can be initiated. Once this vector has been established, then one stage of the optimization is said to be complete and the numerical value of φ can be computed so that it is non increasing and dependent upon the size of the polyhedron.

i.e. $$\varphi^{(k)} = \min \left(\varphi^{(k-1)}, \frac{(m+1)}{(r+1)} \sum_{i=1}^{r+1} | x_i{}^{(k)} - x_{r+2}{}^{(k)} | \right) \qquad (D.1)$$

The initial value of φ, i.e. $\varphi^{(0)}$ is determined by the number of equality constraints and the value of the initial size of the polyhedron so that this parameter can be varied by the user at the initiation of the search. The number of equality constraints, m, is used so that the initial tolerance is proportional to the available hyperspace.

$$\varphi^{(0)} = 2*(m+1)\,t \qquad (D.2)$$

where

t = size of a side in the initial polyhedron

m = number of equality constraints

$x_i^{(k)}$ = i^{th} component of the polyhedron at stage k of the search

x_{r+2} = the vertex corresponding to the centroid of the polyhedron.

r = (m-n) = number of degrees of freedom, since when an equality constraint is specified this automatically reduces the number of independent variables by one. In the event that r < 3, then r is set equal to 3 so that a triangular polyhedron can be established.

$\varphi^{(k-1)}$ was the value of the tolerance during the previous stage.

$$\frac{(m+1)}{(r+1)}\sum_{i=1}^{r+1} | x_i^{(k)} - x_{r+2}^{(k)} | = \left[\frac{(m+1)}{(r+1)}\sum_{i=1}^{r+1}\sum_{j=1}^{m+1} [(x_{ij}^{(k)} - x_{r+2}^{(k)})^2]\right]^{1/2}$$

(D.3)

$x_{ij}^{(k)}$ j=1....n are the coordinates of the i^{th} vertex of the flexible polyhedron and therefore $\varphi^{(k)}$ is set to the minimum of either the previous value of the tolerance or the average distance from each $x_i^{(k)}$ i=1...r+1, to the centroid of the polyhedron and hence φ must be positive and non increasing in value.

i.e. $\varphi^{(0)} \geq \varphi^{(1)} \geq ..... \varphi^{(k)} ..... \geq 0$

Hence φ becomes progressively smaller as the average distance between the vertices and the centroid shrinks until at the point of solution, when $\varphi^{(k)} \leq$ tolerance.

The constraints functional t(x) is defined as the positive square root of the sum of the squares of all the violated constraints, i.e.

$$t(x) = \left(\sum_{i=1}^{m} h_{i(x)}{}^2 + \sum_{i=m+1}^{p} \eta_i \, g_i(x)^2 \right)^{1/2} \qquad \text{(D.4)}$$

$\eta_i = 0$ for $g_i(x) \geq 0$

$\eta_i = 1$ for $g_i(x) \leq 0$

The value of the constraints functional only has to be reduced to less than the value of the tolerance during that stage of the search.. That is, it does not have to produce a feasible point, only a *'near-feasible'* point.

i.e. if

i) $t(x^{(k)}) = 0$: vector is feasible

ii) $0 \leq t(x^{(k)}) \leq \varphi^{(k)}$: vector is near-feasible

iii) $t(x^{(k)}) \geq \varphi^{(k)}$: vector is non-feasible.

In the search for the minimum, only feasible or near-feasible points are accepted to continue the optimization. If the vector $x^{(k)}$ is non-feasible then it is changed by minimizing $t(x^{(k)})$. Thus a new polyhedron is created $x_i{}^{(s)}$ i=1...n+1, and the unconstrained procedure of Nedler and Mead is used to minimize $t(x)$.

The termination of this part of the search is accepted when $t(x^{(s)}) \leq \varphi^{(k)}$

If the simplex is reflected out of the feasible region, the minimization of $t(x)$ will return it to the feasible region. However, depending upon the nature of the objective function, the point at which it re-enters the feasible is critical to the next stage in the search. For

example, if the value of the functional is greater at this re-entry point than the other points of the simplex, then a reflection will take the point out of the feasible once again. Therefore, quadratic intrerpolation is used so that a point can be determined near to the position where the constraints are only just non-violated. That is, if $x^{(s)}$ is a feasible point and $x^{(s-1)}$ is the nearest non-feasible point obtained by the minimization of $t(x)$, then any point that lies on the line between $x^{(s)}$ and $x^{(s-1)}$ can be represented by:

$$x = x^{(s)} + \lambda s \qquad 0 \leq \lambda^{(s)} \leq \lambda^{*(s)} \tag{D.5}$$

$$\lambda^* = [\sum_{j=1}^{n} (x_j{}^{(s-1)} - x_j{}^{(k)})^2]^{1/2} = \text{distance from } x^{(s)} \text{ to } \hat{x}^{(s-1)} \tag{D.6}$$

$$s = \frac{(x^{(s-1)} - x^{(s)})}{[\sum_{j=1}^{n} (x_j{}^{(s-1)} - x_j{}^{(k)})^2]^{1/2}} \tag{D.7}$$

Now assuming $Z(x) = \sum_{i=1}^{\hat{p}} g_i{}^{(x)}$ where $\hat{p}$ = total number of constraints violated. then

the values can be assigned:

$$z_1 = Z(\hat{x}^{(s)}),\ z_2 = Z(\hat{x}^{(s)} + 0.5\lambda\hat{s}),\ z_3 = Z(\hat{x}^{(s-1)})$$

That is, z_1, z_2 and z_3 are the values of $Z(x)$ at three equally spaced points along the vector $x^{(s)}$ to $x^{(s-1)}$ and because of the notation used, the value of z_1 will be non-zero even

though it lies in the feasible region. Threrefore, a quadratic interpolation can be applied between $x^{(s)}$ and $x^{(s-1)}$ with the point x^* required where $Z(x^*) = 0$.

The quadratic interpolation is of the form

$$y = \frac{(x-b)(x-c)f(a)}{(a-b)(a-c)} + \frac{(x-a)(x-c)f(b)}{(b-a)(b-c)} + \frac{(x-a)(x-b)f(c)}{(c-a)(c-b)} \qquad \text{(D.8)}$$

and since in this interpolation a,b and c are three equally spaced points they can be assigned the values,

a=0, b=0.5 and c=1.0.

Therefore,

$$Z(x) = 2z_1(x^2 - \tfrac{3}{2}x + \tfrac{1}{2}) + 4z_2(x^2 - x) + 2z_3(x^2 - \tfrac{1}{2}x)$$

$$\text{i.e. } Z(x) = x^2(2z_1 + 4z_2 + 2z_3) + x(-3z_1 - 4z_2 - z_3) + z_1 \qquad \text{(D.9)}$$

The point of interest is where $Z(x) = 0$, when

$$x^* = \hat{x}^{(s)} + \left(\frac{\beta + \sqrt{\beta^2 - 8\alpha z_1}}{4\alpha}\right)\lambda^* \hat{s} \qquad \text{(D.10)}$$

$\alpha = z_1 + 2z_2 + z_3$ and $\beta = 3z_1 + 4z_2 + z_3$

and only the positive square roots of $(\beta^2 - 8\alpha z_1)$ are considered.

APPENDIX E

UNIDIMENSIONAL LINE MINIMIZATIONS

E.1 Quadratic Interpolation

This is an efficient technique to find the minimum of a single variable. To initially bracket the minimum, a small step Δx is taken in one direction. If this step has improved the value of the objective function or constraints functional, then a second step is taken in the same direction of magnitude $2\Delta x$. However, if the value of f(x) at $(x + \Delta x)$ has increased, then a step is taken $(x - 2\Delta x)$ and the value of the objective function calculated at this position. Fig(E.1) shows the successive steps until four equally spaced points bracket the minimum. The value of x furthest away from the point with the lowest value of the objective function is discarded and a point inserted equidistant to the two extreme positions bracketing the minimum. By differentiating the quadratic for the three remaing points the expression

$$x_{min} = x_2 + \frac{\Delta x\,[f(x_1) - f(x_3)]}{2\,[f(x_1) - 2f(x_2) + x(x_3)]} \qquad \text{(E.1)}$$

can be obtained and the process repeated with the value of Δx halved.

Problems exist if $f(x_1) - 2f(x_2) + f(x_3) = 0$, since the above equation is then singular. In this special case, the value of the point with the largest objective function value is displaced by $\frac{\Delta x}{10}$ and the process repeated.

E.2 Golden Section Interpolation

This technique is based upon the splitting of a line into two segments with the ratio of the whole line to the larger segment being equal to the ratio of the larger segment to the smaller segment. Bracketing of the minimum is performed in the same way as for the quadratic interpolation, to obtain the points x_1, x_2 and x_3, for which the following relationship can be applied:

$$\frac{x_2 - x_1}{x_3 - x_1} = R_1 \text{ and } \frac{x_3 - x_2}{x_3 - x_1} = 1 - R_1. \qquad \text{(E.2)}$$

If a new trial point x_4 is taken between x_2 and x_3 then the new ratio can be assumed

$$\frac{x_4 - x_2}{x_3 - x_1} = R_2 \qquad \text{(E.3)}$$

Therefore, the next bracket will be either of length $(R_1 + R_2)$ or $(1 - R_1)$. To minimize the worst possible case, the value of R_2 is chosen to make the bracketing intervals equal

i.e. $(R_1 + R_2) = (1 - R_1)$

and hence $$R_2 = (1 - 2R_1) \qquad \text{(E.4)}$$

Finally, it is assumed that for the bracketing of the previous interval, the same technique was applied, and therefore,

$$\frac{x_4 - x_2}{x_3 - x_2} = \frac{x_2 - x_1}{x_3 - x_1} \qquad \text{(E.5)}$$

$$\text{i.e. } \frac{R_2}{(1 - R_1)} = R_1 \qquad \text{(E.6)}$$

equating (E.4) and (E.6) $R_1^2 - 3R_1 + 1 = 0$, giving:

$$R_1 = \frac{3 - \sqrt{5}}{2} \text{ and } R_1 = \frac{3 + \sqrt{5}}{2}$$

of which only the first of these lie within the braket, i.e. $R_1 \sim 0.382$ and $(1 - R_1) \sim 0.618$.

Therefore, once the initial bracket has been obtained on the minimum of f(x), the last three values are designated $x_1^{(0)}, x_2^{(0)}$ and $x_3^{(0)}$, where $f(x_3^{(0)} \geq f(x_2^{(0)})$ and $\Delta^{(k)} = x_3^{(k)} - x_1^{(k)}$.

The search then follows the routine:

$x_4^{(k)} = x_1^{(k)} + R_1 \Delta^{(k)}$

$x_5 = x_1^{(k)} + (1 - R_1) \Delta^{(k)}$

If $f(x_4^{(k)}) < f(x_5^{(k)})$ then $\Delta^{(k+1)} = (x_5^{(k)} - x_1^{(k)})$

and $x_1^{(k+1)} = x_1$, $x_3^{(k+1)} = x_5^{(k)}$.

If $f(x_4^{(k)}) > f(x_5^{(k)})$ then $\Delta^{(k+1)} = (x_3^{(k)} - x_4^{(k)})$

and $x_1^{(k+1)} = x_4^{(k)}$, $x_3^{(k+1)} = x_3^{(k)}$

If $f(x_4^{(k)}) = f(x_5^{(k)})$ then $\Delta^{(+1)} = (x_5^{(k)} - x_1^{(k)}) = (x_3^{(k)} - x_4^{(k)})$

and $x_1^{(k+1)} = x_1^{(k)}$, $x_3^{(k+1)} = x_5^{(k)}$

or $x_1^{(k+1)} = x_4^{(k)}$, $x_3^{(k+1)} = x_3^{(k)}$

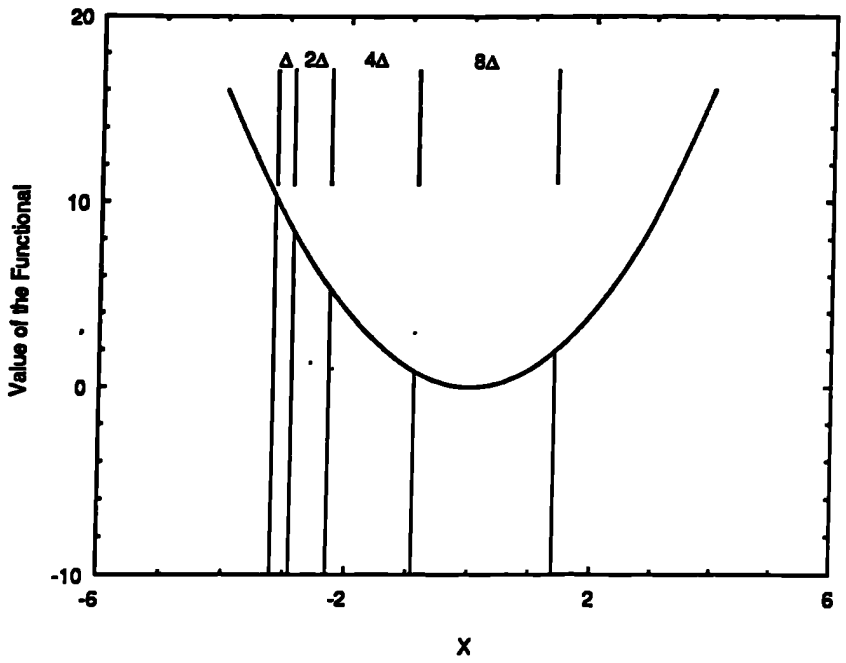

Fig E.1 One dimensional bracketing of a minimum.

APPENDIX F

TOROIDAL WINDING INDUCTANCE

The winding inductance of the toroidally wound actuator was found by using the simplifying assumption that the rotor is removed, which should not be of great significance for ferrite and rare-earth magnet arc devices.

Fig(F.1) shows the flux patten for one half of a 2-pole device.

The density of the equivalent current sheet is given by

$$J = \frac{NI}{2\pi r}$$

where N is the number of turns

I is the current

and r is the radius.

The Fourier series expansion of the square current sheet gives(for odd harmonics, n)

$$j = \frac{4J}{\pi} \sum_{n=1}^{\infty} \frac{\sin n\theta}{n}$$

or

$$j = \left\{ \frac{2NI}{\pi^2 r} \right\} \sum_{n=1}^{\infty} \frac{\sin n\theta}{n}$$

and using the substitutions $I_i = \frac{2NI}{\pi^2 R_i}$ and $I_0 = \frac{2NI}{\pi^2 R_0}$

$$j_0 = I_0 \sum_{n=1}^{\infty} \frac{\sin n\theta}{n} \text{ and } j_i = I_i \sum_{n=1}^{\infty} \frac{\sin n\theta}{n}$$

where the suffixes o and i refer to the outer and inner surfaces of the toroid in fig(F.1).

Using the technique of separation of variables, let the vector potential A, for each harmonic be given by

$$A = G(\theta) F(r)$$

where G and F are functions of θ and r respectively. The solution gives

$$A = (B \sin(k\theta) + C \cos(k\theta)) (D r^k + E r^{-k})$$

As the potential must vary according to the number of poles, then k =n and,

$$A = (B \sin(n\theta) + C \cos(n\theta)) (D r^n + E r^{-n})$$

And since the current density is a function of sin$n$ θ, then C = 0and the general equation for the vector potential becomes

$$A = (C_1 r^n + C_2 r^{-n}) \sin n\theta$$

Applying boundary conditions

region 1

as $r \rightarrow \infty, A \rightarrow 0$, therefore $C_1 = 0$, so

$$A_1 = C_2 r^{-n} \sin n\theta \tag{F.1}$$

region 2

$$A_2 = (C_3 r^n + C_4 r^{-n}) \sin n\theta \tag{F.2}$$

region 3

as $r \to 0, A \to 0$ so

$$A_3 = C_5 r^n \sin n\theta \tag{F.3}$$

At $r = R_o$, $B_{n1} = B_{n2}$, i.e $\frac{1}{R_0}\frac{\partial A_1}{\partial \theta} = \frac{1}{R_0}\frac{\partial A_2}{\partial \theta}$, therefore

$$n C_2 R_0^{-n} \cos n\theta = n(C_3 R_0^n + C_4 R_0^{-n}) \cos n\theta$$

$$C_2 R_0^{-n} = C_3 R_0^n + C_4 R_0^{-n}. \tag{F.4}$$

Also from Amperes law $H_{n1} - H_{n2} = \frac{I_1}{n} \sin n\theta$, therefore,

$$-(-n)\frac{C_2 R_0^{-n-1}}{\mu_0} \sin n\theta + \left\{\frac{n C_3 R_0^{n-1} - n C_4 R_0^{-n-1}}{\mu_0 \mu_r}\right\} \sin n\theta = \frac{I_1}{n} \sin n\theta$$

$$\mu_r n C_2 R_o^{-n-1} + n C_3 R_0^{n-1} - n C_4 R_0^{-n-1} = \frac{\mu_o \mu_r}{n} I_1 \tag{F.5}$$

At $r = R_i$, $B_{n2} = B_{n3}$, i.e. $\frac{1}{R_i}\frac{\partial A_2}{\partial \theta} = \frac{1}{R_i}\frac{\partial A_3}{\partial \theta}$, therefore,

$$n\,(C_3 R_i^n + C_4 R_i^{-n})\cos n\theta = nC_5 R_0^{-n}\cos n\theta$$

$$C_5 R_i^n = C_3 R_i^n + C_4 R_i^{-n} \qquad \text{(F.6)}$$

By applying Amperes law $H_{n2} - H_{n3} = \frac{I_2}{n}\sin n\theta$, therefore,

$$\frac{C_5 R_i^{n-1}}{\mu_o} n \sin n\theta + \left\{\frac{n C_3 R_i^{n-1} - n C_4 R_i^{-n-1}}{\mu_o \mu_r}\right\} \sin n\theta = -\frac{I_2}{n}\sin n\theta$$

$$-\mu_r n C_5 R_i^{n-1} + nC_3 R_i^{n-1} - nC_4 R_i^{-n-1} = \frac{\mu_0 \mu_r}{n} I_2 \qquad \text{(F.7)}$$

Using equations(F.4) to (F.7), it is possible to solve for C_2 to C_5, but simplifications of the equations are possible by assuming the following:

1) $\mu_r = \infty$

2) $I_1 = I_2$

From (F.5) $\quad nC_2 R_o^{-n-1} = \frac{\mu_0}{n} I_1$, therefore,

$$C_2 = \frac{\mu_0 I_1}{n^2 R_o^{-n-1}}$$

therefore in (F.1) $\quad A_1 = \frac{\mu_o I_1}{n^2 R_0^{-n-1}} \sin n\theta$

$$B_{radial,r=R_o} = \frac{1}{R_o}\frac{\partial A_1}{\partial \theta}\,(r = R_0) = \frac{1}{R_0}\frac{n\mu_0 I_1 R_o^{-n}\cos n\theta}{n^2 R_o^{-n-1}}$$

$$B_{radial,r=R_o} = \frac{\mu_0 I_1}{n} \cos n\theta$$

Substitute for I_1

$$B_{radial,r=R_o} = \frac{\mu_0 2NI}{n\pi^2 R_O} \qquad \text{(for all odd n)}$$

Similarly from (F.7)

$$nC_5 R_i^{n-1} = \frac{\mu_0 I_2}{n} \text{ therefore } C_5 = \frac{\mu_0 I_2}{n^2 R_i^{n-1}}$$

in (F.3) $A_3 = \frac{\mu_0 I_2}{n^2 R_i^{n-1}} r^n \sin n\theta$ therefore,

$$B_{radial,r=R_i} = \frac{1}{R_0}\frac{\partial A_3}{\partial \theta} \ (r=R_i) = \frac{\mu_o I_2}{n} \cos n\theta$$

Substitute for I_2

$$B_{radial,r=R_i} = \frac{\mu_o 2NI}{n\pi^2 R_i} \cos n\theta$$

The elemental flux at the surface due to the current sheet is given by

$$\partial\Phi = \frac{\mu_0 2NI}{n\pi^2 R} \cos n\theta \, R \, W_s \, \partial\theta = \frac{2\mu_0 NI W_s}{\pi^2 n^2} \cos n\theta \partial\theta$$

The inductance is defined as $L = \frac{1}{I^2}\sum i \, \partial \, \Phi$

$$\partial\Phi = \int_0^{\theta} \partial\varphi = \frac{2\mu_o N I W_s}{\pi^2 n^2} \sin n\theta$$

and $i = \frac{NI}{2\pi R} R\partial\theta = \frac{NI}{2\pi}\partial\theta$

therefore $i \,.\, \partial\theta\Phi = \frac{\mu_0 (NI)^2 W_s}{\pi^3 n^2} \sin n\theta \, \partial\theta$

For the inductance L_n of each harmonic, n:

$$L_n = \frac{4}{I^2} \int_o^{\theta} \frac{2\mu_0 (NI)^2 W_s}{\pi^2 n^2} \sin n\theta$$

$$L_n = \frac{4\mu_0 N^2 W_s}{\pi^3 n^3} \cos n\theta \Big|_o^{\pi} \qquad \text{(for odd n summed to infinity}$$

$$L = \sum_1^{\infty} L_n = \sum \frac{8\mu_0 N^2 W_s}{\pi^3 n^3} \qquad \text{for each odd harmonic}$$

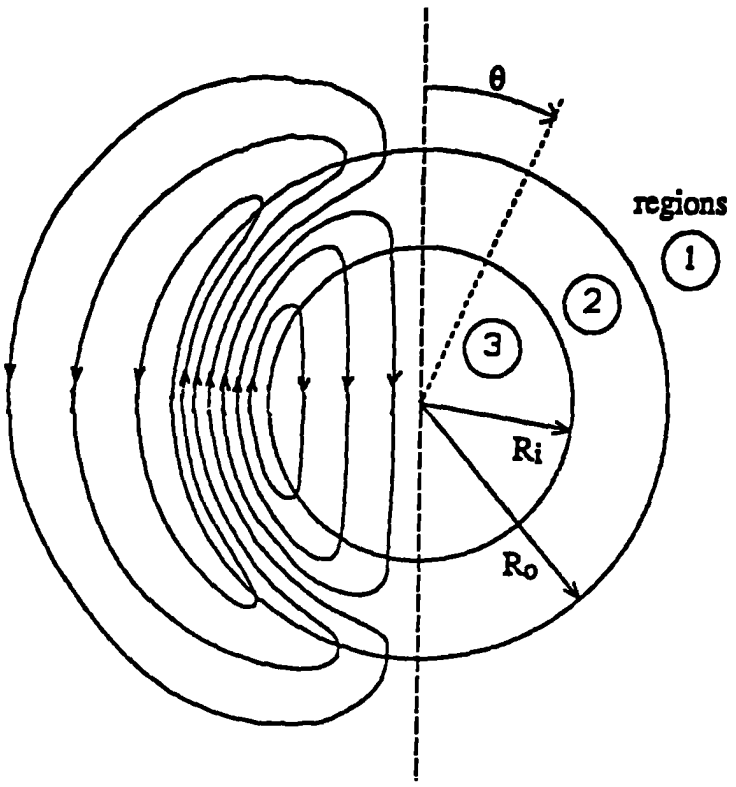

Fig F.1 Flux pattern for a 2-pole LAT with the rotor removed. For clarity, only the flux pattern for the left hand winding is shown.

APPENDIX G

TOROIDAL ACTUATOR ROTOR INERTIAS

G.1 Cylindrical Shaft Rotor Inertia

The moment of inertia of the cylinder illustrated in fig(G.1.a) can be evaluated from:

$$J = \int mr^2 \tag{G.1}$$

and the mass of the cylinder is $m = 2\pi r\,\delta r\, w\,\sigma$ (G.2)

therefore $$J = \int_{r=r_i}^{r=r_o} 2\pi w\,\sigma\, r^3\,\delta r$$

and hence $$J = \frac{\pi w\,\sigma}{2}\,[r_o^4 - r_i^4] \tag{G.3}$$

adapting equation(G.3) to the toroidal actuator of fig(5.10) gives

$$J = \pi\frac{[W_s - 2L_g]\sigma_{steel}(\frac{I_d}{2})^4}{2} + \frac{\sigma_{mag}[W_s - 2L_g]\,p\,\psi_r((\frac{I_d + 2L_m}{2})^4 - (\frac{I_d}{2})^4)}{4}$$

(G.4)

where σ_{steel} is the density of steel

σ_{mag} is the density of magnet

Therefore, for first order design the torque/inertia improves as the allowable $\frac{\Psi_r}{\Psi_s}$ is increased, since the inertia of the inner steel and shaft remains constant. However, the maximum angular displacement attainable is subsequently decreased.

G.2 Slab Rotor Inertia

Fig(G.1.b) shows the construction for a slab rotor design and separates the inertia into three parts. These being: the inertia associated with the slab iron, the segment iron and the magnets respectively

$$J_{total} = J_{slab} + J_{segments} + J_{magnets} \tag{G.5}$$

$$J_{slab} = \frac{I_{d1}\, I_{d2}}{3}\, \sigma_{steel}\, (W_s - 2\, L_g)\, \left(\left\{\frac{I_{d1}}{2}\right\}^2 + \left\{\frac{I_{d2}}{2}\right\}^2\right) \tag{G.6}$$

Fig(G.1.c) shows the iron segments and the inertia can be evaluated considering:

i.e. the area of the strip at y = $a_{segment} = x\, \delta y$ (G.7)

$$a_{segment} = \int_{y=b}^{y=r} \sqrt{r^2 - y^2}\, \delta y \tag{G.8}$$

and hence the mass $$m_{segment} = (W_s - 2\, L_g)\, \sigma_{steel} \int_{y=b}^{y=r} \sqrt{r^2 - y^2}\, \delta y \tag{G.9}$$

therefore,

$$J_{segments} = (W_s - 2L_g)\,\sigma_{steel} \int_{y=\sqrt{r^2-y^2}}^{y=r} 2y^2\sqrt{r^2-y^2}\,\delta y$$

The 2 is introduced because there are two segments.

which is a standard integral with the solution

$$J_{segments} = 2(W_s - 2L_g)\,\sigma_{steel} \Big|_{y=\sqrt{r^2-y^2}}^{r} -\frac{y}{4}\sqrt{(r^2-y^2)^3} + \frac{r^2}{8}\sqrt{r^2-y^2} + \frac{r^4}{8}\sin^{-1}\frac{y}{r}\Big|$$

i.e.

$$J_{segments} = 2(W_s - 2L_g)\,\sigma_{steel}\left(\frac{(D_{iron})^4}{64}\left(\frac{\pi}{2} - \sin^{-1}\left(\frac{I_{d2}}{D_{iron}}\right)\right) + \frac{I_{d1}\,I_{d2}}{16}\left(\left\{\frac{I_{d1}}{2}\right\}^2 - \frac{D_{iron}^{\,2}}{8}\right)\right) \qquad \text{(G.10)}$$

Assuming the magnets to be radial, which will slightly overestimate the magnet inertia, their inertias can be evaluated in the same way as equation(G.4), i.e.

$$J_{magnets} = \frac{p\,\psi_r}{4}(W_s - 2L_g)\,\sigma_{mag}\left(\left(\frac{I_{d1}}{2}\right)^4 - \left(\frac{I_{d1}}{2}\right)^4\right) \qquad \text{(G.11)}$$

Therefore,

$$J = \frac{I_{d1}\,I_{d2}}{3}\,\sigma_{steel}\,(W_s - 2L_g)\left(\left\{\frac{I_{d1}}{2}\right\}^2 + \left\{\frac{I_{d2}}{2}\right\}^2\right) +$$

$$\frac{p\,\psi_r}{4}(W_s - 2L_g)\,\sigma_{mag}\left(\left(\frac{I_{d1}}{2}\right)^4 - \left(\frac{I_{d1}}{2}\right)^4\right)$$

$$2(W_s - 2L_g)\,\sigma_{steel}\left(\frac{(D_{iron})^4}{64}\left(\frac{\pi}{2} - \sin^{-1}\left(\frac{I_{d2}}{D_{iron}}\right)\right) + \frac{I_{d1}\,I_{d2}}{16}\left(\left\{\frac{I_{d1}}{2}\right\}^2 - \frac{D_{iron}^{\,2}}{8}\right)\right)$$

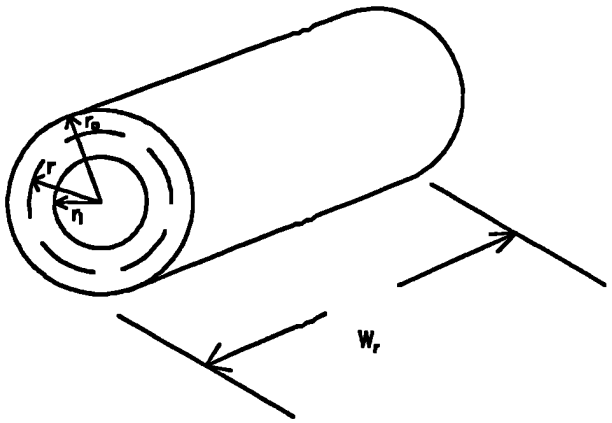

FigG.1.a Cylindrical rotor.

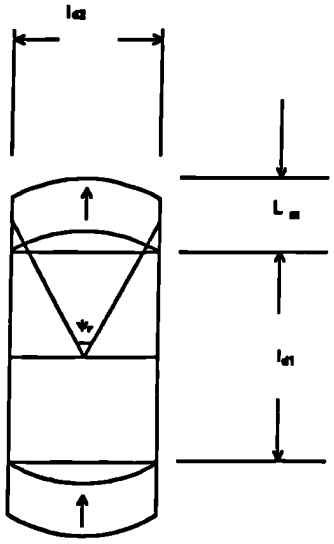

FigG.1.b Slab rotor.

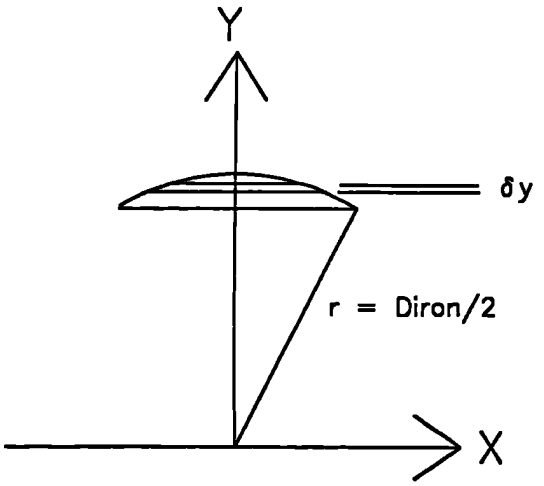

FigG.1.c Exploded view of segments.

FigG.1 Cylindrical and slab toroidal actuator type rotors.

APPENDIX H

PUBLICATION RESULTING FROM THIS THESIS

Widdowson G.P., Howe D., and Evison P.R., 'Computer aided optimization of rare-earth permanent magnet actuators', Proceedings of the I.E.E. Computation in electromagnetics, Publication No. 350, 1991.